



Title	Studies on Corrosion Resistance and its Mechanism of Carbon Nanofibers in Alkaline Electrolyte
Author(s)	佐藤, 優樹
Citation	北海道大学. 博士(総合化学) 甲第14893号
Issue Date	2022-03-24
DOI	10.14943/doctoral.k14893
Doc URL	http://hdl.handle.net/2115/88667
Type	theses (doctoral)
File Information	SATO_Yuki_20220607.pdf



[Instructions for use](#)

Studies on Corrosion Resistance and its Mechanism of Carbon Nanofibers in Alkaline Electrolyte

カーボンナノファイバーのアルカリ電解液中における
耐食性と耐食機構に関する研究

By Yuki SATO

(佐藤 優樹)

A Thesis

Submitted to the Graduate School of Chemical Sciences and
Engineering in Partial Fulfillment of the Requirement for the

Degree of Doctor of Philosophy

at Hokkaido University

Laboratory of Interfacial Electrochemistry
Graduate School of Chemical Sciences and Engineering

March 2022

Seeing is believing.

- *Microscopies always illuminate the truth.*

Contents

Chapter 1	General introduction	1
1-1	Overview of the carbon materials	3
1-2	Importance of aqueous zinc-air rechargeable batteries	4
1-2-1	Fundamental and working mechanism	4
1-2-2	Air electrode	7
1-2-3	Role of the carbon materials in the air-electrode	9
1-3	Carbon corrosion in energy devices	12
1-3-1	Fundamentals of the carbon corrosion	12
1-3-2	Examples of carbon corrosion in the energy devices	14
1-3-3	Measures for the carbon corrosion	18
1-4	Aim of this thesis	20
1-4-1	Platelet-type carbon nanofibers and their properties	21
1-4-2	Objectives of this thesis	22
1-5	Outlines of this thesis	23
1-6	References	24
Chapter 2	Characterizations of pCNFs	34
2-1	Introduction	34
2-2	Experimental	35
2-2-1	Carbon materials used in this study	35
2-2-2	Synthesis of pCNFs via liquid-phase carbonization using an AAO template	36
2-2-3	Electron microscopy observations	37
2-2-4	X-ray diffraction analysis	37
2-2-5	Raman scattering spectroscopy	38
2-2-6	Nitrogen adsorption/desorption analysis	38
2-3	Results and Discussion	39
2-3-1	SEM/TEM observations and temperature dependency of nanostructure	39
2-3-2	XRD study of graphitization degree	43
2-3-3	Raman study of carbon materials	45
2-3-4	BET surface areas	47
2-3-5	Discussion	48
2-4	Conclusions	50
2-5	References	51

Chapter 3 Corrosion of pCNFs at high potentials in alkaline electrolyte	54
3-1 Introduction	54
3-2 Experimental	54
3-2-1 ILSEM study	54
3-2-2 XPS and Raman measurements	57
3-2-3 Wettability measurements	58
3-3 Results and Discussion	58
3-3-1 ILSEM and TEM studies	58
3-3-2 Characterization of anodized carbon materials by XPS and Raman	66
3-3-3 Electron-energy loss spectroscopy analysis	71
3-3-4 Wettability of anodized carbon materials	73
3-3-5 Mechanism of the slow degradation of pCNFs	76
3-4 Conclusions	80
3-5 References	81
Chapter 4 OER activity and durability of pCNF/CFCO hybrid electrode	84
4-1 Introduction	84
4-2 Experimental	84
4-2-1 Metal-oxide electrocatalyst preparation	84
4-2-2 Electrocatalytic activity evaluation by the rotating-disk electrode system	85
4-2-3 Durability test	86
4-2-4 Characterization techniques	87
4-3 Results and Discussion	87
4-3-1 Characterizations of metal-oxides used in this study	87
4-3-2 OER activity of carbon/CFCO electrodes	88
4-3-3 ORR activity of carbon/CFCO electrodes	92
4-3-5 Durability of carbon/CFCO electrodes	94
4-3-6 Characterization of carbon/CFCO electrodes after the durability tests	97
4-3-7 TEM observation of pCNF after the durability tests	99
4-3-8 Discussion	100
4-4 Conclusions	103
4-5 References	104

Chapter 5 Air electrode performance of gas-diffusion electrodes using pCNFs	106
5-1 Introduction	106
5-2 Experimental	107
5-2-1 Hybridization of metal-oxides and pCNF via solvothermal synthesis	107
5-2-2 Electrocatalytic activity evaluation by the rotating ring-disk electrode system ..	109
5-2-3 GDE study	110
5-2-4 Characterization	112
5-3 Results and Discussion	112
5-3-1 Characterization of carbon/metal oxide hybrids	112
5-3-2 Improved OER/ORR activity by carbon/metal oxide hybridization	116
5-3-3 Electrocatalysis evaluation by the gas-diffusion electrode tests	122
5-3-4 Characterization of the gas-diffusion electrode after the durability tests	125
5-3-5 Discussion	132
5-4 Conclusions	135
5-5 References	136
Chapter 6 General Conclusions and Future Prospects	140
6-1 Conclusions	140
6-2 Future prospects	143
6-3 References	146
Lists of academic contributions	148
Acknowledgments	153

Chapter 1
General introduction

Chapter 1 General Introduction

The United Nations adopted the 17 sustainable development goals (SDGs) in 2015 as a universal call [1]. The SDGs highlight the sustainable global challenges in different fields, including society, blue growth, peace, justice, climate change, and environmental degradation. So many solutions have been already proposed to achieve these goals and to cope with a low-carbon society, attention is being paid to developing eco-friendly energy conversion and storage systems. However, this development needs to be done while maintaining the business development that has taken place to date. Electrochemical energy conversion and storage systems, such as the electrochemical water splitting, fuel cells, metal-air rechargeable batteries, and other related devices, have been considered to be promising candidates due to the low emission of pollution, improvability of energy efficiency of sustainable energies such as solar, wind and hydraulic power due to the higher energy density. In order to realize these electrochemical energy conversion systems, it is necessary to research and develop technologies for power grids, device control technology, and materials that make up the devices. Typically, electrochemical energy conversion devices contain electrolytes and electrodes. The electrode materials directly affect the electrochemical performance in these components because the electrochemical reactions, which convert chemical energy to electrical energy, occur on the electrode surface. Thus, electrode materials developments are critical to obtaining superior electrochemical properties [2, 3].

Among the electrode materials, carbon materials primarily cover many applications because of the earth-abundance, lightweight, higher electrical conductivity, relatively large surface areas, chemical stability, and ease of processability [3-6]. Due to these advantages, for instance, carbon materials are used in lithium-ion batteries [7-9], electrochemical capacitors [10-12], polymer

electrolyte fuel cells (PEMFC) [13-15], and zinc-air rechargeable batteries (ZAB), which is one of the promising new-generation batteries because of the larger energy densities [16-19]. For such applications, many types of carbon materials, such as carbon nanotubes [20, 21], graphene [22, 23], carbon blacks [24, 25], and carbon nanofibers [26, 27], have attracted increased attention. However, they are not necessarily stable in the operating environment of such electrochemical energy devices due to the anodic corrosion, as speculated from the pH-potential diagram (Figure 1-1) [28, 29]. Hence, to enhance the carbon materials' lifetime as electrode materials, improvement of the corrosion resistance is needed. This thesis study tried to tune the carbon materials' corrosion resistance by optimizing nanocarbon nanostructure. In this introduction part, firstly, the overview and fundamentals of carbon materials are briefly introduced. Secondary, the detail of the usage of carbon materials in the energy devices, especially ZAB, including the operation fundamental of the devices, is described. Then, past studies on carbon materials' corrosion in the energy devices and its measures are briefly reviewed. Finally, the objectives of this thesis and the approaches of this thesis study are given.

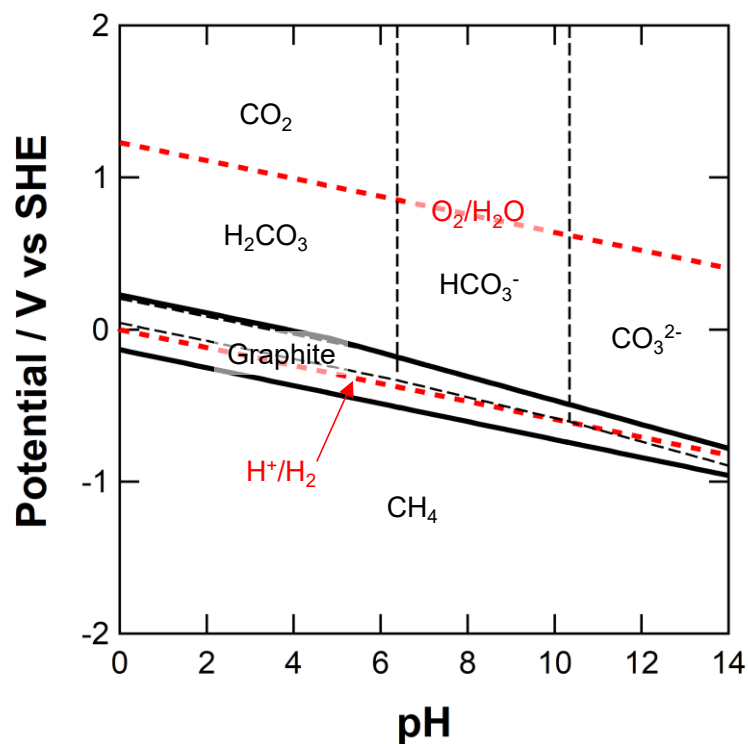


Fig. 1-1 Potential-pH equilibrium diagram for the carbon-water system at 25°C [28].

1-1 Overview of the carbon materials

The properties of carbon strongly depend on the nanostructure and the electronic state. For example, diamond and graphite, allotropes of carbon, have opposite physicochemical properties from the viewpoint of electrical conductivity, *i.e.*, diamond is the insulator material, while graphite is the conductive material. This difference comes from the electric state of carbon: – sp^3 carbon-rich or sp^2 carbon-rich. Such electronic state also affects various properties, such as mechanical properties, electronic properties, and color [30]. As the electrode materials, sp^2 rich carbon materials, *i.e.*, the graphite-based materials including carbon black, are often considered, and they are classified by the sp^3/sp^2 ratio, crystalline structure, stacking state of the graphene, surface area, and macro-structures like fibers, particles, or tubes. Figure 1-2 shows the primary carbon materials. Such various structures and properties provide the broader application of the carbon materials, and their corrosion resistance as the electrode materials are entirely different. The corrosion behavior of a range of carbon materials is discussed in the following sections in detail.

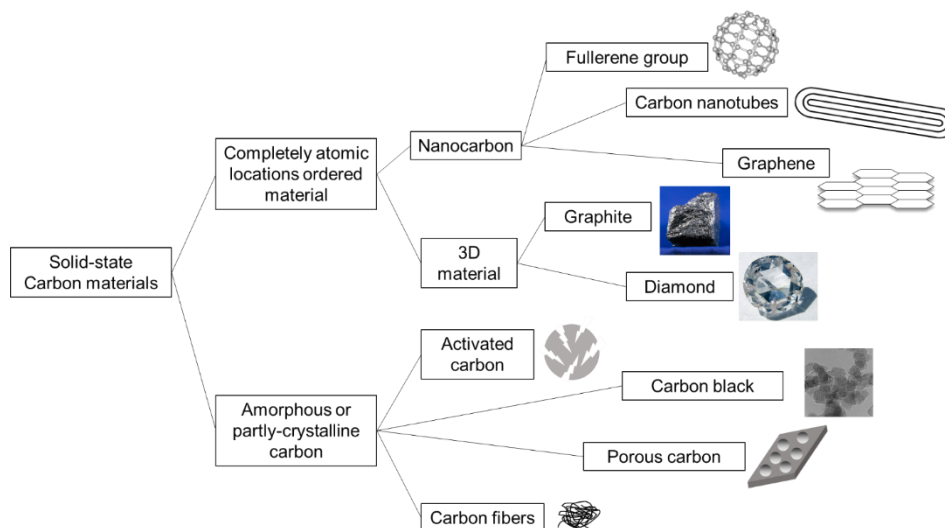


Fig. 1-2 Major carbon materials and their structure.

The picture of fullerene is cited from <https://commons.wikimedia.org/w/index.php?curid=350254> under the Creative Commons Attribute-Share Alike 3.0 unported license.

The picture of the diamond is cited from <https://www.flickr.com/photos/jurvetson/156830367> under the Creative Commons Attribution 2.0 unported license.

1-2 Importance of aqueous zinc-air rechargeable batteries

Goal No. 9 of the SDGs, "Build resilient infrastructure, promote inclusive and sustainable industrialization and foster innovation", emphasizes the need for not only durable and ubiquitous infrastructure but also sustainable infrastructure technologies for energy use. To achieve this goal in the traffic infrastructures, including buses and trucks, motorization using portable batteries is one of the options because of the lower environmental load compared with the current petrol-type engines. Such batteries are required the same level of energy densities as the current petrol engines [31, 32]. As large energy densities batteries, many candidates are proposed nowadays, and zinc-air rechargeable batteries (ZABs) are promising candidates because their relatively high theoretical energy density exceeds 1000 W h kg^{-1} [33-35]. This section describes the fundamentals and advantages of ZAB and the technological problems to be solved. Then, the importance of carbon materials in ZAB will also be discussed.

1-2-1 Fundamental and working mechanism

As mentioned above, rechargeable batteries with higher energy density and durability than lithium-ion batteries are required to promote the electrification of vehicles. Such batteries realization is desired for the motorization of vehicles and the higher performance information and communication equipment, energy storage for the clean energies, and electrification of airplanes. Each application can contribute to achieving the SDGs, and thus the development of such high-performance rechargeable batteries is important [36]. As the candidates of such batteries, many types, including metal-sulfur, fluoride-shuttle, Ni-MH, are proposed as candidate batteries. Among them, an alkaline-aqueous electrolyte type ZAB has the following advantages: (1) high theoretical energy density, which is close to the current internal combustion engine (Figure 1-3), (2) better safety than organic electrolyte type one, (3) high ionic conductivity resulting in high power density.

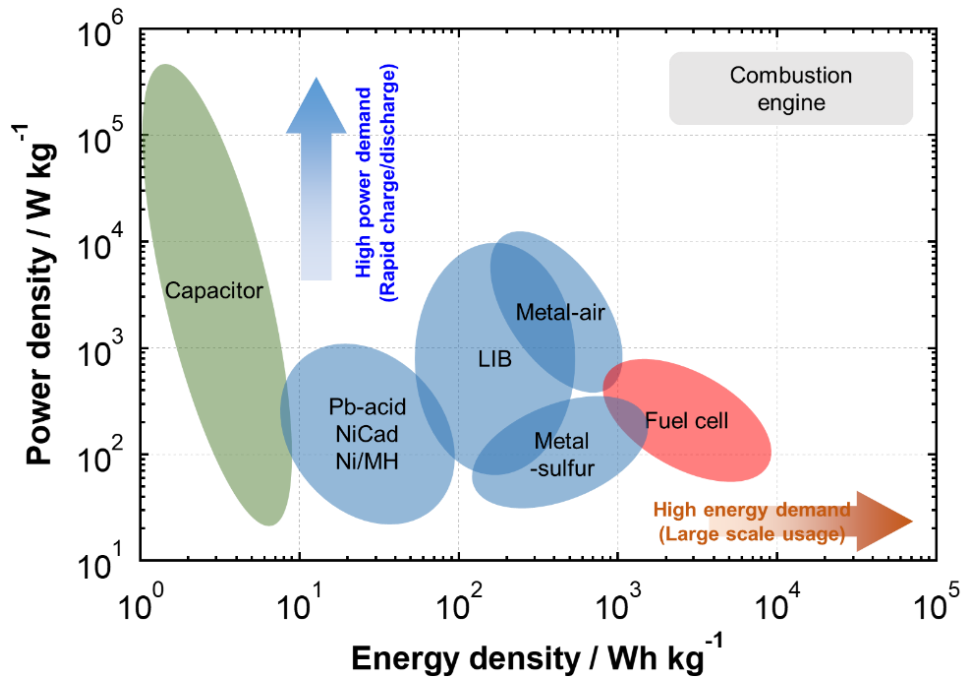


Fig. 1-3 Ragone plots comparing the performance of various batteries (energy density vs. output density). This plot is described with reference [37, 38].

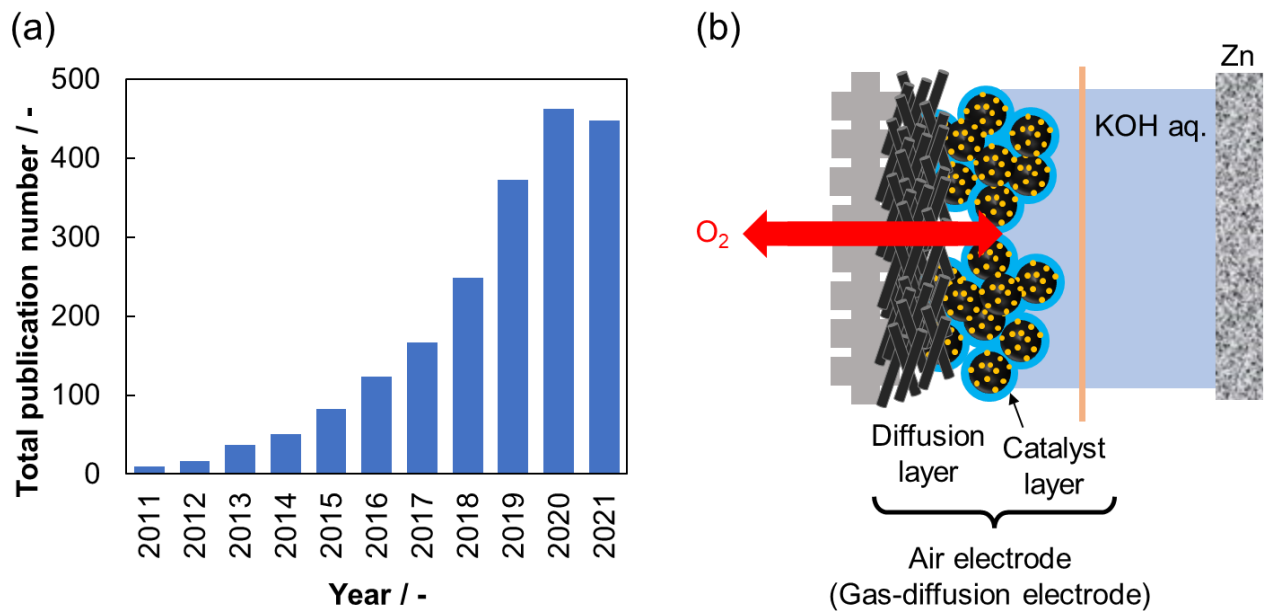
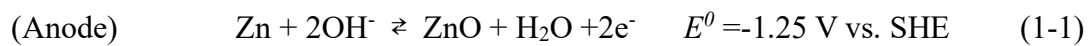


Fig. 1-4 (a) The number of publications on zinc-air batteries in the past 11 years (data from Web of Science) and (b) schematic illustration of a zinc-air rechargeable battery.

Due to these advantages, ZAB has been recently studied actively, and the number of papers related to ZAB increases exponentially year by year (Figure 1-4a). The ZAB consists of a zinc anode and an air cathode. The electrolyte to be used is typically a highly concentrated KOH aqueous solution (over 4.0 mol dm^{-3} , $\text{pH} > 14$). The active cathode material is oxygen in the air; thus, we can form a low-weight rechargeable battery. The schematic illustration of ZAB is shown in Figure 1-4b, and the electrochemical reactions of the ZAB can be described as follows:



The standard electrode potentials of the anode and cathode are -1.25 V vs SHE and 0.40 V vs SHE at $\text{pH} = 14$, respectively, and hence, the theoretical emf becomes 1.65 V . This value is enough higher than the Ni-H system (1.20 V), and this large emf with low weight provides high theoretical energy density. However, three main issues need to be addressed to commercialize such attractive ZABs [39].

- (1) Degradation of the anode materials (dendrites deposition and morphology change)
- (2) CO_2 poisoning (ionic conductivity degradation and carbonate salt formation)
- (3) Large overpotentials of charge/discharge reactions on the air electrodes
- (4) Degradation of the air electrode materials

Regarding issue (1), some researchers reported that organic additives in the electrolyte effectively inhibit the growth of such dendrites [40]. Furthermore, for issue (2), Zhao *et al.* demonstrated that the hydrogel type electrolyte inhibits pH change and carbonate salt formation, resulting in the long-term ZAB operation [33]. The recent studies on issues (3) and (4), including the air electrode's function, are discussed in the next section.

1-2-2 Air electrode

Normally, as an air electrode of ZAB, a gas-diffusion electrode, which can carry out a gas supply from the backside of the electrode, is used. This electrode typically consists of the catalyst and gas-diffusion layers and the current collector (Fig. 1-4b). The gas-diffusion layer prevents the electrolyte leaking and enables the gas transfer during charge/discharge. Due to its porous structure, the triple-phase boundaries, which consist of the liquid phase (electrolytes), gas phase (air), and solid phase (electrocatalyst), can be established on the catalyst layer surface. As the diffusion layer, due to these requirements, hydrophobic carbon cloths or sheets are mainly used. On the catalyst layer, the charge/discharge reactions of the air electrode, *i.e.*, the oxygen evolution reaction (OER) and oxygen reduction reaction (ORR), occur (Fig. 1-5). This electrode reaction is described as (1-4).



The four-electron reaction pathway described in (1-4) results in a relatively large overpotential for both OER and ORR [41]. In order to promote both OER and ORR in alkaline media, a reversible air electrode with high durability is necessary for repeated charging/discharging.

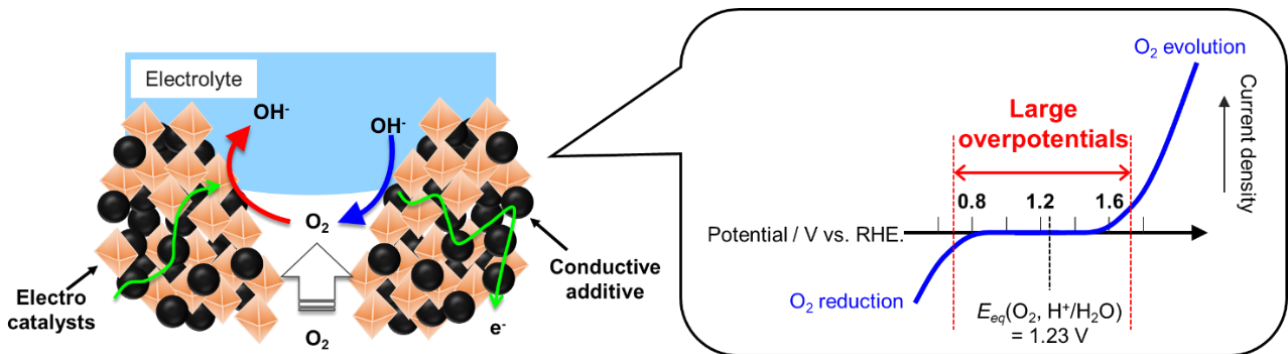


Fig. 1-5 Schematic illustrations of the catalyst layer of ZAB.

The state-of-the-art electrocatalysts for OER are typically composed of precious metals such as RuO₂ and IrO₂ [42, 43], and Pt/C hybrids are used for ORR [44]. Such materials are expected to be very rare and expensive; thus, they are not suitable for commercialization. Therefore, precious metal-free bi-functional electrocatalysts are demanded to realize ZAB commercialization. Recently, many

researchers reported highly active electrocatalysts for OER, ORR, or both reactions in alkaline media. Risch *et al.* reported that the perovskite $\text{Ba}_{0.5}\text{Sr}_{0.5}\text{Co}_{0.8}\text{Fe}_{0.2}\text{O}_{3-\delta}$ shows high OER activity in alkaline media [45]. Brownmillerite type metal oxide $\text{Ca}_2\text{FeCoO}_5$ and Fe-doped CoOOH were reported as active and stable electrocatalysts for OER in concentrated alkaline media by Habazaki *et al.* [46-48]. Moreover, Zahran *et al.* reported that the nickel sulfide nanowire hybrid with the carbon nitride shows notable OER activity, *i.e.*, the overpotential value under 50 mV [49]. Many ORR active materials have been developed. Perovskites containing Mn or Co species have been widely reported to show excellent ORR activity [50-54]. The carbon nanotubes and Co-based metal oxides hybrids also should be noted because of their remarkable ORR activity in alkaline media [55-57]. It must be added that the bi-functional electrocatalyst is better than the electrocatalyst that is active only one of them, to realize ZAB; however, the bi-functional electrodes were still less reported compared with the mono-functional OER or ORR catalysts because of the difference in the affinity of the intermediates for catalytic sites [58, 59]. Therefore, the materials with good inherent activity for OER usually show poor activity toward ORR and vice versa.

The common problem of these precious metal-group-free electrocatalysts is their not-enough moderate charge transfer characteristics as electrode materials [16, 60-62]. Some electrocatalysts with enough conductivity are already reported; however, their number is limited [62]. Thus, typically, these materials are hybridized or mixed with conductive materials such as carbon [15-18, 61], CeO_2 [63], Ni [64, 65], and some electron-conductive metal oxides [66, 67]. Among such conductive additives, carbon materials have advantages because of (1) co-catalysis for ORR, (2) good electrochemical characteristics, (3) lightweight, and (4) earth abundance. The following sections deeply discuss these advantages, weaknesses, and the detailed role of carbon materials.

1-2-3 Role of the carbon materials in the air-electrode

As described above, carbon materials are suitable conductive additives in ZABs. For instance, Alegre *et al.* tried to optimize the electrocatalysts and carbon black combination to obtain stable and high OER/ORR electrocatalysis [25, 68]. Moreover, the effect of carbon materials structure on ORR electrocatalytic properties was examined using various carbon supports [15, 69]. These studies revealed that carbon materials play vital roles in providing the conductive pathway and the ORR co-catalyst function so that the “Synergistic” effect of carbon and electrocatalysts were often discussed [16, 70-87]. Figure 1-6 compares the OER and ORR activities in 0.1 mol dm⁻³ KOH electrolyte and XANES spectra for Ba_{0.5}Sr_{0.5}Co_{0.8}Fe_{0.2}O_{3-δ} electrode with and without a carbon additive [70]. The carbon addition increased the current and decreased the overpotential for ORR. In addition, OER electrocatalytic activity was also enhanced (Fig. 1-6a). This behavior cannot be explained only by the electronic conductivity enhancement.

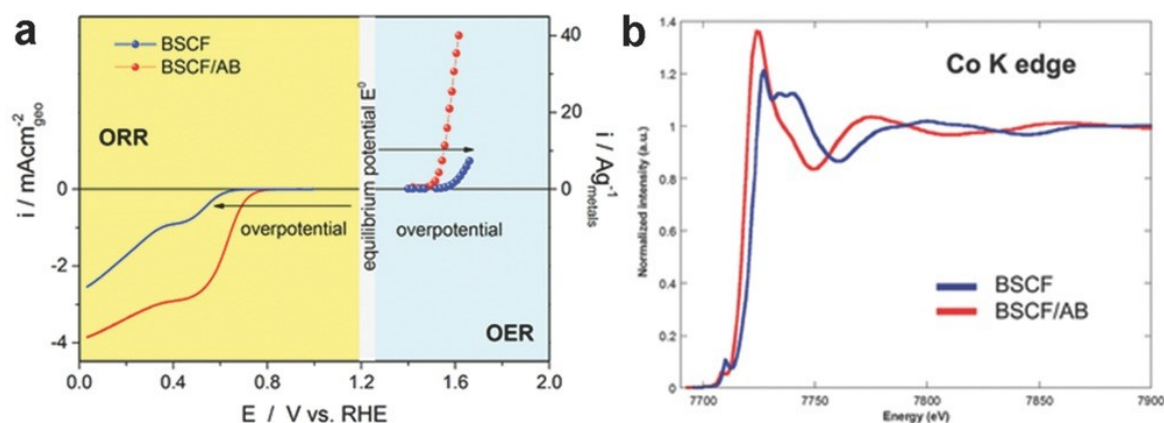


Fig. 1-6 (a) ORR and OER LSV curves of BSCF and BSCF/AB hybrid electrodes in O₂-saturated 0.1 mol dm⁻³ KOH electrolyte. (b) XANES spectra at the Co edge for the BSCF and BSCF/AB electrodes. Copyright 2017, Wiley-VCH [16].

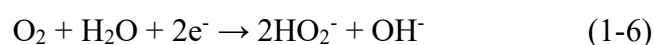
The first factor that needs to be considered is the effect of the electronic state (Fig. 1-7a). XANES spectra (Fig. 1-6b) after carbon addition clearly shows the reduced cobalt oxidation state. Such a reduced electronic state can provide more favorable adsorption energy of the oxygenated species, which may be responsible for the observed enhanced ORR/OER activities [16]. Similar electronic state modifications were also reported elsewhere [70-74].

The second factor is the spill-over effect (Fig. 1-7b). For ORR, there are three routes of the reaction ways, *i.e.*, directly 4 electrons, 2 electrons, and 2+2-electrons transfer pathway [16];

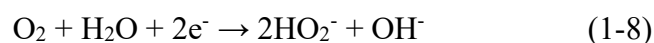
(1) Direct 4e⁻ pathway



(2) (2+2) e⁻ pathway



(3) 2e⁻ pathway



In general, carbon shows a low OER activity and moderate activity for the ORR in alkaline media [16, 88] because of easy molecular oxygen adsorption on the carbon surface. Additionally, the preferred ORR pathways on the carbon materials are estimated as the 2e⁻ pathway [88], *i.e.*, reaction (1-6) and (1-8). On the other hand, combinations with electrocatalyst like perovskite oxides accelerate the ORR complete by the following mechanisms: (1) HO₂⁻ products on the carbon materials spill over to the perovskite oxide surface, and they are reduced or decomposed according to (1-7) or (1-9), and (2) the rapid OH⁻ desorption from the carbon surface and adsorption to the perovskite oxide surface, because of the more favorable adsorption of OH⁻ on the perovskite oxides [16, 70, 75-80]. These adsorption/desorption events relax the ORR reaction barrier by releasing more active sites on the

carbon surface. This phenomenon is referred to as co-catalysis of carbon for ORR, and this concept has been widely accepted. In addition to ORR, recently, some researchers proposed the existence of such spill-over contribution for OER [77-81].

The third factor is forming a new phase at the interface (Fig. 1-7c). This factor is often discussed in the electrocatalyst/carbon materials hybrid [82-87]. For example, Zhao *et al.* reported that the hybridization of Cu nanoparticles and carbon nanotubes decreased the work function of carbon surfaces and improved the adsorption of hydroxyl ions onto the carbon surfaces, enhancing the OER/ORR activity [82]. In addition to such electronic state modification [83,84], the interfacial phase was reported to be developed and acted as the catalytic center for OER or ORR due to its adequate adsorption/desorption energy [85-87]. Thus, the direct loading of the electrocatalyst on the carbon surface is recently paid attention as the novel material design.

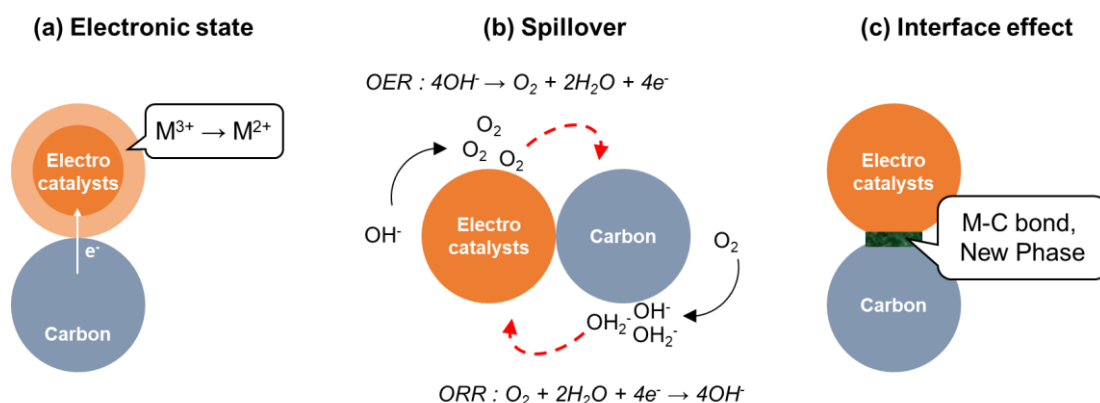


Fig. 1-7 Schematic illustrations of “Synergistic Effect” of electrocatalyst and carbon materials. These illustrations are described based on reference [16].

In summary, carbon plays the conductive support and ORR co-catalyst role and provides the synergistic effect with electrocatalysts. Such synergistic effect was not reported in the inorganic conductive supports; therefore, the carbon materials are currently considered the best option to provide a highly active OER/ORR bifunctional electrode. However, unfortunately, as shown in Figure 1-1, the

narrow potential window of carbon materials in the potential-pH diagram can be found. Depending on the (1-4), the air electrode undergoes the potential over 1.23 V vs RHE during the charging process. Typically, the charging proceeds at high anodic potentials around 1.7 V vs RHE [34]. Carbon cannot keep its elemental state in terms of the thermodynamics point of view under such high potentials in the alkaline electrolyte (pH > 14). Many researchers reported the instability of carbon materials in the ZAB environments [15-18, 61, 64-67, 89-91]. Due to this corrosion issue, the rechargeable ZAB development was believed to be difficult at the end of the 20th century [34]. Thus, to realize the ZAB, the development of corrosion-resistant carbon materials is required because carbon is the only material to provide reasonable bifunctional electrocatalytic properties.

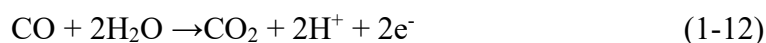
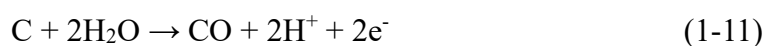
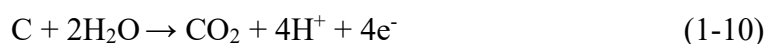
1-3 Carbon corrosion in energy devices

As mentioned in 1-2, ZAB is an attractive battery that can achieve SDGs and become post-lithium-ion batteries due to its higher energy density. However, the carbon corrosion issue hinders the realization of rechargeable ZAB. In this section, the fundamentals of carbon corrosion are firstly discussed. Then, the carbon corrosion examples in energy devices and recent countermeasures are reviewed.

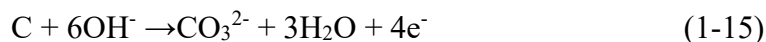
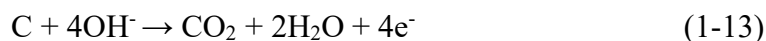
1-3-1 Fundamentals of the carbon corrosion

As shown in Figure 1-1, carbon materials undergo anodic dissolution. The electrochemical carbon oxidation reactions can be described as follows:

In acid or neutral condition



In alkaline condition



Among them, the standard electrode potential of (1-10) is estimated as 0.207 V vs NHE [26]. Additionally, the standard electrode potential of (1-15) is -0.682 V vs a Hg/HgO reference electrode (0.242 V vs RHE at pH 14) at 25°C in 0.1 mol dm⁻³ CO₃²⁻ solution [92]. In addition to such direct dissolution, carbon corrosion produces oxygen-containing functional groups on the surface. Some researchers reported the suppression of carbon corrosion by such functional groups [93]. Whether the subsequent oxidative dissolution proceeds or not depends on the corrosive environment, and there is no unified view. It should be added that some researchers reported that such functional group formation is not a predominant reaction in alkaline [29, 94].

Carbon corrosion is influenced by the temperature, pH, and electrode potential [94-98]. The carbon structure also influences the corrosion resistance (Figure 1-8). For example, the crystallinity of carbon material, *i.e.*, graphitization degree, strongly influences corrosion resistance [99-102]. Ross *et al.* studied this influence by electrochemical measurements combined with liquid/gas chromatography, as well as mass spectrometry [99, 100]. It was demonstrated that highly graphitized carbon has a 10 times lower corrosion rate than carbon with a low graphitization degree. The number of defect sites and the degree of edge planes exposure (Figure 1-8b) influences the corrosion rate because these sites are the possible corrosion priority sites [99, 100, 104-106]. Imai observed that the carbon corrosion proceeded from the edge sites of highly ordered pyrolytic graphite (HOPG) substrate in acidic media in the potential range of 0.8-1.2 V vs RHE in 0.1 mol dm⁻³ HClO₄ [106]. Ross *et al.* proposed the relationship between the corrosion rate and edge sites number, estimated by the temperature-programmed desorption [99, 100].

The third factor is the metal/metal oxides species acceleration [95, 106-109]. Miyazaki *et al.* reported that metal oxides or metal particles loaded carbon materials show severe corrosion, especially around these particles, because of the catalytic action of nanoparticles on carbon corrosion [106]. Similar acceleration was reported for Pt/C, used in the PEMFC [95, 107, 108]. The detail of this acceleration is described in the subsequent sections.

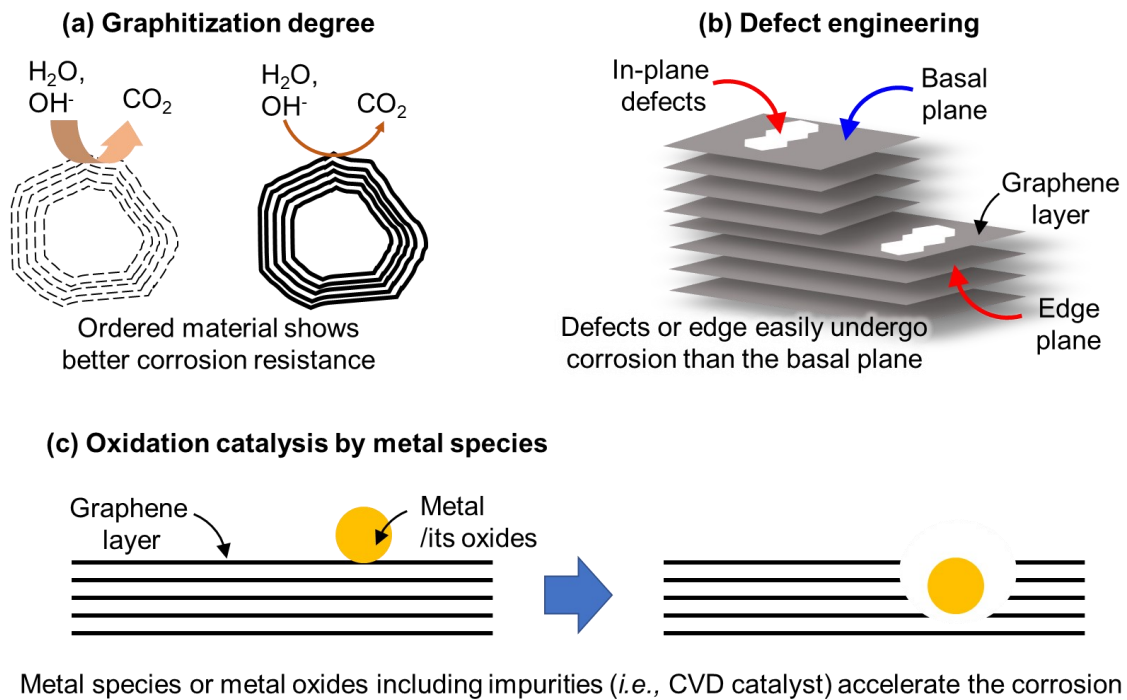


Fig. 1-8 Main factors of carbon corrosion.

1-3-2 Examples of carbon corrosion in the energy devices

As discussed above, carbon corrosion proceeds at high potentials and such potential range are in the working environment of the energy devices. This section explains the corrosion examples in the energy devices, including ZAB and PEMFC.

Firstly, the carbon corrosion in the PEMFC is briefly presented. The carbon corrosion in the PEMFC is better studied than in the ZAB cases and has many similarities in carbon corrosion in both devices. Carbon corrosion has often been observed at the cathode of PEMFC. The potential of the

cathode under PEMFC operation is negative than 1.23 V vs RHE, at which carbon corrosion is less significant. However, the cathode is exposed to high potentials > 1.2 V vs RHE during the shutdown or startup [110-112]. Such high potential during the startup/shutdown accelerates the carbon corrosion in PEMFC. In addition, this corrosion of carbon is also promoted by the loading of catalysts such as Pt [95, 107, 108]. Kinumoto *et al.* directly observed the carbon corrosion along the trajectory of Pt particle migration and reported that carbon corrosion occurs even at 0.6 V vs RHE, where no corrosion is observed on the Pt-free carbon [95]. Kinumoto also suggested that corrosion was accelerated by H_2O_2 species, one of the by-products of the oxygen reduction reaction. The carbon corrosion causes the following problems: (1) detachments of the platinum catalyst and electrochemically active surface area (ECSA) loss, (2) an increase of the surface hydrophilicity, which decreases gas permeability, and (3) direct volume changes of the gas-diffusion layer (GDL) which is a result of carbon corrosion in GDL [107]. For instance, Castanheira *et al.* observed the Pt detachment from the carbon support after the durability test under fuel-cell air cathode operation by TEM [112]. TEM observation also revealed the Pt catalyst agglomerations during the durability test. ECSA was also decreased, resulting in the PEMFC performance degradation during the durability test. In addition to the electrocatalyst degradation, carbon corrosion also produces oxygen-containing functional groups on the surface. Since these functional groups are usually hydrophilic, the catalyst layer is covered with a liquid phase, causing a decrease in gas permeability [113]. Morphological changes in the GDL due to carbon corrosion have been reported to cause delamination of the GDL from the cathode catalyst layer and reduction of water repellency in the GDE. These events eventually lead to performance degradation of the PEMFC.

Comparing the carbon corrosion in ZAB and PEMFC (Fig.1-9), the ZAB environment is considered a more severe condition than PEMFC for the following reasons. (1) only reverse current is applied in PEMFC, but in ZAB, a high potential is always applied during charging, and OER occurs

at the air electrode; (2) it is highly alkaline, which makes it difficult for functional groups to form on the surface as a passivation film [94]. Furthermore, as with PEMFCs, some electrocatalysts can promote carbon corrosion during air electrode operation. As mentioned above, the carbon material of the air electrode is an important component of the ZAB. Therefore, understanding the behavior of carbon materials in ZABs and improving their corrosion resistance is important to realize ZABs.

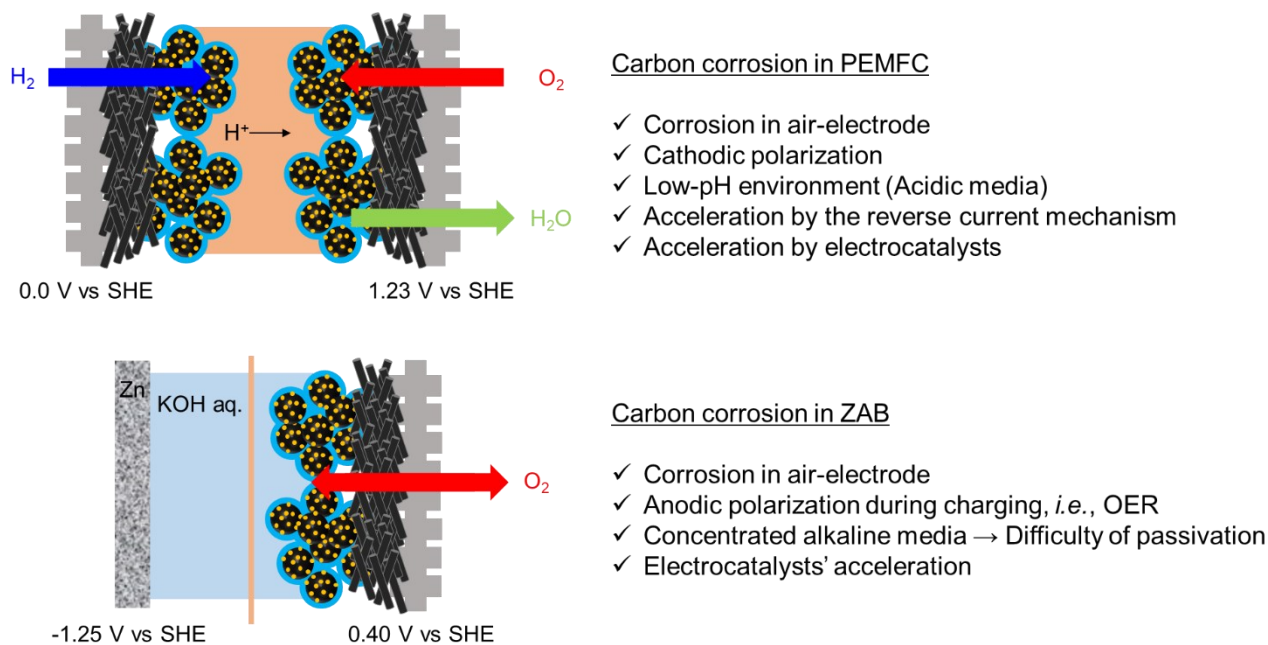


Fig. 1-9 Comparison of carbon corrosion in PEMFC and ZAB.

The carbon dissolution causes the degradation of OER/ORR electrocatalysis. Sugawara *et al.* performed 2000 cycles polarization for carbon nanotube/ $\text{Ba}_{0.5}\text{Sr}_{0.5}\text{Co}_{0.8}\text{Fe}_{0.2}\text{O}_{3-\delta}$ electrode, in the range of 1.2 V to 1.8 V vs RHE in 1.0 mol dm^{-3} KOH electrolyte [67]. After the durability test, they observed the carbon nanotube dissolution by TEM (Fig. 1-10a). The OER activity also degraded after the durability test, *i.e.*, the OER overpotential increased from 0.37 V to 0.57 V. Alegre investigated the degradation behavior of Pd/C electrode during charge/discharge condition of ZAB and demonstrated the degradation of both OER and ORR after the durability test (Fig. 1-10b) [89]. The corrosion of carbon produces CO_2 , which is converted to CO_3^{2-} in alkaline media. Then, metal carbonates, such as K_2CO_3 , precipitate on the electrode surface [90, 91]. Sumboja *et al.* observed the carbonate deposition

on the electrode surface after the durability test by SEM and XRD (Fig. 1-10c) and concluded that this surface coverage was one of the degradation factors [90]. Surface hydrophilization proceeds as a result of carbon corrosion. Like the PEMFC corrosion case, surface hydrophilization occurs due to the development of the surface functional group. Wang and coworkers conducted the anodic polarization of high-surface-area carbon black in 1.0 mol dm⁻³ KOH electrolyte, and after the durability test, they confirmed the hydrophilization of the electrode surface and formation of -OH, -C=O, and -COOH group by XPS [114]. Due to such hydrophilization, electrolyte leaking from GDE and gas permeability loss occurred, causing the electrode degradation [90].

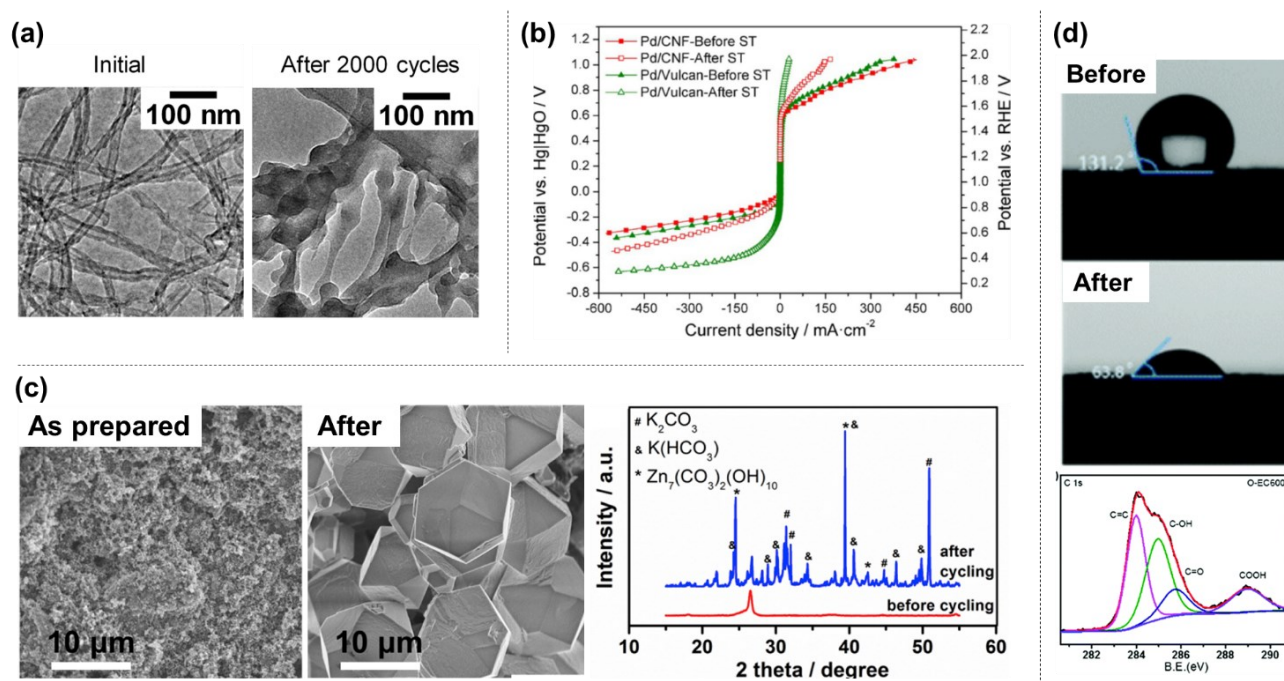


Fig. 1-10 (a) TEM images of CNT before and after repeated potential cycles, Copyright 2021, Royal Society of Chemistry [67], (b) polarization curves for the ORR and OER before (filled symbols) and after (empty symbols) the stress test for the investigated catalysts, Copyright 2015, Wiley-VCH [89], (c) surface SEM image and XRD pattern of the MnO_x/carbon paper electrodes before and after the durability test, Copyright 2016, Elsevier [90], and (d) water contact angles of carbon black before and after the anodic polarization test, and High-resolution C1s XPS spectra for the carbon black after the anodic polarization test, Copyright 2017, Royal Society of Chemistry [114].

In summary, the carbon corrosion phenomena occur in the energy device operation environment like PEMFC or ZAB. The carbon corrosion causes electrode performance loss and influences the lifetime of the energy device. However, carbon has many advantages as an electrode material. Thus, breaking down these corrosion problems is the only way to enhance the corrosion resistance of carbon materials. In the next section, it is described the current ideas to enhance the corrosion resistance of carbon materials.

1-3-3 Measures for the carbon corrosion

There is a growing body of literature that suggests ideas to improve the durability of the carbon-contained electrode. Optimizing graphitization degree and low-defect structure are widely accepted materials design concepts to suppress anodic corrosion [99, 115-120]. Ross *et al.* demonstrated that highly graphitized carbon has a lower corrosion rate than a low graphitization degree carbon due to its highly ordered stable structure [99]. Hung investigated the corrosion behavior of carbon material and the influence of the graphitization degree by using EQCM. Their study visibly showed the graphitized carbon's higher stability at a higher potential than carbon's lower graphitization [116]. However, such graphitized carbon or defect-less carbon usually reduces the electrode activity because (1) the lower surface area and (2) the lower number of defect sites; such sites are active sites for electrocatalysis [118-121]. In contrast, Nishihara *et al.* proposed that the graphene mesosponge with the higher surface area, synthesized by using Al₂O₃ nanoparticle template, shows the oxidation resistance due to the lower defects and comparable properties the ORR electrode support with the conventional carbon blacks [118-120]. They have not yet investigated the stability in the ZAB environment; thus, further investigation is desired.

The second idea is the decreasing of the overpotential applying for carbon. Carbon corrosion has been widely believed to be accelerated with ennobling electrode potential [96, 122]. Hence,

decreasing overpotential should suppress carbon corrosion. Alegre *et al.* reported that the replacement of the electrocatalyst to an OER active one successfully fell the applied overpotential for the electrodes. As a result, this replacement suppressed carbon corrosion and enhanced the electrode's durability [25]. However, some catalysts enhanced the corrosion rate of the carbon materials even at relatively low overpotentials [102-106]. It was also reported that the replacement of Pd to the perovskite-type oxide electrocatalyst enhanced the durability, although the degradation occurred even after the replacement after a prolonged durability test.

Fujigaya *et al.* challenged this corrosion problem issue from the polymer science view [123-129]. They tried to wrap the carbon materials with the polybenzimidazole-based polymer to separate carbon support from the corrosion environment [123]. Such polymer coating can separate carbon and corrosion environments and enable the uniform electrocatalyst particle loading on the carbon support surface [125]. They achieved the low overpotential for OER and ORR using Ni-Co spinel oxides loaded MWCNT wrapped by the polybenzimidazole (PBI) and revealed the electrocatalysis stability in 1.0 mol dm⁻³ KOH aq. [125]. To apply the ZAB environment, further improvement of the polymer stability to the hydroxyl radicals, which is provided by the concentrated alkaline media, is required [130].

In summary, recent countermeasures against carbon corrosion in the operating environment of energy equipment are reviewed in this section. Each study successfully improved the carbon-based electrode durability; however, as the conductive support for ZAB, there is still a lower number of reports of the durable carbon conductive support because of the difficulty to overcome the concentrated alkaline media. Thus, this thesis study tried a new approach to enhancing the corrosion resistance of carbon materials which enables to apply the carbon materials for the ZAB environment keeping the advantages of carbon materials as conductive supports.

1-4 Aim of this thesis

In the above sections, the importance of the electrochemical energy storage/conversion devices, the role of the carbon materials in these devices, and the durability problem of carbon materials in the energy devices are briefly described. In particular, the corrosion issue of carbon materials in rechargeable ZABs is serious because of the high anodic potentials in concentrated alkaline media during charging. This thesis study focused on the tailoring of novel nanocarbon materials exhibiting high resistance to carbon corrosion. The nanofiber structures are suitable for ZABs and PEMFCs because they provide high gas permeability [27, 131, 132]. The carbon nanofibers are typically synthesized by the chemical vapor deposition and classified into three types by their graphene stacking structure, *i.e.*, (a) platelet (pCNF), (b) herringbone / fishbone / stacked-cup (hCNF), and (c) tubular / ribbon (tCNF), as shown in Figure 1-12 [27, 133]. Depending on the stacking structure, the three types of carbon nanofibers show different physicochemical properties, such as electrocatalysis, electronic conductivities, and surface area. This thesis study focused on the pCNFs because of their wider applications as electrode materials and their stability [7, 13, 15, 27, 134-140]. In this section, the fundamental properties of pCNFs are firstly explained, and the application examples of pCNF as the electrode materials are also presented. Then, the aim of this study is shown.

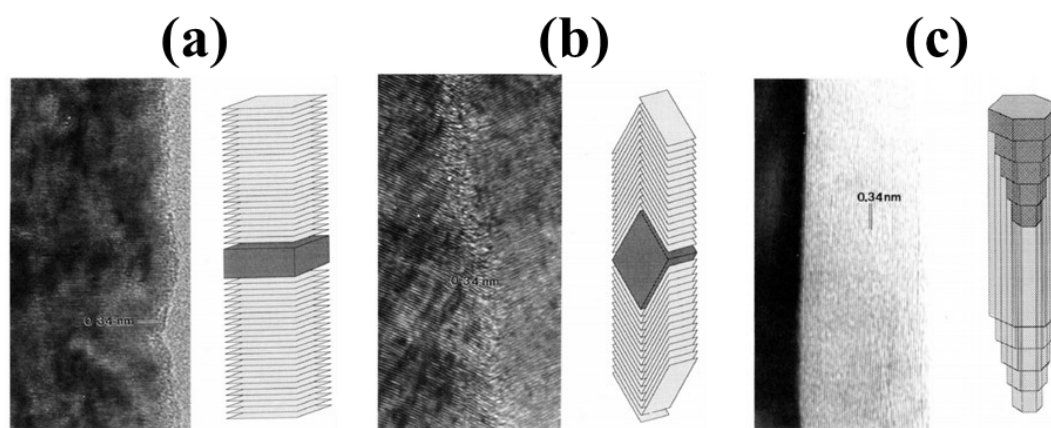


Fig.1-12 HRTEM images and schematic images of CNFs. (a) Platelet type, (b) Herringbone type and (c) Tubular type. Copyright 1995, American Chemical Society [133].

1-4-1 Platelet-type carbon nanofibers and their properties

Platelet-type carbon nanofibers (pCNFs) have graphene layers perpendicular to the fiber axis. Because of this orientation, the fiber's sidewall and both ends of the fiber consist of the carbon edge plane and basal plane, respectively. The edge plane on the sidewall usually contains dangling bonds with larger electron densities. It can quickly release the electrons compared to the π -bonds on basal atoms [27]. Therefore, this sidewall has many functions, *i.e.*, ORR electrocatalysis [134, 135], preferential sites for nanoparticle loading [13, 15], reasonable lithiation / delithiation properties as a negative electrode in Li-ion batteries [7], and hydrocarbon conversions [136-138]. In addition to these attractive functions, pCNFs show higher stability than other carbon materials because of their structure [13, 135, 136]. The pCNFs consist mainly of sp^2 carbon because of their planer structure. Such sp^2 carbon has a much higher oxidation potential than sp^3 carbon [29, 123]. Thus, compared with other carbon materials, pCNFs show better stability. This stability has often been reported as the PEMFC electrode materials. For instance, Tamaki *et al.* examined the durability of Pt/graphitized carbon black (CB) hybrid and Pt/pCNF hybrid in the PEMFC operation condition [139]. The Pt/pCNF shows a lower graphitization degree than the Pt/CB; however, the final durability of Pt/pCNF is higher than Pt/CB. Similar reports were also reported elsewhere [13, 140].

Hence, this thesis study focused on the highly graphitized pCNFs that can be synthesized at high temperatures [27, 141-145]. When pCNFs were heat-treated at $\geq 2000^\circ\text{C}$ under an inert gas atmosphere, it was reported that the exposed carbon edge sites on the sidewall of pCNFs formed bonds with the other adjacent carbon atoms, resulting in a nano-looped structure. The looped carbon layers should be formed to reduce surface energy. As mentioned in 1-3-1, faster carbon corrosion should occur on the carbon edge plane than the basal plane due to their higher reactivity. Thus, the elimination of such a carbon edge plane might enhance the corrosion resistance of pCNFs. Namely, heat-treated pCNFs have three structural characteristics as the corrosion tolerance material; (1) platelet structure,

(2) higher graphitization degree, and (3) uniformly eliminated graphene edge sites (Figure 1-13). These features may suit electrocatalyst carbon supports with high corrosion resistance in the ZAB operation environment.

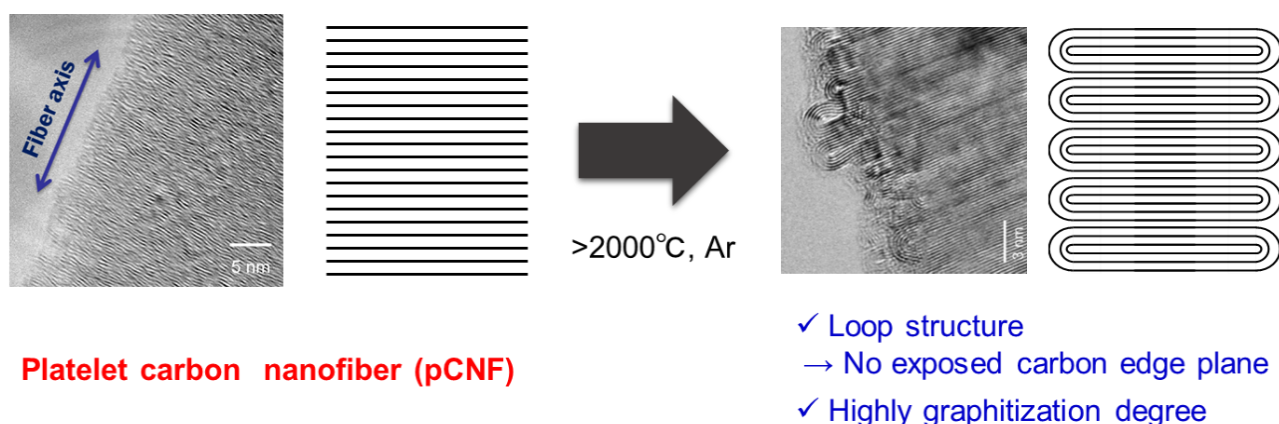


Fig. 1-13 The structural change of pCNF owing to the heat-treatment. Reproduced from [145]. Copyright 2007, Elsevier.

1-4-2 Objectives of this thesis

This thesis study investigated the possibility of pCNFs as corrosion-resistant carbon materials for the positive electrode of rechargeable ZABs. In particular, high-temperature-treated pCNFs at $\geq 2000^\circ\text{C}$ possess a high graphitization degree and no exposure of the carbon edge plane because of the formation of loped carbon layers at the sidewall. After detailed characterization of pCNFs heat-treated at various temperatures, their corrosion behavior was examined and compared with other carbon materials, including carbon blacks and multiwalled carbon nanotubes at high anodic potentials in a concentrated KOH electrolyte. An identical location electron microscopy technique was introduced in this study to examine the morphological change of the carbon materials directly and estimate the corrosion rate quantitatively for the first time. A STEM/EELS analysis was also used to characterize the surface of carbon, and then the corrosion-resistant mechanism was discussed. Furthermore, OER/ORR electrodes were prepared by combining the pCNFs with electrocatalytically active oxide

nanoparticles, and their OER/OER activity and durability were examined. Through such experimental studies, this thesis tried to provide a new concept of corrosion-resistant carbon design to develop durable electrochemical energy conversion devices, including rechargeable ZABs.

1-5 Outlines of this thesis

This thesis consists of six chapters and is organized as follows.

In Chapter 1, the general introduction and proposal of this study are described as well as the science behind this study.

In Chapter 2, pCNFs were prepared using liquid-phase carbonization in a porous anodic alumina template and characterized together with other nanocarbon materials. In particular, structural change with heat treatment temperature of pCNFs was examined in detail.

The corrosion rates of pCNFs and other nanostructured carbon materials under an OER environment in concentrated alkaline media were investigated in **Chapter 3**. An identical location electron microscopy technique was introduced in this chapter to examine the morphological change of the carbon materials directly and estimate the corrosion rate quantitatively. Additionally, a STEM/EELS analysis was also used to characterize the surface of carbon, and then the corrosion-resistant mechanism was discussed.

Furthermore, OER/ORR electrodes were prepared by combining the pCNFs with electrocatalytically active oxide nanoparticles, and their OER/OER activity and durability were examined in **Chapter 4** and **Chapter 5**. In Chapter 4, the electrode conductive support properties and durability of pCNFs for OER in 4.0 mol dm^{-3} KOH electrolyte were demonstrated using $\text{Ca}_2\text{FeCoO}_5$,

one of the novel OER catalysts [46]. In Chapter 5, pCNFs were hybridized with MnCo_2O_4 using solvothermal synthesis [20] to enhance the OER/ORR activity of pCNF based electrodes. Their electrode activity and durability were furtherly evaluated using the gas-diffusion electrode system.

Chapter 6 is the general conclusions of this thesis. This chapter also includes suggestions for future work.

1-6 References

1. United Nations, “Transforming our World: The 2030 Agenda for Sustainable Development”, <https://sustainabledevelopment.un.org/post2015/transformingourworld/publication>, retrieved 24/05/2021.
2. P. Chen, Y. Tong, C. Wu, Y. Xie, “Surface/Interfacial Engineering of Inorganic Low-Dimensional Electrode Materials for Electrocatalysis”, *Acc. Chem. Res.*, **51(11)**, 2857–2866 (2018).
3. R.L. McCreery, “Advanced Carbon Electrode Materials for Molecular Electrochemistry”, *Chem. Rev.* **108(7)**, 2646–2687 (2008).
4. D. Tie, S. Huang, J. Wang, J. Ma, J. Zhang, Y. Zhao, “Hybrid energy storage devices: Advanced electrode materials and matching principles”, *Energy Storage Materials*, **21**, 22-40 (2019).
5. S. Li, C. Cheng, A. Thomas, “Carbon-Based Microbial-Fuel-Cell Electrodes: From Conductive Supports to Active Catalysts”, *Adv. Mater.*, **29(8)**, 1602547 (2017).
6. Q. Wei, Y. Fu, G. Zhang, S. Sun, “Rational design of carbon-based oxygen electrocatalysts for zinc–air batteries”, *Current Opinion in Electrochemistry*, **4(1)**, 45-59 (2017).
7. H. Habazaki, M. Kiri, H. Konno, “High rate capability of carbon nanofilaments with platelet structure as anode materials for lithium ion batteries”, *Electrochemistry Commun.*, **8(8)**, 1275-1279 (2006).
8. M. Takeno, S. Katakura, K. Miyazaki, T. Abe, T. Fukutsuka, “Relation between Mixing Processes and Properties of Lithium-ion Battery Electrode-slurry”, *Electrochemistry (Tokyo)*, **89**, 585-589 (2021).
9. T. Hasegawa, S.R. Mukai, Y. Shirato, H. Tamon, “Preparation of carbon gel microspheres containing silicon powder for lithium ion battery anodes”, *carbon*, **42(12-13)**, 2573-2579 (2004).
10. C. Kim, C. Zhu, Y. Aoki, H. Habazaki, “Heteroatom-doped porous carbon with tunable pore structure and high specific surface area for high performance supercapacitors”, *Electrochimica Acta*, **314**, 173-187 (2019).
11. C. Zhu, M. Takata, Y. Aoki, H. Habazaki, “Nitrogen-doped porous carbon as-mediated by a facile solution combustion synthesis for supercapacitor and oxygen reduction electrocatalyst”, *Chemical Engineering Journal*, **350**, 278-289 (2018).
12. J. Cao, H. Xu, J. Zhong, X. Li, S. Li, Y. Wang, M. Zhang, H. Deng, Y. Wang, C. Cui, M. Hossain, Y. Cheng, L. Fan, L. Wang, T. Wang, J. Zhu, B. Lu, “Dual-Carbon Electrode-Based High-Energy-Density Potassium-Ion Hybrid

- Capacitor”, *ACS Appl. Mater. Interfaces*, **13**(7), 8497–8506 (2021).
13. E. Tsuji, T. Yamasaki, Y. Aoki, S. G. Park, K. Shimizu, H. Habazaki, “Highly durable platelet carbon nanofiber-supported platinum catalysts for the oxygen reduction reaction”, *Carbon*, **87**, 1-9 (2015).
 14. P. J. Kulesza, J. K. Zak, I. A. Rutkowska, B. Dembinska, S. Zoladek, K. Miecznikowski, E. Negro, V. D. Noto, P. Zelenay, “Elucidation of role of graphene in catalytic designs for electroreduction of oxygen”, *Current Opinion in Electrochemistry*, **9**, 257-264 (2018).
 15. N. Yamada, D. Kowalski, C. Zhu, Y. Aoki, H. Habazaki, “High dispersion and oxygen reduction reaction activity of Co₃O₄ nanoparticles on platelet-type carbon nanofibers”, *RSC Adv.*, **9**, 3726-3733 (2019).
 16. Y. Zhu, W. Zhou, Z. Shao, “Perovskite/Carbon Composites: Applications in Oxygen Electrocatalysis”, *Small*, **13**(12), 1603793 (2017).
 17. C. Alegre, C. Busacca, A.D. Blasi, O.D. Blasi, A.S. Aricò, V. Antonucci, E. Modica, V. Baglio, “Electrospun carbon nanofibers loaded with spinel-type cobalt oxide as bifunctional catalysts for enhanced oxygen electrocatalysis”, *J. Energy Storage*, **23**, 269-277 (2019).
 18. C. Alegre, C. Busacca, A.D. Blasi, O.D. Blasi, A.S. Aricò, V. Antonucci, V. Baglio, “Electrocatalysis of Oxygen on Bifunctional Nickel-Cobaltite Spinel”, *ChemElectroChem*, **7**(1), 24-130 (2020).
 19. R. Mohamed, X. Cheng, E. Fabbri, P. Levecque, R. Kotz, O. Conrad, T. J. Schmidt, “Understanding the Influence of Carbon on the Oxygen Reduction and Evolution Activities of BSCF/Carbon Composite Electrodes in Alkaline Electrolyte”, *ECS Trans.*, **58**(36), 9-18 (2014).
 20. Y. Liang, H. Wang, J. Zhou, Y. Li, J. Wang, T. Regier, H. Dai, “Covalent Hybrid of Spinel Manganese–Cobalt Oxide and Graphene as Advanced Oxygen Reduction Electrocatalysts”, *J. Am. Chem. Soc.*, **134**, 3517 (2012)
 21. C. Y. Su, H. Cheng, W. Li, Z. Q. Liu, N. Li, Z. Hou, F. Q. Bai, H. X. Zhang, T. Y. Ma, “Atomic Modulation of FeCo–Nitrogen–Carbon Bifunctional Oxygen Electrodes for Rechargeable and Flexible All-Solid-State Zinc–Air Battery”, *Adv. Energy Mater.*, **7**, 1602420 (2017).
 22. E. Negro, A.B. Delpeuch, K. Vezzù, G. Nawn, F. Bertasi, A. Ansaldo, V. Pellegrini, B. Dembinska, S. Zoladek, K. Miecznikowski, I.A. Rutkowska, M. Skunik-Nuckowska, P.J. Kulesza, F. Bonaccorso, V.D. Noto, “Toward Pt-Free Anion-Exchange Membrane Fuel Cells: Fe–Sn Carbon Nitride–Graphene Core–Shell Electrocatalysts for the Oxygen Reduction Reaction”, *Chem. Mater.*, **30**(8), 2651–2659 (2018).
 23. R. Kumar, S. Sahoo, E. Joanni, R.K. Singh, K. Maegawa, W.K. Tan, G. Kawamura, K.K. Kar, A. Matsuda, “Heteroatom doped graphene engineering for energy storage and conversion”, *Mater. Today*, **39**, 47-65 (2020).
 24. N.H. Wisińska, M. Skunik-Nuckowska, S. Dyjak, P.J. Kulesza, “Factors affecting performance of electrochemical capacitors operating in Keggin-type silicotungstic acid electrolyte”, *Appl. Surf. Sci.*, **530**(15), 147273 (2020).
 25. C. Alegre, E. Modica, M. Rodlert-Bacilieri, F. C. Mornaghini, A. S. Aricò, V. Baglio, “Enhanced durability of a cost-effective perovskite-carbon catalyst for the oxygen evolution and reduction reactions in alkaline environment”, *Int. J. Hydrogen Energy*, **42**, 28063 (2017).
 26. K. Ono, T. Kinumoto, T. Tsumura, M. Toyoda, “Preparation of LaMnO₃-CNF and Its Activity for Oxygen Electrode Reaction in 0.1 mol dm⁻³ KOH Solution”, *ECS Trans.*, **64**(45), 29 -39(2015).
 27. S.G. Peera, R. Koutavarapu, S. Akula, A. Asokan, P. Moni, M. Selvaraj, J. Balamurugan, S.O. Kim, C. Liu, A.K. Sahu, “Carbon Nanofibers as Potential Catalyst Support for Fuel Cell Cathodes: A Review”, *Energy Fuels*, **35**(15), 11761–

11799 (2021).

28. M. Pourbaix, "Atlas of Electrochemical Equilibria in Aqueous Solutions", London: Pergamon Press Ltd., pp 449-457 (1966).
29. M. Tominaga, Y. Yatsugi, N. Watanabe, "Oxidative corrosion potential vs. pH diagram for single-walled carbon nanotubes", *RSC Adv.*, **4**, 27224-27227 (2014).
30. A.C. Ferrari, J. Robertson, "Interpretation of Raman spectra of disordered and amorphous carbon", *Phys. Rev. B*, **61**, 14095-14107 (2000).
31. Y. Balali and S. Stegen, "Review of energy storage systems for vehicles based on technology, environmental impacts, and costs", *Renewable and Sustainable Energy Reviews*, **135**, 110185 (2021).
32. M. Marinaro, D. Bresser, E. Beyer, P. Faguy, K. Hosoi, H. Li, J. Sakovica, K. Amine, M. Wohlfahrt-Mehrens, S. Passerin, "Bringing forward the development of battery cells for automotive applications: Perspective of R&D activities in China, Japan, the EU and the USA", *Journal of Power Sources*, **459(31)**, 228073 (2020).
33. S. Zhao, D. Xia, M. Li, D. Cheng, K. Wang, Y.S. Meng, Z. Chen, J. Bae, "Self-Healing and Anti-CO₂ Hydrogels for Flexible Solid-State Zinc-Air Batteries", *ACS Appl. Mater. Interfaces*, **13(10)**, 12033-12041 (2021).
34. M. Wu, G. Zhang, L. Du, D. Yang, H. Yang, S. Sun, "Defect Electrocatalysts and Alkaline Electrolyte Membranes in Solid-State Zinc-Air Batteries: Recent Advances, Challenges, and Future Perspectives", *Small methods*, **5(1)**, 2000868 (2021).
35. D. Stock, S. Dongmo, J. Janek, D. Schröder, "Benchmarking Anode Concepts: The Future of Electrically Rechargeable Zinc-Air Batteries", *ACS Energy Lett.*, **4(6)**, 1287-1300 (2019).
36. H. Arai, "Recent progress on Zinc-Air Batteries", *Shigen-to-Sozai*, **117**, 177-182 (2001). (in Japanese)
37. University of Tokyo, "FEATURES — Researchers' keyword commentaries, Fuel cell/battery system", https://www.u-tokyo.ac.jp/focus/en/features/f_00047.html, retrieved 22/09/2021.
38. J. Ma, Y. Li, NS. Grundish, J.B. Goodenough, Y. Chen, L. Guo, Z. Peng, X. Qi, F. Ynag, L. Qie, C.A. Wang, B. Huang, Z. Huang, L. Chen, D. Su, G. Wang, X. Peng, Z. Chen, J. Yang, S. He, X. Zhang, H. Yu, C. Fu, M. Jiang, W. Deng, C.F. Sun, Q. Pan, Y. Tang, X. Li, X. Ji, F. Wan, Z. Niu, F. Lian, C. Wang, G.G. Wallace, M. Fan, Q. Meng, S. Xin, Y.G. Guo, L.J. Wan, "The 2021 battery technology roadmap", *J. Phys. D: Appl. Phys.* **54**, 183001 (2021).
39. New Energy and Industrial Technology Development Organization (Japan), "Project Register of Research and Development Initiative for Scientific Innovation of New Generation Batteries 2 (in Japanese)", <https://www.nedo.go.jp/content/100882549.pdf>, retrieved 22/09/2021.
40. A. Nakata, H. Arai, T. Yamane, T. Hirai, Z. Ogumi, "Preserving Zinc Electrode Morphology in Aqueous Alkaline Electrolytes Mixed with Highly Concentrated Organic Solvent", *J. Electrochem. Soc.*, **163**, A50-A56 (2016).
41. K. Kinoshita, "Electrochemical Oxygen Technology", New York: John Wiley & Sons, pp. 289-300 (1992).
42. E. Tsuji, A. Imanishi, K.I. Fukui, Y. Nakato, "Electrocatalytic activity of amorphous RuO₂ electrode for oxygen evolution in an aqueous solution", *Electrochim. Acta*, **56(5)**, 2009-2016 (2011).
43. M. Yagi, E. Tomita, T. Kuwabara, "Remarkably high activity of electrodeposited IrO₂ film for electrocatalytic water oxidation", *J. Electroanal. Chem.*, **579(1)**, 83-88 (2005).
44. A.A. Gewirth, M.S. Thorum, "Electroreduction of Dioxygen for Fuel-Cell Applications: Materials and Challenges", *Inorg. Chem.*, **49(8)**, 3557-3566 (2010).

45. M. Risch, K. A. Stoerzinger, S. Maruyama, W.T. Hong, I. Takeuchi, Y.S. Horn, “La_{0.8}Sr_{0.2}MnO_{3-δ} Decorated with Ba_{0.5}Sr_{0.5}Co_{0.8}Fe_{0.2}O_{3-δ}: A Bifunctional Surface for Oxygen Electrocatalysis with Enhanced Stability and Activity”, *J. Am. Chem. Soc.*, **136**, 5229-5232 (2014).
46. E. Tsuji, T. Motohashi, H. Noda, D. Kowalski, Y. Aoki, H. Tanida, J. Nikura, Y. Koyama, M. Mori, H. Arai, T. Ioroi, N. Fujiwara, Y. Uchimoto, Z. Ogumi, H. Habazaki, “Brownmillerite-type Ca₂FeCoO₅ as a Practicable Oxygen Evolution Reaction Catalyst”, *ChemSusChem.*, **10(14)**, 2864-2868 (2017).
47. D. Kowalski, H. Kiuchi, T. Motohashi, Y. Aoki, H. Habazaki, “Activation of Catalytically Active Edge-Sharing Domains in Ca₂FeCoO₅ for Oxygen Evolution Reaction in Highly Alkaline Media”, *ACS Appl. Mater. Interfaces*, **11(32)**, 28823-28829 (2019).
48. Y. Sato, Y. Aoki, K. Takase, H. Kiuchi, D. Kowalski, H. Habazaki, “Highly Durable Oxygen Evolution Reaction Catalyst: Amorphous Oxyhydroxide Derived from Brownmillerite-Type Ca₂FeCoO₅”, *ACS Appl. Energy Materials*, **3(6)**, 5269-5276 (2020).
49. ZN Zahran, E.A. Mohamed, Y. Tsubonouchi, M. Ishizaki, T. Togashi, M. Kurihara, K. Saito, T. Yui, M. Yagi , “Electrocatalytic water splitting with unprecedentedly low overpotentials by nickel sulfide nanowires stuffed into carbon nitride scabbards”, *Energy Environ. Sci.*, **14**, 5358-5365 (2021).
50. Y. Miyahara, K. Miyazaki, T. Fukutsuka, T. Abe, “Influence of Surface Orientation on the Catalytic Activities of La_{0.8}Sr_{0.2}CoO₃ Crystal Electrodes for Oxygen Reduction and Evolution Reactions”, *ChemElectroChem*, **3(2)**, 214-217 (2016).
51. G. Kéranguéven, S. Royer, E. Savinov, “Synthesis of efficient Vulcan–LaMnO₃ perovskite nanocomposite for the oxygen reduction reaction”, *Electrochem. Comm.*, **50**, 28-31 (2015).
52. M. Risch, “Perovskite Electrocatalysts for the Oxygen Reduction Reaction in Alkaline Media”, *Catalysts*, **7(5)**, 154 (2017).
53. Y. Aoki, E. Tsuji, T. Motohashi, D. Kowalski, H. Habazaki, “La_{0.7}Sr_{0.3}Mn_{1-x}Ni_xO_{3-δ} Electrocatalysts for the Four-Electron Oxygen Reduction Reaction in Concentrated Alkaline Media”, *J. Phys. Chem. C*, **122(39)**, 22301-22308 (2018).
54. Y. Aoki, K. Takase, H. Kiuchi, Y. Sato, H. Toriumi, S. Kitano, D. Kowalski, H. Habazaki, “*in-situ* activation of a manganese perovskite oxygen reduction catalyst in concentrated alkaline media”, *J. Am. Chem. Soc.*, **143(17)**, 6505-6515 (2021).
55. Y. Liang, Y. Li, H. Wang, J. Zhou, J. Wang, T. Regier, H. Dai, “Co₃O₄ nanocrystals on graphene as a synergistic catalyst for oxygen reduction reaction”, *Nature Materials*, **10**, 780-786 (2011).
56. A. Zhang, J. Wu, L. Xue, S. Yan, S. Zeng, “Probing Heteroatomic Dopant-Activity Synergy over Co₃O₄/Doped Carbon Nanotube Electrocatalysts for Oxygen Reduction Reaction”, *Inorg. Chem.*, **59(1)**, 403-414 (2020).
57. J. Shen, J. Gao, L. Ji, X. Chen, C. Wu, “Three-dimensional interlinked Co₃O₄-CNTs hybrids as novel oxygen electrocatalyst”, *Appl. Surf. Sci.*, **497(15)**, 143818 (2019).
58. J. Zhang, Z. Zhao, Z. Xia, L. Dai, “A metal-free bifunctional electrocatalyst for oxygen reduction and oxygen evolution reactions”, *Nat. Nanotechnol.*, **10**, 444-452 (2015).
59. S.-D. Yim, G.-G. Park, Y.-J. Sohn, W.-Y. Lee, Y.-G. Yoon, T.-H. Yang, S. Um, S.-P. Yu, C.-S. Kim, “Optimization of PtIr electrocatalyst for PEM URFC”, *Int. J. Hydrogen Energy*, **30**, 1345-1350 (2005).

60. V. Cascos, R. Martínez-Coronado, J.A. Alonso, M.T. Fernández-Díaz, “Structural and electrical characterization of the Co-doped $\text{Ca}_2\text{Fe}_2\text{O}_5$ brownmillerite: Evaluation as SOFC-cathode materials”, *Int. J. Hydrogen Energy*, **40**(15), 5456-5468 (2015).
61. E. Fabbri, R. Mohamed, P. Levecque, O. Conrad, R. Kötz, T.J. Schmidt, “Composite Electrode Boosts the Activity of $\text{Ba}_{0.5}\text{Sr}_{0.5}\text{Co}_{0.8}\text{Fe}_{0.2}\text{O}_{3-\delta}$ Perovskite and Carbon toward Oxygen Reduction in Alkaline Media”, *ACS Catal.*, **4**(4), 1061–1070 (2014).
62. X. Ge, Y. Du, B. Li, T.S. Andy Hor, M. Sindoro, Y. Zong, H. Zhang, Z. Liu, “Intrinsically Conductive Perovskite Oxides with Enhanced Stability and Electrocatalytic Activity for Oxygen Reduction Reactions”, *ACS Catal.*, **6**(11), 7865-7871 (2016).
63. J. Yang, J. Wang, L. Zhu, W. Zeng, J. Wang, “Multiple hollow CeO_2 spheres decorated MnO_2 microflower as an efficient catalyst for oxygen reduction reaction”, *Mater. Lett.*, **234**(1), 331-334 (2019).
64. Z.P. Cano, M.G. Park, D.U. Lee, J. Fu, H. Liu, M. Fowler, Z. Chen, “New Interpretation of the Performance of Nickel-Based Air Electrodes for Rechargeable Zinc–Air Batteries”, *J. Phys. Chem. C*, **122**(35), 20153-20166 (2018).
65. S.W. Price, S.J. Thompson, X. Li, S.F. Gorman, D. Pletcher, A.E. Russell, F.C. Walsh, R.G.A. Wills, “The fabrication of a bifunctional oxygen electrode without carbon components for alkaline secondary batteries”, *J. Power Sources.*, **259**(1), 43-49 (2014).
66. N. Fujiwara, T. Nagai, T. Ioroi, H. Arai, and Z. Ogumi, “Bifunctional electrocatalysts of lanthanum-based perovskite oxide with Sb-doped SnO_2 for oxygen reduction and evolution reactions”, *J. Power Sources.*, **451**, 227736 (2020).
67. Y. Sugawara, T. Hihara, G.M. Anilkumar, K. Kamata, T. Yamaguchi, “Metal oxide electrocatalyst support for carbon-free durable electrodes with excellent corrosion resistance at high potential conditions”, *Sustainable Energy & Fuels*, **5**, 1374-1378 (2021).
68. C. Alegre, E. Modica, A.S. Aricò, V. Baglio, “Bifunctional oxygen electrode based on a perovskite/carbon composite for electrochemical devices”, *J. Electroanal. Chem.*, **808**(1), 412-419 (2018).
69. Y. Liang, H. Wang, P. Diao, W. Chang, G. Hong, Y. Li, M. Gong, L. Xie, J. Zhou, J. Wang, T. Regier, F. Wei, H. Dai, “Oxygen Reduction Electrocatalyst Based on Strongly Coupled Cobalt Oxide Nanocrystals and Carbon Nanotubes”, *J. Am. Chem. Soc.*, **134**, 15849 (2012).
70. E. Fabbri, M. Nachtegaal, X. Cheng, T. J. Schmidt, “Superior Bifunctional Electrocatalytic Activity of $\text{Ba}_{0.5}\text{Sr}_{0.5}\text{Co}_{0.8}\text{Fe}_{0.2}\text{O}_{3-\delta}$ /Carbon Composite Electrodes: Insight into the Local Electronic Structure”, *Adv. Energy Mater.*, **5**, 1402033 (2015).
71. O. Haas, F. Holzer, S. Müller, J. M. McBreen, X. Q. Yang, X. Sun, M. Balasubramanian, “X-ray absorption and diffraction studies of $\text{La}_{0.6}\text{Ca}_{0.4}\text{CoO}_3$ perovskite, a catalyst for bifunctional oxygen electrodes”, *Electrochim. Acta*, **47**, 3211-3217 (2002).
72. Z. Yang, X. Zhou, H. Nie, Z. Yao, S. Huang, “Facile Construction of Manganese Oxide Doped Carbon Nanotube Catalysts with High Activity for Oxygen Reduction Reaction and Investigations into the Origin of their Activity Enhancement”, *ACS Appl. Mater. Interfaces*, **3**, 2601-2606 (2011).
73. M. Gao, X. Cao, Q. Gao, Y. Xu, Y. Zheng, J. Jiang, S. Yu, “Nitrogen-Doped Graphene Supported CoSe_2 Nanobelt Composite Catalyst for Efficient Water Oxidation”, *ACS Nano*, **8**, 3970-3978 (2014).
74. X. Li, Y. Fang, X. Lin, M. Tian, X. An, Y. Fu, R. Li, J. Jin, J. Ma, “MOF derived Co_3O_4 nanoparticles embedded in

- N-doped mesoporous carbon layer/MWCNT hybrids: extraordinary bi-functional electrocatalysts for OER and ORR”, *J. Mater. Chem. A*, **3**, 17392-17402 (2015).
75. Z. Awaludin, M. Suzuki, J. Masud, T. Okajima, T. Ohsaka, “Enhanced Electrocatalysis of Oxygen Reduction on Pt/TaOx/GC”, *J. Phys. Chem. C*, **115(51)**, 25557–25567 (2011).
 76. X. Ge, F.W.T. Goh, B. Li, TSA Hor, J. Zhang, P. Xiao, X. Wang, Y. Zong, Z. Liu, “Efficient and durable oxygen reduction and evolution of a hydrothermally synthesized La(Co_{0.55}Mn_{0.45})_{0.99}O_{3-δ} nanorod/graphene hybrid in alkaline media”, *Nanoscale*, **7**, 9046-9054 (2015).
 77. Y. Zhu, C. Su, X. Xu, W. Zhou, R. Ran, Z. Shao, “A Universal and Facile Way for the Development of Superior Bifunctional Electrocatalysts for Oxygen Reduction and Evolution Reactions Utilizing the Synergistic Effect”, *Chem. Eur. J.*, **20(47)**, 15533-15542 (2014).
 78. X. Wang, J. Sunarso, Q. Lu, Z. Zhou, J. Dai, D. Guan, W. Zhou, Z. Shao, “High-Performance Platinum-Perovskite Composite Bifunctional Oxygen Electrocatalyst for Rechargeable Zn–Air Battery”, *Adv. Energy Mater.*, **10(5)**, 1903271 (2020).
 79. Y. Bu, H. Jang, O. Gwon, S.H. Kim, S.H. Joo, G. Nam, S. Kim, Y. Qin, Q. Zhong, S.K Kwak, J. Cho, G. Kim, “Synergistic interaction of perovskite oxides and N-doped graphene in versatile electrocatalyst”, *J. Mater. Chem. A*, **7**, 2048-2054 (2019).
 80. P. Ramakrishnan, H. Im, S.H. Baek, J.I. Sohn, “Recent Studies on Bifunctional Perovskite Electrocatalysts in Oxygen Evolution, Oxygen Reduction, and Hydrogen Evolution Reactions under Alkaline Electrolyte”, *Isr. J. Chem.*, **59(8)**, 708-719 (2019).
 81. H. Deng, L. Shu, Z. Wang, J. Mao, F. Liang, “SrTi_{0.1}CoxFe_{0.9-x}O_{3-δ} Perovskites for enhanced oxygen evolution reaction activity”, *Int. J. Hydrogen Energy*, **45(24)**, 13129-13138 (2020).
 82. X. Zhao, F. Li, R. Wang, J.M. Seo, H.J. Choi, S.M. Jung, J. Mahmood, I.Y. Jeon, J.B. Baek, “Controlled Fabrication of Hierarchically Structured Nitrogen-Doped Carbon Nanotubes as a Highly Active Bifunctional Oxygen Electrocatalyst”, *Adv. Funct. Mater.*, **27(9)**, 1605717 (2017).
 83. T. Kondo, Y. Iwasaki, Y. Honma, Y. Takagi, S. Okada, J. Nakamura, “Formation of nonbonding π electronic states of graphite due to Pt-C hybridization”, *Phys. Rev. B*, **80**, 233408.
 84. J.E. Kim, J. Lim, G.Y. Lee, S.H. Choi, U.N. Maiti, W.J. Lee, H.J. Lee, S.O. Kim, “Subnanometer Cobalt-Hydroxide-Anchored N-Doped Carbon Nanotube Forest for Bifunctional Oxygen Catalyst”, *ACS Appl. Mater. Interface*, **8(3)**, 1571–1577 (2016).
 85. W. Gu, J. Liu, M. Hu, F. Wang, Y. Song, “La₂O₂CO₃ Encapsulated La₂O₃ Nanoparticles Supported on Carbon as Superior Electrocatalysts for Oxygen Reduction Reaction”, *ACS Appl. Mater. Interfaces*, **7(48)**, 26914–26922 (2015).
 86. X.R. Wang, J.Y. Liu, Z.W. Liu, W.C. Wang, J. Luo, X.P. Han, X.W. Du, S.Z. Qiao, J. Yang, “Identifying the Key Role of Pyridinic-N–Co Bonding in Synergistic Electrocatalysis for Reversible ORR/OER”, *Adv. Mater.*, **30(23)**, 1800005 (2018).
 87. L. Dai, M. Liu, Y. Song, J. Liu, F. Wang, “Mn₃O₄-decorated Co₃O₄ nanoparticles supported on graphene oxide: Dual electrocatalyst system for oxygen reduction reaction in alkaline medium”, *Nano Energy*, **27**, 185-195 (2016).
 88. S.C. Perry, D. Pangotra, L. Vieira, L.I. Csepei, V. Sieber, L. Wang, C.P. de León, F.C. Walsh, “Electrochemical synthesis of hydrogen peroxide from water and oxygen”, *Nat. Rev. Chem.*, **3**, 442-458 (2019).

89. C. Alegre, E. Modica, C.L. Vecchio, D. Sebastián, M.J. Lázaro, A.S. Aricò, V. Baglio, “Carbon Nanofibers as Advanced Pd Catalyst Supports for the Air Electrode of Alkaline Metal–Air Batteries”, *ChemPlusChem*, **80(9)**, 1384–1388 (2015).
90. A. Sumboja, X. Ge, G. Zheng, F.W.T. Goh, T.S.A. Hor, Y. Zong, Z. Liu, “Durable rechargeable zinc-air batteries with neutral electrolyte and manganese oxide catalyst”, *J. Power Sources*, **332**, 330–336 (2016).
91. S. Velraj, J.H. Zhu, “Cycle life limit of carbon-based electrodes for rechargeable metal–air battery application”, *J. Electroanal. Chem.*, **736**, 76–82 (2015).
92. K. Kinoshita “Carbon: Electrochemical and Physicochemical Properties”, New York: John Wiley & Sons, pp. 316 (1988).
93. K. Kinoshita, J. Bett, “Electrochemical oxidation of carbon black in concentrated phosphoric acid at 135°C”, *Carbon*, **11**, 237–247 (1973).
94. Y. Yi, G. Weinberg, M. Prenzel, M. Greiner, S. Heumann, S. Becker, R. Schlögl, “Electrochemical corrosion of a glassy carbon electrode”, *Catalyst today*, **295**, 32–40 (2017).
95. T. Kinumoto, K. Takai, Y. Iriyama, T. Abe, M. Inaba, Z. Ogumi, “Stability of Pt-Catalyzed Highly Oriented Pyrolytic Graphite Against Hydrogen Peroxide in Acid Solution”, *J. Electrochem. Soc.*, **153**, A58–A63 (2006).
96. J. Kim, J. Lee, Y. Tak, “Relationship between carbon corrosion and positive electrode potential in a proton-exchange membrane fuel cell during start/stop operation”, *J. Power Sources*, **192**, 674–678 (2009).
97. A. Zadick, L. Dubau, N. Sergent, G. Berthomé, M. Chatenet, “Huge Instability of Pt/C Catalysts in Alkaline Medium”, *ACS Catal.*, **5**, 4819–4824 (2015).
98. J. Zhao, X. Huang, H. Chang, S.H. Chan, Z. Tu, “Effects of operating temperature on the carbon corrosion in a proton exchange membrane fuel cell under high current density”, *Energy Conversion and Management: X*, **10**, 100087 (2021).
99. P.N. Ross, M. Sattler, “The Corrosion of Carbon Black Anodes in Alkaline Electrolyte: III. The Effect of Graphitization on the Corrosion Resistance of Furnace Blacks”, *J. Electrochem. Soc.*, **135**, 1464–1470 (1988).
100. N. Staud, H. Sokol, P.N. Ross Jr., “The Corrosion of Carbon Black Anodes in Alkaline Electrolyte: IV. Current Efficiencies for Oxygen Evolution from Metal Oxide-Impregnated Graphitized Furnace Blacks”, *J. Electrochem. Soc.*, **136**, 3570–3576 (1989).
101. P.T. Yu, W. Gu, R. Makharia, F.T. Wagner, H.A. Gasteiger, “The Impact of Carbon Stability on PEM Fuel Cell Startup and Shutdown Voltage Degradation”, *ECS Trans.*, **3**, 797–809 (2007).
102. Z. Qiao, S. Hwang, X. Li, C. Wang, W. Samarakoon, S. Karakalos, D. Li, M. Chen, Y. He, M. Wang, Z. Liu, G. Wang, H. Zhou, Z. Feng, D. Su, J.S. Spendelow, G. Wu, “3D porous graphitic nanocarbon for enhancing the performance and durability of Pt catalysts: a balance between graphitization and hierarchical porosity”, *Energy Environ. Sci.*, **12**, 2830–2841 (2019).
103. R. Tang, K. Taguchi, H. Nishihara, T. Ishii, E. Morallon, D. Cazorla-Amoros, T. Asada, N. Kobayashi, Y. Muramatsu, T. Kyotani, “Insight into the origin of carbon corrosion in positive electrodes of supercapacitors”, *J. Mater. Chem. A*, **7**, 7480–7488 (2019).
104. G.F. Han, B.B. Xiao, S.J. Kim, F. Li, I. Ahmad, I.Y. Jeon, J.B. Baek, “Tuning edge-oxygenated groups on graphitic carbon materials against corrosion”, *Nano Energy*, **66**, 104112 (2019).
105. M. Matsumoto, T. Manako, H. Imai, “Electrochemical STM Investigation of Oxidative Corrosion of the Surface of

- Highly Oriented Pyrolytic Graphite”, *J. Electrochem. Soc.*, **156**, B1208-1211 (2009).
106. K. Miyazaki, M. Nose, T. Kinumoto, T. Abe, T. Fukutsuka, Z. Ogumi, “Influences of metal oxides on carbon corrosion under imposed electrochemical potential conditions”, *Carbon*, **50(4)**, 1644-1649 (2012).
107. Z. Siroma, K. Ishii, K. Yasuda, Y. Miyazaki, M. Inaba, A. Tasaka, “Imaging of highly oriented pyrolytic graphite corrosion accelerated by Pt particles”, *Electrochem. Commun.*, **7**, 1153-1156 (2005).
108. O.V. Cherstiouk, A.N. Simonov, N.S. Moseva, S.V. Cherepanova, P.A. Simonov, V.I. Zaikovskii, E.R. Savinova, “Microstructure effects on the electrochemical corrosion of carbon materials and carbon-supported Pt catalysts”, *Electrochem. Acta*, **55**, 8453-8460 (2010).
109. N. Staud, P. N. Ross, “The Corrosion of Carbon Black Anodes in Alkaline Electrolyte: II. Acetylene Black and the Effect of Oxygen Evolution Catalysts on Corrosion”, *J. Electrochem. Soc.*, **133**, 1079-1084 (1986).
110. R. Borup, J. Meyers, B. Pivovar, Y. Seung Kim, R. Mukundan, N. Garland, D. Myers, M. Wilson, F. Garzon, D. Wood, P. Zelenay, K. More, K. Stroh, T. Zawodzinski, J. Boncella, J.E. McGrath, M. Inaba, K. Miyatake, M. Hori, K. Ota, Z. Ogumi, S. Miyata, A. Nishikata, Z. Siroma, Y. Uchimoto, K. Yasuda, K. Kimijima, N. Iwashita, “Scientific Aspects of Polymer Electrolyte Fuel Cell Durability and Degradation”, *Chem. Rev.*, **107**, 13904-3951 (2007).
111. C.A. Reiser, L. Bregoli, T.W. Patterson, J.S. Yi, J.D. Yang, M.L. Perry, T.D. Jarvi, “A Reverse-Current Decay Mechanism for Fuel Cells”, *Electrochem. Solid-State Lett.*, **8**, A273-276 (2005).
112. L. Castanheira, W.O. Silva, F.H.B. Lima, A. Crisci, L. Dubau, F. Maillard, “Carbon Corrosion in Proton-Exchange Membrane Fuel Cells: Effect of the Carbon Structure, the Degradation Protocol, and the Gas Atmosphere”, *ACS Catal.*, **5**, 2184-2194 (2015).
113. G. Chen, H. Zhang, H. Ma, H. Zhong, “Electrochemical durability of gas diffusion layer under simulated proton exchange membrane fuel cell conditions”, *Int. J. Hydrogen Energy*, **34**, 8185-8192 (2009).
114. W. Wang, J. Luo, S. Chen, “Carbon oxidation reactions could misguide the evaluation of carbon black-based oxygen-evolution electrocatalysts”, *Chem. Commun.*, **53**, 11556-11559 (2017).
115. C.C. Hung, P.Y. Lim, J.R. Chen, H.C. Shih, “Corrosion of carbon support for PEM fuel cells by electrochemical quartz crystal microbalance”, *J. Pow. Sou.*, **196(1)**, 140-146 (2011).
116. S.P. Rodríguez, D. Sebastián, M.J. Lázaro, “Electrochemical oxidation of ordered mesoporous carbons and the influence of graphitization”, *Electrochimica Acta*, **303**, 167-175 (2019).
117. Y.P. Hsieh, M. Hofmann, K.W. Chang, J.G. Jhu, Y.Y. Li, K.Y. Chen, C.C. Yang, W.S. Chang, L.C. Chen, “Complete Corrosion Inhibition through Graphene Defect Passivation”, *ACS Nano*, **8(1)**, 443-448 (2014).
118. H. Nishihara, T. Simura, S. Kobayashi, K. Nomura, R. Berenguer, M. Ito, M. Uchihara, H. Iden, K. Arihara, A. Ohma, Y. Hayasaka, T. Kyotani, “Oxidation-Resistant and Elastic Mesoporous Carbon with Single-Layer Graphene Walls”, *Adv. Funct. Mater.*, **26(35)**, 6148-6427 (2016).
119. K. Nomura, H. Nishihara, N. Kobayashi, T. Asada, T. Kyotani, “4.4 V supercapacitors based on super-stable mesoporous carbon sheet made of edge-free graphene walls”, *Energy Environ. Sci.*, **12**, 1542-1549 (2019).
120. A. Ohma, Y. Furuya, T. Mashio, M. Ito, K. Nomura, T. Nagao, H. Nishihara, H. Jinnai, T. Kyotani, “Elucidation of oxygen reduction reaction and nanostructure of platinum-loaded graphene mesosponge for polymer electrolyte fuel cell electrocatalyst”, *Electrochimica Acta*, **370**, 137705 (2021).
121. L. Tao, Q. Wang, S. Dou, Z. Ma, J. Huo, S. Wang, L. Dai, “Edge-rich and dopant-free graphene as a highly efficient

- metal-free electrocatalyst for the oxygen reduction reaction”, *Chem. Commun.*, **52**, 2764–2767 (2016).
122. S.G. Ji, H. Kim, W.H. Lee, H.S. Oh, C.H. Choi, “Real-time monitoring of electrochemical carbon corrosion in alkaline media”, *J. Mater. Chem. A*, **9**, 19834-19839 (2021).
123. T. Fujigaya, S. Hirata, N. Nakashima, “A highly durable fuel cell electrocatalyst based on polybenzimidazole-coated stacked graphene”, *J. Mater. Chem. A*, **2**, 3888-3893 (2014).
124. T. Fujigaya, S. Hirata, M.R. Berber, N. Nakashima, “Improved Durability of Electrocatalyst Based on Coating of Carbon Black with Polybenzimidazole and their Application in Polymer Electrolyte Fuel Cells”, *ACS Appl. Mater. Interfaces*, **8(23)**, 14494-14502 (2016).
125. J. Yang, T. Fujigaya, N. Nakashima, “Decorating unoxidized-carbon nanotubes with homogeneous Ni-Co spinel nanocrystals show superior performance for oxygen evolution/reduction reactions”, *Sci. Rep.*, **7**, 45384 (2017).
126. T. Fujigaya, Y. Shi, J. Yang, H. Li, K. Ito, N. Nakashima, “A highly efficient and durable carbon nanotube-based anode electrocatalyst for water electrolyzers”, *J. Mater. Chem. A*, **5**, 10584-10590 (2017).
127. K. Ghuman, T. Fujigaya, “Electronic Structure of Polybenzimidazole-Wrapped Single-Wall Carbon Nanotube”, *J. Phys. Chem. C*, **122**, 15979-15985 (2018).
128. S. M. Jayawickrama, T. Fujigaya, “Effect of polymer-coating on carbon blacks for Pt utilization efficiency of polymer electrolyte membrane fuel cells”, *J. Power Sources*, **482**, 228932 (2020).
129. S. M. Jayawickrama, D. Wu, R. Nakayama, S. Ishikawa, X. Liu, G. Inoue, T. Fujigaya, “Effect of a Polybenzimidazole Coating on Carbon Supports for Ionomer Content Optimization in Polymer Electrolyte Membrane Fuel Cells”, *J. Power Sources*, **496**, 229855 (2021).
130. S. Miyanishi, T. Yamaguchi, “Ether cleavage-triggered degradation of benzyl alkylammonium cations for polyethersulfone anion exchange membranes”, *Phys. Chem. Chem. Phys.*, **18**, 12009-12023 (2016).
131. T. Fujigaya and N. Nakashima, “Fuel Cell Electrocatalyst Using Polybenzimidazole-Modified Carbon Nanotubes As Support Materials”, *Adv. Mater.*, **25** (2013) 1666-1681.
132. K. Sakai, S. Iwamura, R. Sumida, I. Ogino, S.R. Mukai, “Carbon Paper with a High Surface Area Prepared from Carbon Nanofibers Obtained through the Liquid Pulse Injection Technique”, *ACS Omega*, **3**, 691–697 (2018).
133. N. M. Rodriguez, A. Chambers, R.T.K. Baker, “Catalytic Engineering of Carbon Nanostructures”, *Langmuir*, **11**, 3862-3866 (1995).
134. J.S. Zheng, X.S. Zhang, P. Li, X.G. Zhou, W.K. Yuan, “Microstructure effect of carbon nanofiber on electrocatalytic oxygen reduction reaction”, *Catal. Today*, **131**, 270-277 (2008).
135. E.J. Biddinger, U.S. Ozkan, “Role of Graphitic Edge Plane Exposure in Carbon Nanostructures for Oxygen Reduction Reaction”, *J. Phys. Chem. C*, **114**, 15306–15314 (2010).
136. R.T.K. Baker, K. Laubernds, A. Wootsch, Paál, “Pt/graphite nanofiber catalyst in n-hexane test reaction”, *J Catal*, **193**, 165-167 (2000).
137. R.T.K. Baker, N. Rodriguez, Á. Mastalir, U. Wild, R. Schlögl, A. Wootsch, Z. Paál, “Platinum/graphite nanofiber catalysts of various structure: characterization and catalytic properties”, *J. Phys. Chem. B*, **108**, 14348-14355 (2004).
138. P. Li, Y. Huang, D. Chen, J. Zhu, T. Zhao, X. Zhou, “CNFs-supported Pt catalyst for hydrogen evolution from decalin”, *Catal. Commun.*, **10**, 815-818 (2009).
139. T. Tamaki, H. Wang, N. Oka, I. Honma, S.H. Yoon, T. Yamaguchi, “Correlation between the carbon structures and

- their tolerance to carbon corrosion as catalyst supports for polymer electrolyte fuel cells”, *Int. J. Hydrogen Energy*, **43**(12), 6406-6412 (2018).
140. S.W. Lee, S.R. Choi, J. Jang, G.G. Park, S.H. Yu, J.Y. Park, “Tolerance to carbon corrosion of various carbon structures as catalyst supports for polymer electrolyte membrane fuel cells”, *J. Mater. Chem. A*, **7**, 25056-25065 (2019).
141. S.V. Rotkin, Y. Gogotsi, “Analysis of non-planar graphitic structures: from arched edge planes of graphite crystals to nanotubes”, *Mater. Res. Innovations*, **5**, 191-200 (2002).
142. S.H. Yoon, S. Lim, S.H. Hong, I. Mochida, B. An, K. Yokogawa, “Carbon nano-rod as a structural unit of carbon nanofibers”, *Carbon*, **42**, 3087-3095 (2004).
143. S. Lim, S.H. Yoon, I. Mochida, J. H. Chi, “Surface Modification of Carbon Nanofiber with High Degree of Graphitization”, *J. Phys. Chem. B*, **108**, 1533-1536 (2004).
144. S.H. Yoon, S. Lim, S.H. Hong, W. Qiao, DD. Whitehurst, I. Mochida, B. An, K. Yokogawa, “A conceptual model for the structure of catalytically grown carbon nanofibers”, *Carbon*, **43**, 1828-1838 (2005).
145. H. Habazaki, M. Kiri, M. Hayashi, H. Komno, “Structure of the carbon nanofilaments formed by liquid phase carbonization in porous anodic alumina template”, *Mater. Chem. Phys.*, **105**, 367-372 (2007).

Chapter 2
Characterizations of
pCNFs

Chapter 2 Characterizations of pCNFs

2-1 Introduction

As mentioned in the previous chapter, the structure/shape of carbon materials strongly affects electrochemical behavior [1, 2]. Thus, structural characterization is required to understand the electrochemical behavior of the electrodes. This thesis focuses the platelet-type carbon nanofibers (pCNFs) as the novel electrode conductive supports with high oxidation resistance. The pCNFs have been typically prepared by chemical vapor deposition [3]. However, this thesis study used a template-assisted liquid phase carbonization method because of the formation of nanofibers with well-controlled diameters [4]. The template used in this study was porous anodic alumina (AAO) (Fig. 2-1). The platelet-type orientation remains unchanged regardless of heat treatment temperature, but the graphitization degree is enhanced with heat treatment temperature [5]. In this chapter, the pCNFs prepared by the template-assisted liquid-phase carbonization method using AAO template and polyvinyl chloride carbon precursor were characterized by various techniques to understand better the correlation between the corrosion behavior and structural characteristics.

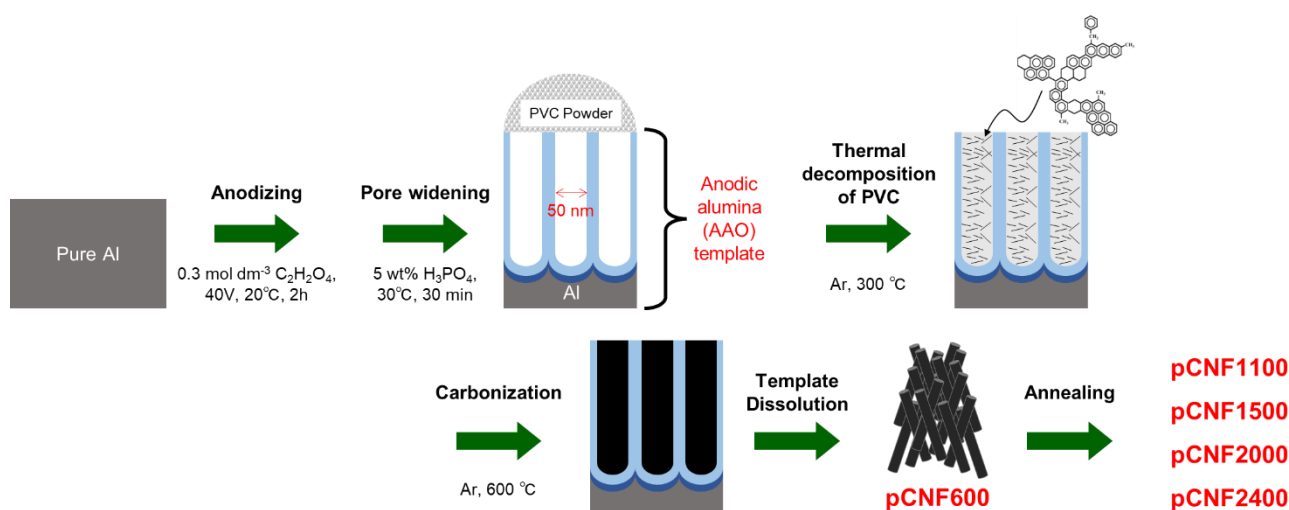


Fig. 2-1 The schematic image of the liquid-phase carbonization process using an AAO template.

2-2 Experimental

2-2-1 Carbon materials used in this study

Three main types of nanocarbon materials were used in this thesis, as illustrated in Fig. 2-2. Type 1 refers to a structure in which the graphene layer is aligned perpendicular to the fiber axis of the nanofiber (pCNFs), type 2 is a structure with graphene layers parallel to the fiber axis of the nanofiber (MWCNTs), and type 3 is a particle-like structure with randomly distributed graphene layers (carbon blacks).

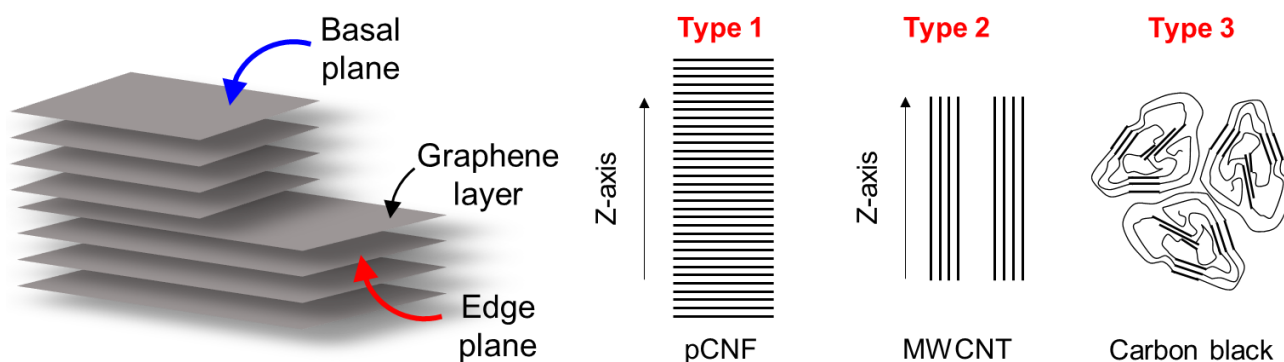


Fig. 2-2 Schematic illustrations of the carbon materials used in this thesis.

Hereafter, based on the heat-treatment temperature of pCNFs, pCNFs were denoted, for instance, pCNF1500. The type 1 carbons used in this thesis were pCNF600, pCNF1100, pCNF1500, pCNF2000, pCNF2400, pCNF3000, the type 2 was multi-walled carbon nanotubes supplied from Sigma-Aldrich (MW), and the type 3 carbon materials were Denka Black (DB), DB annealed at 2400°C (DB2400), Toka Black 3800 (TB), and acetylene black (AB) (Type 3). The suppliers and synthesis methods are summarized in Table 2-1.

Table 2-1 Carbon materials used in this thesis.

	Supplier	Structure type	Synthesis method	Remarks
pCNF600	Home-made	1		
pCNF1100	Home-made	1	Liquid-Phase Carbonization	Annealed at 1100°C
pCNF1500	Home-made	1		Annealed at 1500°C
pCNF2000	Home-made	1		Annealed at 2000°C
pCNF2400	Home-made	1		Annealed at 2400°C
pCNF3000	Sigma-Aldrich	1	CVD	799017-500MG
MW	Sigma-Aldrich	2	CVD	PR-25-XT-HHT
AB	STREAM Chemicals	3	Acetylene method	06-0025, 100% compressed
TB	Tokai Carbon	3	Furnace method	TB#3800
DB	Denka	3	Acetylene method	DB Powder
DB2400	Denka	3	Acetylene method	Annealed DB at 2400°C

2-2-2 Synthesis of pCNFs via liquid-phase carbonization using an AAO template

According to previous reports [5, 6], the pCNFs were prepared by liquid-phase carbonization in a porous anodic alumina (AAO) template. AAO template was prepared by anodizing 99.99 % pure aluminum sheets (TOYO Aluminum, 10 × 10 cm², thickness 0.1 mm) at 40 V in 0.3 mol dm⁻³ oxalic acid aqueous solution at 20 °C for 2 h. The size of the nanopores in the anodic alumina layer was controlled by subsequent pore widening treatment in 5 wt% H₃PO₄ for 30 min at 30 °C [7]. Under these conditions, the thickness and pore size of the AAO template were controlled to approximately 16 μm and 50 nm, respectively (Fig. 2-3). Polyvinyl chloride powder (PVC, SHIN-ETSU CHEMICAL Co., Ltd., TK-2500) was used as a carbon precursor. The AAO template and PVC powders were mixed and heat-treated at 350 °C for 30 min with a temperature ramp of 400 K h⁻¹ in a stream of high-purity argon (99.999 %) followed by heat treatment at 600 °C for 1 h. During this heat treatment, PVC was converted into a liquefied pitch-like intermediate at ~350°C [8-10], penetrating into the cylindrical pores of the AAO template. Then, during further heat treatment at 600°C, carbonization of the pitch-like intermediates proceeded [4, 5, 8-10]. After cooling, the template was dissolved in 20 % NaOH solution under ultrasonication, and pCNF600 nanofibers were filtered. Further heat treatment was

performed in an Ar atmosphere using the high-temperature furnace (Kurata-Giken, KVA-40/50). The heat treatment temperatures chosen were 1100, 1500, 2000, and 2400°C. The temperature of 2400°C was the highest temperature of the available furnace. To examine pCNFs with higher graphitization degree, the commercial pCNF3000 (Carbon Nanochips, Sigma-Aldrich 799017-500MG) [11], which was heat-treated at 3000°C, was also used in this study.

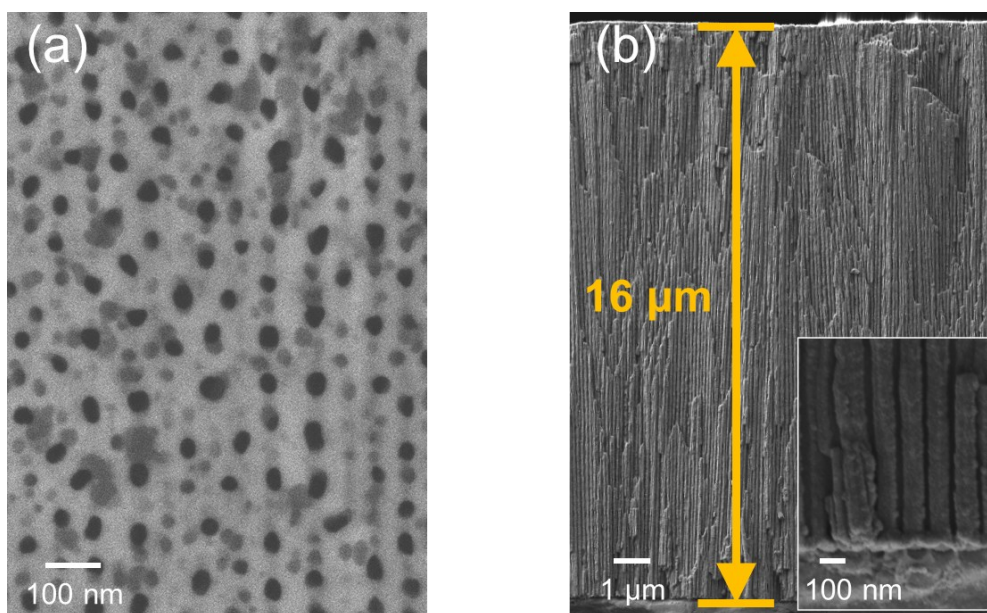


Fig. 2-3 (a) Surface and (b) cross-sectional SEM images of anodic aluminum anodized in 0.3 mol dm^{-3} oxalic acid aqueous solution at 40 V, 20°C for 2 h.

2-2-3 Electron microscopy observations

The surface morphology was observed using a low-voltage scanning electron microscope (Zeiss, Sigma-500) operated at 1.5 kV. The detailed structure was further evaluated using transmission electron microscopy (TEM; JEOL, JEM-2000FX, JEM-2010 F, and JEM-ARM200 F), operated at 200 kV.

2-2-4 X-ray diffraction analysis

The phase purities and the graphitization degrees of the carbon materials used in this study were examined by X-ray powder diffraction (XRD; Rigaku, Ultima IV) using Cu $K\alpha$ radiation

($\lambda = 0.15418$ nm) operated at 40 kV and 20 mA. Typically, the XRD patterns of the carbon materials showed the 002 diffraction peak around $2\theta = 26^\circ$. This 002 peak is often used to evaluate the graphitization degree of the carbon materials [12]. Hence, to estimate the graphitization degree, the interplanar spacing, d_{002} , was calculated according to the Bragg equation described as Eq. (2-1):

$$d_{002} = \frac{\lambda}{2\sin\theta} \quad (2-1)$$

2-2-5 Raman scattering spectroscopy

The graphitization degree was also examined by Raman spectroscopy (Horiba Scientific, XploRA) using a 532 nm laser beam. The intensity of the laser beam was 2.5 mW. In the Raman spectra of carbon materials, mainly three peaks were observed around 1350, 1580, and 1620 cm^{-1} , which could be assigned with A_{1g} vibration of disordered carbon (D band), E_{2g} vibration mode of graphite (G band), and E_{2g} vibration of the disordered carbon (D' band), respectively. The area intensity ratio of the D and G bands serves as an indicator for the graphitization degree [13] using the following formula:

$$\text{Graphitization degree} = I_D/I_G \quad (2-2)$$

where I_D and I_G represent the peak area of the D band (1350 cm^{-1}) and G band (1580 cm^{-1}), respectively.

2-2-6 Nitrogen adsorption/desorption analysis

Nitrogen gas adsorption/desorption isotherm measurements (Bel Japan, Belsorp-mini instrument) were conducted at -196°C to obtain the BET surface area of carbon materials. The obtained isotherms were analyzed using the following equation [14]:

$$\frac{P}{V(P_s - P)} = \frac{1}{V_m c} + \frac{c - 1}{V_m c} \cdot \frac{P}{P_s} \quad (2-3)$$

where P_s , P , V , V_m , and c are adsorbate's saturation and equilibrium pressures (Nitrogen), the actual and monolayer adsorption volume, and BET C-constant, respectively.

2-3 Results and Discussion

2-3-1 SEM/TEM observations and temperature dependency of nanostructure

SEM surface images of the carbon materials used in this thesis are shown in Fig. 2-4. Carbon black (CB) type materials, *e.g.*, AB, DB, DB2400, and TB, have granular morphology with the size around 40 - 150 nm. From the comparison between DB and DB2400, no morphological changes such as agglomeration and particle shrinking were observed upon heat treatment. Platelet-type carbon nanofibers, *e.g.*, pCNF600, 1100, 1500, 2000, 2400, and 3000, have nano-rod-like morphology. Due to this feature, it is obvious that pCNFs have a high aspect ratio. The diameters of homemade pCNFs, are around 55 nm, which agrees with the pore size of the AAO template (Fig. 2-3a). These diameters did not change with the heat treatment temperature. Hence, it is suggested that the diameter is independent of heat treatment temperature up to 2400°C. The lengths of the pCNFs were less than 2 μm , which were much shorter than the length of the cylindrical pore channel (16 μm) in the template. Additionally, those lengths become shorter, from more than several micrometers to less than 1 μm , with increasing heat treatment temperature. The formation of short nanofibers was associated with the trapping of gaseous species generated during carbonization of the PVC precursor in the cylindrical pores of the AAO template and the poor mechanical strength of platelet-type nanofibers [5, 15]. The shortening of pCNFs during further heat treatment also should be associated with this poor mechanical strength. The commercially available pCNF3000, prepared by CVD, have wider diameters of 80–300 nm and lengths distributions within 0.5–5 μm , respectively. The MW (Fig. 2-4k) has a fiber length in the range of 0.5–10 μm and a diameter of 50–200 nm.

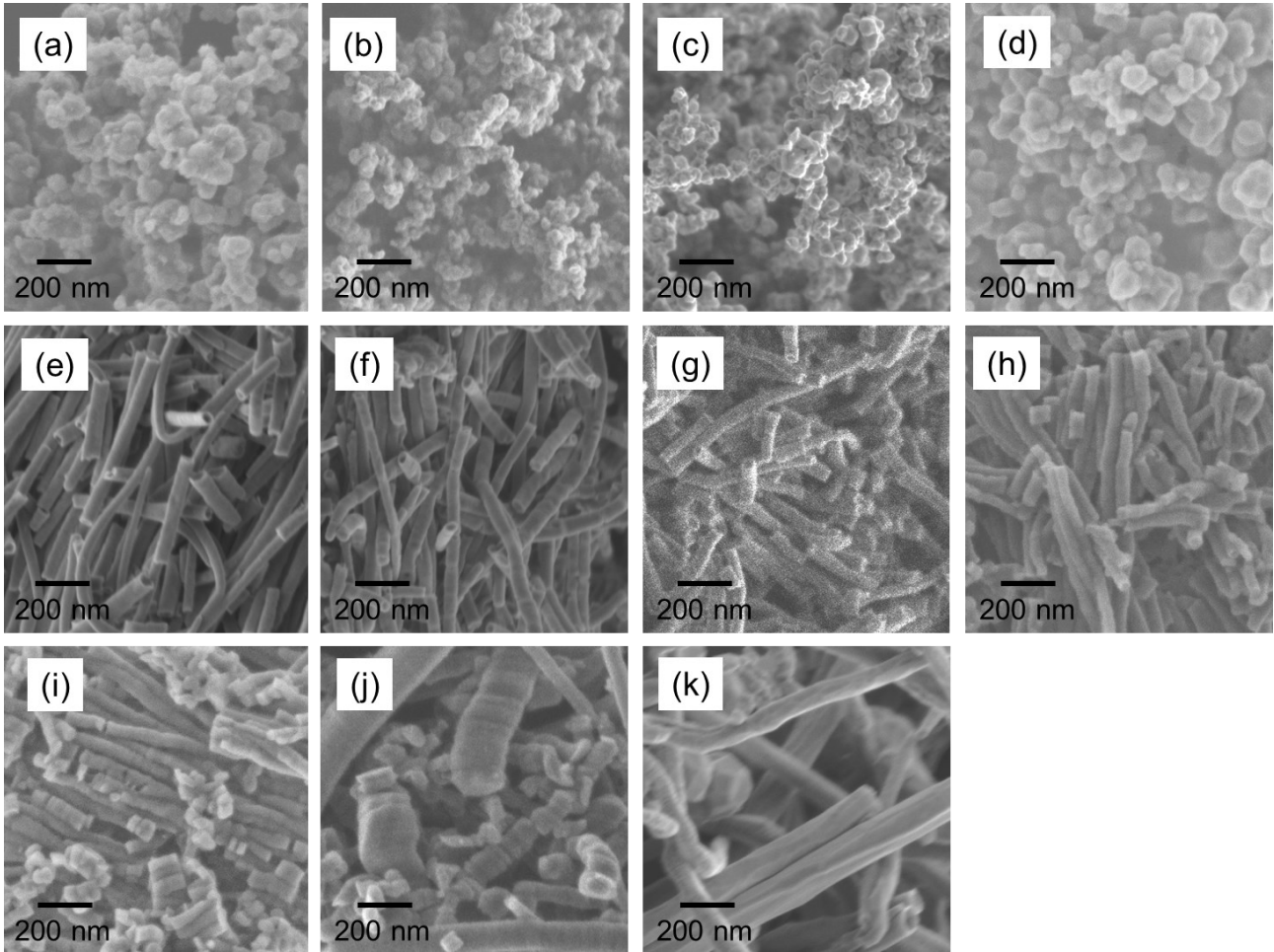


Fig. 2-4 SEM images of (a) AB, (b) DB, (c) DB2400, (d) TB, (e) pCNF600, (f) pCNF1100, (g) pCNF1500, (h) pCNF2000, (i) pCNF2400, (j) pCNF3000, and (k) MW carbon materials.

The detailed carbon structure was further investigated by TEM (Fig. 2-5). Due to the low graphitization degree, pCNF600 shows a mosaic-like pattern of the amorphous phase, while pCNFs heat-treated at $\geq 1100^\circ\text{C}$ have platelet structures with graphene layers perpendicularly oriented to the fiber axis of the nanofibers, regardless of the preparation method. Because of this feature, surfaces of pCNFs consist of two types of surfaces: the carbon basal plane on both ends of the fiber and the carbon edge plane on the sidewall. The well-developed (002) lattice fringes of these images look more evident with the increase of heat treatment temperature. This fact suggests that the graphitization proceeds with an elevation of heat treat temperature. Because of the platelet structure, the carbon edge sites are

exposed at the sidewall for pCNF1500 and 1100. It is noted that higher numbers of defect sites are expected on such an edge plane than on the basal plane, which acts as hosts for molecules to adsorb, especially for gas species altering the electrochemistry of the carbon [16, 17]. On the other hand, pCNFs annealed at $\geq 2000^\circ\text{C}$ shows looped graphene edges on the sidewall. Each loop contains 3-5 graphene layers; each stack comprises 6-10 graphene layers. The curvature of this part is high, suggesting that this region contains the sp^3 like carbon atom compared to the bulk. The surface reconstruction occurs at $\geq 2000^\circ\text{C}$, developing this loop structure, and as a result, the surface energy of the sidewall is reduced because of the disappearance of the dangling bond or edge defects [3]. As explained later, the presence of loops may cause the low graphitization degree estimated by the Raman spectra.

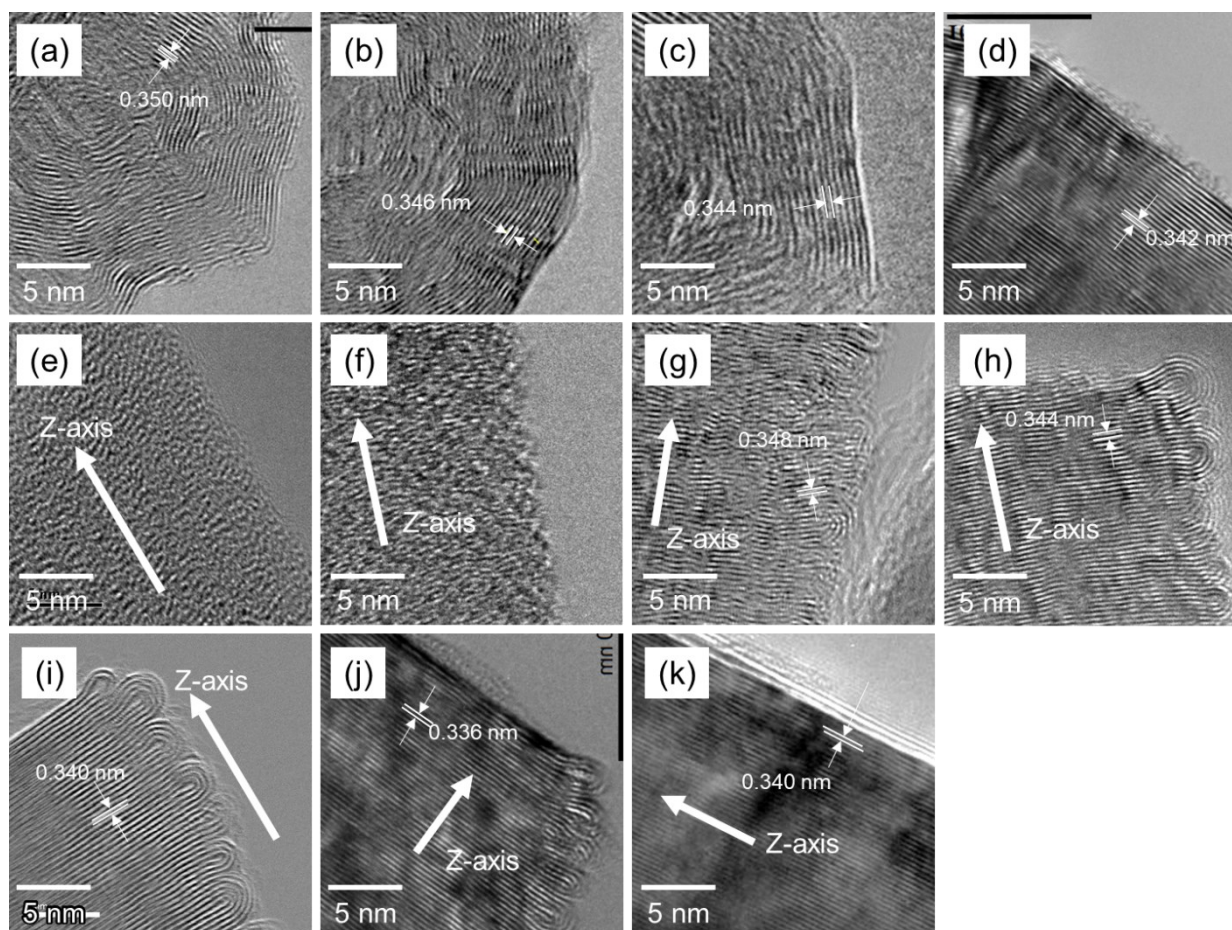


Fig. 2-5 HRTEM images of (a) AB, (b) DB, (c) DB2400, (d) TB, (e) pCNF600, (f) pCNF1100, (g) pCNF1500, (h) pCNF2000, (i) pCNF2400, (j) pCNF3000, and (k) MW carbon materials.

Fig. 2-5k shows the TEM image for the MW, in which the carbon layers are oriented parallel to the fiber-axis of the nanotube. In this configuration, the carbon basal plane was predominantly exposed at the sidewalls of the MWs. In the case of the type 3 structures studied, the carbon basal plane was mainly exposed on the surface. The TEM image shows that TB clearly shows lattice fringes while AB and DB show undeveloped fringes. These lattice fringes were incompletely developed even for DB2400, and therefore, random regions were formed on the carbon particles.

Lattice spacing distances were measured to evaluate the graphitization degree from the TEM images. Unclear fringes are observed in pCNF600 and pCNF1100, indicating a lower graphitization degree. In contrast, other materials show clear lattice fringes. In particular, the lattice spacing distances of heat-treated pCNFs over 2000°C were narrower than pCNF1500; 0.340 nm for pCNF2400 and 0.336 nm for pCNF300 while pCNF1500 have the lattice spacing distance of 0.348 nm. These narrower distances are close to TB (0.342 nm) and MW (0.340 nm). In addition, such narrowing due to the graphitization degree enhancement during the heat treatment was not observed for DB and DB2400. Thus, from TEM observation, the graphitization degrees are expected in the ordering to pCNF600, pCNF1100 \ll AB, pCNF1500, DB, DB2400 \leq pCNF2000 $<$ TB, pCNF2400, MWCNT, and pCNF3000.

In summary, from TEM observations, this thesis study obtained the following results: the carbon basal plane was predominantly exposed on the surface in the case of type 2 and type 3 carbon. On the other hand, the surface of pCNFs annealed at lower than 2000°C consisted mainly of the carbon edge plane. When pCNFs were annealed at $\geq 2000^\circ\text{C}$, the graphitization degree enhanced, and looped carbon layers were developed on the sidewall. Therefore, the carbon basal plane was exposed on the surface of heat-treated pCNFs. In these TEM observations, DB's enhanced graphitization degree was not confirmed even after the heat-treatment at 2400°C.

2-3-2 XRD study of graphitization degree

X-ray diffraction patterns of the carbon materials used in this study are shown in Fig. 2-6a. All patterns show a strong peak around $2\theta = 26^\circ$ and a relatively weaker diffraction peak around $2\theta = 42^\circ$, assigned as the 002 and 10 reflections, respectively. Peak widths, intensities, and shapes provide information about the graphitization of these carbon materials. While pCNF600, pCNF1100, AB, and DB show a weaker and broader 002 reflection peak, other carbon materials have an intense and narrow 002 reflection peak. Thus, pCNF600, pCNF1100, AB, and DB should have a relatively lower graphitization degree than other carbon materials used in this thesis. In addition, the 10 reflection is split into 100 and 101 reflections for pCNF2400, pCNF3000, and MW (Fig. 2-6b). It is noted that the overlapping of 100 and 101 reflection peaks is brought by the insufficient development of graphite structure for the z-axis direction [12]. In fact, the peak shape of the 10 reflection peak is asymmetric and suggests the presence of a turbostratic region [5]. Hence, the narrower 002 reflection peak and split of the 10 reflection peak suggest the higher graphitization of each carbon material. Therefore, carbon materials used in this thesis can be classified into the following three classes: (a) The narrower 002 peak and the sufficient structural development for the z-axis direction (pCNF2400, pCNF3000, MW); (b) The narrower 002 peak with a turbostratic region (TB, DB2400, pCNF2000); (c) The broader 002 peak with a turbostratic region (DB, AB, pCNF600, pCNF1100, pCNF1500). It should be noted that the weak peak around 40.0° in the XRD profile for pCNF1500 is possibly assigned with Al_2O_3 from the AAO template.

The heat treatments for pCNFs provide reasonable graphitization development. The 002 reflection peak of pCNFs becomes intense and sharp with an increase in the heat treatment temperature. Additionally, the peak position shifts towards higher angles with increasing heat treat temperature, *i.e.*, from 25.2° for pCNF600 to 26.2° for pCNF2400 (Fig. 2-6c), which is closer to the natural graphite value (26.58°). These results are associated with the increased graphitization degree of heat-treated

pCNFs. The 002 lattice spacing, d_{002} , of the carbon materials used in this study was calculated using the Bragg equation and summarized in Table 2-2. The d_{002} values of the pCNFs reduce with the heat treatment temperature (Fig. 2-6d), approaching the graphite value (0.3354 nm). The d_{002} values of TB and MW are between pCNF2000 and pCNF3000, and AB has the highest value in carbon blacks examined in this study. The influence of heat treatment for the graphitization degree is different in the three types of carbon materials. While pCNF2400 shows the comparable graphitization with TB or MW, DB2400 still has the relatively wider 002 lattice spacing and the turbostratic region, indicating the asymmetric and single 10 reflection peak. Thus, DB-type carbon materials have difficulty enhancing the graphitization degree compared with pCNF type carbon materials.

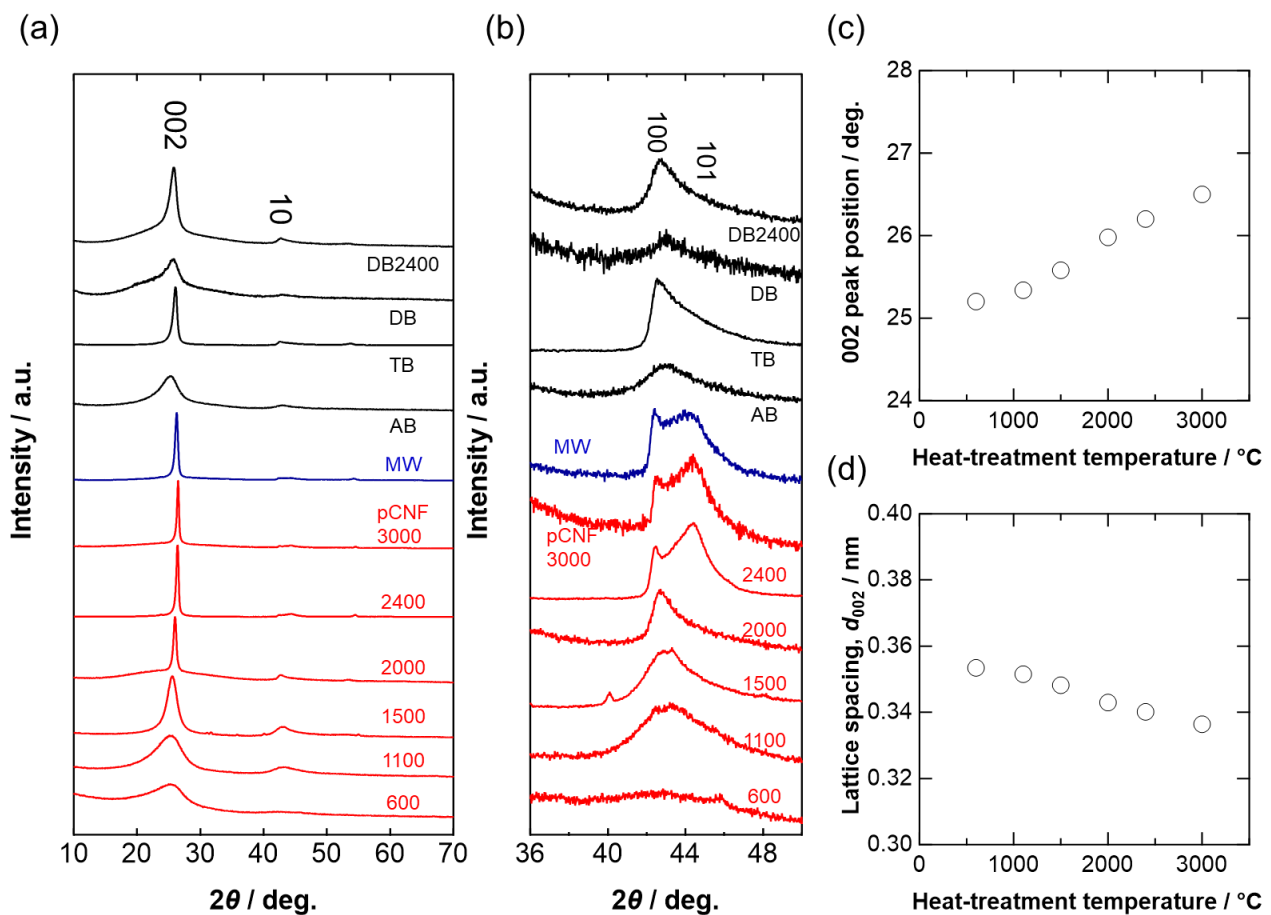


Fig. 2-6 (a, b) XRD patterns of carbon materials used in this thesis, (c) relationship between the heat treatment temperature and 002 peak position of pCNFs, and (d) relationship between the heat treatment temperature and lattice spacings of pCNFs.

Table 2-2 Physicochemical properties of carbon materials used in this thesis.

	Structure type	Peak position of 002 / deg.	Lattice spacing d_{002} / nm	Graphitization degree I_D/I_G / -	FWHM of G band / cm^{-1}	BET surface area / m^2g^{-1}
pCNF600	1	25.20	0.353	3.19	75.7	296
pCNF1100	1	25.34	0.351	2.02	70.6	46.0
pCNF1500	1	25.58	0.348	1.53	70.9	32.0
pCNF2000	1	25.98	0.343	1.71	47.1	27.0
pCNF2400	1	26.20	0.340	1.51	29.7	28.0
pCNF3000	1	26.50	0.336	0.725	27.8	40.3
MW	2	26.26	0.339	0.193	29.0	72.1
AB	3	25.30	0.352	1.04	84.9	78.0
TB	3	26.06	0.342	0.392	31.0	26.4
DB	3	25.78	0.346	0.938	70.2	59.4
DB2400	3	25.80	0.345	0.832	44.9	42.7

2-3-3 Raman study of carbon materials

The graphitization degree was also investigated using Raman spectroscopy (Fig. 2-7). Graphite's E_{2g} vibration mode in the Raman spectra is attributed to the stretching vibration in the aromatic layers and appears at a Raman shift of approximately 1580 cm^{-1} [18]. Additional bands are also found at approximately 1350 and 1620 cm^{-1} for less ordered carbon materials. The 1350 cm^{-1} band, known as the defect band (D band), is typically assigned to the A_{1g} mode [19-21]. The Raman spectra for the lower graphitization sample, *i.e.*, pCNF600, 1100, 1500, AB, and DB, show two broad overlapping bands located at $\sim 1580 \text{ cm}^{-1}$ (G band) and $\sim 1350 \text{ cm}^{-1}$ (D band). The additional signal, which seems to be a weak shoulder peak, was found at $\sim 1620 \text{ cm}^{-1}$ for higher graphitization carbon materials, *i.e.*, pCNF2000, 2400, 3000, MW, TB, and DB2400, corresponding to the D' band. The graphitized carbon materials, classified by TEM and XRD, show a narrow and intense G band peak and D' band peak. For the pCNFs, with the increase in the heat treatment temperature, both G and D bands become narrower, their intensities increase, and the maxima move towards lower wavenumbers. These changes are associated with the increased graphitization degree and reduced number of defects.

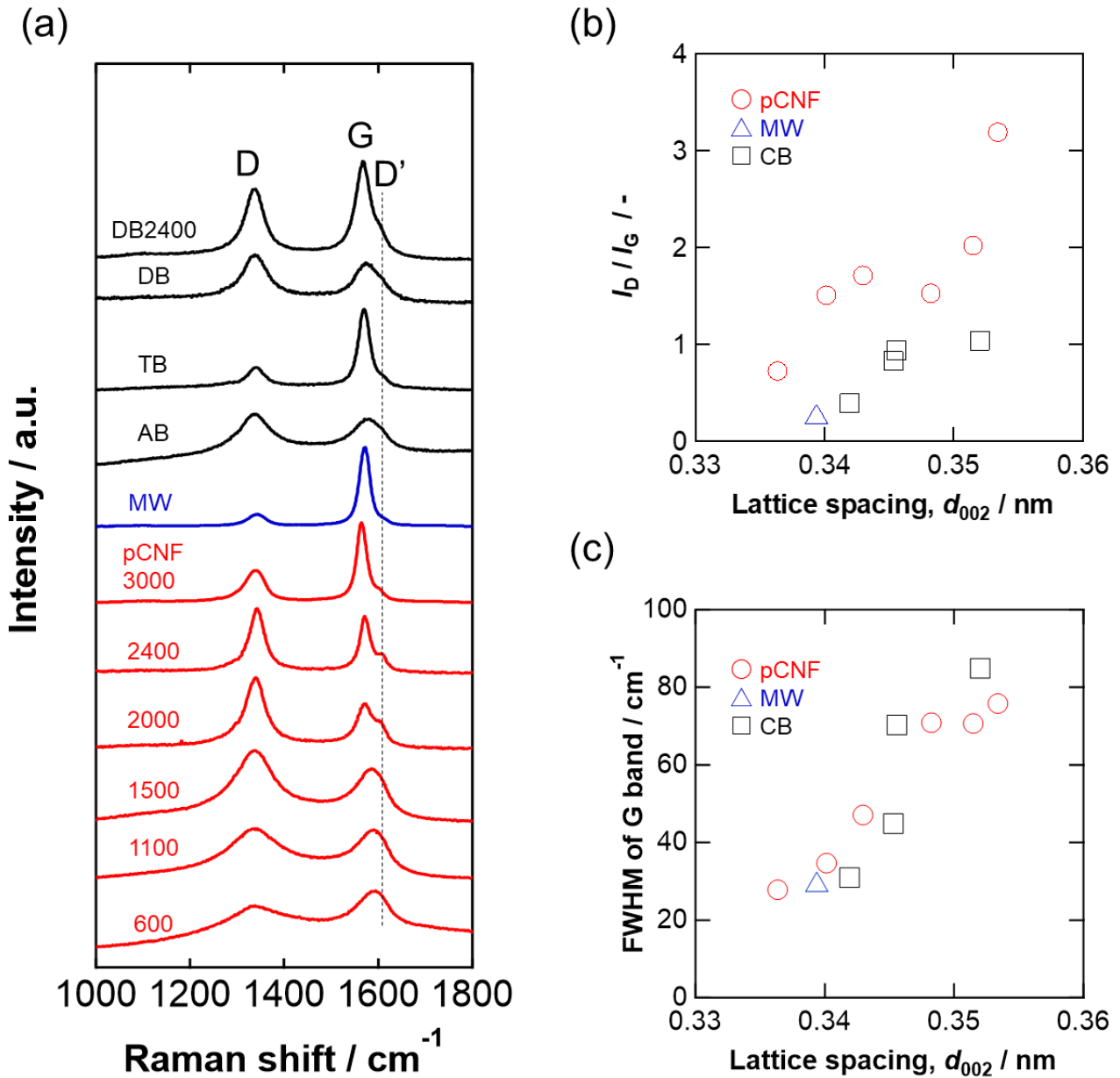


Fig. 2-7 (a) Raman spectra of carbon materials used in this thesis and the changes in (b) I_D/I_G and (c) FWHM of G band with 002 lattice spacing.

The peak area ratio of I_D/I_G often used to evaluate the graphitization degree of the carbon materials [13] is summarized in Table 2-2. The peak width of the G band is another parameter to be used to evaluate the graphitization degree [13]. The correlations between the I_D/I_G and d_{002} and the peak width of the G band and d_{002} are plotted in Fig. 2-7b and 2-7c, respectively. There is a good correlation between the I_D/I_G value and d_{002} for the heat-treated pCNFs system, but not for all the

carbon materials used in this thesis. In contrast, a linear correlation is seen between the G band's width and d_{002} for all the carbon materials. Thus, the I_D/I_G value can discuss the graphitization degree of only similar types of nanocarbon materials, whereas the peak width of the G band can be applied to the graphitization degree of a wide range of carbon materials.

2-3-4 BET surface areas

Fig. 2-8a and b show nitrogen gas adsorption/desorption isotherms for the carbon materials. Besides pCNF600, all isotherms shapes are similar to the IUPAC type III pattern, suggesting a limited number of micropores. The pCNF600 shows the increment of adsorption in the lower pressure region due to the presence of micropores. The BET surface areas are summarized in Table 2-2. All carbon materials except pCNF600 show similar BET surface areas of 25-80 m^2g^{-1} , typical carbon conductive additives for electrode applications. Additionally, from the comparison of DB and DB2400, the negligible influence on the surface area of DB, due to the heat treatment, indicated. For the pCNFs heat-treated from 600 to 2400°C, the BET surface areas decrease with an increase in heat treatment temperature up to 1500°C, above which the surface area becomes almost constant ($\sim 25 \text{ m}^2\text{g}^{-1}$) (Fig. 2-8c). Since the calculated specific surface area, assuming a density of 3.0 g cm^{-3} [5] and a length of $1.0 \mu\text{m}$, for a carbon nanofiber of 55 nm in diameter without any porosity is also about $25 \text{ m}^2\text{g}^{-1}$, the carbon nanofiber heat-treated at high temperatures should have a negligible amount of pores.

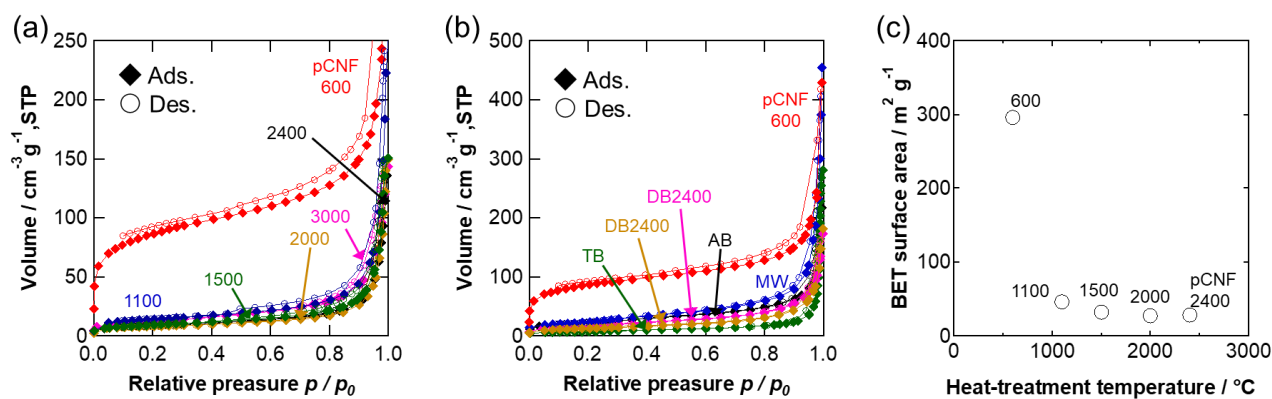


Fig. 2-8 (a, b) N₂ adsorption/desorption isotherms, measured at -196°C , of the carbon materials used in this thesis. (c) Change in BET specific surface area of pCNFs with heat treatment temperature.

2-3-5 Discussion

In this chapter, pCNFs were successfully prepared using the liquid-phase carbonization using the AAO template. The heat treatment of pCNFs at higher temperatures effectively enhanced their graphitization degree. In contrast, DB did not show such graphitization degree enhancement after the same heat treatment. Hence, in this section, the difference in graphitization behavior of pCNFs and DB is explained. In addition, the structural change of pCNFs during the graphitization degree enhancement is also given.

Some carbon materials have difficulty for graphitization because of the macro and microstructure. It is often discussed that the difficulty of the graphitization degree depends on the precursor of each carbon material; for instance, carbon materials synthesized from polyvinyl chloride are graphitizable; however, polyimide (PI) is non-graphitizable [22-26]. This explanation is insufficient because highly graphitized carbon can be obtained even from the PI precursor when the PI film with enough orientation is carbonized [23-26]. Thus, carbon film from PI film was highly graphitized at 2800°C [24]. Inagaki *et al.* proposed the basic structural unit (BSU) effect, *i.e.*, a long-range statistical orientation of small aromatic layer stacks or dicoronene [27-30]. This BSU is initially developed during carbonization, *i.e.*, the conversion of carbon precursors to carbon materials, and their stacking/structure ordering is also decided simultaneously [27]. This BSU orientation affects the graphitizability of carbon materials. In the case of the particle-type carbon materials, their BSUs receive the constraint from their macrostructure, resulting in the non-graphitizability compared with other nanostructured carbon materials [31-34]. Therefore, the non-graphitizability of DB might be caused by (1) their small diameter and (2) the non-ordered BSU orientation coming from their turbostratic structure.

On the other hand, in the case of pCNFs synthesized using the template-assisted liquid-phase carbonization, the intermediates produced from the thermal decomposition of polymer precursor can interact with AAO templates and other intermediates [35-40]. This interaction enables the intermediates to be arranged with ordering [35]. As a result, BSU ordering can be provided for pCNFs because the intermediates ordering is kept during the carbonization. Due to this BSU ordering, pCNFs, synthesized by the template-assisted liquid-phase carbonization, pCNFs are graphitizable at high temperatures. Kiriu demonstrated the structural development of pCNF synthesized from polyacrylamide precursor [40], which is one of the non-graphitizing carbon [22].

In addition to the graphitization, pCNFs show the looped carbon edge structure on their sidewalls after heat treatment over 2000°C. As shown in the Raman spectra, heat-treated pCNFs show a relatively intense D band peak while the similar d_{002} value carbon materials, *i.e.*, TB and MW, show a little D band peak. D band peak is often assigned to the defect on the graphene plane or graphene edges and the sp^3 like carbon [41]. Hence, a relatively intense D band peak of heat-treated pCNFs suggests the existence of a not-covered edge plane by the looped carbons or sp^3 type carbon in the pCNFs. As the later species, looped edge structure is a possible candidate because this looped region contains seven- or five-membered rings [3]. It is often discussed that these loop structure formations occur because of the high reactivity of the dangling bond on the edge plane on the sidewall of pCNF [6, 42-45]. Loop formation decreases the number of such dangling bonds and provides thermodynamical stability due to the surface energy reduction [3]. Such reactive edge sites have often been discussed as oxidation priority sites [46]. In the case of heat-treated pCNFs, such edge sites are entirely covered by the loop edge structure. Hence, it is expected a higher oxidation resistance for the electrochemical environment.

2-4 Conclusions

In summary, in this chapter, pCNFs were prepared by the liquid-phase carbonization using an AAO template and compared their properties with other nanostructured carbon materials and the commercially available pCNF3000. The following conclusions are drawn:

- (1) While commercially available pCNF3000 shows broader diameters and lengths distributions, pCNFs prepared from the template have well-controlled diameters of 55 nm and micro-meter-order lengths. This controlled diameter is one of the characteristics of pCNFs synthesized using template-assisted liquid-phase carbonization. The macrostructure of pCNFs is a fiber structure with a higher aspect ratio. Due to the low graphitization degree, pCNF600 shows a mosaic-like pattern of the amorphous phase. At the same time, pCNFs heat-treated at $\geq 1100^\circ\text{C}$ have platelet structures with graphene layers perpendicularly oriented to the fiber axis of the nanofibers, regardless of the preparation method. Because of this feature, surfaces of pCNFs consist of two types of surfaces: the carbon basal plane on both ends of the fiber and the carbon edge plane on the sidewall. Even with such an amorphous structure of pCNF600, the basic structural unit was developed during the liquid-phase carbonization. As a result, graphitization developments proceeded during the further heat-treatment. Thus, pCNFs via liquid-phase carbonization can be classified as graphitizing carbon. The loop structure covers the edge sites dangling bonds during this heat treatment due to the surface energy reduction. This graphitization degree development was furtherly confirmed by the Raman spectroscopy and X-ray diffraction analysis. However, because loop regions are Raman active species as the disordered carbon, the I_D/I_G value of pCNFs shows a higher value than the expectation from the lattice-spacing value.

- (2) The carbon black type materials (CB) have a granular morphology around 40-150 nm. TEM observation revealed the carbon basal plane exposure on their surface for these types of materials. Raman spectroscopy and X-ray diffraction analysis results suggest that CB has various range graphitization degrees. According to the comparison of DB and DB2400, CB-type material has difficulty graphitization development compared with pCNFs. This relatively non-graphitizability might come from their small diameters and the existence of the turbostratic region.
- (3) MWCNT has a nanostructure in which the carbon layers are oriented parallel to the fiber-axis of the nanotube. Their lengths and diameters are in the range of 0.5–10 μm and 50–200 nm, respectively. Their graphitization degree is well developed and comparable with heat-treated pCNF. On their surfaces, the carbon basal plane is exposed.

2-5 References

1. P. Chen, Y. Tong, C. Wu, Y. Xie, "Surface/Interfacial Engineering of Inorganic Low-Dimensional Electrode Materials for Electrocatalysis", *Acc. Chem. Res.*, **51(11)**, 2857–2866 (2018).
2. R.L. McCreery, "Advanced Carbon Electrode Materials for Molecular Electrochemistry", *Chem. Rev.* **108(7)**, 2646–2687 (2008).
3. S.G. Peera, R. Koutavarapu, S. Akula, A. Asokan, P. Moni, M. Selvaraj, J. Balamurugan, S.O. Kim, C. Liu, A.K. Sahu, "Carbon Nanofibers as Potential Catalyst Support for Fuel Cell Cathodes: A Review", *Energy Fuels*, **35(15)**, 11761–11799 (2021).
4. H. Konno, S. Sato, H. Habazaki, M. Inagaki, "Formation of platelet structure carbon nanofilaments by a template method", *Carbon*, **42(12-13)**, 2756-2759 (2004).
5. H. Habazaki, M. Kiri, M. Hayashi, H. Konno, "Structure of the carbon nanofilaments formed by liquid phase carbonization in porous anodic alumina template", *Mater. Chem. Phys.*, **105**, 367-372 (2007).
6. N. Yamada, D. Kowalski, C. Zhu, Y. Aoki, H. Habazaki, "High dispersion and oxygen reduction reaction activity of Co_3O_4 nanoparticles on platelet-type carbon nanofibers", *RSC Adv.*, **9**, 3726-3733 (2019).
7. T. Inoue, A. Koyama, D. Kowalski, C. Zhu, Y. Aoki, H. Habazaki, "Fluorine-Free Slippery Liquid-Infused Porous Surfaces Prepared Using Hierarchically Porous Aluminum", *Phys. Status Solidi A*, **217(13)**, 190836 (2020).
8. D. Dollimore, G.R. Heal, "The degradation of selected polymers to carbons in an inert atmosphere", *Carbon*, **5**, 65-72 (1967).

9. R. Hurt, G. Krammer, G. Crawford, K. Jian, C. Rulison, "Polyaromatic Assembly Mechanisms and Structure Selection in Carbon Materials", *Chem. Mater.*, **14**, 4558-4565 (2002).
10. Y. Bai, Z. Wang, C. Wu, R. Xu, F. Wu, Y. Liu, H. Li, Y. Li, J. Lu, K. Amine, "Hard Carbon Originated from Polyvinyl Chloride Nanofibers As High-Performance Anode Material for Na-Ion Battery", *ACS Appl. Mater. Interfaces*, **7**, 5598-5604 (2015).
11. S. George, H.K. Lee, "Direct Electrochemistry and Electrocatalysis of Hemoglobin in Nafion/Carbon Nanochip Film on Glassy Carbon Electrode", *J. Phys. Chem. B*, **113**, 15445-15454 (2003).
12. N. Iwashita, "Characterization of Crystal Structure of Carbon Materials by X-ray Powder Diffraction", *TANSO*, **188**, 147-151 (1999).
13. T. Tamaki, H. Wang, N. Oka, I. Honma, S.H. Yoon, T. Yamaguchi, "Correlation between the carbon structures and their tolerance to carbon corrosion as catalyst supports for polymer electrolyte fuel cells", *Int. J. Hydrogen Energy*, **43(12)**, 6406-6412 (2018).
14. S. Brunauer, P. H. Emmett, E. Teller, "Adsorption of Gases in Multimolecular Layers", *J. Am. Chem. Soc.*, **60**, 309-319 (1938).
15. H. Habazaki, M. Kiriu, H. Konno, "High rate capability of carbon nanofilaments with platelet structure as anode materials for lithium ion batteries", *Electrochemistry Commun.*, **8**, 1275-1279 (2006).
16. M. Acik, Y.J. Chabal, "Nature of Graphene Edges: A Review", *J. Appl. Phys.*, **50**, 070101 (2011).
17. M. Velický, P.S. Toth, C.R. Woods, K.S. Novoselov, R.A.W. Dryfe, "Electrochemistry of the Basal Plane versus Edge Plane of Graphite", *J. Phys. Chem. C*, **123**, 11677-11685 (2019).
18. K.K. Mani, R. Ramani, "Lattice Dynamics of Graphite", *Phys. Status Solidi B*, **61**, 659-668 (1974).
19. Y. Kawashima, G. Katagiri, "Observation of the out-of-plane mode in the Raman scattering from the graphite edge plane", *Phys. Rev. B*, **59**, 62 (1999).
20. F. Tuinstra, J.L. Koenig, "Raman Spectrum of Graphite", *J. Chem. Phys.*, **53**, 1126 (1976).
21. M.S. Dresselhaus, A. Jorio, M. Hofmann, G. Dresselhaus, R. Saito, "Perspectives on Carbon Nanotubes and Graphene Raman Spectroscopy", *Nano Lett.*, **10**, 751 (2010).
22. D. Dollimore, G.R. Heal, "The degradation of selected polymers to carbons in an inert atmosphere", *Carbon*, **5**, 65-72 (1967).
23. M. Inagaki, L.J. Meng, T. Ibuki, M. Sakai, Y. Hishiyama, "Carbonization and graphitization of polyimide film "Novax"", *Carbon*, **29**, 1239-1243 (1991).
24. T. Takeichi, Y. Eguchi, Y. Kaburagi, Y. Hishiyama, M. Inagaki, "Carbonization and graphitization of BPDA/PDA polyimide films: effect of structure of polyimide precursor", *Carbon*, **37**, 569-575 (1999).
25. Y. Suhng, K. Hashizume, T. Kaneko, S. Otani, S. Yoshimura, "The study of the graphitization behavior for polyimide and polyamide films", *Synthetic Metals*, **71**, 1751-1752 (1995).
26. S. Zhao, Z. Shi, C. Wang, M. Chen, "Structure and surface elemental state analysis of polyimide resin film after carbonization and graphitization", *J. Appl. Polym. Sci.*, **108**, 1852-1856 (2008).
27. S. De Fonton, A. Oberlin, M. Inagaki, "Characterization by electron microscopy of carbon phases (intermediate turbostratic phase and graphite) in hard carbons when heat-treated under pressure", *J Mater Sci* **15**, 909-917 (1980).
28. J.N. Rouzaud, A. Oberlin, "Structure, microtexture, and optical properties of anthracene and saccharose-based

- carbons”, *Carbon*, **27**, 517-529 (1989).
29. C. Bourgerette, A. Oberlin, M. Inagaki, “Structural and textural changes from polyimide Kapton to graphite: Part I. Optical microscopy and transmission electron microscopy”, *J. Mater. Res.*, **7**, 1158-1173 (1992).
 30. M. Inagaki, T. Tsumura, T. Kinumoto, M. Toyoda, “Graphitic carbon nitrides (g-C₃N₄) with comparative discussion to carbon materials”, *Carbon*, **141**, 580-607 (2019).
 31. Y. Sugiyama, K. Nagasaka, “炭素質の本質並にその黒鉛化性に関する研究(第6報)カーボンブラックの黒鉛化性に関する研究”, *Kogyokagakuzasshi*, **56**, 135-138 (1953).
 32. W. D. Schaeffer, W. R. Smith, M. H. Polley, “Structure and Properties of Carbon Black - Changes Induced by Heat Treatment”, *Ind. Eng. Chem.*, **45**, 1721-1725 (1953).
 33. I. Noda, M. Inagaki, N. Fujisawa, “各種原料炭素の加熱処理による結晶子の成長”, *Kogyokagakuzasshi*, **64**, 1518-1523 (1961).
 34. M. Inagaki, “Microtexture of Carbon Materials”, *TANSO*, **1985**, 114-121 (1985).
 35. K. Jian, H.S. Shim, A. Schwartzman, G.P. Crawford, R.H. Hurt, “Orthogonal carbon nanofibers by template-mediated assembly of discotic mesophase pitch”, *Adv. Mater.*, **15**, 164-167 (2003).
 36. K. Jian, H.S. Shim, D. Tuhus-Dubrow, S. Bernstein, C. Woodward, M. Pfeffer, D. Steingart, T. Gournay, S. Sachsmann, G.P. Crawford, R.H. Hurt, “Liquid crystal surface anchoring of mesophase pitch”, *Carbon*, **41**, 2073-2083 (2003).
 37. H. Konno, S. Sato, H. Habazaki, M. Inagaki, “Formation of platelet structure carbon nanofilaments by a template method”, *Carbon*, **42**, 2756-2759 (2004).
 38. C. Chan, G. Crawford, Y. Gao, R. Hurt, K. Jian, H. Li, B. Sheldon, M. Sousa, N. Yang, “Liquid crystal engineering of carbon nanofibers and nanotubes”, *Carbon*, **43**, 2431-2440 (2005).
 39. H. Orikasa, T. Akahane, M. Okada, Y. Tong, J. Ozaki, T. Kyotani, “Electrochemical behavior of carbon nanorod arrays having different graphene orientations and crystallinity”, *J. Mater. Chem.*, **19**, 4615-4621 (2009).
 40. M. Kiri, K. Fushimi, H. Konno and H. Habazaki, “Electrochemical capacitance of nitrogen-containing nanocarbons prepared using porous anodic alumina template”, *Electrochemistry (Tokyo)*, **76**, 197-202 (2008).
 41. H. Sumi, S. Ogawa, M. Sato, A. Saikubo, E. Ikenaga, M. Nihei, Y. Takakuwa, “Effect of Carrier Gas (Ar and He) on the Crystallographic Quality of Networked Nanographite Grown on Si Substrates by Photoemission-Assisted Plasma-Enhanced Chemical Vapor Deposition”, *Jpn. J. Appl. Phys.*, **49**, 076201 (2010).
 42. K. Moriguchi, S. Munetoh, M. Abe, M. Yonemura, K. Kamei, A. Shintani, Y. Maehara, A. Omaru, M. Nagamine, “Nano-tube-like surface structure in graphite particles and its formation mechanism: A role in anodes of lithium-ion secondary batteries”, *J. Appl. Phys.*, **88**, 63-69 (2000).
 43. S. Lim, S.H. Yoon, I. Mochida, J. Chi, “Surface Modification of Carbon Nanofiber with High Degree of Graphitization”, *J. Phys. Chem. B*, **108**, 1533-1536 (2004).
 44. L. Tao, Q. Wang, S. Dou, Z. Ma, J. Huo, S. Wang, L. Dai, Edge-rich and dopant-free graphene as a highly efficient metal-free electrocatalyst for the oxygen reduction reaction, *Chem. Commun.*, **52**, 2764-2767 (2016).
 45. K. Nomura, H. Nishihara, N. Kobayashi, T. Asada, T. Kyotani, “4.4 V supercapacitors based on super-stable mesoporous carbon sheet made of edge-free graphene walls”, *Energy Environ. Sci.*, **12**, 1542-1549 (2019).
 46. M. Matsumoto, T. Manako, H. Imai, “Electrochemical STM Investigation of Oxidative Corrosion of the Surface of Highly Oriented Pyrolytic Graphite”, *J. Electrochem. Soc.*, **156**, B1208-1211 (2009).

Chapter 3
Corrosion of pCNFs at
high potentials in
alkaline electrolyte

Chapter 3 Corrosion of pCNFs at high potentials in alkaline electrolyte

3-1 Introduction

Recently, the high oxidation resistance of pCNFs was reported as the electrode materials for PEMFC [1-3]. In Chapter 2, pCNFs were prepared at several heat-treatment temperatures. The pCNFs annealed at $\geq 2000^\circ\text{C}$ show a high graphitization degree, and they developed looped carbon layers on the carbon edge plane. Thus, no carbon edge plane is exposed to the surface. Such pCNFs are possibly highly durable in more harsh oxidative environments such as ZAB operation environment. Hence, in this chapter, the corrosion behavior of carbon materials under an oxygen evolution reaction condition in 4.0 mol dm^{-3} KOH electrolyte, *i.e.*, ZAB charging condition, is investigated using identical-location scanning electron microscopy (ILSEM) observations to examine the oxidation rate quantitatively. Additionally, the carbon surface was characterized to elucidate the corrosion process through spectroscopic studies using X-ray photoelectron spectroscopy (XPS), Raman scattering spectroscopy, and Electron Energy Loss Spectroscopy (EELS) at high anodic potentials in the concentrated alkaline electrolyte.

3-2 Experimental

3-2-1 ILSEM study

In this chapter, highly graphitized pCNFs (pCNF2000, pCNF2400, pCNF3000), TB and AB were used. These materials were served to the electrochemical measurements. In order to investigate the corrosion rate of each carbon material and the crystalline plane dependency of corrosion, the ILSEM technique was used [4-7]. This method is typically employed for fuel cell research, and gold mesh-type grids were used as a substrate [4, 6, 7]. It is necessary to apply a high potential in concentrated alkaline media; therefore, the gold mesh electrode is suitable for working electrode

support because of its high chemical stability [8]. There is a high risk of particle detachment induced by the generation of oxygen bubbles during the anodic polarization. For suppressing the detachment of carbon powders, the surface of the gold mesh was roughened in this study [9-11]. Fabrication of roughness surface on the gold grids was achieved by the anodizing of gold mesh [12, 13]. Gold mesh grid (Alliance Biosystems, SlimBar Index Grids Gold, 2290G-XA) was anodized in 0.3 mol dm^{-3} oxalic acid aqueous solution at 273 K. Platinum foil and Ag/AgCl/Saturated KCl electrodes were used as counter and reference electrodes, respectively. The potential was firstly ramped from the open circuit potential to 2.4 V vs SHE at a potential sweeping rate of 10 mV s^{-1} , then kept at 2.4 V for 12 min. The anodizing curve and comparison of surface morphology before and after the anodizing were shown in Fig. 3-1.

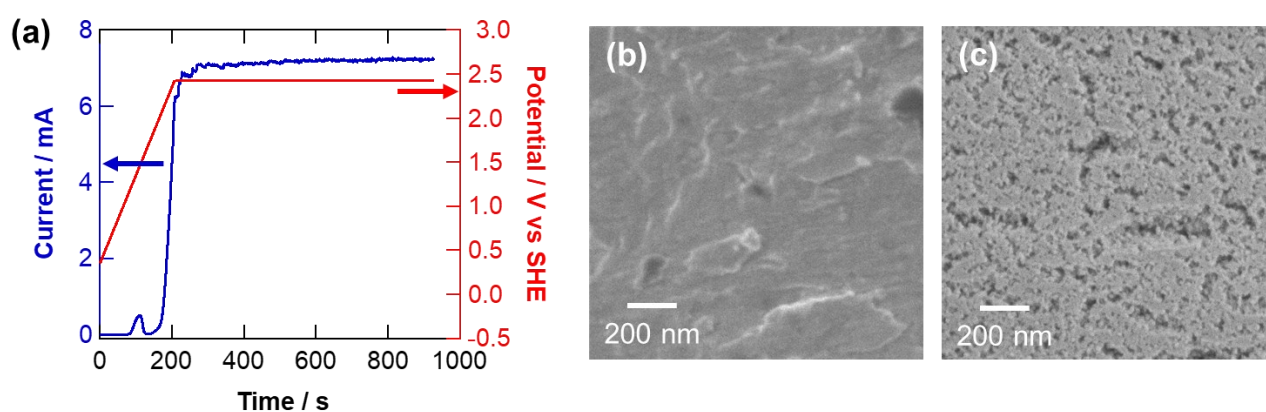


Fig. 3-1 (a) Typical anodizing curve of an Au grid in 0.3 mol dm^{-3} oxalic acid solution at 2.4 V, (b, c) surface SEM images of the Au grid (b) before and (c) after the anodizing for 960 s.

After the anodizing, the grid was irradiated with oxygen plasma for 5 minutes using a Harrick Plasma PDC-32G air plasma cleaner to remove a contaminant hydrocarbon surface layer [14]. Then, the carbon materials were loaded on the gold grid by immersing it into the ethanol solution containing 10 mg mL^{-1} carbon and 5% Nafion. Finally, the carbon-loaded Au grid was dried in the incubator (Yamato, DKN302) at 250°C .

The carbon-loaded grid was firstly observed by a low-acceleration voltage SEM (Zeiss, Sigma-500) operated at 1.5 kV. Then, the grid was anodically polarized at 1.8 V vs RHE in 4.0 mol dm⁻³ KOH aqueous electrolyte for selected periods at room temperature, followed by SEM observations to estimate the corrosion rate from the outer shape changes (Fig. 3-2). The electrochemical measurements were conducted using a potentiostat (Princeton Applied Research VersaSTAT3) controlled by the computer. Platinum foil and Hg/HgO/4 mol dm⁻³ KOH electrodes were used as counter and reference electrodes, respectively. The electrode potential was converted from the Hg/HgO/4 mol dm⁻³ KOH reference scale to the RHE using the following equation [15]:

$$E \text{ vs RHE} = E \text{ vs Hg/HgO/4 mol dm}^{-3} \text{ KOH} + 0.9260 \quad (3-1)$$

The anodized specimens were also examined by the image-aberration-corrected scanning transmission electron microscopy (STEM, Titan G2 60-300, 300 kV, FEI) and the electron energy-loss spectroscopy (EELS) attached with STEM.

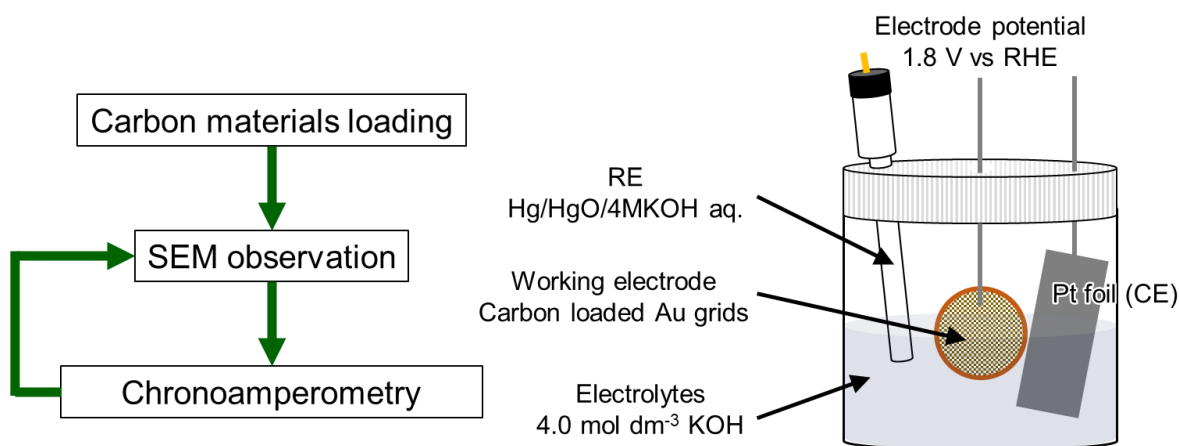


Fig. 3-2 The procedure and electrochemical cell of ILSEM study.

3-2-2 XPS and Raman measurements

The carbon samples before and after anodic polarization were characterized by XPS and Raman spectroscopy. For these characterizations, the samples were prepared as shown in Fig. 3-3. Carbon-dispersed ethanol solution, free from Nafion, was dropped onto the Ni plate (ASONE, 99.9 %) until the loading carbon mass reached 5.0 mg cm^{-2} . Then, the carbon layer is sandwiched between the Ni plate and PTFE filter paper (ADVANTEC, H010A047A, pore size = $0.1 \text{ }\mu\text{m}$), tightened by the O-ring and PTFE tube parts. Platinum wire and Hg/HgO/ 4 mol dm^{-3} KOH electrodes were used as counter and reference electrodes, respectively. The anodic polarization of carbon materials was conducted in a 4 mol dm^{-3} KOH aqueous solution at 1.8 V vs RHE for 24 h at room temperature ($\sim 25^\circ\text{C}$). The chemical state of the elements in the anodized carbon was examined using a JEOL JPS-9200 X-ray photoelectron spectrometer with Mg K α excitation ($h\nu = 1253.6 \text{ eV}$). The spectra were obtained under vacuum better than $1 \times 10^{-7} \text{ Pa}$, and the analyzer pass energy was set to 10 eV . The graphitization degree was also examined by Raman spectroscopy (Horiba Scientific, XploRA) using a 532 nm laser beam at 2.5 mW .

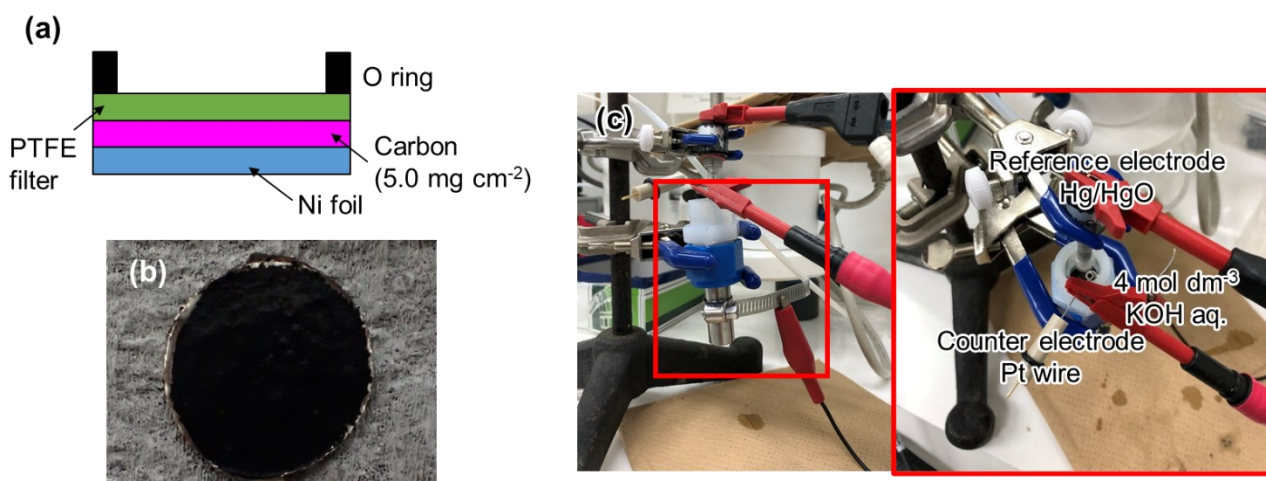


Fig. 3-3 (a) The schematic illustration of the Ni-Carbon-PTFE sandwich electrode, (b) typical surface photograph of the electrode, and (c) the picture of the electrochemical cell for the bulk material electrolysis.

3-2-3 Wettability measurements

Carbon materials loaded on a glassy carbon electrode (GC, Pine, AFED050P040GC, $\phi = 5$ mm) with flat surfaces were used to evaluate the wettability of carbon materials before and after polarization. Before the carbon layer preparation, GC surfaces were polished using polishing pads and 0.3 μm diameter alumina particles. The carbon layer on GC was prepared using the carbon-Nafion mixture solution pipetting on the GC. This carbon-Nafion mixture was prepared by the following method; selected carbon powders (10 mg) were dispersed ultrasonically in a mixture of 0.2 mL of 5 wt% Na^+ -exchanged Nafion solution and 4.8 mL of ethanol. Then, the carbon dispersion was loaded onto GC with the loading amount of 1.0 mg cm^{-2} . Prior to the electrochemical treatment, the carbon-loaded GC was dried in air at room temperature overnight. After drying, each carbon electrode was subjected to anodic polarization in Ar-saturated 4.0 mol dm^{-3} KOH electrolyte at 1.8 V vs RHE for 2 h. Before the chronoamperometry, cyclic voltammetry (CV) was carried out until achieving stable CV curves. CV was conducted in the range of 0.4 – 1.1 V vs RHE with the potential sweep rate of 300 mV s^{-1} , and typically repeated for 30 cycles. Change in the water contact angle of each carbon material by anodic polarization was measured by an optical contact angle meter (Kyowa Interface Science, DM-CE1). The static water contact angle was measured using a Milli-Q water droplet of 1 μL . In addition, the surface roughness of each electrode was estimated using a laser scanning microscope (Keyence, VK-8700) and a VK-H1A1 analyzer software (Keyence).

3-3 Results and Discussion

3-3-1 ILSEM and TEM studies

Firstly, to estimate the corrosion rates of the carbon materials at 1.8 V vs RHE in 4.0 mol dm^{-3} KOH electrolyte, identical locations of the electrodes before and after anodic polarization were

observed by SEM (ILSEM technique). Examples of ILSEM study for TB and AB nanoparticles are shown in Fig. 3-4.

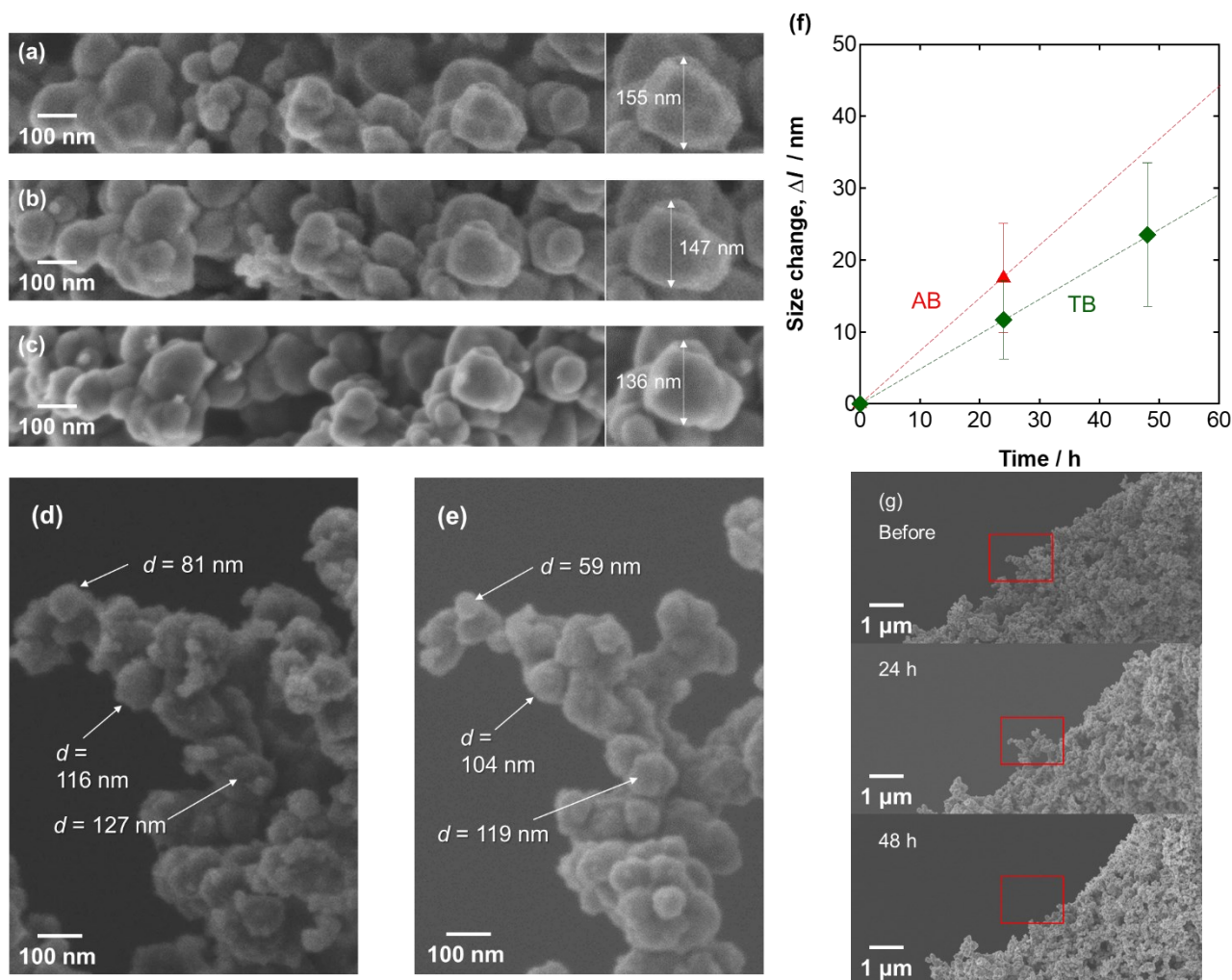


Fig. 3-4 (a-c) ILSEM observation images of TB loaded electrode (a) before and (b) after polarization at 1.8 V vs RHE for 24 h and (c) for 48 h. (d, e) ILSEM observation images of AB loaded electrode (a) before and (b) after polarization at 1.8 V vs RHE for 24 h, and (f) change in the size of nanoparticles with polarization time.

The TB particle size reduces with the polarization time without significantly changing the shape of the particles, suggesting the uniform oxidation of TB nanoparticles. The diameter decrement was measured for more than 10 nanoparticles and plotted as a function of polarization time (Fig. 3-4f).

The diameter of the TB reduces linearly with time at an average rate of 0.46 nm h^{-1} . A higher oxidation rate was found for the AB nanoparticles, which have a lower graphitization degree than the TB nanoparticles. From Fig. 3-4d and 4e; the diameter decrement was $17.5 \pm 7.6 \text{ nm}$ after polarization for 24 h, corresponding to the diameter reduction rate of 0.73 nm h^{-1} . More prolonged polarization for the AB was conducted, but the diameter decrement was not successfully measured because of the significant detachment of the nanoparticles (Fig. 3-4g).

Fig. 3-5 shows the ILSEM results of pCNFs. The lengths of the pCNFs decreased during polarization at 1.8 V vs RHE. For pCNF2400, the fiber length decrements are $10.9 \pm 6.4 \text{ nm}$, $20.2 \pm 9.9 \text{ nm}$ after 24 h and 48 h polarization, respectively. Thus, assuming the linear length reduction with polarization time, the length reduction rate was estimated to be 0.42 nm h^{-1} . This value was reduced by increasing the heat treatment temperature of pCNFs from 0.62 nm h^{-1} for pCNF2000 to 0.34 nm h^{-1} for pCNF3000. The carbon oxidation rate of the carbon blacks and pCNFs was estimated from the diameter and length decrement rate and plotted as a function of d_{002} (Fig. 3-5k). An approximately linear relationship is seen, indicating that the carbon oxidation is controlled by the graphitization degree. The outer surface of carbon blacks and the end surface of nanofibers consist of the carbon basal plane. The results of Fig. 3-5k indicate that the basal plane's carbon oxidation resistance improves with the graphitization degree.

The most striking results are found in the carbon oxidation rate of the sidewall of pCNFs. The nanofiber diameter, estimated from the corrosion rates of the length change of the pCNFs, should become roughly half after polarization for 48 h, but the actual change in the nanofiber diameter is negligible, especially between 24 and 48 h for all the pCNFs (Fig. 3-5a-i). The markedly reduced oxidation rate of the pCNFs sidewall is obvious in Fig. 3-5j, so that it can be concluded that the sidewall of pCNFs, comprising the carbon edge plane, is much more resistant than the highly graphitized carbon

basal plane. The diameter reduction of the pCNF2000 and pCNF2400 was 5 nm within the initial 24 h, decreasing to 2 nm or less in the next 24 h. The slightly higher oxidation rate within the initial 24 h will be discussed later.

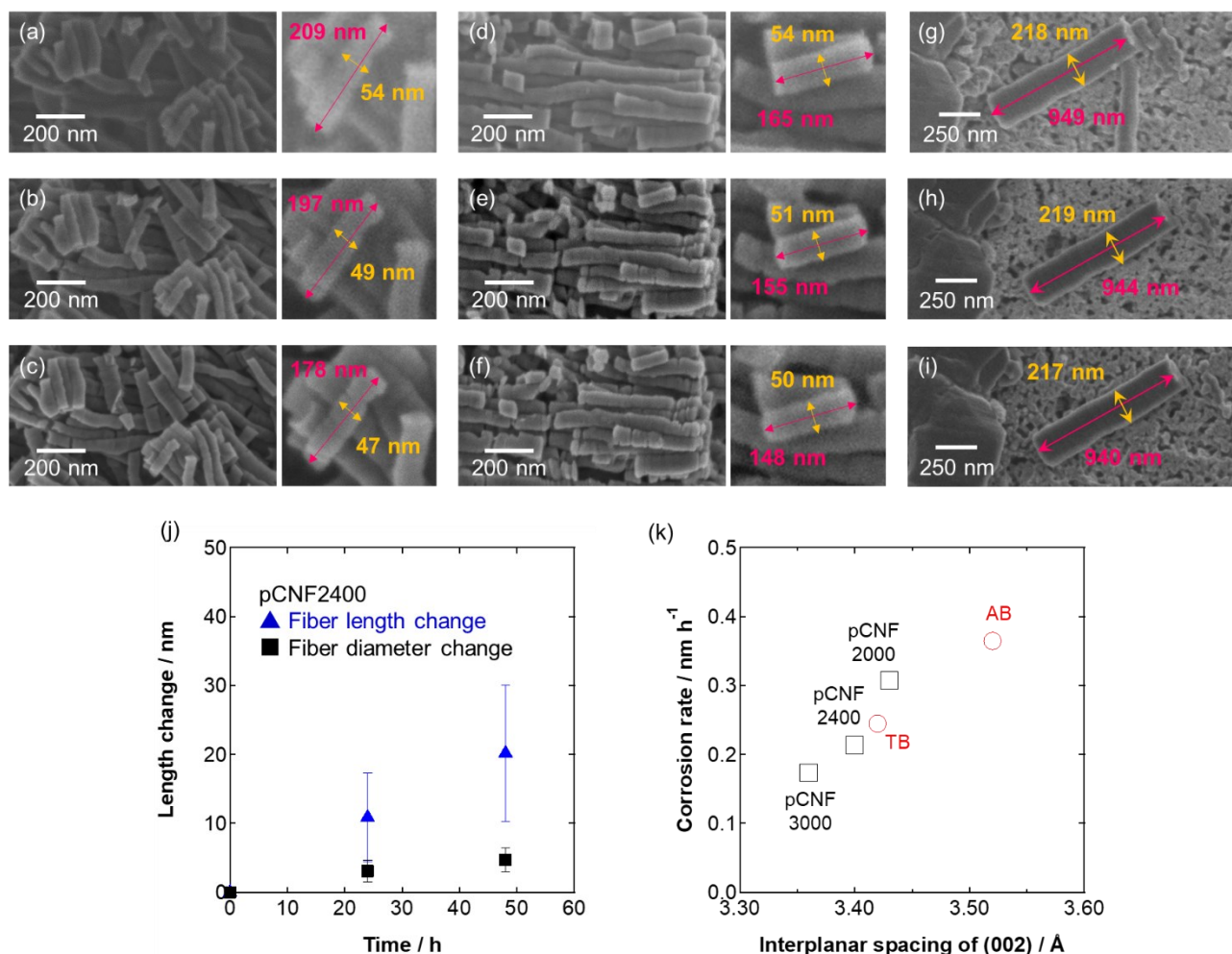


Fig. 3-5 ILSEM images of pCNF loaded electrodes for (a-c) pCNF2000, (d-f) pCNF2400, and (g-i) pCNF3000. Each electrode was observed (a, d, g) before and (b, e, h) after polarization at 1.8 V vs RHE for 24h, and (c, f, i) for 48 h. (j) The relationship between the amount of diameter and length changes of pCNF2400 and the duration time calculated from Fig. 3-4 (d-f). (k) The relationship between the interplanar spacing of 002 and basal plane corrosion rates.

The carbon structural change by corrosion was further examined by TEM. Fig. 3-6 shows the TEM images of AB before and after polarization for 24 and 48 h. The 002 lattice fringes, observed in the pristine AB, become obscure after polarization, suggesting the decrease in the graphitization degree. In addition, some particles are hollow after polarization, being developed by preferential oxidation of carbon at the inner core regions. The inner core regions of the pristine AB appear to have a lower graphitization degree, leading to the faster corrosion loss of carbon.

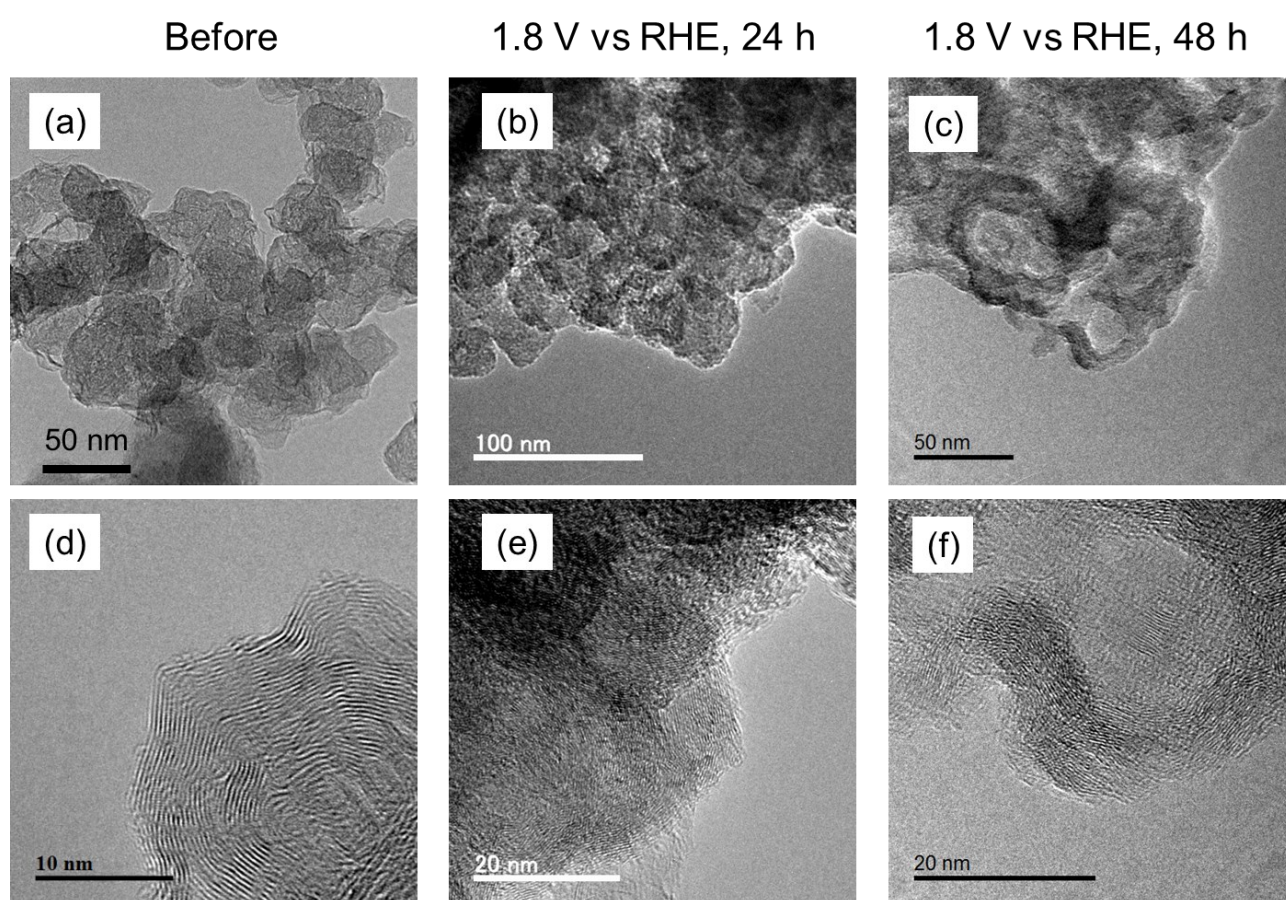


Fig. 3-6 TEM images of AB (a, d) before and after the polarization at 1.8 V vs RHE in 4.0 mol dm^{-3} KOH aq. electrolyte for (b, e) 24 h and (c, f) 48 h.

A similar morphological change is observed for the TB (Fig. 3-7). In contrast to the AB, the 002 lattice fringes of TB remain unchanged even after polarization for 48 h; thus, the oxidation of TB proceeds without degradation of high graphitization degree. The thickness of the well-developed graphene layers from the outer surface is 14.3 ± 5.5 nm in the pristine TB, being reduced to ~ 7.2 and ~ 4.3 nm after polarization for 24 h and 48 h. The oxidative removal of TB appears to proceed by consuming the graphene layer uniformly from the outer surface.

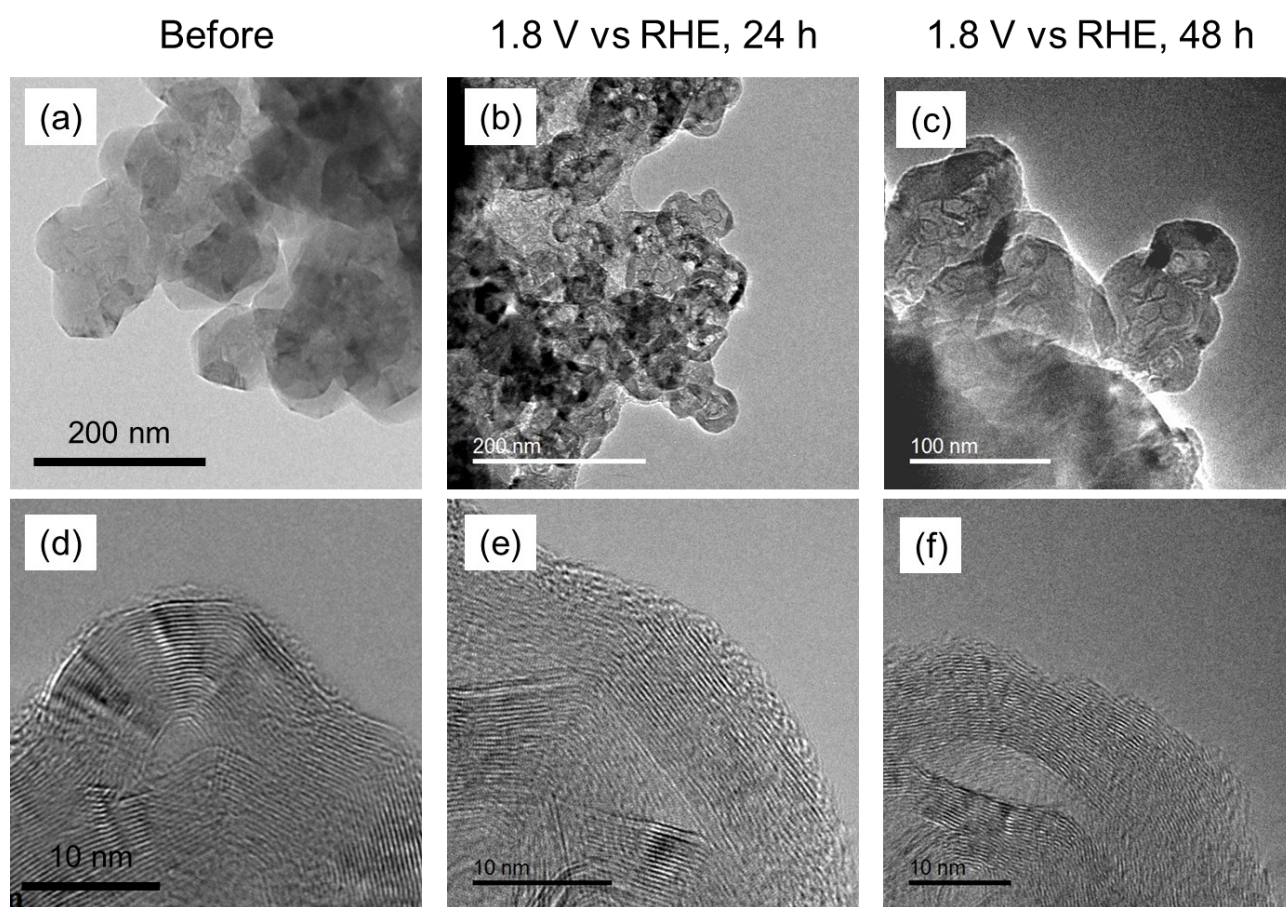


Fig. 3-7 TEM images of TB (a, d) before and after the polarization at 1.8 V vs RHE in 4.0 mol dm^{-3} KOH aq. electrolyte for (b, e) 24 h and (c, f) 48 h.

Changes in the carbon edge plane by exposing pCNFs to the electrolyte at the high potential were examined, and an example of pCNF2400 was shown in Fig. 3-8. The TEM images of pCNF2000 and pCNF3000 are shown in Fig. 3-9 and 3-10, respectively. In all pCNFs, the loops developed at the sidewall of the nanofibers disappeared, and the carbon edge plane was directly exposed to electrolyte after polarization for 24 and 48 h. The thickness of the looped carbon layer is ~ 2 nm, so that the oxidative removal of the loops leads to the diameter reduction pCNFs of ~ 4 nm, corresponding to the actual diameter reduction within 24 h (Fig. 3-5j).

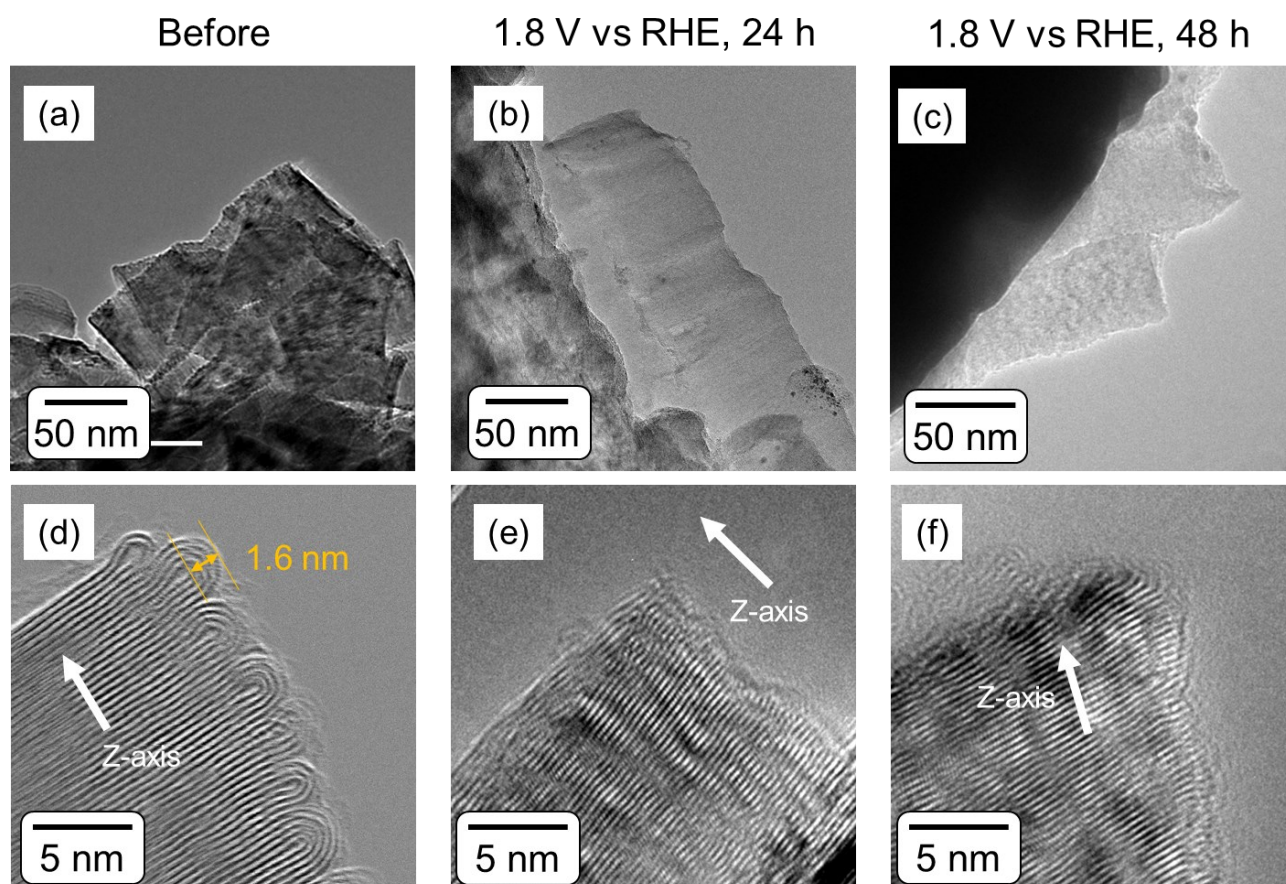


Fig. 3-8 TEM images of pCNF2400 (a, d) before and after the polarization at 1.8 V vs RHE in 4.0 mol dm^{-3} KOH aq. electrolyte for (b, e) 24 h and (c, f) 48 h.

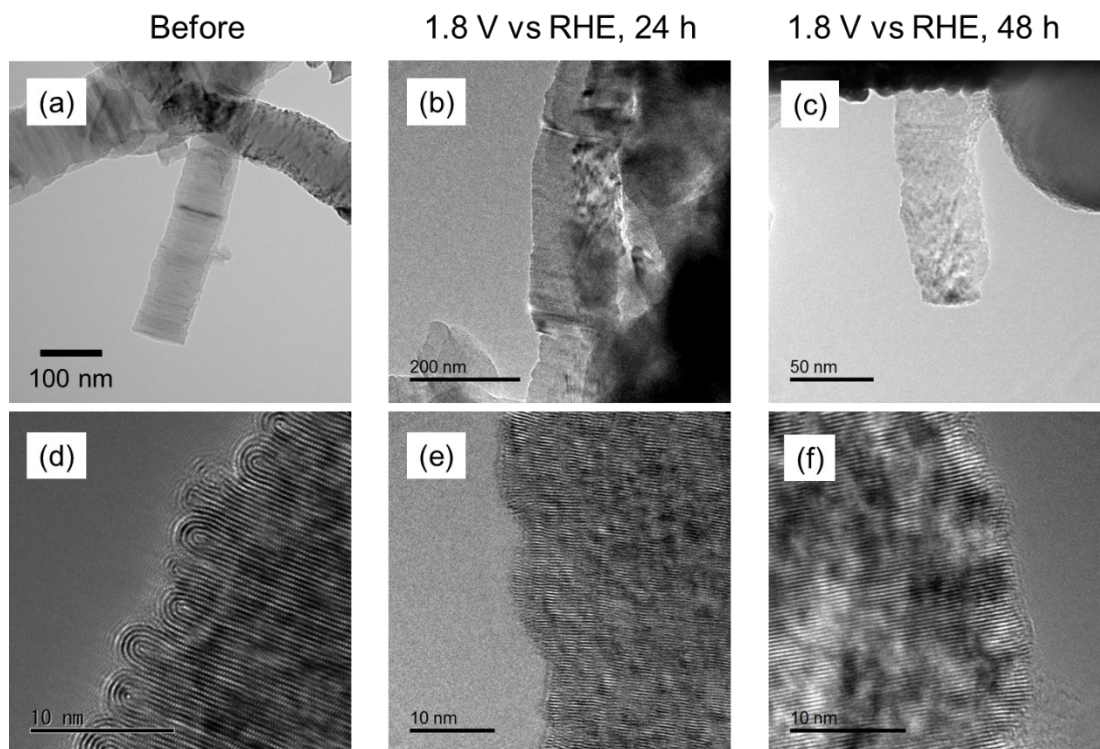


Fig. 3-9 TEM images of pCNF3000 (a, d) before and after the polarization at 1.8 V vs RHE in 4.0 mol dm⁻³ KOH aq. electrolyte for (b, e) 24 h and (c, f) 48 h.

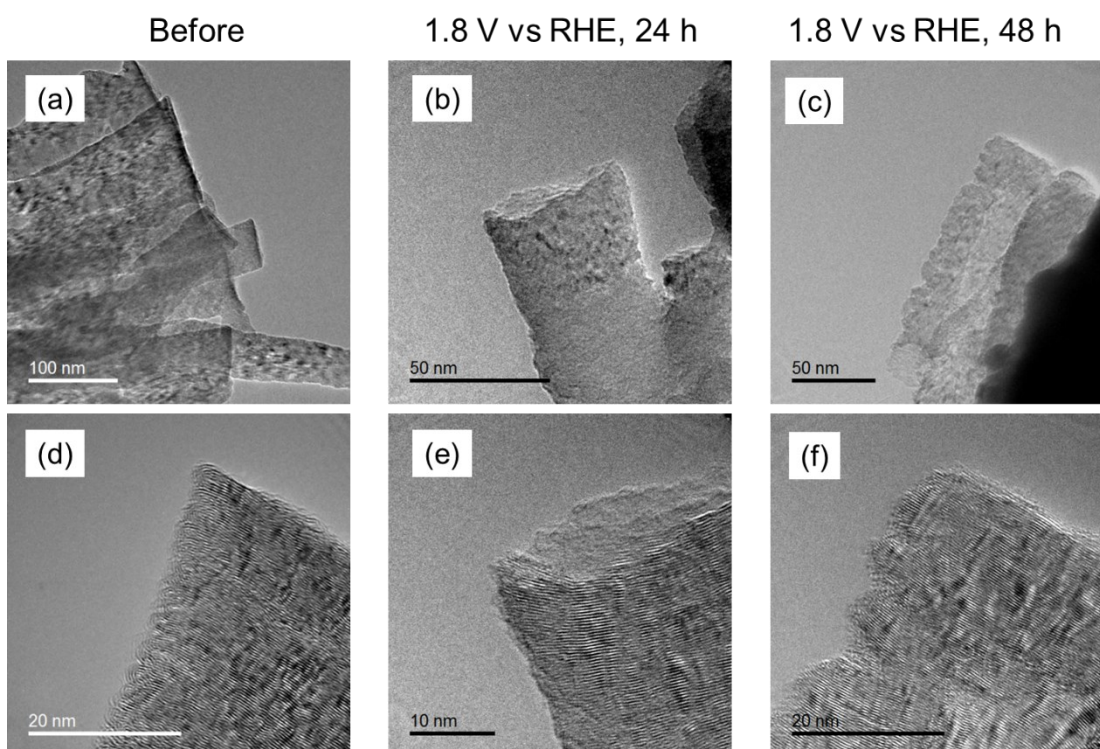


Fig. 3-10 TEM images of pCNF2000 (a, d) before and after the polarization at 1.8 V vs RHE in 4.0 mol dm⁻³ KOH aq. electrolyte for (b, e) 24 h and (c, f) 48 h.

Thus, it can be concluded that the diameter reduction of the pCNFs within 24 h is mainly due to the oxidation of looped carbon, and the carbon corrosion becomes negligible after exposure of the carbon edge plane to the electrolyte. The carbon corrosion rates at the sidewall of the pCNFs were almost independent of the heat treatment temperature, despite the reduced corrosion rate of the carbon basal plane with increasing the graphitization degree (Fig. 3-5k). The graphitization degree influences the corrosion of the basal plane but less significantly than that of the edge plane.

3-3-2 Characterization of anodized carbon materials by XPS and Raman

The graphitization degree and chemical state of each carbon material after the anodic oxidation were examined by the XPS as well as the Raman spectroscopy. Fig. 3-11 shows the Raman spectra of each carbon material before and after the 24 h polarization in 4.0 mol dm⁻³ KOH electrolyte at 1.8 V vs RHE. After the polarization, the Raman spectra of pCNFs show the enhanced G band (~ 1580 cm⁻¹) peak and reduced D band peak (~ 1380 cm⁻¹). Additionally, because of the reduction of the peak width of the G band, the peak splitting of the G band and D' band (~ 1620 cm⁻¹) is clearer than that before polarization. Changes in the peak widths and the intensity ratio of G band and D band peaks (I_D/I_G) before and after the polarization are summarized in Table 3-1. The intense and narrower G band peak after the polarization suggests the increase of the graphitization degree. TEM observation results suggest the lattice spacing values did not change even after the polarization. Additionally, the reduction of the D band peak was observed after the polarization. Therefore, this increment of the graphitization degree should come from the removal of the lower graphitized region. As the lower graphitized region, the looped carbon, which is observed on the sidewall of heat-treated pCNFs, is the considerable region. Such region contains seven- or five-membered rings, *i.e.*, sp³ like carbon, which is also Raman active species as the disordering carbon [2, 16-18]. These looped carbons were removed during the polarization in 4.0 mol dm⁻³ KOH aq., as shown in the TEM observation.

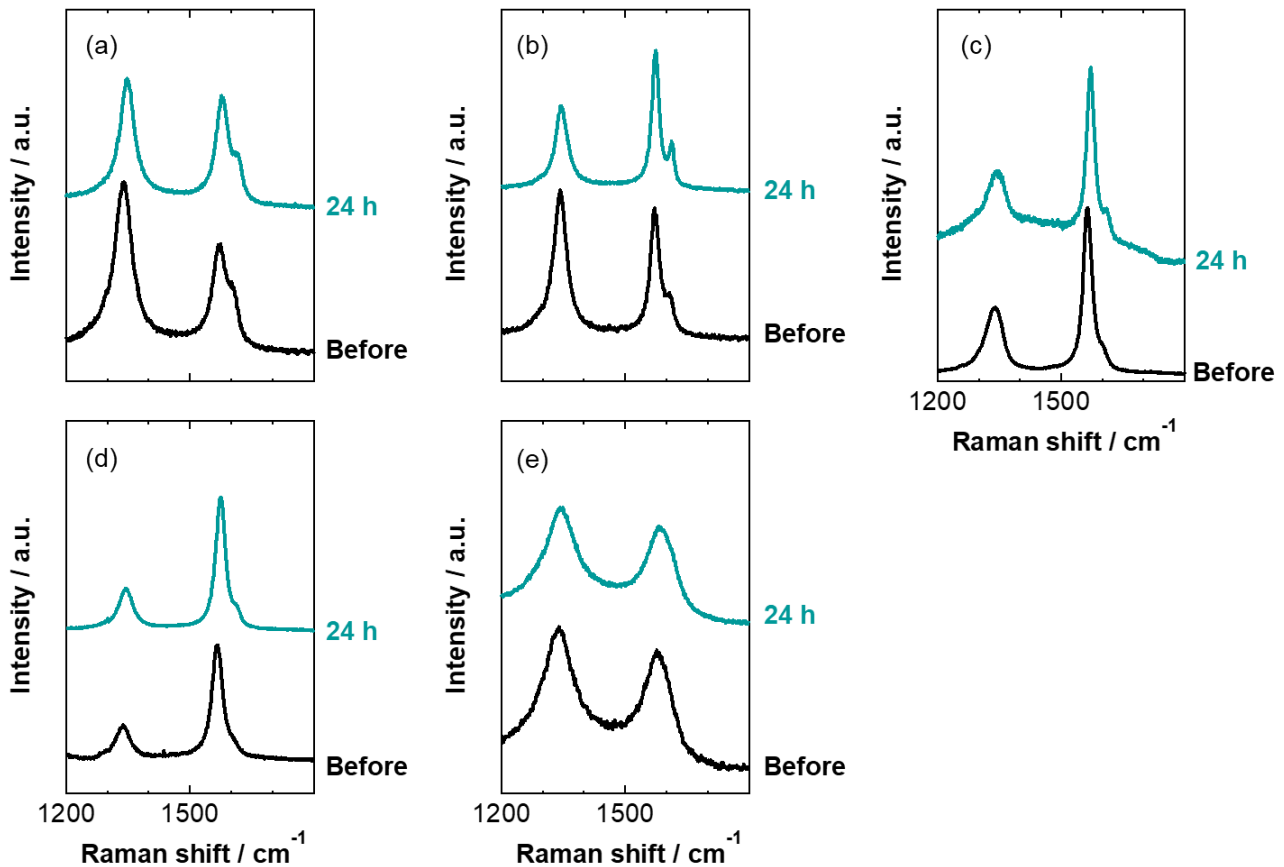


Fig. 3-11 Raman spectra of five different carbon materials (a) pCNF2000, (b) pCNF2400, (c) pCNF3000, (d) TB, (e) AB before and after the polarization at 1.8 V vs RHE in 4.0 mol dm⁻³ KOH aq. for 24 h.

Table 3-1 The I_D/I_G and G band peak width obtained from Raman spectra of five different carbon materials before and after the polarization at 1.8 V vs RHE in 4.0 mol dm⁻³ KOH aq. for 24 h.

Polarization time / h		pCNF2000	pCNF2400	pCNF3000	AB	TB
		0	I_D/I_G / -	1.71	1.51	0.73
	FWHM of G band / cm ⁻¹	47.1	29.7	27.8	84.9	31.0
24	I_D/I_G / -	1.17	0.92	0.62	1.09	0.46
	FWHM of G band / cm ⁻¹	41.2	25.4	24.2	85.6	35.0

On the other hand, the Raman spectra of carbon black type carbons show the opposite change after the polarization: reducing the graphitization degree (the increased I_D/I_G value and the increased G band peak width). TEM observations of carbon blacks also suggested the reduced graphitization degree because of oxidative consumption. Thus, polarization influences different ways depending on the type of carbon materials.

The chemical state of each carbon material after the polarization was examined using XPS. Fig. 3-12 shows the O 1s photoelectron spectra of each carbon material before and after the polarization. All carbon materials after the polarization show broad and asymmetric peaks around 532 eV. There are only a few oxygen-containing functional groups with this energy value. Hence, these O1s peaks after polarization can be assigned to the overlapping peak of O=C (531.5 eV) and HO-C (533 eV) (Table 3-2) [19-24]. Therefore, after the polarization, O=C groups and HO-C groups were produced on each carbon material surface.

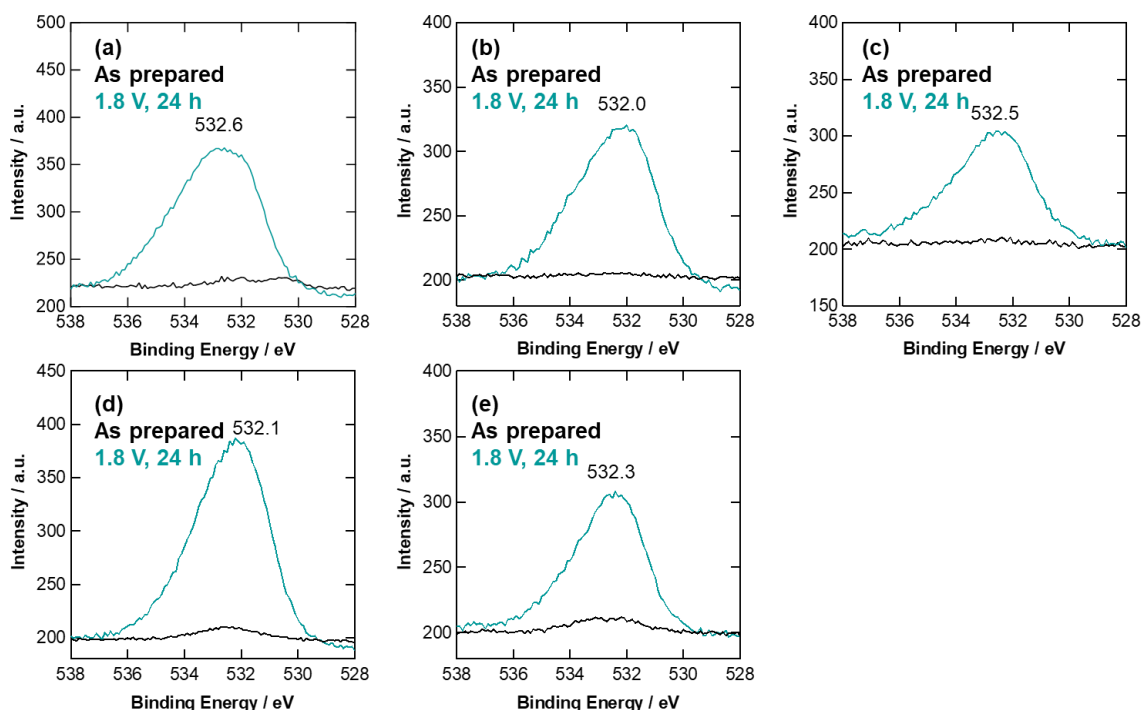


Fig. 3-12 XPS spectra of O 1s photoelectrons for (a) pCNF2000, (b) pCNF2400, (c) pCNF3000, (d) AB, (e) TB before and after the polarization at 1.8 V vs RHE in 4.0 mol dm⁻³ KOH aq. for 24 h.

Table 3-2 O 1s photoelectron peak list of functional groups of carbon materials.

Ref.	O=C / eV	-C-O-C- / eV	-C-OH / eV	-COOH / eV
[19]	531.4	533.4	533.4	
[20]	531.8 – 532.6	533.3 – 533.9	533.3 – 533.9	
[21]	531.0 - 532.1	533.5 - 534.0	533.5 - 534.0	
[22]	530.4 - 530.8	532.4 - 533.1	532.4 - 533.1	
[23]	532.8-533.6	533.6	533.6-534.4	534.9
[24]	533.3	532.3	533.3	534.2

The C1s photoelectron spectra in Fig. 3-13 provide additional information on the carbon material surface after polarization. After polarization, three peaks can be found and are assigned to C 1s main peak (~284.6 eV), K 2p_{3/2} (~293.7 eV), and K 2p_{1/2} (~296.5 eV), respectively. The peak position of each K2p peak is agreed with the monovalent K⁺ [25]. Therefore, the O=C peak shown in Fig. 3-12 was possibly reflected by the carbon surface functional group and surface carbonates, like K₂CO₃. We also can find the shoulder C 1s main peak, located around 286 eV, after polarization. Typically, this energy peak is assigned to the C-OH group on the carbon material surface (Table 3-3) [21-24, 26, 27]. Such -OH group on the carbon surface was also confirmed in the O 1s spectra. Therefore, after the polarization at 1.8 V vs RHE in 4.0 mol dm⁻³ KOH aq., the -OH group is produced on the carbon surface.

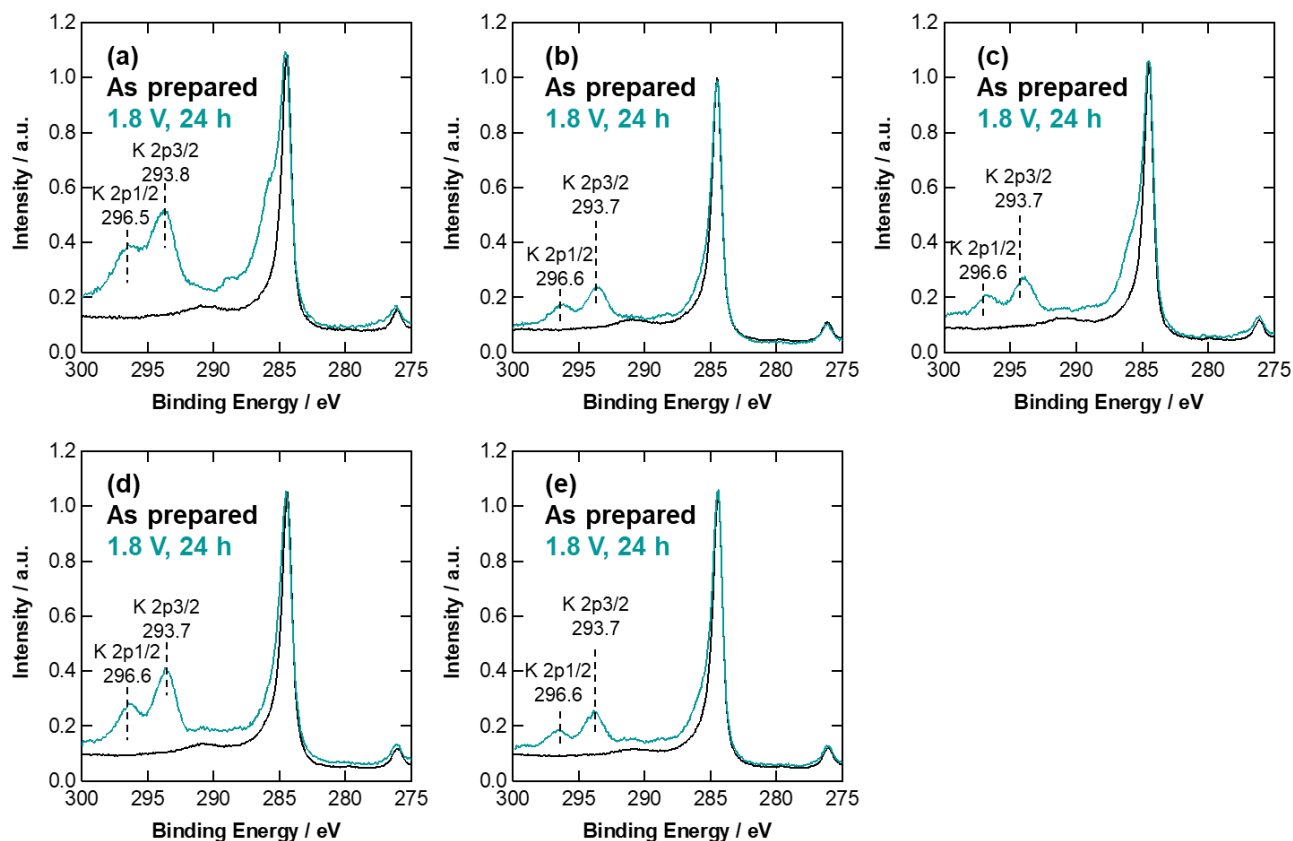


Fig. 3-13 XPS spectra of O 1s photoelectrons for (a) pCNF2000, (b) pCNF2400, (c) pCNF3000, (d) AB, (e) TB before and after the polarization at 1.8 V vs RHE in 4.0 mol dm⁻³ KOH aq. for 24 h.

Table 3-3 C 1s photoelectron peak list of functional groups of carbon materials.

Ref.	Alkyl, Aryl / eV	-C-OH / eV	Ether / eV	Keto / eV	-C=O / eV	-COOR / eV	-COOH / eV
[21]	284.6	286.1	286.1		287.6	290.1	
[22]	284.6-285.1	286.3-287.0		287.6-288.1	289.3-290		
[23]		288.6		287.6	289		
[24]	284.6		286.1	286.4	287.6	288.1	
[26]		285-287	285-287		288		289.5
[27]	284.6	286.3			287.6		288.8

3-3-3 Electron-energy loss spectroscopy analysis

Electron energy-loss spectroscopy (EELS) provides information on the electronic structure of a local area. Fig. 3-14 shows the TEM images of TB and pCNF2400 after 24 h anodic polarization at 1.8 V vs RHE and their low-loss region EELS spectra. Area analysis was conducted for three regions: bulk area, edge plane surface, and basal plane surface. In the low-loss region spectra of carbon materials, the broader peak appears around 26 eV and is identified as the combination of π and σ electronic excitations [28-30]. The spectra of the bulk region for TB and pCNF2400 shows $\pi+\sigma$ peak around 26 eV, which energy agrees with the pure graphene one.

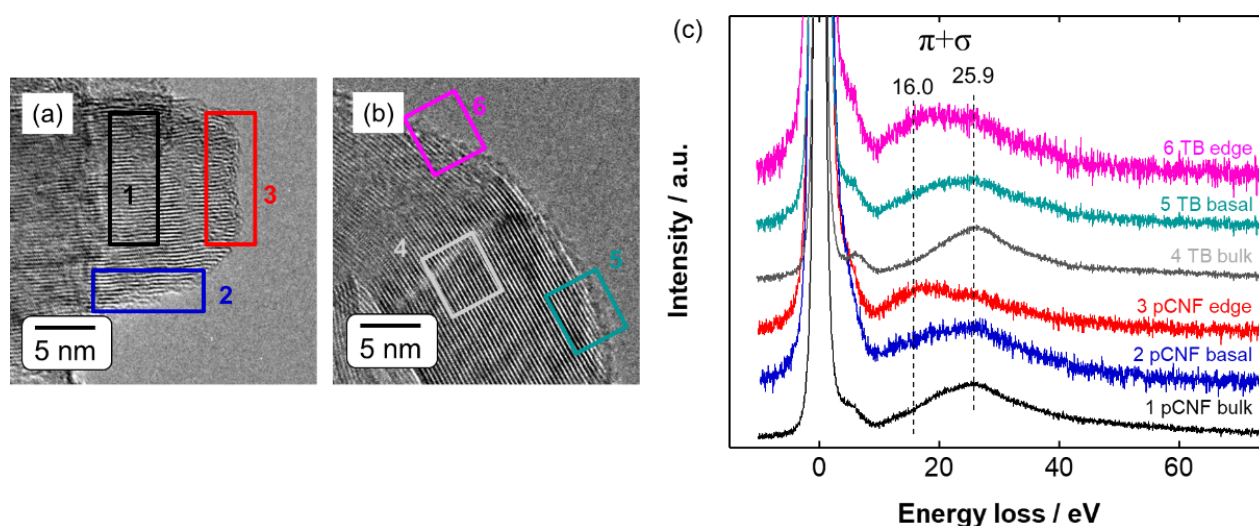


Fig. 3-14 TEM/EELS area analysis results for pCNF2400 and TB after the polarization at 1.8 V vs RHE in 4.0 mol dm⁻³ KOH aq. for 24 h. (a, b) TEM image of pCNF2400 (a) and TB (b). The analysis area is shown as the colored box. (c) EEL spectra around low-energy loss electrons for each analysis area.

On the other hand, the $\pi+\sigma$ peak of the basal plane surface and the edge plane surface shifted around 16-20 eV. Mkhoyan *et al.* reported that this plasmon peak tends to shift to a lower energy direction when sp³ type carbon or oxygen is incorporated into graphitic carbon, *i.e.*, amorphous carbon or graphene oxide [28]. Hence, this shift probably means the incorporation of oxygen species on the

surface after the anodic polarization. Additionally, the peak shift of the edge plane surface is lower than the basal plane one. This difference probably reflects the incorporation degree of oxygen on the edge plane surface and basal plane surface, *i.e.*, oxygen should be more enriched on the edge plane surface.

The detailed chemical state of the edge plane surface was examined by the EELS point analysis. Fig. 3-15 is the carbon K-edge EELS spectra of pCNF2400 and TB after 24 h anodic polarization at 1.8 V vs RHE in 4.0 mol dm⁻³ KOH aq. The point analysis ($\phi < 1.0$ nm) was conducted for the edge plane surface, basal plane surface, and bulk region. All spectra show the peak around 285.5 eV, corresponding to the π^* electronic transition of sp² type carbon [29-34]. Only edge surface spectra of TB and pCNF2400 show the shoulder for the higher energy region around 286 eV. This region is assigned to the C–OH bond of a hydroxyl group (Table 3-4) [29-33]. Therefore, these EELS results reveal the existence of hydroxyl group on the edge plane surface after the anodic oxidation at 1.8 V vs RHE in 4.0 mol dm⁻³ KOH aq. As mentioned above, the ILSEM study and TEM observation demonstrate that the carbon corrosion for the edge plane direction is negligibly slower than the corrosion for the basal plane direction. Thus, these edge sites hydroxyl groups can suppress the proceeding of the anodic oxidation from edge sites. This functional group formation is one of the reasons why the carbon edge sites are not the priority corrosion site under the OER environment in 4.0 mol dm⁻³ KOH aq.

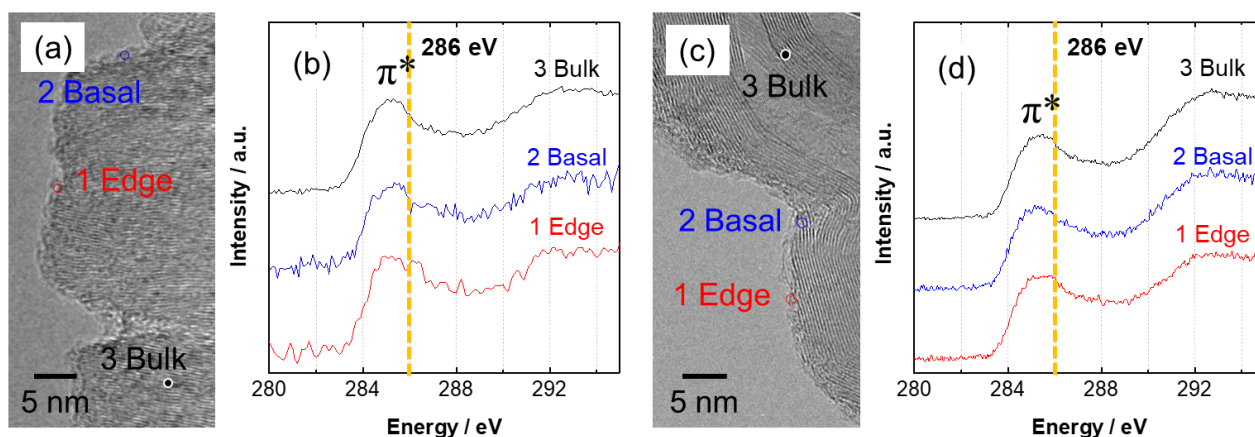


Fig. 3-15 TEM/EELS point analysis ($\varphi < 1$ nm) results for pCNF2400 and TB after the polarization at 1.8 V vs RHE in 4.0 mol dm⁻³ KOH aq. for 24 h. (a, c) TEM image of (a) pCNF2400 and (c) TB. (b, d) C-K edge of core-loss EEL spectra for each analysis points of (b) pCNF2400 and (d) TB.

Table 3-4 EELS peak list of functional groups of carbon materials.

Energy / eV	Functional group
285	Aromatic C-C
286.0 – 286.8	Ketone O=C Nitrile N≡C Phenol HO-C
286.6	Ether C-O-C
287.2–288.3	Aliphatic C–C
288.5 – 288.7	Carboxyl O=CO-
290.3	Carbonate CO ₃ ²⁻

3-3-4 Wettability of anodized carbon materials

Static contact angles of a Milli-Q water droplet of 1 μ L for each carbon material were evaluated to reveal the existence of the edge plane phenol species. Fig. 3-16 shows contact angles of Milli-Q water on each carbon material before and after the anodic oxidation using GC in 4.0 mol dm⁻³ KOH for 2 h. It is noted that longer time polarization on the glassy-carbon electrode causes the peeling of the coated carbon layer from GC so that this shorter polarization time was utilized here. It should also be noted that even with a shorter polarization time, the looped carbon disappearance of pCNF2400

was confirmed by TEM observation (Fig. 3-17). All electrodes show a similar contact angle around 110° before the anodic polarization. After the anodic polarization, every electrode reduces contact angle, and that decrement range depends on the carbon materials. In the case of carbon black type materials, *i.e.*, TB and AB, the contact angles after the anodic oxidation were around 70° , while pCNF type materials show relatively lower contact angles of around 25° after the anodic polarization.

The water contact angle is dependent on the surface roughness in addition to the surface chemistry. Thus, the surface roughness of the carbon materials was also examined from the laser scanning microscope observation. Fig. 3-18 shows the laser-scanning micrographs of carbon materials after the anodic polarization. It is known that the surface roughness enhances the wettability of the surface, *i.e.*, surface roughening of a hydrophilic surface reduces the water contact angle [35]. The water contact angles of all carbon materials are similar before anodic polarization. This similarity of the water contact angle, also supported from Fig. 3-18, suggested similar roughness of the carbon materials on the GC electrode. The hydrophilization is induced by the oxygen-containing functional group, which is formed due to the electrochemical carbon oxidation, on the carbon surface after electrochemical oxidation [36]. In this thesis, the hydrophilization for all carbon materials was observed after electrochemical oxidation, and the degree of hydrophilization was more significant for the pCNF type materials. As discussed above, the major of the pCNF surface is carbon edge planes, and the -OH group is preferentially formed on such edge plane after the anodic polarization in 4.0 mol dm^{-3} KOH aq. Hence, the higher hydrophilization should occur on the pCNF surface rather than the carbon black type materials. Thus, the higher hydrophilization on the pCNF surface is evidence of -OH group formation on the edge plane surface.

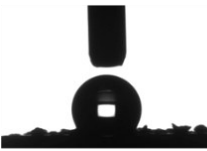

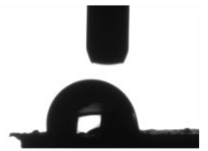
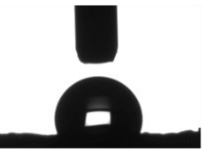
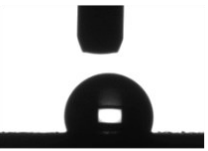
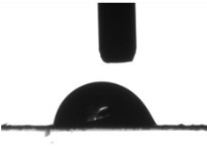
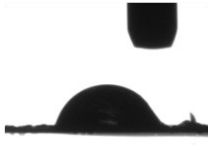



	TB / deg.	AB / deg.	pCNF2000 / deg.	pCNF2400 / deg.	pCNF3000 / deg.
Before	 115.7 ± 14.5	 108.0 ± 13.8	 108.5 ± 5.8	 109.8 ± 2.3	 108.9 ± 7.7
1.8 V vs RHE, 2h	 79.6 ± 7.7	 61.7 ± 8.3	 23.8 ± 10.1	 25.5 ± 8.0	 23.3 ± 9.8

Fig. 3-16 Contact angles for the static Mili-Q water on the carbon electrodes before and after the anodic oxidation at 1.8 V vs RHE in 4.0 mol dm⁻³ KOH for 2 h.

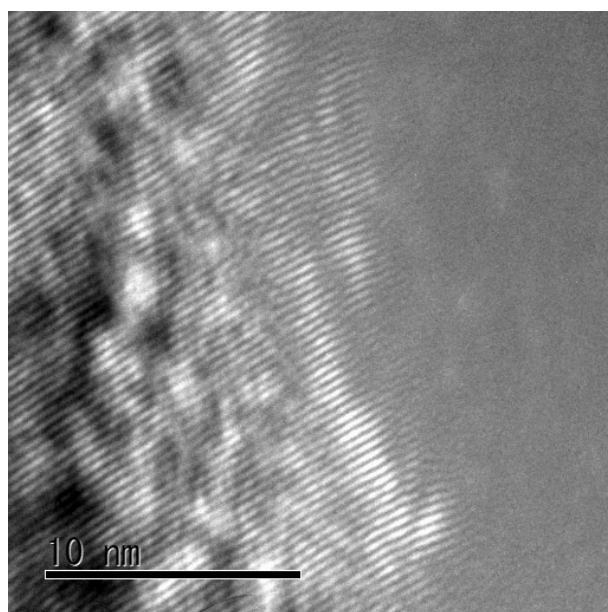


Fig. 3-17 The HRTEM image of the sidewall of pCNF2400 after 2 h anodization in 4.0 mol dm⁻³ KOH aq. at 1.8 V vs RHE.

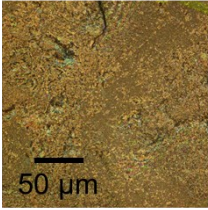
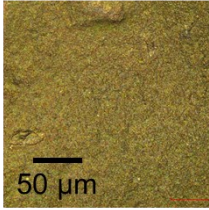
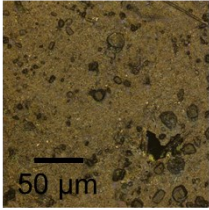
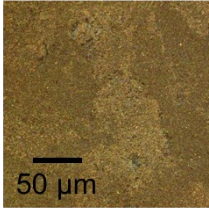
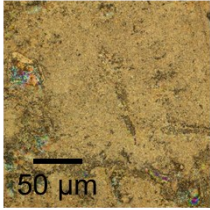
TB	AB	pCNF2000	pCNF2400	pCNF3000
				
$R_a = 4.04 \mu\text{m}$	$R_a = 3.36 \mu\text{m}$	$R_a = 1.09 \mu\text{m}$	$R_a = 1.13 \mu\text{m}$	$R_a = 1.46 \mu\text{m}$

Fig. 3-18 Laser scanning micrographs of carbon materials after the anodic polarization at 1.8 V vs RHE in 4.0 mol dm⁻³ KOH for 2 h.

3-3-5 Mechanism of the slow degradation of pCNFs

In this chapter, the corrosion behavior of platelet-type carbon nanofibers was investigated using an identical location observation technique, as well as spectroscopic studies. ILSEM studies indicate that the carbon oxidation proceeds almost linearly with time on the carbon basal plane of carbon blacks and pCNFs at 1.8 V vs RHE in 4 mol dm⁻³ KOH electrolyte (Fig. 3-4). The carbon oxidation rate on the basal plane decreases as the graphitization degree of the carbon materials enhances. The increase in the peak width of the G band in Raman spectra and d_{002} lattice spacing value calculated from XRD profiles of graphitic carbon materials is associated with the structural disorder. The disordered carbon atoms may be preferential sites of carbon corrosion so that the carbon materials with the lower disorder show lower carbon oxidation rates on the basal plane.

In contrast, the carbon oxidation of the edge plane of pCNFs is extremely slow, regardless of the graphitization degree (Fig. 3-5). The carbon loops present in the pristine pCNFs disappear within 2 h anodic polarization. The looped carbon may corrode at a similar rate with the carbon basal plane, but the corrosion rate becomes extremely slow after the exposure of the carbon edges. As shown in

Chapter 2, the platelet structure was developed at the heat treatment temperature of 2000°C, although the disorder appears to be present from the TEM image. Findings suggest that the carbon oxidation on the edge plane is not influenced by the graphitization degree or disorder structure when the carbon edge plane is uniformly exposed to the alkaline electrolyte. A passive surface appears to be developed on the carbon edge plane to suppress the carbon corrosion to a negligible level.

The present STEM/EELS study indicates that the carbon edge plane of pCNFs is covered with the hydroxyl species, which appear to passivate the surface to electrochemical corrosion. Lin *et al.* proposed the two-step forming process of hydroxyl species via active radicals based on the density functional theory calculations [37]. They also reported that hydroxyl-adsorbed zigzag carbon edges become an active site for oxygen evolution reaction (OER). During OER, the hydroxy species is converted to C-O and C-OOH intermediates, but no C-O bond cleavage occurs, probably leading to the suppression of carbon corrosion. The hydroxyl group does not form on the carbon basal plane at the high density, which is evident from the low oxygen concentration in the STEM/EELS analysis. Thus, sufficient passivation cannot occur, and electrochemical corrosion of carbon proceeds continuously on the basal plane of carbon blacks and pCNFs. This insufficient passivation on the basal plane probably comes from the hydroxyl group stability on the basal plane. Fig. 3-19 is the average binding energy (E_b) calculation results for hydroxyl groups on the edge plane and basal plane surface. E_b is calculated by the DFT method referring to the reports by Han *et al.* [38]. In this calculation, the lower E_b value mentions the stronger bond strength of the functional group. The hydroxyl group on the edge plane surface shows a lower E_b (-3.59 eV) than the basal plane one (1.16 eV), because of the strong planer direction binding energy, which is due to the aromatic ring and effects on the basal plane direction. Therefore, the hydroxyl group tends to more likely be generated on the edge plane surface than on the basal plane surface. Han *et al.* also reported that the hydroxyl group on the carbon edge sites provides the electronic stability due to (1) the low Fermi level, (2) the electron serving from

oxygen atoms to the higher energy level orbital, and (3) lower average binding energy of -5.32 eV than the binding energy of hydrogen termination case of -5.14 eV [38] (Fig. 3-20). Therefore, the surface hydroxyl group formation on the pCNF edge plane possibly enhances the corrosion resistance like a passivation film.

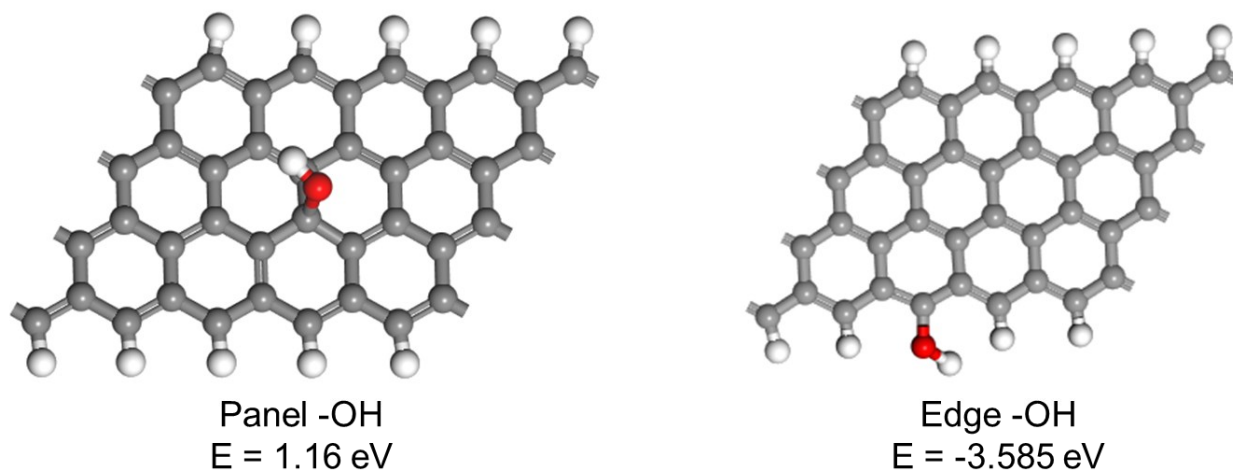


Fig. 3-19 DFT structural optimization results for -OH group addition on the graphene surface.

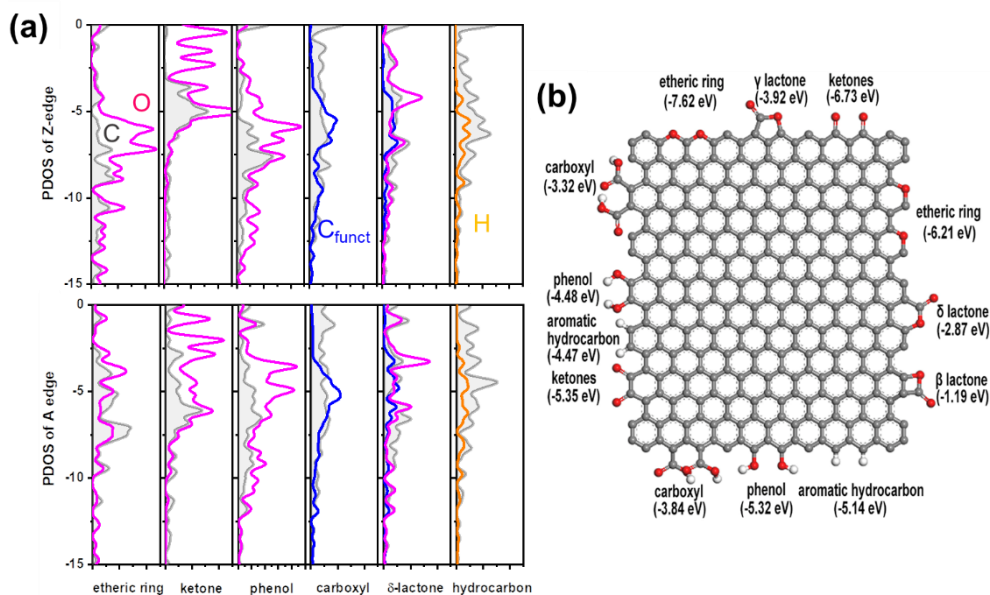


Fig. 3-20 Theoretical analysis results of different oxygenated groups: (a) The projected density of states (PDOS), (b) The average binding energy (E_b). Reproduced from Reference [38], Copyright 2019, Elsevier.

Changes in the edge and basal planes of pCNFs during anodic polarization are illustrated in Fig. 3-21. The sidewall of pCNFs is initially covered with the looped carbon layers, which are oxidized relatively readily during anodic polarization, and carbon edges are exposed. Then, the hydroxyl species cover the edge surface at high density, causing passivation of the sidewall of pCNFs. After anodic polarization at 1.8 V vs RHE for 2 h, the water contact angle was reduced to as low as $28.5 \pm 8.0^\circ$. Such a low water contact angle suggests the presence of a high density of hydroxyl species on the sidewall of pCNFs. In contrast, the coverage of the carbon basal plane at both ends of pCNFs and carbon black surface is relatively low, making the passivation insufficient. Thus, continuous oxidation of carbon proceeds on the basal plane with the oxidation rate depending on the graphitization degree. The present findings disclosed that the uniform exposure of the carbon edge plane to the alkaline electrolyte is of great importance to suppress carbon corrosion at high anodic potentials. Such surface can be passivated by covering the carbon edge plane with the high density of hydroxyl species. The highly graphitized pCNFs are promising carbon materials with high resistance to carbon corrosion.

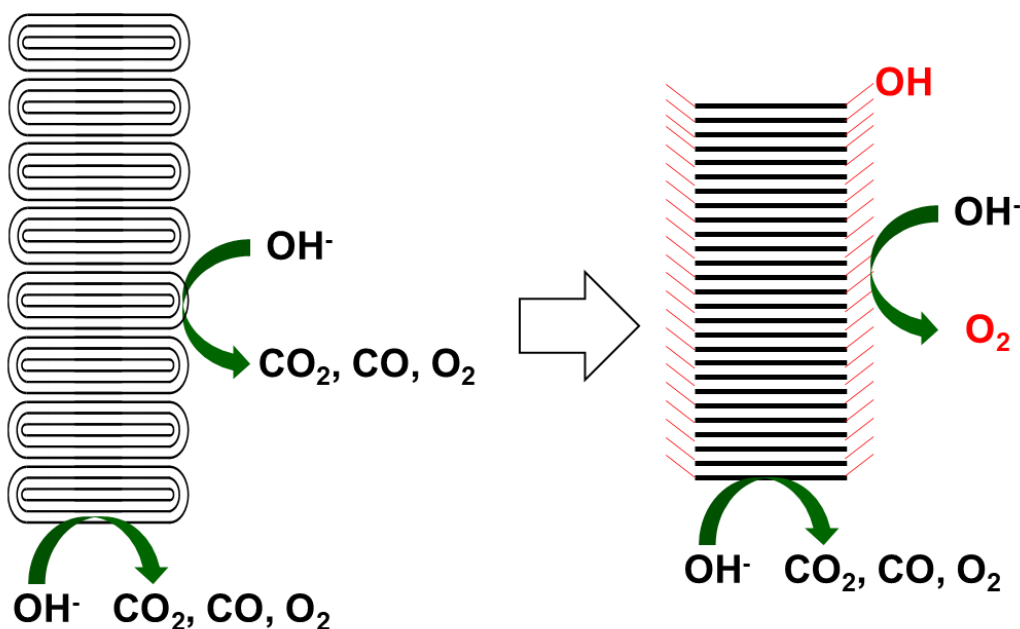


Fig. 3-21 Schematic illustration of the proposed corrosion mechanism of carbon materials under oxygen evolution reaction in $4.0 \text{ mol dm}^{-3} \text{ KOH aq.}$ at 1.8 V vs RHE.

3-4 Conclusions

In this chapter, the corrosion behavior of platelet-type carbon nanofibers and the carbon blacks under oxygen evolution reaction in alkaline media, i.e., 1.8 V vs RHE in 4.0 mol dm⁻³ KOH aq., were examined using the ILSEM studies and spectroscopic studies. Based on the experimental findings, the following conclusions were drawn.

- (1) ILSEM study reveals that the carbon corrosion from surface edge sites is significantly slower than the corrosion from the basal plane. The corrosion rate of the basal plane is strongly influenced by the graphitization degree.
- (2) TEM observations reveal that the carbon edge plane of pCNFs exposes during the anodic oxidation because of the oxidation removal of the looped carbon layer. The pCNFs with exposed carbon edge planes reveal an extremely slow corrosion rate. The hydroxyl species cover the carbon edge plane and passivate the pCNFs.
- (3) According to (1) and (2), high graphitization degree (chemical stability) and edge exposure (Functional group formation) provide corrosion-tolerant carbon materials. This new carbon design concept will be helpful to realize new generation carbon electrode materials.

3-5 References

1. E. Tsuji, T. Yamasaki, Y. Aoki, S. G. Park, K. Shimizu, H. Habazaki, “Highly durable platelet carbon nanofiber-supported platinum catalysts for the oxygen reduction reaction”, *Carbon*, **87**, 1-9 (2015).
2. T. Tamaki, H. Wang, N. Oka, I. Honma, S.H. Yoon, T. Yamaguchi, “Correlation between the carbon structures and their tolerance to carbon corrosion as catalyst supports for polymer electrolyte fuel cells”, *Int. J. Hydrogen Energy*, **43(12)**, 6406-6412 (2018).
3. S.W. Lee, S.R. Choi, J. Jang, G.G. Park, S.H. Yu, J.Y. Park, “Tolerance to carbon corrosion of various carbon structures as catalyst supports for polymer electrolyte membrane fuel cells”, *J. Mater. Chem. A*, **7**, 25056-25065 (2019).
4. N. Hodnik, G. Dehm, K.J.J. Mayrhofer, “Importance and Challenges of Electrochemical in Situ Liquid Cell Electron Microscopy for Energy Conversion Research”, *Acc. Chem. Res.*, 2016, **49**, 2015–2022.
5. N. Hodnik, M. Zorko, M. Bele, S. Hočevar, M. Gaberšček, “Identical Location Scanning Electron Microscopy: A Case Study of Electrochemical Degradation of PtNi Nanoparticles Using a New Nondestructive Method”, *J. Phys. Chem. C*, **116**, 40, 21326–21333 (2012).
6. T. Kinumoto, H. Nishihara, M. Matsuoka, N. Eguchi, T. Tsumura, M. Toyoda, “Degradation of the Pt/C Electrode Catalyst Monitored by Identical Location Scanning Electron Microscopy during Potential Pulse Durability Tests in HClO₄ Solution”, *Electrochemistry (Tokyo)*, **83(1)** 12-17 (2015).
7. A. Ooi, Y. Shigihara, E. Tada, A. Nishikata, “Identical-Location Scanning Electron Microscopy Observation of Surface Morphological Changes of Pt–Cu Nanoparticles”, *Materials Transactions*, **61(10)**, 1949-1957 (2020).
8. N. P. Finkelstein, R. D. Hancock, “A new approach to the chemistry of gold”, *Gold Bulletin*, **7**, 72-77(1974).
9. H. Konno, K. Oyamada, M. Inagaki, “Formation of carbonaceous-coatings on aluminium using poly(vinyl alcohol)”, *J. Euro. Ceramic Soc.*, **20(9)**, 1391-1396 (2000).
10. H.H. Elsentriecy, K. Azumi, “Electroless Ni–P Deposition on AZ91 D Magnesium Alloy Prepared by Molybdate Chemical Conversion Coatings”, *J. Electrochem. Soc.*, **156**, D70-D77 (2009).
11. Y. Konno, E. Tsuji, Y. Aoki, T. Otsuka, H. Habazaki, “Corrosion protection of iron using porous anodic oxide/conducting polymer composite coatings”, *Faraday Discussions*, **180**, 479-493 (2015).
12. K. Nishio, H. Masuda, “Anodization of Gold in Oxalate Solution To Form a Nanoporous Black Film”, *Angew. Chem. Int. Ed.*, **50(7)**, 1603-1607 (2011).
13. K. Nishio, H. Masuda, “Formation of Nanoporous Anodic Gold Oxide Films in Carboxylic Acids and Spontaneous Reduction to Nanoporous Gold”, *Bulletin of the Chemical Society of Japan*, **86(10)**, 1144-1150 (2013).
14. T. Inoue, A. Koyama, D. Kowalski, C. Zhu, Y. Aoki, H. Habazaki, “Fluorine-Free Slippery Liquid-Infused Porous Surfaces Prepared Using Hierarchically Porous Aluminum”, *Phys. Status Solidi A*, **217(13)**, 190836 (2020).
15. E. Tsuji, T. Motohashi, H. Noda, D. Kowalski, Y. Aoki, H. Tanida, J. Nikura, Y. Koyama, M. Mori, H. Arai, T. Ioroi, N. Fujiwara, Y. Uchimoto, Z. Ogumi, H. Habazaki, “Brownmillerite-type Ca₂FeCoO₅ as a Practicable Oxygen Evolution Reaction Catalyst”, *ChemSusChem.*, **10(14)**, 2864-2868 (2017).

16. S.G. Peera, R. Koutavarapu, S. Akula, A. Asokan, P. Moni, M. Selvaraj, J. Balamurugan, S.O. Kim, C. Liu, A.K. Sahu, “Carbon Nanofibers as Potential Catalyst Support for Fuel Cell Cathodes: A Review”, *Energy Fuels*, **35(15)**, 11761–11799 (2021).
17. G. Katagiri, H. Ishida, A. Ishitani, “Raman spectra of graphite edge planes”, *Carbon*, **26**, 565-571 (1988).
18. H. Sumi, S. Ogawa, M. Sato, A. Saikubo, E. Ikenaga, M. Nihei, Y. Takakuwa, “Effect of Carrier Gas (Ar and He) on the Crystallographic Quality of Networked Nanographite Grown on Si Substrates by Photoemission-Assisted Plasma-Enhanced Chemical Vapor Deposition”, *Jpn. J. Appl. Phys.*, **49**, 076201 (2010).
19. Y. Yi, G. Weinberg, M. Prenzel, M. Greiner, S. Heumann, S. Becker, R. Schlögl, “Electrochemical corrosion of a glassy carbon electrode”, *Catal. Today*, **295**, 32-40 (2017).
20. J. Harvey, C. Kozłowski, Peter M. A. SHERWOOD, “X-ray photoelectron spectroscopic studies of carbon fibre surfaces”, *J. Mater. Sci.*, **22**, 1585-1596 (1987).
21. H. Darmstadt, C. Roy, S. Kaliaguine, “ESCA characterization of commercial carbon blacks and of carbon blacks from vacuum pyrolysis of used tires”, *Carbon*, **32**, 1399-1406 (1994).
22. S. Biniak, G. Szymański, J. Siedlewski, A. Świątkowski, “The characterization of activated carbons with oxygen and nitrogen surface groups”, *Carbon*, **35**, 1799-1810 (1997).
23. D.T. Clark, A. Dilks, “Esca applied to polymers. XXIII. RF glow discharge modification of polymers in pure oxygen and helium–oxygen mixtures”, *J. Polymer Sci.*, **17**, 957-976 (1979).
24. U. Zielke, K.J. Hüttinger, W.P. Hoffman, “Surface-oxidized carbon fibers: I. Surface structure and chemistry”, *Carbon*, **34**, 983-998 (1996).
25. M. Kantschewa, E.V. Albano, G. Ertl, H. Kno“zinger, “Infrared and x-ray photoelectron spectroscopy study of $K_2CO_3/\gamma-Al_2O_3$ ”, *Applied Catalysis*, **8**, 71-84 (1983).
26. F. Atamny, J. Blöcker, A. Dübotzky, H. Kurt, O. Timpe, G. Loose, W. Mahdi, R. Schlögl, “Surface chemistry of carbon: activation of molecular oxygen, Molecular Physics”, *Molecular Physics*, **76**, 851-886 (1992).
27. M.T. Martínez, M.A. Callejas, A.M. Benito, M. Cochet, T. Seeger, A. Ansón, J. Schreiber, C. Gordon, C. Marhic, O. Chauvet, J.L.G. Fierro, W.K. Maser, “Sensitivity of single wall carbon nanotubes to oxidative processing: structural modification, intercalation and functionalization”, *Carbon*, **41**, 2247–2256 (2003).
28. K.A. Mkhoyan, A.W. Contryman, J. Silcox, D.A. Stewart, G. Eda, C. Mattevi, S. Miller, M. Chhowalla, “Atomic and Electronic Structure of Graphene-Oxide”, *Nano Lett.*, **9(3)**, 1058–1063 (2009).
29. K. Miyazawa, T. Nagai, K. Kimoto, M. Yoshitake, Y. Tanaka, “Cross-sectional structural characterization of the surface of exfoliated HOPG using HRTEM-EELS”, *Surf. Interface Anal.*, **53(1)**, 84-89 (2021).
30. K. Miyazawa, T. Nagai, K. Kimoto, M. Yoshitake, Y. Tanaka, “HRTEM-EELS cross-sectional structural analyses of glassy carbon substrate irradiated by platinum ions using a coaxial arc plasma gun”, *Surf. Interface Anal.*, **52(1-2)**, 23-33 (2020).
31. D.D’ Angelo, C. Bongiorno, M. Amato, I. Deretzi, A. La Magna, G. Compagnini, S.F. Spanò, S. Scalese, “Electron energy-loss spectra of graphene oxide for the determination of oxygen functionalities”, *Carbon*, **93**, 1034-1041 (2015).
32. M. Pelaez-Fernandez, A. Bermejo, A.M. Benito, W.K. Maser, R. Arenal, “Detailed thermal reduction analyses of graphene oxide via in-situ TEM/EELS studies”, *Carbon*, **178(30)**, 477-487 (2021).

33. A. Braun, F.E. Huggins, N. Shah, Y. Chen, S. Wirick, S.B. Mun, C. Jacobsen, G.P. Huffman, “Advantages of soft X-ray absorption over TEM-EELS for solid carbon studies—a comparative study on diesel soot with EELS and NEXAFS”, *Carbon*, **43(1)**, 117-124 (2005).
34. C. Vollmer, D. Kepaptsoglou, J. Leitner, H. Busemann, N.H. Spring, Q.M. Ramasse, P. Hoppe, L.R. Nittler, *PNAS*, **2014**, *111*, 15338-15343
35. R. Yamamoto, D. Kowalski, R. Zhu, K. Wada, Y. Sato, S. Kitano, C. Zhu, Y. Aoki, H. Habazaki, “Fabrication of superhydrophobic copper metal nanowire surfaces with high thermal conductivity”, *Appl. Surf. Sci.*, **537**, 147854 (2021).
36. W. Wang, J. Luo, S. Chen, “Carbon oxidation reactions could misguide the evaluation of carbon black-based oxygen-evolution electrocatalysts”, *Chem. Commun.*, **53**, 11556-11559 (2017).
37. Y. Lin, Q. Lu, F. Song, L. Yu, A.K. Mechler, R. Schlögl, S. Heumann. “Oxygen Evolution Reaction at Carbon Edge Sites: Investigation of Activity Evolution and Structure–Function Relationships with Polycyclic Aromatic Hydrocarbons”, *Angew. Chem. Int. Ed.*, **58(26)**, 8917-8921 (2019).
38. G.F. Han, B.B. Xiao, S.J. Kim, F. Li, I. Ahmad, I.Y. Jeon, J.B. Baek, “Tuning edge-oxygenated groups on graphitic carbon materials against corrosion”, *Nano Energy*, **66**, 104112 (2019).

Chapter 4
OER activity and
durability of
pCNF/CFCO hybrid
electrode

Chapter 4 OER activity and durability of pCNF/CFCO hybrid electrode

4-1 Introduction

As described in Chapter 1, carbon materials are an essential component for the air-electrode of ZABs as the electron conductive support [1-3]. Carbon materials are suitable electron conductive supports and cause the synergistic effect with the electrocatalyst for OER and ORR [1]. Additionally, some researchers reported that the anodic corrosion of the carbon materials in the air electrode caused the degradation of the air electrode in ZAB [1, 4, 5]. Thus, the type of carbon materials used in the air-electrode is expected to strongly affect the air-electrode performance, such as the electrode activity and lifetime. pCNFs were durable carbon materials for carbon corrosion [6-8]. In addition, it was found in Chapter 3 that pCNFs show an extremely low corrosion rate under OER in a concentrated KOH electrolyte due to passivation on their surface, being promising as durable conductive support of the air electrode in rechargeable ZABs. In this chapter, the electron-conductive support properties of pCNFs were examined by mixing with Brown-millerite type $\text{Ca}_2\text{FeCoO}_5$ (CFCO), which was recently reported as the highly active electrocatalyst for OER [9]. The long-term durability test of the pCNFs/CFCO electrode extending to one month was examined in this chapter to see the lifetime of pCNFs under the actual OER environment.

4-2 Experimental

4-2-1 Metal-oxide electrocatalyst preparation

CFCO was synthesized according to a procedure described elsewhere [9-11]. Following reagents were used as precursors: $\text{Ca}(\text{NO}_3)_2 \cdot 4\text{H}_2\text{O}$ (Kanto Chemical), $\text{Fe}(\text{NO}_3)_3 \cdot 9\text{H}_2\text{O}$ (Kanto Chemical) and $\text{Co}(\text{NO}_3)_2 \cdot 6\text{H}_2\text{O}$ (Kanto Chemical). Appropriate amounts of these reagents and citric

acid (CA; Kanto Chemical, 98%) were dissolved in Milli-Q water (Ca:Co:Fe:CA molar ratio = 2:1:1:4). The citrate solution was stirred and heated at 60°C for 3 h to promote polymerization. The gelatinous product was annealed in air at 450°C for 1 h and then fired at 600°C for 12 h.

4-2-2 Electrocatalytic activity evaluation by the rotating-disk electrode (RDE) system

In this chapter, the following carbon materials were used as conductive supports: pCNF1100, pCNF1500, pCNF2400, Denka black (DB), Denka black heat-treated at 2400°C (DB2400) and multiwalled carbon nanotubes (MW). Details of the preparation methods and physical characteristics of these carbon materials were described in Chapter 2. The electrocatalytic activity was evaluated by a rotating disk electrode (RDE; Pine Instrument Co. Ltd.) system using the catalyst-loaded glassy carbon disk electrodes ($1.0 \text{ mg}_{\text{cat}} \text{ cm}^{-2}$). Catalyst inks were prepared as follows. Ten milligrams of selected carbon material and 50 mg of CFCO were dispersed ultrasonically in a mixture of 0.2 mL of 5 wt% Na^+ -exchanged Nafion solution and 4.8 mL of ethanol. Nafion was added as a binder and neutralized before dispersion to prevent CFCO from acidic dissolution due to the lower pH of the Nafion-dispersed solution [12]. The electrochemical measurements were carried out in a three-electrode system using a potentiostat (Hokuto Denko, HZ-7000) and RDE system. PTFE-coated carbon sheet (ElectroChem, Inc., EC-TP1-060T) and Hg/HgO/4 mol dm^{-3} KOH were used as counter and reference electrodes, respectively. All measurements were carried out at room temperature ($\sim 25^\circ\text{C}$) in a 4 mol dm^{-3} KOH aqueous solution (pH = 14). The electrocatalytic activity was evaluated using linear sweep voltammetry (LSV) with a potential sweep rate of 1 mV s^{-1} . The electrolytes were saturated by Ar and O_2 for OER and ORR evaluation, respectively. The potential was converted from the Hg/HgO/4 mol dm^{-3} KOH reference scale to the RHE using the following equation:

$$E \text{ vs RHE} = E \text{ vs Hg/HgO/4 mol dm}^{-3} \text{ KOH} + 0.9260 \quad (4-1) [9]$$

The suitability of this potential conversion was confirmed from the direct potential measurements using a commercial reversible hydrogen electrode (ET070 HydroFlex, Gaskatel). Electrochemical

impedance spectroscopy (EIS) measurements were also conducted at a constant potential of 1.6 V vs RHE in 4 mol dm⁻³ KOH electrolyte with the amplitude of the AC perturbation signal of 10 mV in the frequency range from 10⁵ Hz to 10⁻² Hz.

4-2-3 Durability test

The durability tests were continuously carried out for each carbon/CFCO electrode for a maximum of 1 month, in which cycles of 2 h chronopotentiometry at +40 mA cm⁻² and subsequent 15 min at open-circuit potential (OCP) were repeated in a 4 mol dm⁻³ KOH electrolyte. The carbon/CFCO electrodes are prepared by immersing PTFE-coated carbon sheets (ElectroChem, Inc., EC-TP1-060T) in the catalyst ink, the same as the RDE evaluation. The total catalyst mass loaded on each electrode was 1.0 mg cm⁻². The schematic illustration of the electrode is shown in Fig. 4-1a. The electrochemical measurements were carried out in a three-electrode system using a Princeton Applied Research VersaSTAT3 potentiostat. A carbon sheet and Hg/HgO/4 mol dm⁻³ KOH with N₂ saturation were used as counter and reference electrodes, respectively. Fig. 4-1b shows the schematic illustration of the electrochemical cell for the durability test.

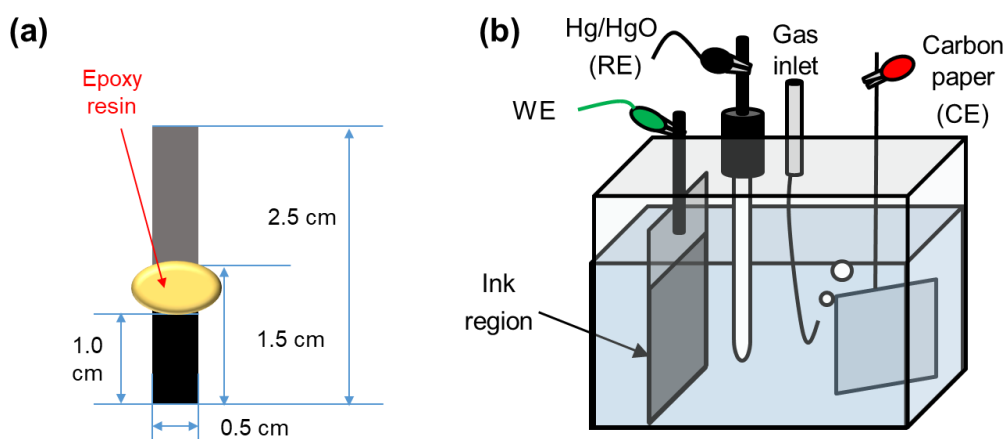


Fig. 4-1 The schematic illustrations of the experimental setup or the durability test.

(a) The carbon-paper electrode and (b) the electrochemical cell.

4-2-4 Characterization techniques

The electrode surface was observed using a low-voltage scanning electron microscope (Zeiss, Sigma-500) operated at 1.5 kV. Additional detailed structure observations were carried out using transmission electron microscopy (TEM; JEOL, JEM-2000FX, JEM-2010F, and JEM-ARM200F) operated at 200 kV. The BET surface area of the CFCO was determined by N₂ gas adsorption/desorption isotherm measurements (Bel Japan, Belsorp-mini instrument) at -196°C. The phase purity of the CFCO was examined by the X-ray powder diffraction (XRD; Rigaku, Ultima IV) using Cu K α radiation ($\lambda = 0.15418$ nm).

4-3 Results and Discussion

4-3-1 Characterizations of metal-oxides used in this study

The brownmillerite-type (BM) structure (Fig. 4-2a) is one of the oxygen-deficiency-ordered perovskites containing a layered arrangement of tetrahedral (T_d) BO₄ and octahedral (O_h) BO₆ [9]. Due to this layered structure, the oxides of this type have many stable oxygen vacancy sites and are well-studied as the oxygen storage material and solid-oxides fuel cell electrodes [13, 14]. Such vacancy sites are also suitable for OER. CFCO shows an OER current of 5.0 mA per oxide-catalyst surface area at 1.6 V vs RHE, which is an order of magnitude larger than the corresponding value for RuO₂ [9, 10]. The XRD pattern of CFCO is shown in Fig. 4-2b, in which all peaks are assigned to a BM structure, confirming the formation of single-phase CFCO at 600°C. The morphology of the CFCO particles was observed by SEM (Fig. 4-2c). The CFCO consists of nanoparticles with an average diameter of 40 nm. TEM image (Fig. 4-2d) reveals well-developed lattice fringes corresponding to the (141) plane of the BM structure. The surface areas of CFCO were estimated by the N₂ gas adsorption/desorption isotherm measurements. Fig. 4-2e is the N₂ gas adsorption/desorption isotherms of CFCO at -196°C. The isotherms suggested the presence of a limited amount of micropores and mesopores on the CFCO surface. The BET surface area of CFCO was estimated to 21.0 m² g⁻¹.

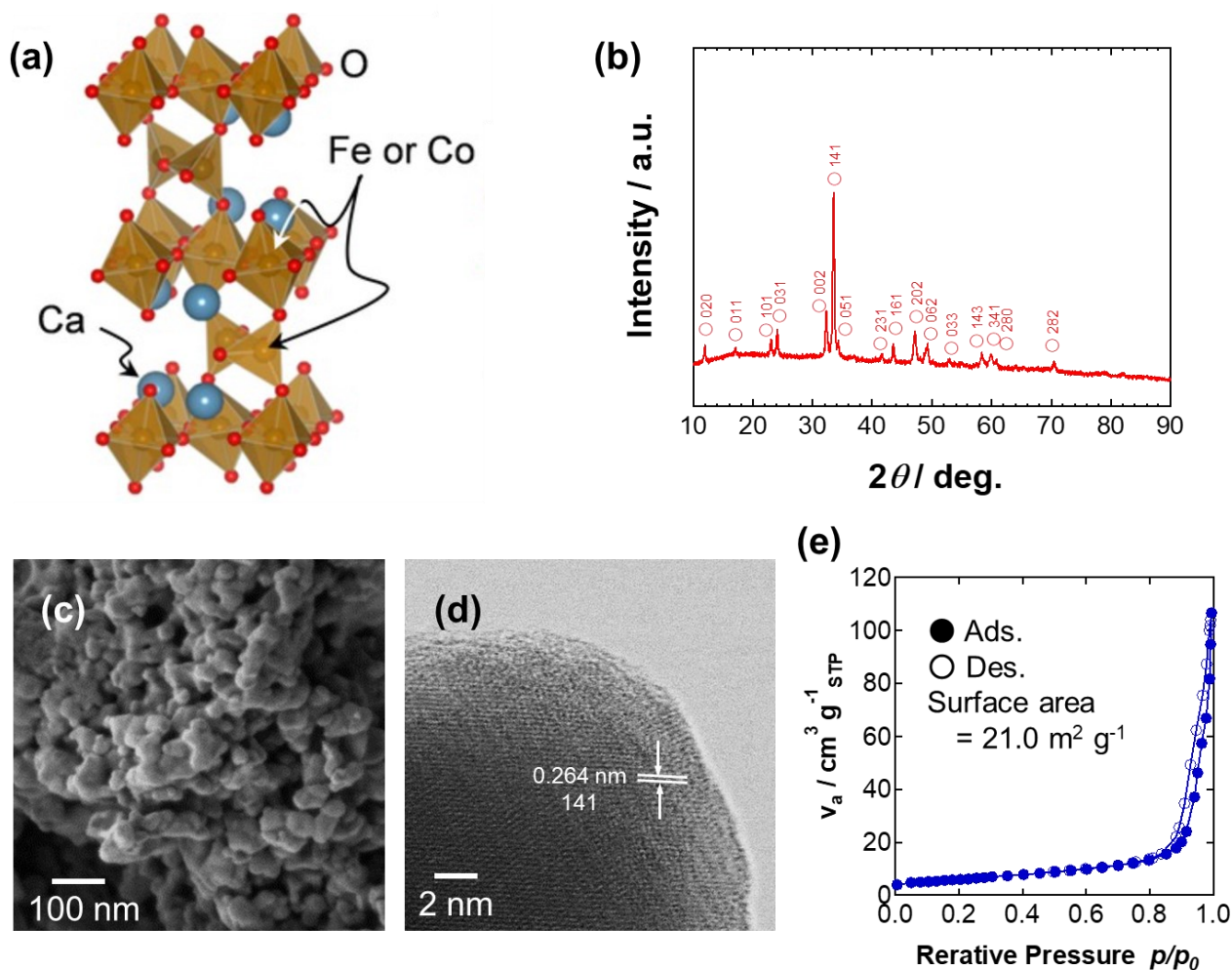


Fig. 4-2 Characterization results of CFCO; (a) Crystal structure of brownmillerite-type $\text{Ca}_2\text{FeCoO}_5$ (CFCO) [9]; (b) XRD pattern of CFCO; (c) SEM image of CFCO; (d) HRTEM image of CFCO; (e) N_2 adsorption/desorption isotherms of CFCO at -196°C .

4-3-2 OER activity of carbon/CFCO electrodes

OER electrocatalysis of carbon/CFCO electrodes was examined using the linear sweep voltammetry (LSV) in $4 \text{ mol dm}^{-3} \text{ KOH}$ (Fig. 4-3). For comparison, LSV of the carbon-free CFCO electrode is also shown. The onset potential (E_{OER}), defined as the potential at $1.5 \text{ mA cm}^{-2}_{\text{disk}}$, equals 1.50 V vs RHE for the carbon-free CFCO. The addition of carbon conductive support to CFCO shifts the onset potential to 1.47 V vs RHE, independent of the type of carbon materials mixed with CFCO (Table 4-1). CFCO has a relatively low conductivity [14], so the addition of conductive support is

necessary to obtain the intrinsic OER activity of CFCO. The overpotential at high current densities was reduced in the following order: DB2400/CFCO = DB/CFCO \leq pCNF1500/CFCO \leq pCNF2400/CFCO < MW/CFCO < pCNF1100/CFCO < pristine-CFCO. The relatively larger overpotential for the pCNF1100/CFCO electrode is possibly related to the lower electrode conductivity coming from the not-enough graphitization degree of pCNF1100. Such relatively larger overpotentials were also observed in the case of highly graphitized samples, *i.e.*, pCNF2400 and MW. The possible explanation for the shift is the insufficient dispersion of carbon material within the electrocatalyst matrix. Fig. 4-4 shows SEM-Backscattered-Electron (BSE) images for DB/CFCO and pCNF2400/CFCO, where the carbon materials and CFCO appear as dark and bright domains, respectively, due to the atomic number contrast. In the case of pCNF2400/CFCO, the agglomeration of pCNF2400 is visible as the large darker region. The better carbon dispersion is apparent in the DB/CFCO composite. It is worth noting that the better distribution of carbon material within the composite matrix facilitates electron transfer for the electrocatalyst.

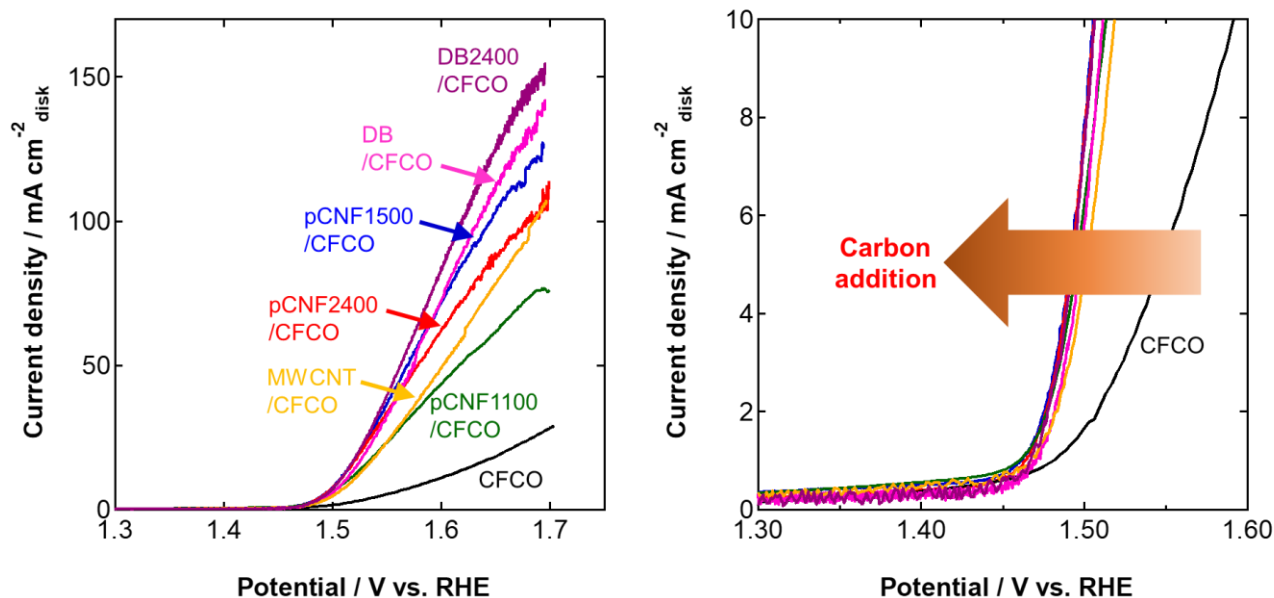


Fig. 4-3 Linear sweep voltammograms of the carbon/CFCO electrodes for OER in 4 mol dm⁻³ KOH aqueous solution. The current density was normalized by the geometric surface area of the disk electrode.

Table 4-1 The OER parameters of each carbon/CFCO electrodes.

	$E_{\text{OER}} / \text{V vs RHE}$	Current density @ 1.65 V / mA cm^{-2}
pCNF1100/CFCO	1.47	61.1
pCNF1500/CFCO	1.47	103
pCNF2400/CFCO	1.47	88.0
DB/CFCO	1.47	111
DB2400/CFCO	1.47	142
MW/CFCO	1.47	77.2
CFCO only	1.50	16.8

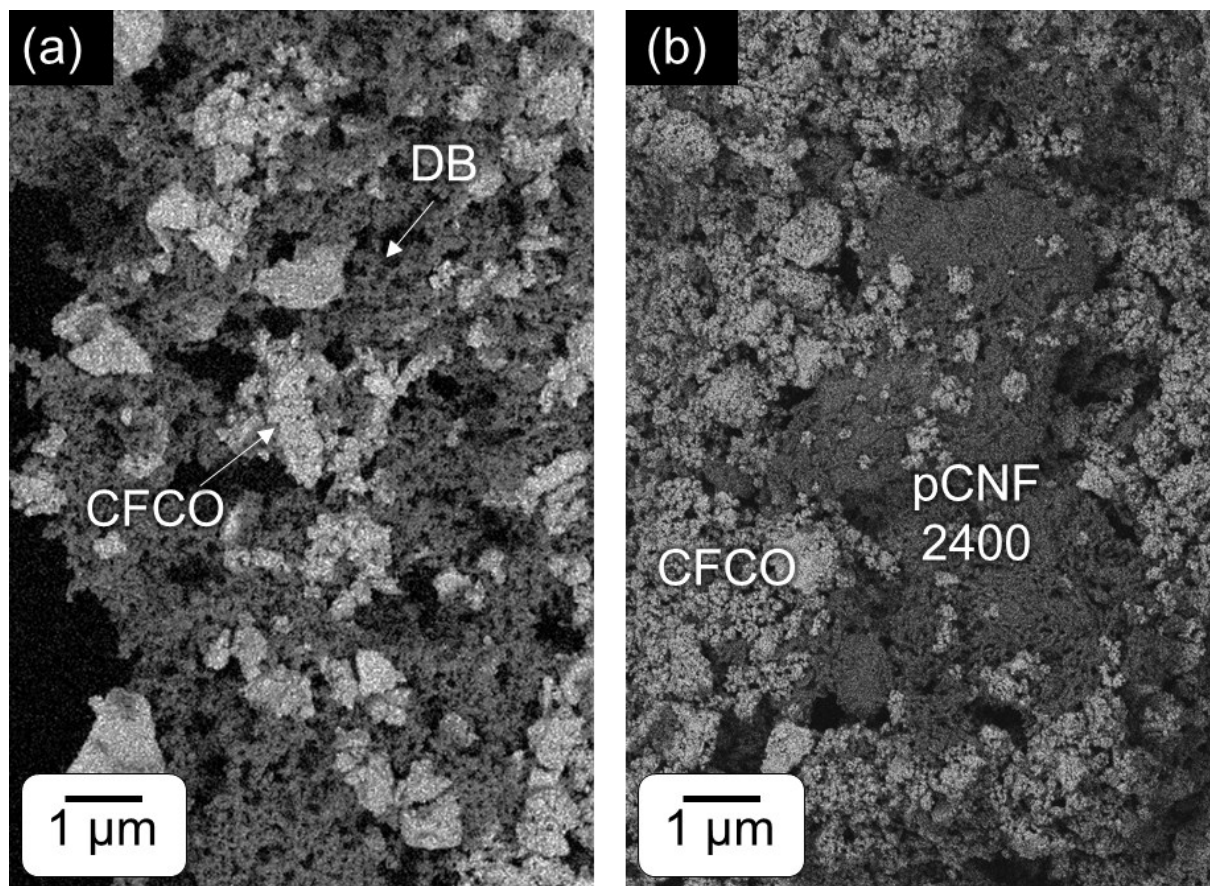


Fig. 4-4 SEM-BSE images of (b) DB/CFCO and (c) pCNF2400/CFCO electrodes on a GC substrate.

The electrochemical characteristics of the catalyst under OER conditions were investigated using EIS measurements at a constant potential of 1.6 V vs RHE in 4 mol dm⁻³ KOH electrolyte (Fig. 4-5). The Nyquist plots for DB/CFCO and pCNF2400/CFCO catalysts deposited on GC electrodes are shown for comparison. The impedance spectrum for pCNF2400/CFCO consists of two semicircles; the high-frequency arc is associated with the resistance and capacitance of the catalyst layer (R_{ox} and C_{ox}), whereas the low-frequency arc corresponds to a charge transfer resistance and a double layer capacitance (R_{ct} and C_{ct}). Two-component impedance spectra, with one component associated with a metal oxide catalyst and the second corresponding to a charge transfer reaction, are typically observed for many other carbon/metal oxide catalysts [15, 16]. In contrast, the Nyquist plot of DB/CFCO is characterized by almost one semicircle, which suggests the disappearance of either impedance component. This disappearance component should be assigned with the resistance of the CFCO and caused by the moderate carbon additive dispersion in the CFCO matrix. It is evident from Fig. 4-4 that the DB/CFCO electrode with better carbon dispersion shows a more negligible charge transfer resistance than the pCNF2400/CFCO electrode with agglomerated carbon.

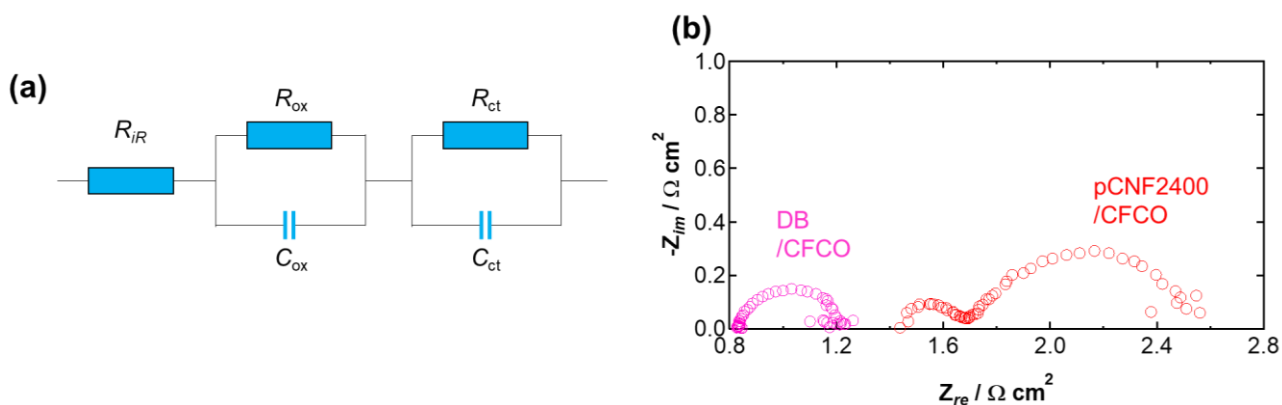


Fig. 4-5 EIS Nyquist plots of DB/CFCO and pCNF2400/CFCO electrodes at 1.6 V vs RHE.

In summary, pCNF2400, suggested as the corrosion tolerance carbon material in Chapter 3, shows conductive support properties for CFCO electrocatalyst. This property can be comparable with the commercially available DB. However, the agglomeration of pCNF provides a negative effect on

the OER activity of the pCNF2400/CFCO electrode. Thus, to furtherly enhance the OER activity of pCNF2400/CFCO, mixing process optimization or direct catalyst loading are probably needed. The pCNF3000/CFCO electrode shows improved OER activity than the pCNF2400/CFCO electrode (Fig. 4-6 a). This improvement came from the sufficient dispersion of pCNF3000 in the CFCO matrix (Fig. 4-6 b). Fig. 4-6b shows SEM-BSE images for pCNF3000/CFCO. While pCNF2400/CFCO electrode showed the agglomeration of pCNF2400, pCNF3000 revealed the improved dispersion in the CFCO matrix. Hence, the improved dispersion of pCNF3000 in the electrocatalysts matrix possibly enhances the electrocatalysis activity of the pCNF3000 based electrode.

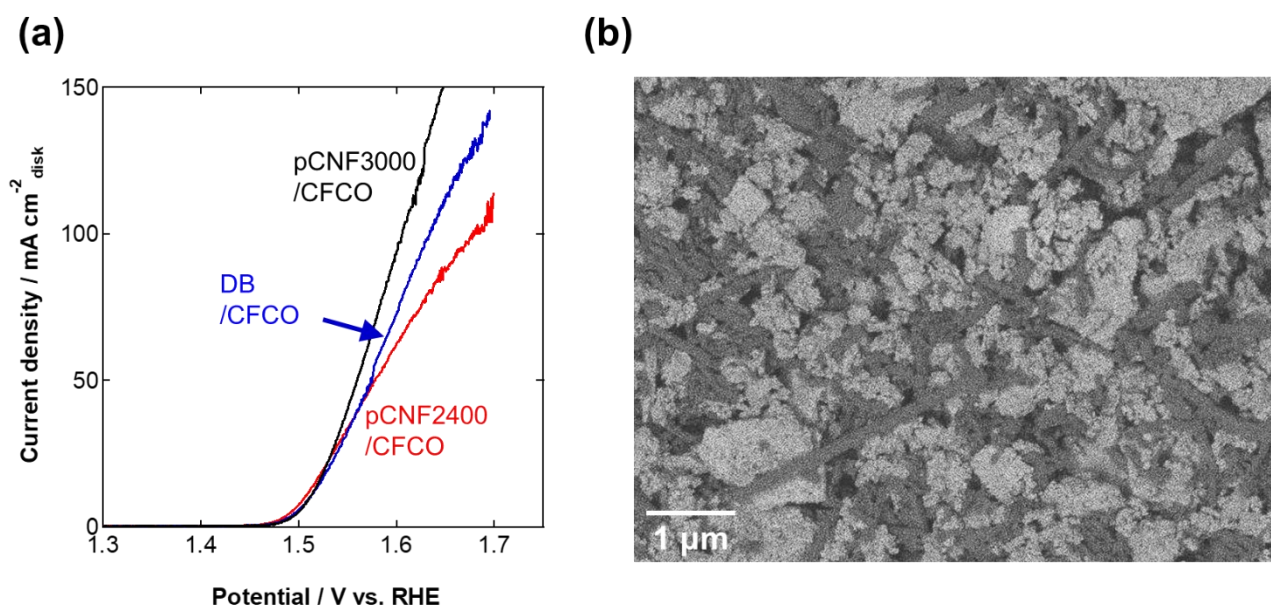


Fig. 4-6 (a) Linear sweep voltammograms of the pCNF3000/CFCO electrodes for OER in 4 mol dm^{-3} KOH aqueous solution. The current density was normalized by the geometric surface area of the disk electrode. (b) SEM-BSE images of pCNF3000/CFCO electrodes on a GC substrate.

4-3-3 ORR activity of carbon/CFCO electrodes

The ORR activity of carbon/CFCO electrodes was also examined in oxygen-saturated 4.0 mol dm^{-3} KOH aq. Fig. 4-7 shows the cathodic LSVs for each carbon/CFCO electrode measured by using a rotating-disk electrode system with a rotation speed of 1600 rpm. For comparison, LSVs of carbon-

free CFCO electrode, GC electrode, and Pt/C are also shown. All CFCO electrodes showed larger overpotentials for ORR than Pt/C electrodes (Table 4-2). This inferior ORR activity comes from the insufficient ORR activity of CFCO [17]. Because of the insufficient ORR activity of CFCO, the ORR activity of carbon/CFCO electrodes depends on the carbon materials (Table 4-2). The onset potential (E_{ORR}), defined as the potential at $-50 \mu\text{A cm}^{-2}_{\text{disk}}$, was reduced in the following order: pCNF1100/CFCO > pCNF1500/CFCO > DB/CFCO > DB2400/CFCO > pCNF2400/CFCO \cong MWCNT/CFCO > pristine-CFCO. This ordering might be reflected the ORR electrocatalysis activity of each carbon material. As mentioned in Chapter 2, pCNF1100 and pCNF1500 have exposed a carbon edge plane on the sidewall. The heat treatment at $\geq 2000^\circ\text{C}$ eliminates these edges due to the loop formation on the sidewall. In addition, such edge sites are widely accepted as the ORR electrocatalysis center in the alkaline media [18]. Thus, CFCO electrodes containing pCNF1100 or pCNF1500 show better ORR electrocatalysis activity than pCNF2400 or MWCNT, which have a limited number of carbon edge sites.

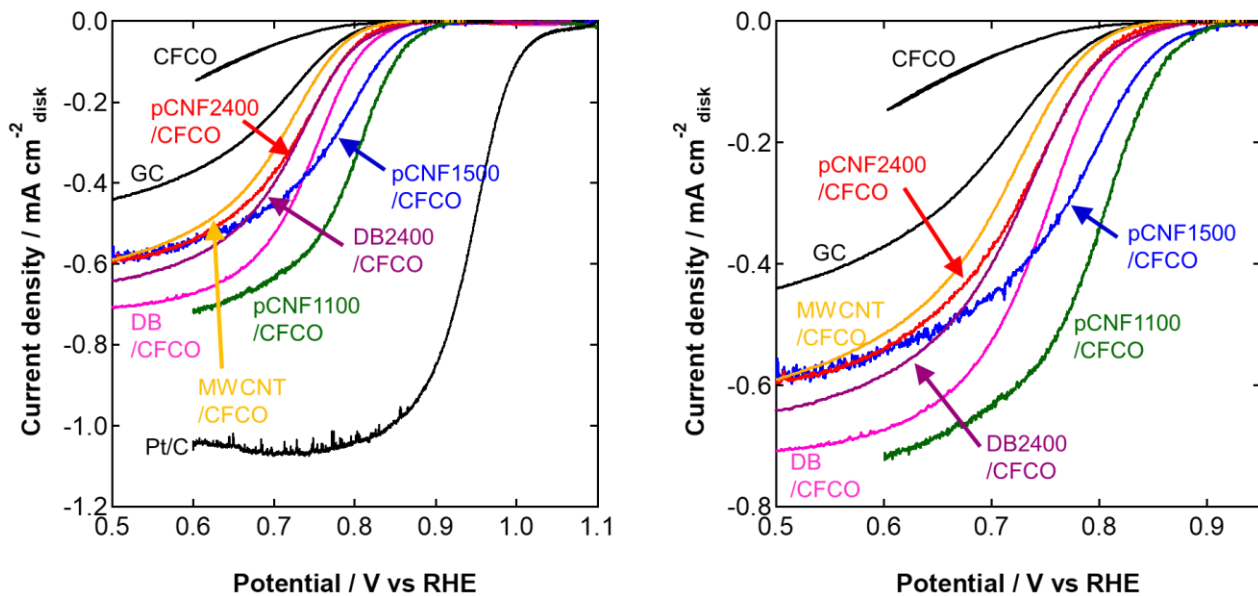


Fig. 4-7 Linear sweep voltammograms of the carbon/CFCO electrodes for ORR in O_2 saturated 4 mol dm^{-3} KOH aqueous solution. The current density was normalized by the geometric surface area of the disk electrode. Scanning rates were 1.0 mV s^{-1} .

Table.4-2 The ORR parameters of carbon/CFCO electrodes.

	$E_{\text{ORR}} / \text{V vs RHE}$	Current density @ 0.60 V / mA cm^{-2}
pCNF1100/CFCO	0.870	-0.722
pCNF1500/CFCO	0.855	-0.541
pCNF2400/CFCO	0.810	-0.541
DB/CFCO	0.823	-0.693
DB2400/CFCO	0.811	-0.584
MWCNT/CFCO	0.790	-0.515
CFCO only	0.713	-0.150
Pt/C	1.02	-1.04

4-3-5 Durability of carbon/CFCO electrodes

The long-term durability of carbon/CFCO electrodes under OER conditions was investigated by polarization at $+40 \text{ mA cm}^{-2}$ in 4 mol dm^{-3} KOH. For this study, pCNF1100 was excluded because of its insufficient electric conductivity and graphitization degree. The anodic LSV curves for the carbon/CFCO electrodes before and after durability tests are shown in Fig. 4-8. The electrocatalytic activity of DB/CFCO, DB2400/CFCO, and pCNF1500/CFCO towards OER was significantly reduced, with the current density at 1.7 V vs RHE dropping to 53%, 54%, and 67% of the original value (Fig. 4-8f), respectively. The deactivation of the catalyst is possibly caused by oxidative decomposition of the carbon support and, therefore, the deficiency of electron-conducting path to CFCO. A similar decrease in the OER current for perovskite oxide/carbon electrodes, related to carbon corrosion, was reported elsewhere [19]. The MWCNT/CFCO electrode showed deactivation towards OER, with the current density dropping to 87% at 1.7 V vs RHE. However, this performance decrease was slightly smaller than that of other carbon materials due to this sample having the highest graphitization degree and better oxidation resistance. The electrocatalytic activity of pCNF2400/CFCO towards OER essentially remained unchanged under the same conditions for one month.

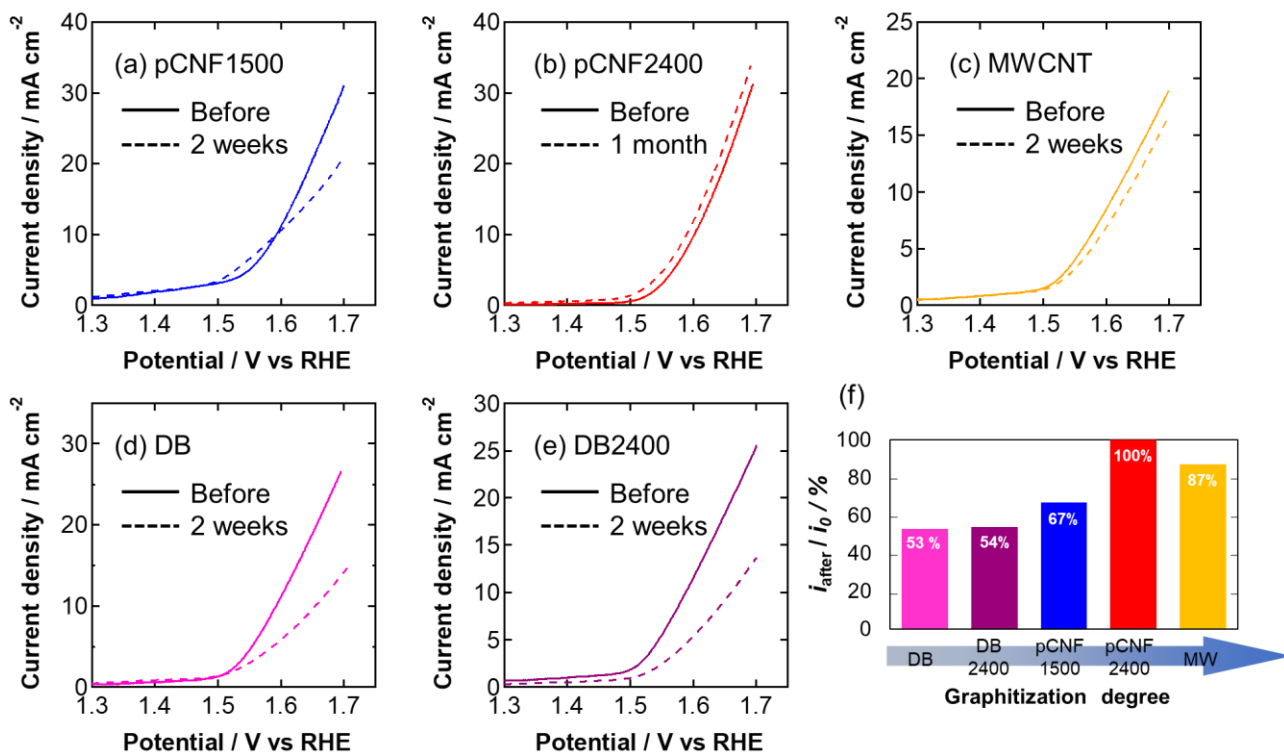


Fig. 4-8 Linear sweep voltammograms of carbon/CFCO electrodes for OER in 4 mol dm⁻³ KOH aqueous solution before and after the durability tests. The current density was normalized by the geometric surface area of the carbon paper electrode.

Fig. 4-9 shows the cathodic LSV curves for the carbon/CFCO electrodes under a long-term durability test in oxygen-saturated 4 mol dm⁻³ KOH. The voltammograms were obtained by running the LSV experiment while the durability test cycles were rest mode. While DB/CFCO electrode shows the degradation of ORR current during the durability test, it is found that the ORR current of pCNF2400/CFCO gradually increases during the durability test. It is generally accepted that the ORR electrocatalytic activity of carbon/perovskites is linked to a synergistic effect between carbon and metal oxide [1]. Therefore, the degradation of ORR for DB/CFCO electrode is probably related to the carbon disappearance due to the carbon corrosion. The enhancement of catalytic activity for the oxidized carbon material has been observed by other researchers [20-22]. Herein, the enhancement of the ORR activity of pCNF2400/CFCO is most likely related to the partial oxidation of pCNF2400, without any

significant effect on the OER activity. One of the possible explanations for the change in the ORR activity could be the stronger affinity of the oxygen molecules to adsorb on the edge sites compared with the plane sites [18, 23]. Density functional theory (DFT) calculations have shown that dangling bonds at the edge sites of graphene have a strong ability for O₂ adsorption [23]. The slow ORR kinetics for pristine pCNF2400 would be linked to the presence of looped carbon layers, which hinder the exposure of the carbon edge plane. Therefore, as observed in Chapter 3, the looped carbon layers on the sidewall of pCNF disappear during the long-term durability test, and the carbon edge site exposure should enhance the ORR kinetics as O₂ adsorption on the edge plane becomes more favorable.

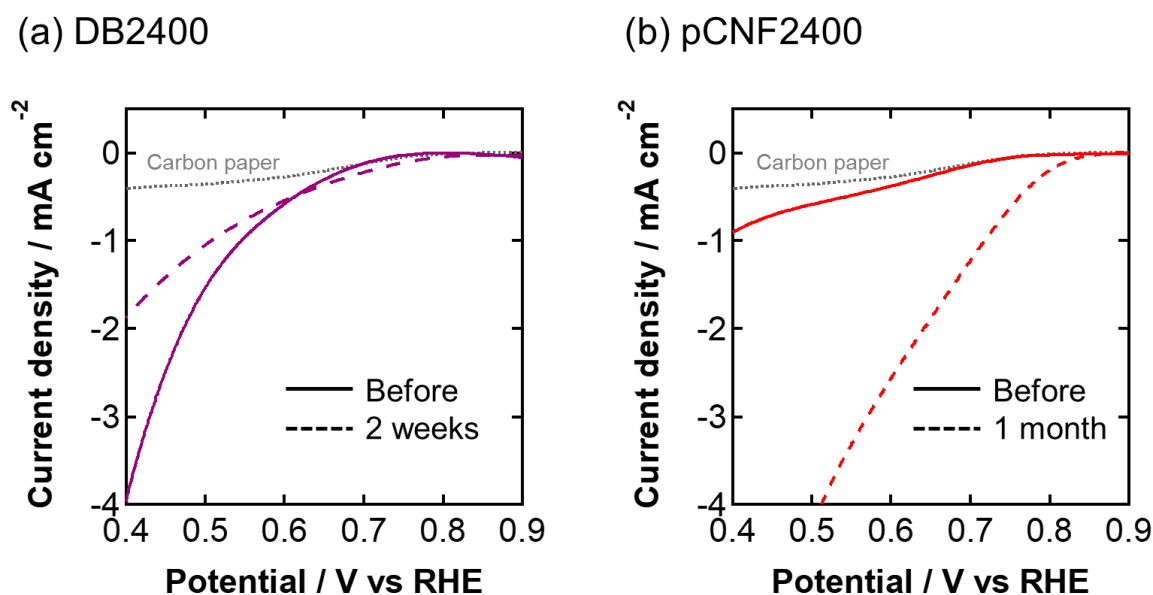


Fig. 4-9 Linear sweep voltammograms of carbon/CFCO electrodes for ORR in oxygen-saturated 4 mol dm⁻³ KOH aqueous solution before and after the durability tests. The current density was normalized by the geometric surface area of the carbon paper electrode.

4-3-6 Characterization of carbon/CFCO electrodes after the durability tests

After a two-week durability test, the morphological changes of carbon, associated with carbon corrosion were observed by SEM-BSE observations (Fig. 4-10). After the durability test, the dark particles are absent for the pCNF1500/CFCO and DB/CFCO electrodes; only the substrate and/or Nafion binder film is visible due to the loss of carbon caused by the oxidative decomposition. Upon polarization of the specimen, the morphology of CFCO particles changes from a particle-like shape into a plate-like shape. This effect may be related to the *in situ* chemical change of CFCO to oxyhydroxide, described in elsewhere [10, 11]. DB2400 shows a similar tendency regarding surface morphology. In contrast, no morphological changes were observed for the pCNF2400/CFCO electrodes under the durability test. The pCNF nanofibers sustained their geometrical shape, and no exposed Nafion binders were observed, indicating that pCNF2400 is durable under OER conditions.

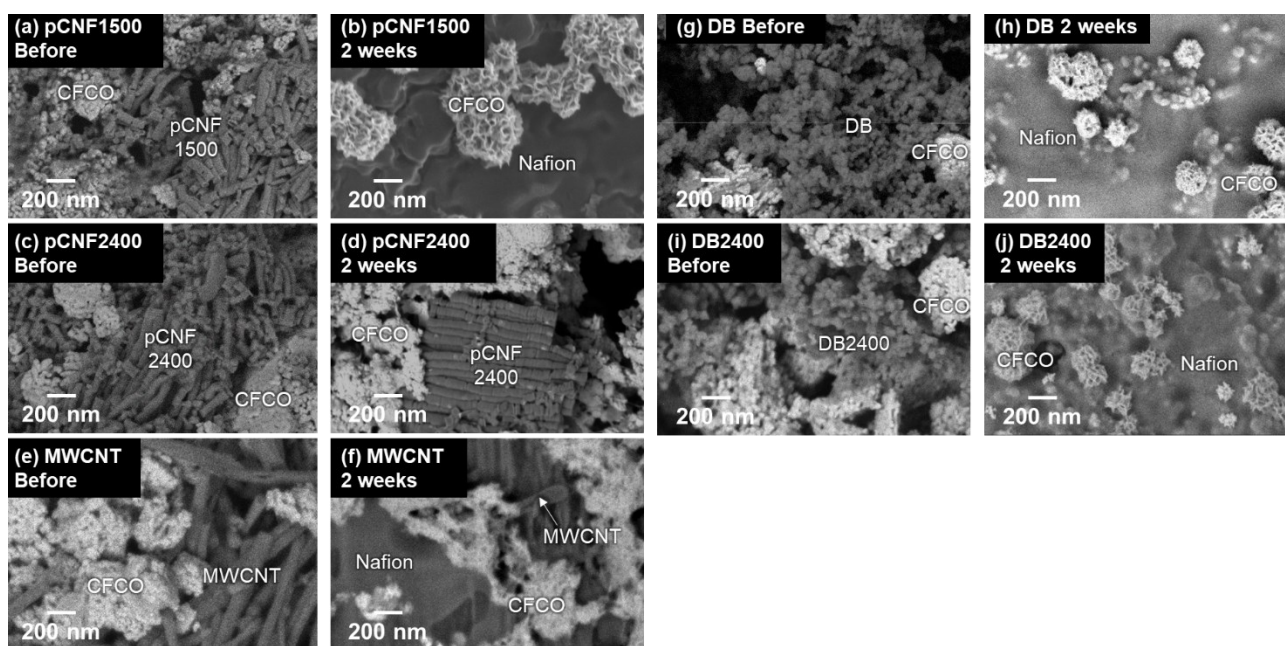


Fig. 4-10 SEM-BSE images of carbon/CFCO electrodes before and after the durability test for 2 weeks.

Fig. 4-11 shows TEM images before and after the two-week durability test for MWCNT/CFCO. After the durability test, the MWCNT is partially corroded, with a reduced tube diameter. The TEM observations suggest that the oxidation proceeds locally and perpendicularly to the fiber axis of MWCNTs, with a pit-like morphology. In other words, the corrosion of MWCNTs occurs from the basal plane of carbon. The localized attack of graphitic carbon has been reported previously [24-26]. The local oxidation may be associated with the presence of some structural defects in the basal planes, as reported previously [26].

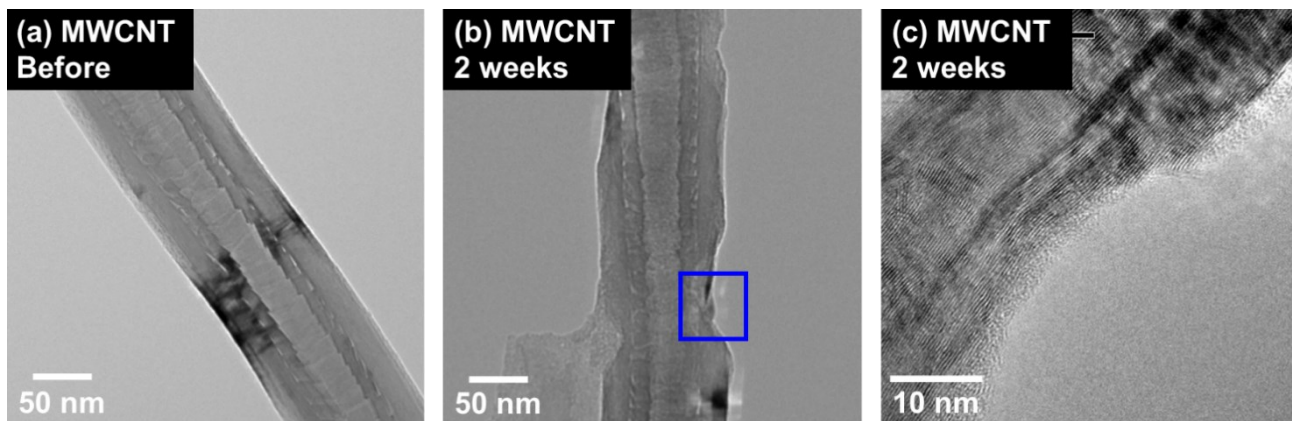


Fig. 4-11 High-resolution TEM images of MWCNT (a) before and (b, c) after the durability test.

4-3-7 TEM observation of pCNF after the durability tests

TEM images of pCNF2400 before and after the durability test (Fig. 4-12) reveal that the nanofiber diameters of pCNF2400 remained almost unchanged even after the durability test for one month. However, high-magnification images (Fig. 4-12e, f) reveal the change in the sidewall structure of pCNF2400. Before the durability test, the specimen is characterized by the presence of loops consisting of 3-5 graphene layers at the sidewalls of pCNF2400. After two weeks of polarization, those loops are entirely opened. Therefore, in the case of pCNF2400, this loop edge structure can be considered the priority site for corrosion. The similar diameter of pCNF2400 nanofibers after the durability test for two weeks and one month and the similar carbon edge structure at the sidewalls indicate that the oxidation of pCNF2400 at the exposed carbon edge planes is extremely slow, contributing to the high durability of pCNF2400 under OER conditions.

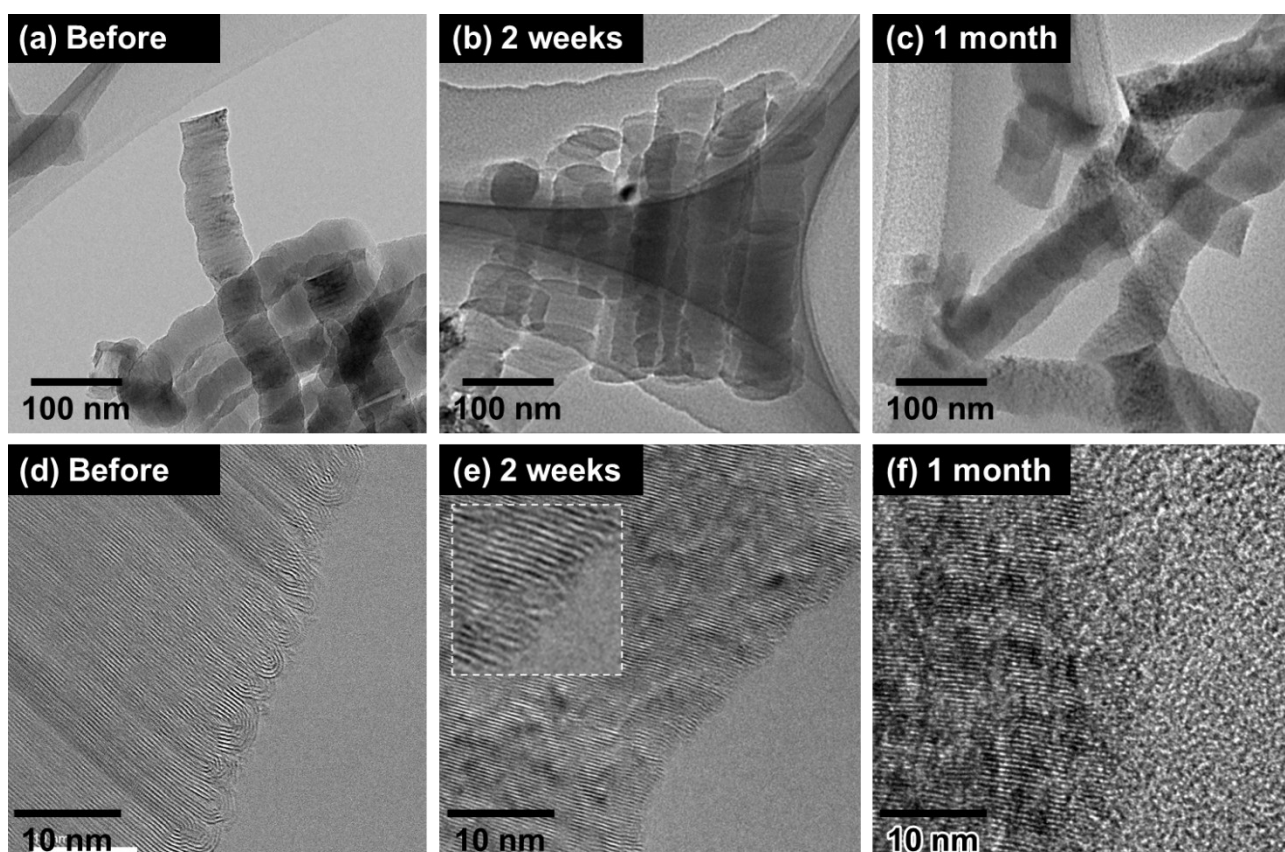


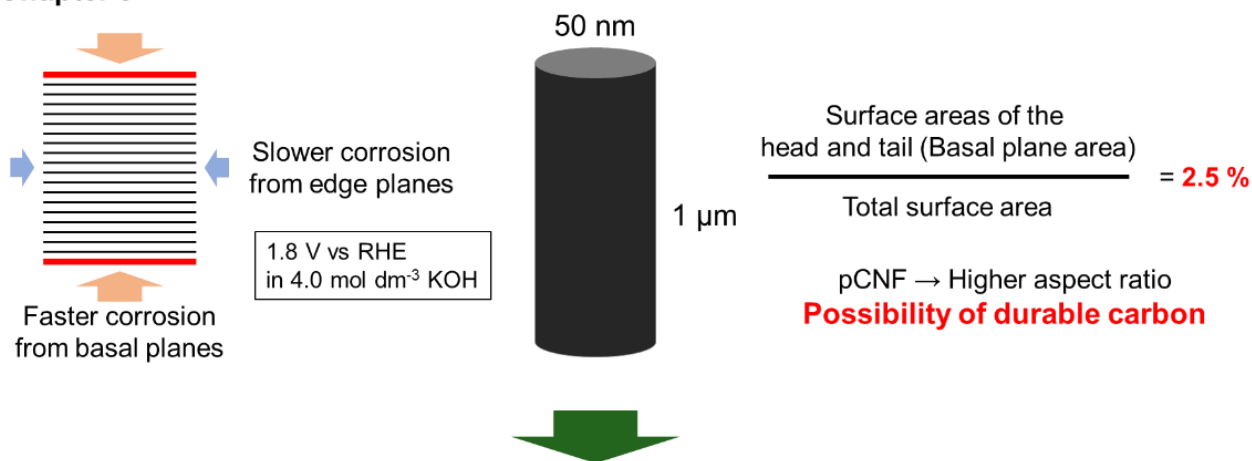
Fig. 4-12 TEM images of pCNF2400 (a, d) before and (b, c, e, f) after the durability tests of the pCNF2400/CFCO electrode for (b, e) 2 weeks and (c, f) 1 month.

4-3-8 Discussion

In Chapter 3, the high corrosion resistance of highly graphitized pCNFs was demonstrated at 1.8 V vs RHE in a KOH electrolyte due to the slow corrosion at the carbon edge plane. This result expects the sufficient durability of pCNF as the conductive support for OER electrodes. Hence, in this chapter, the durability and the conductive support properties of pCNF2400 mixed with CFCO that is highly active for OER were investigated. Based on the results obtained in this chapter, the carbon corrosion under OER in concentrated alkaline media with OER catalyst is discussed.

Firstly, the effect of the structural factor for carbon corrosion is briefly reviewed. In this chapter, the pCNF2400/CFCO electrode shows the highest durability. The diameter of pCNF2400 remained almost unchanged even after the durability test at 40 mA cm⁻² for one month. Because of the high OER activity of CFCO, the electrode potential during the durability test was ~1.8 V vs RHE, which was less noble than the potential used in Chapter 3. pCNFs have a structure in which the graphene layer is aligned perpendicular to the fiber axis of the nanofiber. In addition, pCNFs have a high-aspect-ratio macrostructure. Thus, only the head and tail of pCNFs consist of the basal plane, and mainly their surfaces consist of the edge plane. The basal plane and edge plane surface ratio are calculated as 1:40 (Fig. 4-13). As described in Chapter 3, the sidewall of pCNFs shows higher corrosion resistance due to the preferent hydroxyl group formation on the edge plane surface. This aspect ratio and preferent hydroxyl group formation expect the durability of pCNF2400. On the other hand, although the edge exposed structure and platelet structure, pCNF1500 shows inferior durability because of the lower graphitization degree. Thus, in addition to the platelet structure, the graphitization degree is an important parameter to obtain the excellent durability of carbon for the OER environment.

Chapter 3



Chapter 4

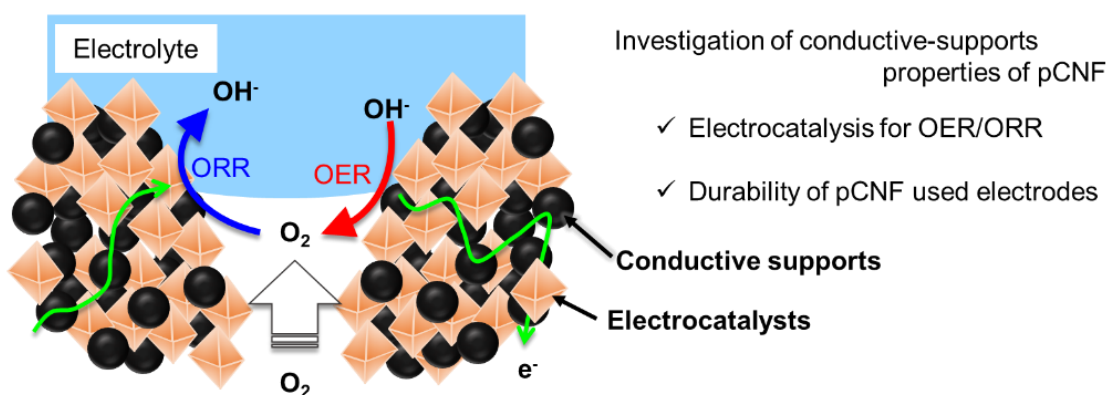


Fig. 4-13 Schematic illustration of pCNFs and the relationship of this chapter and Chapter 3.

According to the LSV curves obtained prior to the durability test, the electrode potential during the durability test is almost similar or lower level as Chapter 3, *i.e.*, between 1.7 V to 1.8 V vs RHE. Hence, the corrosion rate of the basal plane of pCNF2400 is expected to be the same or lower than 0.21 nm h⁻¹. This value expects that pCNF2400 should be disappeared 21 days in the case the length of pCNF2400 is 210 nm. However, pCNF2400 seems to remain even after a one-month durability test. For the edge plane direction, *i.e.*, the fiber diameter direction, the proceeds of carbon corrosion are suppressed by the hydroxyl group formation on their sidewall. In addition, the remain of pCNF2400 suggests corrosion suppression for the basal plane direction. It is often discussed that some electrocatalysts accelerate carbon corrosion under the energy device operation [27, 28]. However, this result suggests that Ca₂FeCoO₅ did not enhance carbon corrosion in the investigated condition. Even

with such softer corrosion conditions, carbon materials except pCNF2400 show oxidative consumption during the durability test. Therefore, pCNF with a higher graphitization degree is most likely to show the corrosion tolerance under OER in 4.0 mol dm⁻³ KOH aq.

Secondary, the ORR current behavior is discussed. As shown in Fig. 4-9, the ORR current of pCNF2400/CFCO electrodes increased after the durability test, while those of DB/CFCO electrodes decreased. It is generally accepted that the ORR electrocatalytic activity of carbon and metal oxide hybrids is brought by the synergistic effect of carbon and metal oxide [1]. Therefore, the degradation of ORR for DB/CFCO electrode is probably related to the carbon disappearance due to the carbon corrosion. In Chapter 3, it is discussed the hydroxyl group formation on the edge plane during the anodic oxidation of pCNF under OER in concentrated alkaline media. Such hydroxyl group shows the improved ORR activity in alkaline media than the bare carbon surface [29]. In addition, density functional theory (DFT) calculations have shown that the edge sites of graphene have a strong ability for O₂ adsorption [23]. Thus, the loop structure disappearance and following hydroxyl group formation during the anodic oxidation of pCNF enable improvement of the ORR activity of pCNFs. After the durability test, this structural reconstruction possibly enhanced the ORR current of the pCNF2400/CFCO electrode.

4-4 Conclusions

In this chapter, the OER/ORR activity and OER durability of various carbon nanomaterials combined with a state-of-the-art brownmillerite CFCO electrocatalyst for OER/ORR were studied in a 4 mol dm⁻³ KOH electrolyte. Following findings were obtained.

(1) pCNF2400 works as a conductive support of CFCO for OER/ORR electrocatalysts. However, insufficient dispersion of pCNF2400 in the electrode results in increased overpotential at the high current region of OER. The agglomeration of pCNFs should be avoided to provide a sufficient conductive path to CFCO.

(2) The pCNF2400/CFCO electrode shows lower ORR activity compared with the carbon blacks/CFCO electrodes because of the poor co-catalysis effect of pCNF2400, which is associated with the almost absence of the exposed carbon edge sites. However, the ORR activity is improved during the durability test because of the oxidative removal of the looped carbon layers and subsequent carbon edge exposure.

(3) The CFCO electrode with pCNF2400 exhibits the highest durability in the OER durability test; no OER activity degradation occurs during the durability test for one month. SEM observations disclose the complete consumption of DB, DB2400, and pCNF1500 within two weeks, whereas pCNF2400 remains unchanged even after one month. The anodic corrosion of carbon results in the loss of the conducting path, causing the reduction of OER activity in carbon/CFCO electrodes. After the durability test, the carbon edge sites exposure on the sidewall were observed in pCNF2400; thus, as suggested in Chapter 3, corrosion resistance of pCNF2400 mainly originated from the slow kinetics carbon corrosion at the carbon edge sites.

4-5 References

1. Y. Zhu, W. Zhou, Z. Shao, “Perovskite/Carbon Composites: Applications in Oxygen Electrocatalysis”, *Small*, **13(12)**, 1603793 (2017).
2. C. Alegre, E. Modica, A.S. Aricò, V. Baglio, “Bifunctional oxygen electrode based on a perovskite/carbon composite for electrochemical devices”, *J. Electroanal. Chem.*, **808(1)**, 412-419 (2018).
3. Y. Liang, H. Wang, P. Diao, W. Chang, G. Hong, Y. Li, M. Gong, L. Xie, J. Zhou, J. Wang, T. Regier, F. Wei, H. Dai, “Oxygen Reduction Electrocatalyst Based on Strongly Coupled Cobalt Oxide Nanocrystals and Carbon Nanotubes”, *J. Am. Chem. Soc.*, **134**, 15849 (2012).
4. C. Alegre, E. Modica, C.L. Vecchio, D. Sebastián, M.J Lázaro, A.S. Aricò, V. Baglio, “Carbon Nanofibers as Advanced Pd Catalyst Supports for the Air Electrode of Alkaline Metal–Air Batteries”, *ChemPlusChem*, **80(9)**, 1384-1388 (2015).
5. Y. Sugawara, T. Hihara, G.M. Anilkumar, K. Kamata, T. Yamaguchi, “Metal oxide electrocatalyst support for carbon-free durable electrodes with excellent corrosion resistance at high potential conditions”, *Sustainable Energy & Fuels*, **5**, 1374-1378 (2021).
6. E. Tsuji, T. Yamasaki, Y. Aoki, S. G. Park, K. Shimizu, H. Habazaki, “Highly durable platelet carbon nanofiber-supported platinum catalysts for the oxygen reduction reaction”, *Carbon*, **87**, 1-9 (2015).
7. T. Tamaki, H. Wang, N. Oka, I. Honma, S.H. Yoon, T. Yamaguchi, “Correlation between the carbon structures and their tolerance to carbon corrosion as catalyst supports for polymer electrolyte fuel cells”, *Int. J. Hydrogen Energy*, **43(12)**, 6406-6412 (2018).
8. S.W. Lee, S.R. Choi, J. Jang, G.G. Park, S.H. Yu, J.Y. Park, “Tolerance to carbon corrosion of various carbon structures as catalyst supports for polymer electrolyte membrane fuel cells”, *J. Mater. Chem. A*, **7**, 25056-25065 (2019).
9. E. Tsuji, T. Motohashi, H. Noda, D. Kowalski, Y. Aoki, H. Tanida, J. Nikura, Y. Koyama, M. Mori, H. Arai, T. Ioroi, N. Fujiwara, Y. Uchimoto, Z. Ogumi, H. Habazaki, “Brownmillerite-type $\text{Ca}_2\text{FeCoO}_5$ as a Practicable Oxygen Evolution Reaction Catalyst”, *ChemSusChem*, **10(14)**, 2864-2868 (2017).
10. D. Kowalski, H. Kiuchi, T. Motohashi, Y. Aoki, H. Habazaki, “Activation of Catalytically Active Edge-Sharing Domains in $\text{Ca}_2\text{FeCoO}_5$ for Oxygen Evolution Reaction in Highly Alkaline Media”, *ACS Appl. Mater. Interfaces*, **11**, 28823-28829 (2019).
11. Y. Sato, Y. Aoki, K. Takase, H. Kiuchi, D. Kowalski, H. Habazaki, “Highly Durable OER Catalyst: Amorphous Oxyhydroxide Derived from Brownmillerite-type $\text{Ca}_2\text{FeCoO}_5$ ”, *ACS Appl. Energy Mater.*, **3**, 5269-5276 (2020).
12. J. Suntivich, H.A. Gasteiger, N. Yabuuchi, Y.S. Horn, “Electrocatalytic Measurement Methodology of Oxide Catalysts Using a Thin-Film Rotating Disk Electrode”, *J. Electrochem. Soc.*, **157**, B1263-B1268 (2010).
13. T. Motohashi, Y. Hirano, Y. Masubuchi, K. Oshima, T. Setoyama, S. Kikkawa, “Oxygen Storage Capability of Brownmillerite-type $\text{Ca}_2\text{AlMnO}_{5+\delta}$ and Its Application to Oxygen Enrichment”, *Chem. Mater.*, **25**, 372–377 (2013).
14. V. Cascos, R. Martínez-Coronado, J.A. Alonso, M.T. Fernández-Díaz, “Structural and electrical characterization of the Co-doped $\text{Ca}_2\text{Fe}_2\text{O}_5$ brownmillerite: Evaluation as SOFC -cathode materials”, *Int. J. Hydrogen Energy*, **40**, 5456-5468 (2015).
15. Y. Meng, W. Song, H. Huang, Z. Ren, S. Y. Chen, S. L. Sui, “Structure–Property Relationship of Bifunctional MnO_2

- Nanostructures: Highly Efficient, Ultra-Stable Electrochemical Water Oxidation and Oxygen Reduction Reaction Catalysts Identified in Alkaline Media”, *J. Am. Chem. Soc.*, **136**, 11452-11464 (2014).
16. H. Antoni, D. M. Morales, J. Bitzer, Q. Fu, Y. T. Chen, J. Masa, W. Kleist, W. Schuhmann, M. Muhler, “Enhancing the water splitting performance of cryptomelane-type α -(K) MnO_2 ”, *J. Catal.*, **374**, 335-344 (2019).
 17. S. Thundiyil, S. Kurungot, R.N. Devi, “Bifunctional Oxygen Reduction and Evolution Activity in Brownmillerites $\text{Ca}_2\text{Fe}_{(1-x)}\text{Co}_x\text{O}_5$ ”, *ACS Omega*, **4**, 31–38 (2019).
 18. L. Tao, Q. Wang, S. Dou, Z. Ma, J. Huo, S. Wang, L. Dai, “Edge-rich and dopant-free graphene as a highly efficient metal-free electrocatalyst for the oxygen reduction reaction”, *Chem. Commun.*, **52**, 2764–2767 (2016).
 19. Y.J. Min, S.J. Oh, M.S. Kim, J.H. Choi, S. Eom, “Effect of carbon properties on the electrochemical performance of carbon-based air electrodes for rechargeable zinc–air batteries”, *J. Appl. Electrochem.*, **48**, 405-413 (2018).
 20. P. J. Kulesza, J. K. Zak, I. A. Rutkowska, B. Dembinska, S. Zoladek, K. Miecznikowski, E. Negro, V. D. Noto, P. Zelenay, “Elucidation of role of graphene in catalytic designs for electroreduction of oxygen”, *Current Opinion in Electrochemistry*, **9**, 257-264 (2018).
 21. X. Y. Yan, X. L. Tong, Y. F. Zhang, X. D. Han, Y. Y. Wang, G. Q. Jin, Y. Qina, X. Y. Guo, “Cuprous oxide nanoparticles dispersed on reduced graphene oxide as an efficient electrocatalyst for oxygen reduction reaction”, *Chem. Commun.*, **48**, 1892-1894 (2012).
 22. H. Tang, H. Yin, J. Wang, N. Yang, D. Wang, Z. Tang, “Molecular Architecture of Cobalt Porphyrin Multilayers on Reduced Graphene Oxide Sheets for High-Performance Oxygen Reduction Reaction”, *Angew. Chem. Int. Ed.*, **52**, 5585-5589 (2013).
 23. M. Acik, Y.J. Chabal, “Nature of Graphene Edges: A Review”, *J. Appl. Phys.*, **50**, 070101 (2011).
 24. E. L. Evans, R. J. M. Griffiths, J. M. Thomas, “Kinetics of Single-Layer Graphite Oxidation: Evaluation by Electron Microscopy”, *Science*, **171**, 174-175 (1971).
 25. A. Tracz, G. Wegner, J. P. Rabe, “Kinetics of surface roughening via pit growth during the oxidation of the basal plane of graphite. 1. Experiments”, *Langmuir*, **9**, 3033-3038 (1993).
 26. Y. Yi, J. Tornow, E. Willinger, M. G. Willinger, C. Ranjan, R. Schlögl, “Electrochemical Degradation of Multiwall Carbon Nanotubes at High Anodic Potential for Oxygen Evolution in Acidic Media”, *ChemElectroChem*, **2**, 1929-1937 (2015).
 27. K. Miyazaki, M. Nose, T. Kinumoto, T. Abe, T. Fukutsuka, Z. Ogumi, “Influences of metal oxides on carbon corrosion under imposed electrochemical potential conditions”, *Carbon*, **50(4)**, 1644-1649 (2012).
 28. N. Staud, P. N. Ross, “The Corrosion of Carbon Black Anodes in Alkaline Electrolyte: II. Acetylene Black and the Effect of Oxygen Evolution Catalysts on Corrosion”, *J. Electrochem. Soc.*, **133**, 1079-1084 (1986).
 29. A. Dumitru, M. Mamlouk, K. Scott, “Effect of different chemical modification of carbon nanotubes for the oxygen reduction reaction in alkaline media”, *Electrochimica Acta*, **125**, 428-438 (2014).

Chapter 5
Air electrode
performance of gas-
diffusion electrodes
using pCNFs

Chapter 5 Air electrode performance of gas-diffusion electrodes using pCNFs

5-1 Introduction

As previous chapters described, highly graphitized pCNFs are promising conductive supports for ZAB air electrodes because of their high durability under OER in alkaline media. In contrast, conventional carbon materials, such as carbon blacks, were consumed within a week. The pCNFs exhibit excellent stability in OER environments, but when physically mixed with an oxide electrocatalyst, the enhancement of ORR activity of the oxide by the carbon is limited. This limitation is owing to the poor co-catalytic properties of pCNFs. For ORR in alkaline media, carbon co-catalysis for ORR is an essential factor, and carbon edge and defect sites are commonly regarded as catalytic sites for ORR [1, 2]. In the previous chapter, the high durability of the pCNF24000/CFCO electrode was demonstrated, but its ORR activity was not high enough for the rechargeable metal-air batteries. Direct loading of electrocatalyst nanoparticles onto the carbon surface is an effective strategy in enhancing ORR activities by modifying the electronic state of the electrocatalyst [1,3-6]. Moreover, it is often discussed that the interface between carbon material and metal oxide catalyst provides reasonable electrocatalytic centers for OER and ORR [1, 7, 8]. Therefore, it is supposed that the construction of the hybrids of oxide electrocatalyst and pCNF can improve the ORR electrocatalysis of pCNF.

This chapter tried to prepare a hybrid of electroactive oxide nanoparticles uniformly dispersed on highly graphitized pCNFs for highly active bifunctional electrodes for ORR and OER in an alkaline environment (Fig. 5-1). Spinel-type MnCo_2O_4 (MCO) nanoparticles, which are promising as a catalyst for OER and ORR [4], were supported on the pCNF via solvothermal synthesis, and their ORR and OER activities were examined by rotation disk electrodes (RDE). Additionally, pCNF/MCO hybrids were used to evaluate the durability of pCNFs under a more realistic ZAB operation environment. A half-cell using a gas-diffusion electrode (GDE) was used to evaluate the air electrode performance [9].

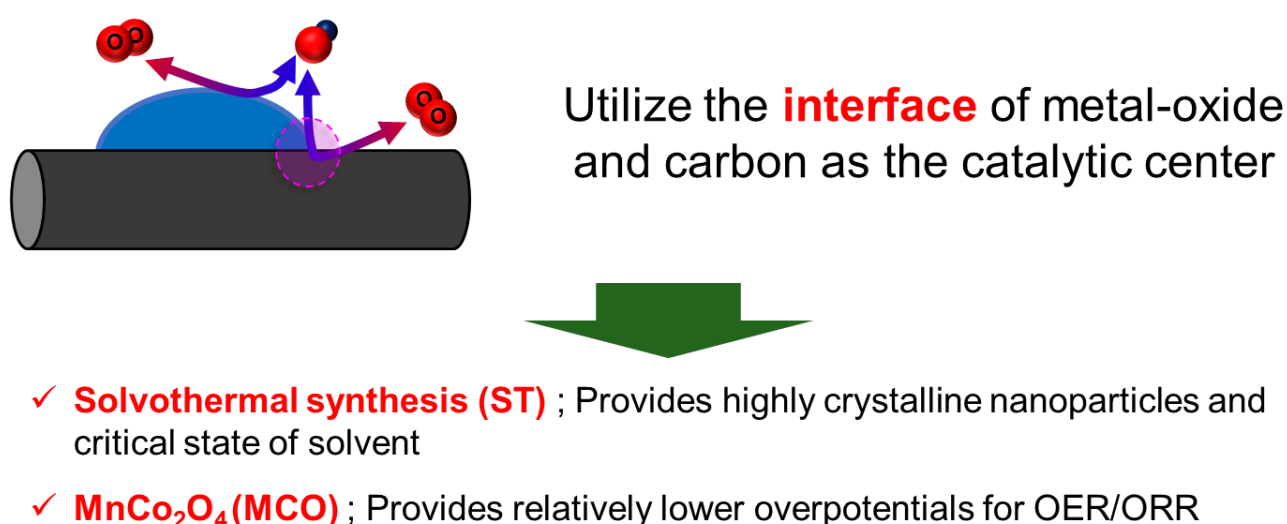


Fig. 5-1 Concept of this chapter to improve the OER/ORR activity of pCNF based electrodes.

5-2 Experimental

5-2-1 Hybridization of metal-oxides and pCNF via solvothermal synthesis

pCNF3000 (Commercially available pCNF; Sigma-Aldrich, 799017-500MG) was used in this chapter. DB (Denka, Denka Black Powder) was also used for comparison. Each carbon support was treated in a concentrated HNO_3 aqueous solution at 110°C for the surface activation [4]. Although this nitric acid treatment improved the adhesion of the oxide nanoparticles, the morphology of the DB and pCNF3000 remained unchanged, as shown in Fig. 5-2. MCO nanoparticles were loaded on each carbon

support by a solvothermal synthesis method based on the previous report [3]. pCNF3000 or DB (100 mg) was dispersed in ethanol (50 mL) ultrasonically for 30 min. After the addition of an aqueous solution (2.0 mL) containing 0.2 mol dm^{-3} manganese(II) acetate and 0.4 mol dm^{-3} cobalt(II) acetate, the amount of which corresponded to desired MCO content of 50 wt% in products, the mixture was stirred for 45 min at room temperature. Then, 0.75 mL of ultrapure water and 1.25 mL of 30% aqueous ammonia solution were added. After mixing all precursors, the mixture was refluxed at 80°C with stirring for 20 h. The mixture was transferred to a 100 mL autoclave, and the container was heated at 150°C for 3 h. The products were filtered and dried in a vacuum at 80°C for 1 h. Carbon-free MCO nanoparticles were also prepared through the same procedure without adding carbon materials. Hereafter, MCO-loaded DB and pCNF3000 hybrids synthesized by the solvothermal method are designated as DB/MCO and pCNF/MCO, respectively.

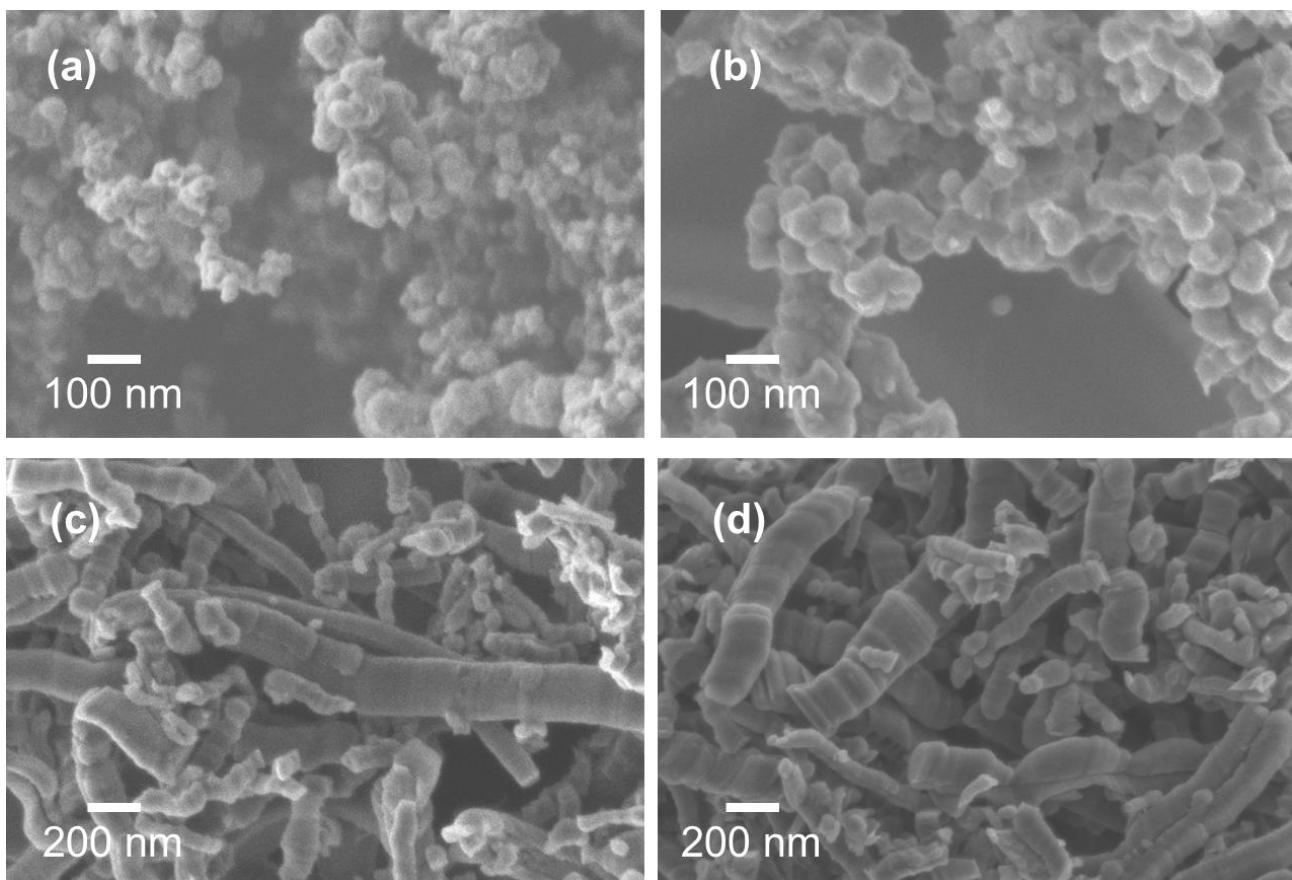


Fig. 5-2 SEM images of (a, c) before and (b, d) after the acid treatment; (a, b) DB and (c, d) pCNF3000.

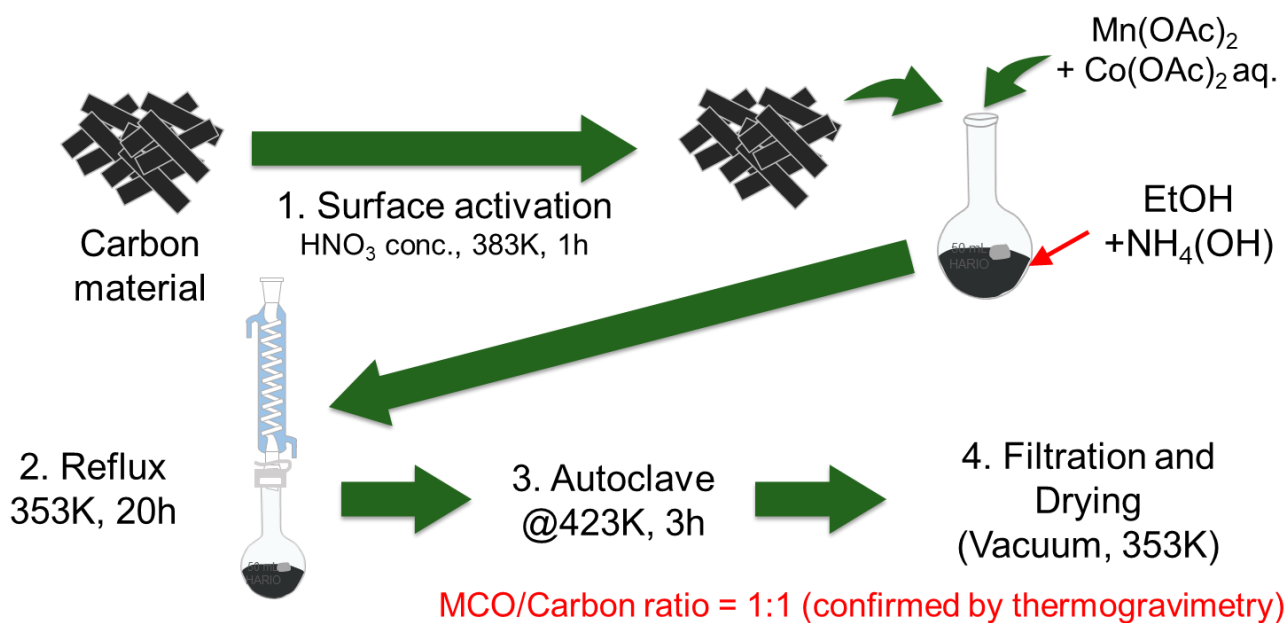


Fig. 5-3 Scheme of the solvothermal treatment to load MCO nanoparticles on the carbon materials.

5-2-2 Electrocatalytic activity evaluation by the rotating ring-disk electrode system

The electrocatalytic activity was evaluated by the rotating ring-disk electrode (RRDE; Pine Instrument Co. Ltd.) system using the catalyst-loaded glassy carbon disk electrodes ($1.0 \text{ mg}_{\text{cat}} \text{ cm}^{-2}$) and a Pt ring electrode. For the preparation of catalyst inks, 50 mg of carbon/MCO hybrids, pristine carbon, or physical mixtures of the pristine MCO and carbon materials with a 1:1 mass ratio were dispersed ultrasonically in a mixture of 0.2 mL of 5 wt% Na⁺-exchanged Nafion solution and 4.8 mL of ethanol. Nafion was added as a binder and neutralized before dispersion to prevent MCO from undergoing acidic dissolution due to the lower pH of the Nafion binder [10]. Physically mixed samples of carbon materials and MCO were designated as DB+MCO and pCNF+MCO. The electrochemical measurements were carried out in a four-electrode system using a potentiostat (Hokuto Denko, HZ-7000) and an RRDE system. A carbon sheet and Hg/HgO/4 mol dm⁻³ KOH were used as counter and reference electrodes, respectively. The Pt ring electrode was chosen to detect a peroxide byproduct.

Cyclic voltammetry (CV) was performed to investigate the electrochemical capacitance and redox reaction of the prepared electrode by applying 30 potential cycles between 1.1 and 0.4 V vs. RHE with a sweep rate of 50 mV s⁻¹, prior to electrocatalysis evaluation. The 30th cycle of the CV curve was adopted as the result. The electrode capacitances C were calculated from this cyclic voltammogram area by using the following equation [11]:

$$C = \frac{2 \int IdE}{v\Delta E} \quad (5-1)$$

where I is the current, E is the potential, and v is the potential sweep rate. Linear sweep voltammetry (LSV) at 1600 rpm with a potential sweep rate of 1 mV s⁻¹ was conducted at room temperature in a 4 mol dm⁻³ KOH aqueous solution with O₂ saturation. The potential was converted from the Hg/HgO/4 mol dm⁻³ KOH reference scale to the RHE using the following equation:

$$E \text{ vs RHE} = E \text{ vs Hg/HgO/4 mol dm}^{-3} \text{ KOH} + 0.9260 \quad (5-2) [13]$$

The electron transfer number during ORR was evaluated by the RRDE method under the ring electrode potential of 1.4 V vs RHE [12], and estimated by the following equation [12];

$$n = 4 \left(\frac{I_{disk}}{I_{disk} + \frac{I_{ring}}{\alpha}} \right) \quad (5-3)$$

where, I_{disk} and I_{ring} are the disk current and ring current, respectively. The collection efficiency α was experimentally verified with the Fe(II)(CN)₆⁴⁻/Fe(III)(CN)₆³⁻ redox couple in a potentiostatic experiment and was determined to be 0.178.

5-2-3 GDE study

The long-term durability of carbon/MCO hybrids under the ZAB operation environment was evaluated using the gas-diffusion electrode (GDE), which consisted of the hydrophobic gas-diffusion layer (GDL), carbon/MCO catalyst layer, and Ni meshes current collector (Niraco). The GDE experiments were conducted based on the previous reports [13, 14]. GDL was prepared by rolling a mixture of 70 wt% carbon black (TOKAI CARBON, #3855) and 30 wt% PTFE, and the resultant

sheets were around 0.3 mm thin. Catalyst layers on the GDL were prepared by applying the catalyst ink, which was a mixture of carbon/MCO hybrids, Triton X-100 (Kishida Chemical Co. Ltd.), and 6.0 wt% PTFE dispersion (D-210C, Daikin Industries, Ltd.). The ratio of catalyst to PTFE was controlled to be 83/17 in wt% in the resultant catalyst layer. The catalyst ink was assembled with the GDL with the loading amount of 20 mg cm^{-2} and then heated at 334°C for 1 h under N_2 flow, followed by pressing on to the nickel mesh (Niraco, 100 mesh) current collector.

The electrochemical cell for the GDE test consisted of a Pt wire, a Hg/HgO electrode, and an 8.0 mol dm^{-3} KOH aqueous solution as a counter electrode, a reference electrode, and an electrolyte solution, respectively. The charge-discharge tests were conducted at 40°C in the incubator (Espec, SU-221). The air electrode was exposed to ambient air without forced flow. Charge and discharge curves were obtained by monitoring the potential of the air electrode after applying each current density for 3 min using a galvanostat (Biologic, VSP). A charge-discharge cycle test was conducted by applying 20 mA cm^{-2} for 1 h for each step. The experimental setup of GDE is shown in Fig. 5-4.

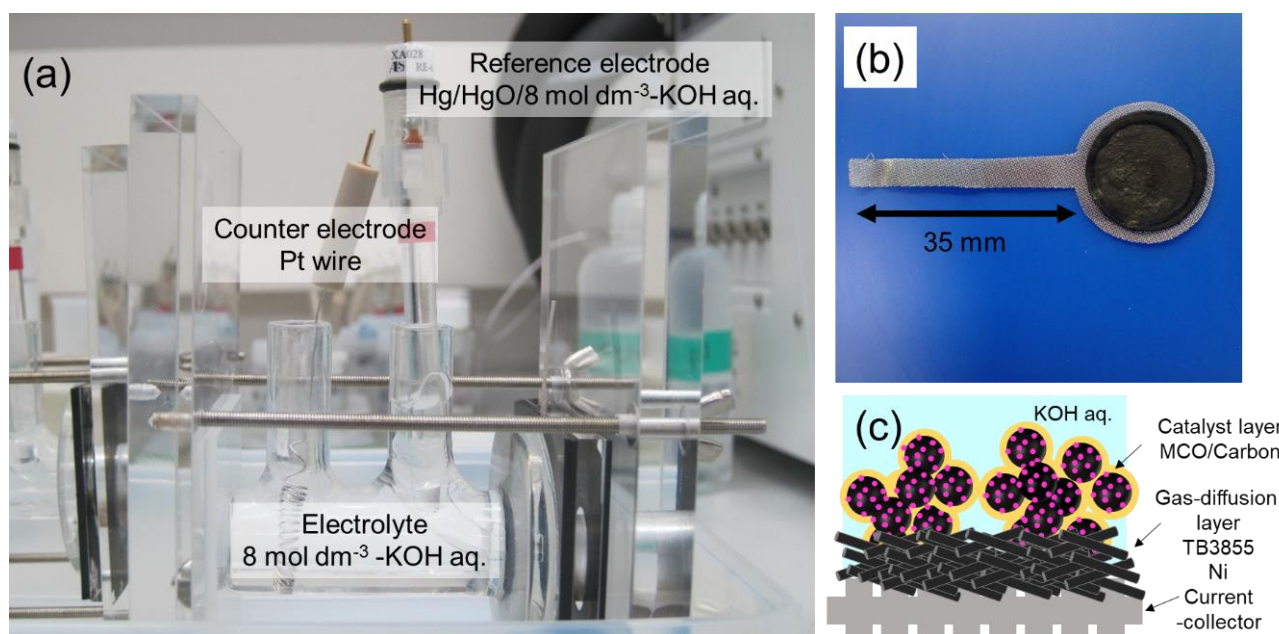


Fig. 5-4 Electrochemical cell used in this study; (a) overall of the electrochemical cell setup, (b) gas-diffusion electrode used in this study, and (c) schematic image of the gas-diffusion electrode.

5-2-4 Characterization

The field-emission scanning electron microscope (SEM; ZEISS, Sigma-500) operated at 1.5 kV, and transmission electron microscopes (TEM; JEOL, JEM-2000FX, and JEM-2010F) operated at 200 kV were used to evaluate the morphology and structure. The chemical composition was estimated by the energy-dispersive X-ray spectroscopy (EDS, Bruker Nano GmbH, XFlash Detector 630) facilities attached to the SEM. The BET surface areas of the carbon materials, pristine MCO, and carbon/MCO hybrids were determined by N₂ gas adsorption isotherm measurements (for carbon materials; Bel Japan, Belsorp-mini instrument and for MCO and its hybrid; Yuasa Ionics, Autosorb 6AG) at -196°C. The loading amounts of MCO on the carbon materials were evaluated by a thermogravimetric analyzer system (TGA; Netzsch, STA 2500 Regulus) in the air at a heating rate of 10 K min⁻¹. The phase purity and the graphitization degree of the carbon materials were examined by Raman spectroscopy (Horiba Scientific, XploRA) using a 532 nm laser beam and X-ray powder diffraction (XRD; Rigaku, Ultima IV) using Cu K α radiation ($\lambda = 0.15418$ nm). The crystallite size was estimated from XRD patterns using the following Scherrer equation:

$$L_{c,hkl} = \frac{K\lambda}{\beta \cos\theta} \quad (5-3) [15]$$

where λ , K, and β are the X-ray wavelength (0.15418 nm), the shape factor, and FWHM of the reflection used, respectively. The K value was 0.9 [15]. A cross-section polisher (JEOL, SM-09010) was used to prepare cross-sections of the GDE. A Kyowa Interface Science DM-CE1 optical contact meter was used to measure the static contact angle of a Milli-Q water droplet of 2 μ L.

5-3 Results and discussion

5-3-1 Characterization of carbon/metal oxide hybrids

Fig. 5-5a shows the Raman spectra of carbon/MCO hybrid and carbon-free MCO samples. All samples showed peaks at around 473 and 609 cm⁻¹, assigned to vibration of E_g mode and F_{2g} mode

of MCO, respectively [16, 17]. In addition to peaks derived from MCO, the carbon/MCO hybrid samples showed peaks at around 1320 and 1580 cm^{-1} , corresponding to the carbon D and G bands, respectively. It is noted that the carbon/MCO hybrid samples showed similar relative intensities of the peaks for G and D bands to those of pristine carbon materials. This result suggests that graphitization degrees of carbon materials after the solvothermal synthesis were not changed. Further investigation for the crystalline of MCO was carried out by XRD. Fig. 5-5b shows XRD patterns of carbon/MCO hybrids and carbon-free MCO samples. The carbon-free MCO sample showed the XRD pattern of spinel-type MnCo_2O_4 , which is similar to previous reports [3, 16, 17]. The carbon/MCO hybrids also showed the pattern of MCO in addition to diffraction peaks around 25 and 40°, assignable to 002 and 10 reflections of carbon, respectively. Nanoparticle crystalline sizes were estimated by using the MCO 311 diffraction peak (Table 5-1). The crystalline sizes of each sample are almost the same, regardless of the presence and type of carbon.

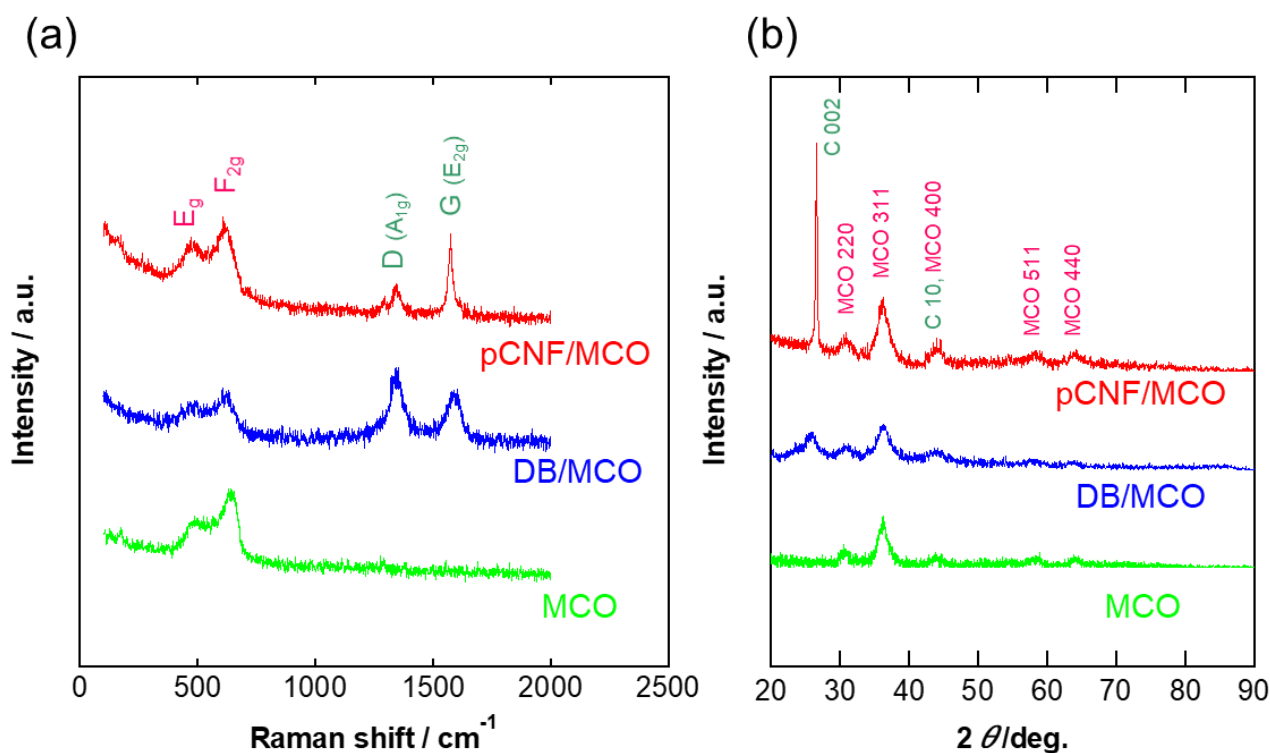


Fig. 5-5 (a) Raman spectra and (b) XRD patterns of carbon/MCO hybrids and pristine MCO nanoparticles.

Table 5-1 Physicochemical properties of MCO nanoparticles with and without carbon

	L_{311} / nm	MCO content / wt%	BET surface area / $\text{m}^2 \text{g}^{-1}$	Calculated surface area / $\text{m}^2 \text{g}^{-1}$	Mn/Co atomic ratio from EDS
pCNF/MCO	4.56	49.5	118	113	0.46
DB/MCO	3.99	45.3	115	118	0.48
MCO	4.76	100	189		0.48

The loading amount of MCO nanoparticles and oxidation resistance of these hybrids were examined by the TGA analysis. Fig. 5-6 shows the TG curves of each carbon/MCO hybrid measured under airflow. For comparison, the TG curve of bare DB is also shown. Each carbon/MCO hybrid shows mass reduction to around 50 wt% above 550°C, in agreement with the target content of metal resources applied for synthesis. All TG curves show the significant weight losses, which started at around 330, 400, and 640°C for DB/MCO, pCNF/MCO, and DB, respectively. These weight losses are derived from the thermal oxidation of carbon materials. In other words, the thermal oxidation starts at a lower temperature after the MCO loading via solvothermal synthesis. The thermal oxidation of carbon materials is typically catalyzed by the metal oxides, including Mn oxides, and this catalysis mechanism is called the Mars and Van Krevelen (MVK) mechanism [18-20]. Thus, MCO loading is a harsher oxidation condition than before loading, and the oxidation temperatures of carbon/MCO hybrids were lower than the pristine carbon. Additionally, the weight loss of pCNF/MCO is slower than that of DB/MCO, indicating the higher oxidation resistance of pCNF3000 compared with DB also in the air at elevated temperatures. The pCNF3000 has the following two structural properties related to oxidation resistance; (1) few-numbers sp^3 carbon, which is the oxidation priority species [21] due to the platelet structure, and (2) well-graphitized structure, which gives the improved chemical stability [22]. It is often discussed that the thermal oxidation resistance is related to the durability of the electrode materials [21, 22]. Thus, this oxidation tendency expects the tolerance of pCNF/MCO under the electrochemical oxidation condition.

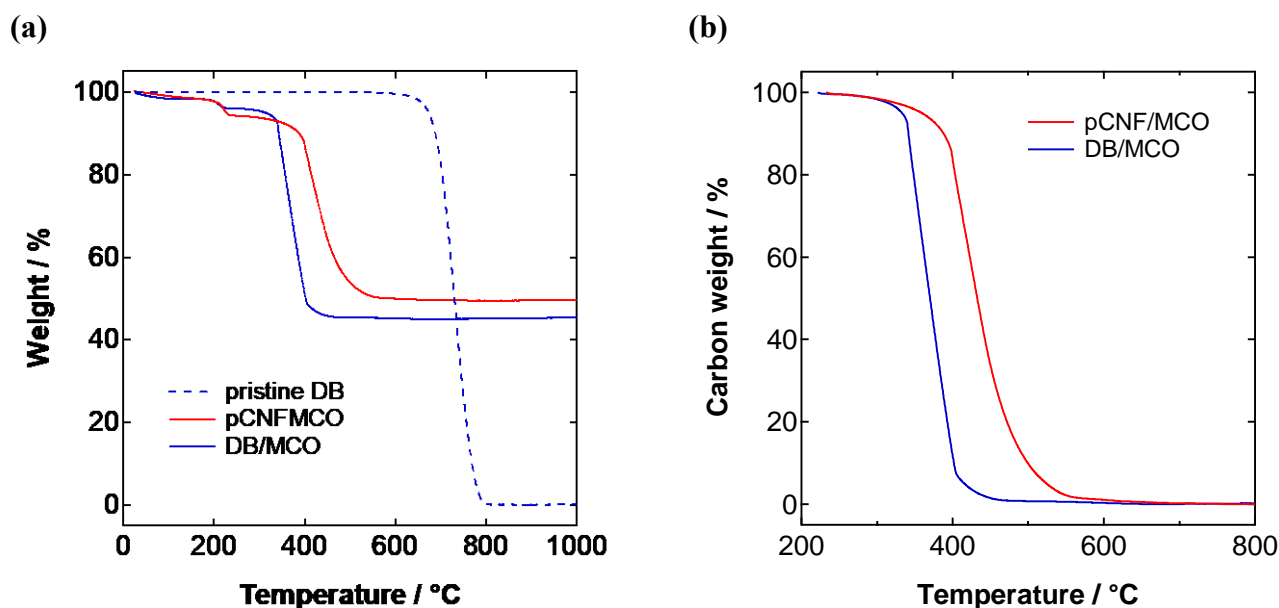


Fig. 5-6 (a) TGA curves of the three materials in the air and (b) the carbon weight loss calculated from Fig. 5-6(a). All measurements are conducted with the temperature elevation speed of 10 K min⁻¹.

The BET surface areas of the carbon/MCO hybrid and MCO were determined from the N₂ gas adsorption isotherm measurements. The results are summarized in Table 5-1. Both carbon/MCO hybrids showed almost identical BET surface area, similar to the physically mixed samples (pCNF+MCO: 113 m²g⁻¹, DB+MCO: 118 m²g⁻¹). The results suggest that the size of MCO and carbon materials for the carbon/MCO hybrids were similar to that for the respective pristine ones.

The distribution of MCO nanoparticles on the carbon materials was evaluated from SEM and TEM observations (Fig. 5-7). Fig. 5-7a and 6e show the scanning electron micrographs of pCNF/MCO and DB/MCO, respectively. The MCO nanoparticles uniformly wrap each carbon material after the solvothermal synthesis. Fig. 5-7 b-c and f-g show transmission electron micrographs of the carbon/MCO hybrids. MCO nanoparticles with an average size around 5 nm were uniformly deposited on both carbon materials, as illustrated in Fig. 5-7d and h. High-resolution TEM observations (Fig. 5-7c and g) reveal the formation of well-crystallized MCO nanoparticles on the carbon surfaces. The EDS analysis confirmed the Mn/Co ratio of 1/2 in both the hybrids (Table 5-1). Even after the

solvothermal synthesis, concentric loops remain at the sidewall of pCNF3000, on which MCO nanoparticles are supported. Yamada *et al.* reported that exposed carbon edge planes were the preferred nucleation sites of oxide nanoparticles, and Co_3O_4 nanoparticles were uniformly dispersed on pCNF1100 that had exposed carbon edge planes at the sidewall [11]. They also found the difficulty of uniform dispersion of Co_3O_4 nanoparticles on multiwalled carbon nanotubes by a conventional supporting method. However, this thesis study demonstrates that solvothermal synthesis enables to obtain uniformly dispersed carbon/MCO hybrids even though the basal plane of carbon is exposed to the surface in pCNF and DB.

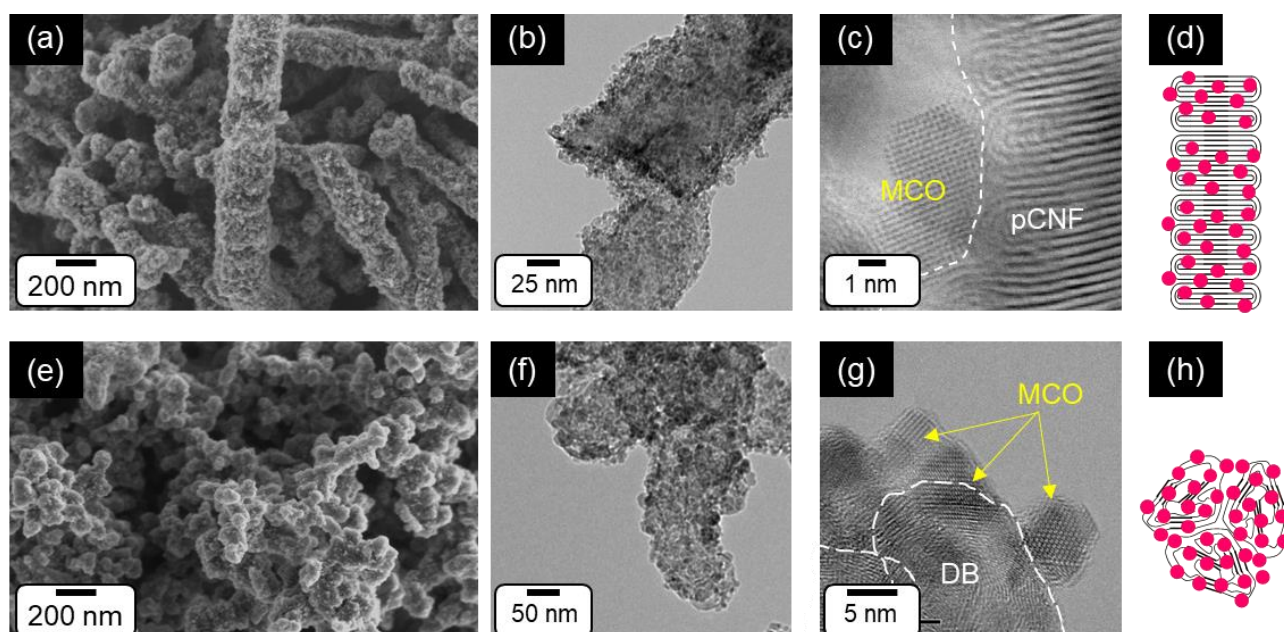


Fig. 5-7 SEM images, TEM images, and the schematic illustrations of (a-d) pCNF/MCO and (e-h) DB/MCO.

5-3-2 Improved OER/ORR activity by carbon/metal oxide hybridization

These carbon/MCO hybrids and MCO were served for the electrocatalysis evaluation. CV measurements were performed in Ar-saturated 4.0 mol dm^{-3} KOH electrolyte (Fig. 5-8). Both pristine pCNF and DB carbon materials, as well as physically mixed carbon and MCO (pCNF+MCO and DB+MCO), exhibit rather low CV areas. On the other hand, solvothermally prepared carbon/MCO hybrids show a relatively high CV area with a redox couple between 0.8-0.9 V vs RHE. This redox is

associated with the Co(II)/Co(III) redox in MCO [3]. The capacitance of each electrode was estimated from the cyclic voltammograms, and the results are summarized in Table 5-2. Despite almost identical BET surface area of the carbon/MCO hybrids and physically mixed electrodes, a significant difference of capacitance suggests that the MCO nanoparticles physically mixed with carbon may not be effectively used electrochemically compared to those in the carbon/MCO hybrids.

The ORR activities were examined from LSV measurements in O₂-saturated 4.0 mol dm⁻³ KOH solution (Fig. 5-9). The pristine pCNF3000 showed a lower onset potential, defined as the potential at -50 μA cm⁻² disk, than the pristine DB due to no exposed carbon edge structure [23]. Since MCO nanoparticles worked as the efficient ORR catalyst, physically mixed samples showed higher activities than the pristine carbon materials. The activities of the pCNF+MCO sample were much lower than those of DB+MCO. This activity difference possibly reflected the co-catalyst effects of the carbon materials for ORR. The carbon/MCO hybrids showed higher activities than the physically mixed samples, indicating that the higher dispersion of MCO nanoparticles on both carbon materials contributed to the enhancement of ORR activities. It is worth noting that the pCNF/MCO exhibited similar activities to the DB/MCO, unlike physically mixed samples. Many reports suggest that the interfaces between carbon materials and metal oxides play an important role for ORR electrocatalysis as the alternative of the carbon edge plane active sites [1, 7, 8]. As clarified by TEM observation, the carbon/MCO hybrids have a uniform and strong connection between the MCO and carbons. Therefore, ORR activities of the carbon/MCO hybrids were primarily affected by such interfaces. It is also confirmed that the carbon/MCO hybrids showed high electron transfer numbers ($n = 3.9$). The results indicate that the construction of the interfaces between pCNF and metal oxides could significantly enhance the ORR activities for the pCNF even without an exposed carbon edge structure. It was reported that the MCO hybrids with N-doped nanocarbon, such as N-doped carbon nanotubes and N-doped reduced graphene oxide, are best in terms of ORR activity [3]. Even without N doping in carbon,

the present study exhibits rather high ORR activity of pCNF/MCO hybrid. Thus, the fabricated hybrid in this study can be positioned as one of the promising electrocatalysts for ORR in highly concentrated alkaline media.

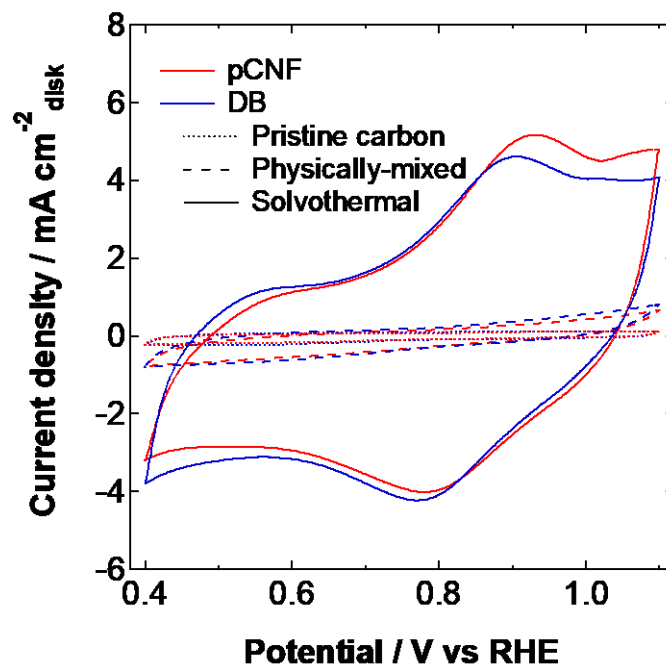


Fig. 5-8 Cyclic voltammograms in Ar saturated 4 mol dm⁻³ KOH recorded at 50 mV s⁻¹.

Table 5-2 Electrochemical properties of MCO electrodes.

	C / mF	$E_{\text{OER}} / \text{V vs RHE}$	$i_{1.65 \text{ V}} / \text{mA cm}^{-2}$	$E_{\text{ORR}} / \text{V vs RHE}$	$i_{0.6 \text{ V}} / \text{mA cm}^{-2}$
pCNF+MCO	2.4	1.56	26.8	0.89	-0.84
pCNF/MCO	21.3	1.52	72.1	0.95	-0.87
DB+MCO	2.8	1.55	36.5	0.92	-1.05
DB/MCO	21.2	1.53	73.4	0.95	-0.87

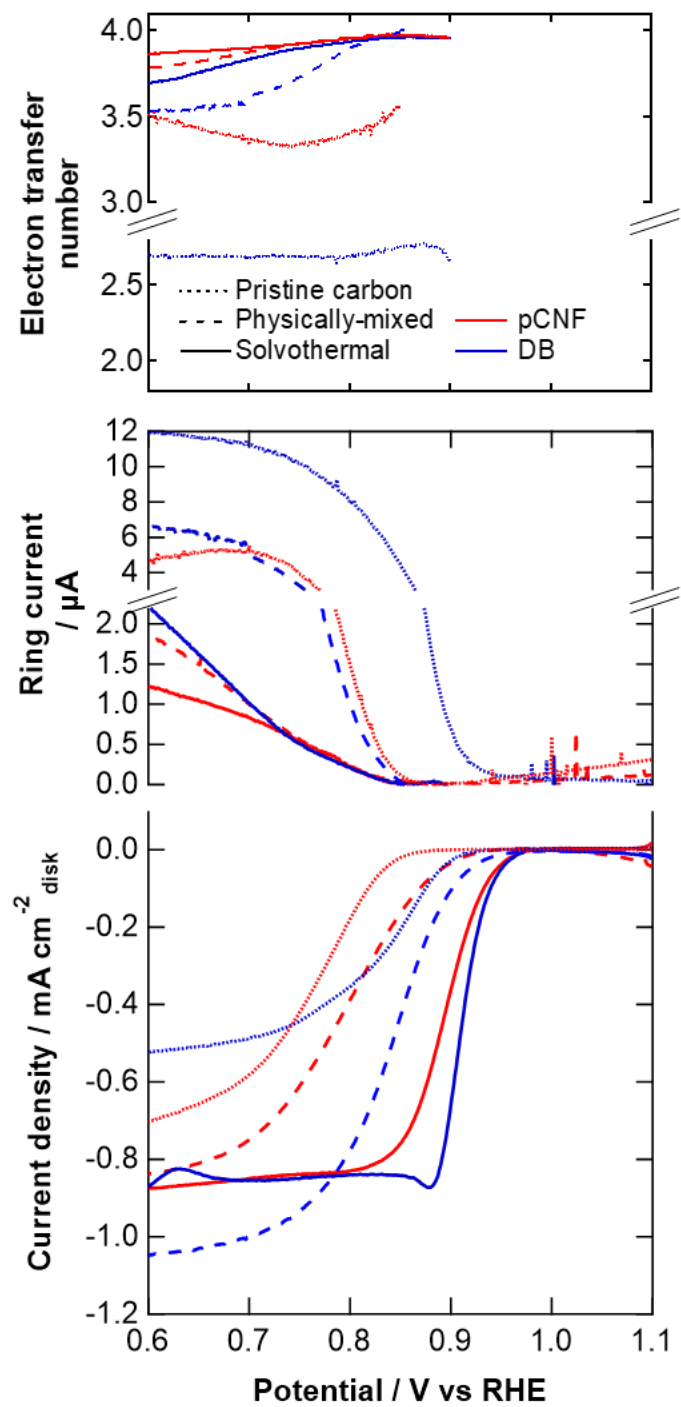


Fig. 5-9 LSV curves for ORR on pCNF and DB samples in O_2 saturated 4 mol dm^{-3} KOH aqueous solution recorded at 1.0 mV s^{-1} .

Fig. 5-10 shows the anodic polarization curves of pristine carbons, physically mixed samples, and carbon/MCO hybrids for OER. Pristine pCNF and DB carbon materials show deficient activities for OER, indicating that OER activities of carbon materials without MCO were negligible. Physically mixed samples showed OER activities originated from MCO nanoparticles. The carbon/MCO hybrids showed higher activities than those of physically mixed samples. The results indicate that higher dispersion of MCO on carbon in the carbon/MCO hybrids led to more appropriated electronic conductivity. The solvothermal synthesis also enabled the improvement of OER activities as well as ORR activities. Therefore, it could be considered that the carbon/MCO interface plays the catalytic center for OER like ORR. The onset potential defined at a current density of 10 mA cm^{-2} is higher than the $\text{Ca}_2\text{FeCoO}_5$ +carbon electrode, which is one of the state-of-art OER electrodes in 4.0 mol dm^{-3} KOH electrolyte (Table 5-3); however, the current density at 1.7 V vs RHE was over 100 mA cm^{-2} , and this can be comparable with $\text{Ca}_2\text{FeCoO}_5$ +carbon electrode [13]. The overpotential of pCNF/MCO at 100 mA cm^{-2} is comparable to the well-known RuO_2 OER active electrocatalyst (Table 5-3).

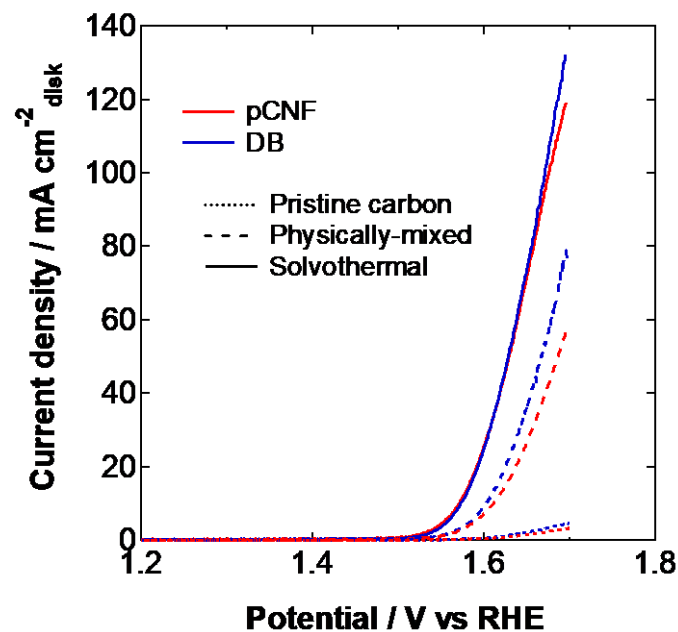


Fig. 5-10 LSV curves for OER on pCNF and DB samples in O_2 saturated 4 mol dm^{-3} KOH aqueous solution recorded at 1.0 mV s^{-1} .

The ORR and OER activities of the carbon/MCO hybrids are compared with those of recently reported bifunctional electrocatalysts (Table 5-3). The bifunctional activity has often been evaluated by ΔE , which is the difference between the OER potential at 10 mA cm⁻² (E_{10}) and the half-wave potential for ORR ($E_{1/2}$) [24]. The ΔE value of the pCNF/MCO is as small as 0.68 V, being comparable to the state-of-the-art bifunctional electrocatalysts. To sum up, it was achieved to prepare the bifunctional electrode, which is comparable with other state-of-arts electrode materials, using the hybridization of carbon and MCO using the solvothermal synthesis. In particular, as mentioned in the previous chapters, the pCNF is the unprecedented corrosion-resistant carbon material under OER in such media due to its structural characters. Thus, the pCNF/MCO hybrid can be considered a candidate for durable air electrode materials with reasonable electrocatalysis properties.

Table 5-3 Comparison of the half-wave potentials for ORR ($E_{1/2}$), the potentials at OER current density of 10 mA cm⁻² (E_{10}), and differences of $E_{1/2}$ and E_{10} (ΔE) of the state-of-the-art electrocatalysts in alkaline media. Each data was obtained by rotating-disk electrode system using catalyst-loaded glassy carbon electrodes. ★ means results obtained in this thesis.

	KOH concentration	$E_{1/2} / \text{V vs RHE}$	$E_{10} / \text{V vs RHE}$	$\Delta E / \text{V}$	Ref
Ca ₂ FeCoO ₅ + Carbon	4.0 M	—	1.50	—	13
Carbon + RuO ₂	4.0 M	—	1.52	—	13
La _{0.7} Sr _{0.3} Mn _{0.9} Ni _{0.1} O _{3-δ} + Carbon	4.0 M	0.91	—	—	25
Pt/C	4.0 M	0.95	—	—	25
CuCoO _x /FeOOH	1.0 M	0.78	1.5	0.72	26
NiO/CoO TINWs	1.0 M	0.82	1.48	0.66	27
Ex-FeN-MC	0.1 M	0.84	1.48	0.64	28
Co ₃ O ₄ /CNT	1.0 M / 0.1 M	0.83 (0.1 M)	1.55 (1.0 M)	0.72	29
MCO/CB	1.0 M	0.75	—	—	3
MCO/N-mGO	1.0 M	0.87	1.55	0.68	3
pCNF/MCO	4.0 M	0.89	1.57	0.68	★
DB/MCO	4.0 M	0.91	1.57	0.66	★

5-3-3 Electrocatalysis evaluation by the gas-diffusion electrode tests

The electrode catalysis performance and durability were further investigated using the gas-diffusion electrode system. Fig. 5-11a shows the charge-discharge performances of carbon/MCO hybrids air electrodes in 8.0 mol dm^{-3} KOH aqueous electrolyte at 40°C . The OER activity is in the following order: DB/MCO > pCNF/MCO > pCNF+MCO, the same as in Fig. 5-11a. While the OER activity difference of the three electrocatalysts is relatively small, the ORR electrocatalysis activities of the carbon/MCO hybrids were markedly higher than those of the pCNF+MCO physical mixture electrode. Thus, the strong carbon-MCO interaction is an important factor in enhancing the OER and ORR activities, and this effect is more significant for ORR than OER in the gas-diffusion air electrode. As mentioned above, direct loading of MCO on the carbon surface possibly provides a new catalytic center, i.e., the interface between the carbon materials and MCO, and this is why both OER and ORR electrocatalysis improved by the hybridization [1]. However, as shown in Fig. 5-11a, the activity enhancement degree is different for OER and ORR, and this difference in activity enhancement is originated from the role of carbon materials [30]. For OER, since the activity of carbon materials was negligible, MCO and the interface between MCO and carbon materials work as the catalytic site. On the other hand, carbon materials work as catalysts for ORR and especially promote peroxide production through the $2e^-$ ORR pathway. It was reported that metal oxides catalyze the electrochemical reduction of peroxide species as well as $4e^-$ ORR [1, 25, 30-34]. Hence, the hybridization of carbon materials and metal oxide possibly accelerates ORR through the pseudo- $4e^-$ ORR mechanism, which combines the $2e^-$ ORR on the carbon surface and further reduces peroxide species on the metal oxide surface. In this mechanism, the diffusion distance of peroxide species produced on the carbon surface is important for the ORR kinetics, and direct loading of MCO on the carbon surface possibly enables to shorten the diffusion distance. Thus, the carbon material strongly affects the ORR, and the hybridization effectively improves the ORR kinetics.

The charge-discharge cycle performance was examined at 20 mA cm^{-2} and plotted in Fig. 5-11b. Stable charge and discharge potentials continue up to 10 cycles for pCNF/MCO and DB/MCO hybrids. The potential difference between charging and discharging is less than 0.7 V. The difference of the onset potential for OER and the half-wave potential for ORR is also as small as 0.68 V for the pCNF/MCO (Table 5-3). The value suggests that the present pCNF/MCO hybrid is the top-class bifunctional electrocatalyst in a range of electrocatalysts reported [24].

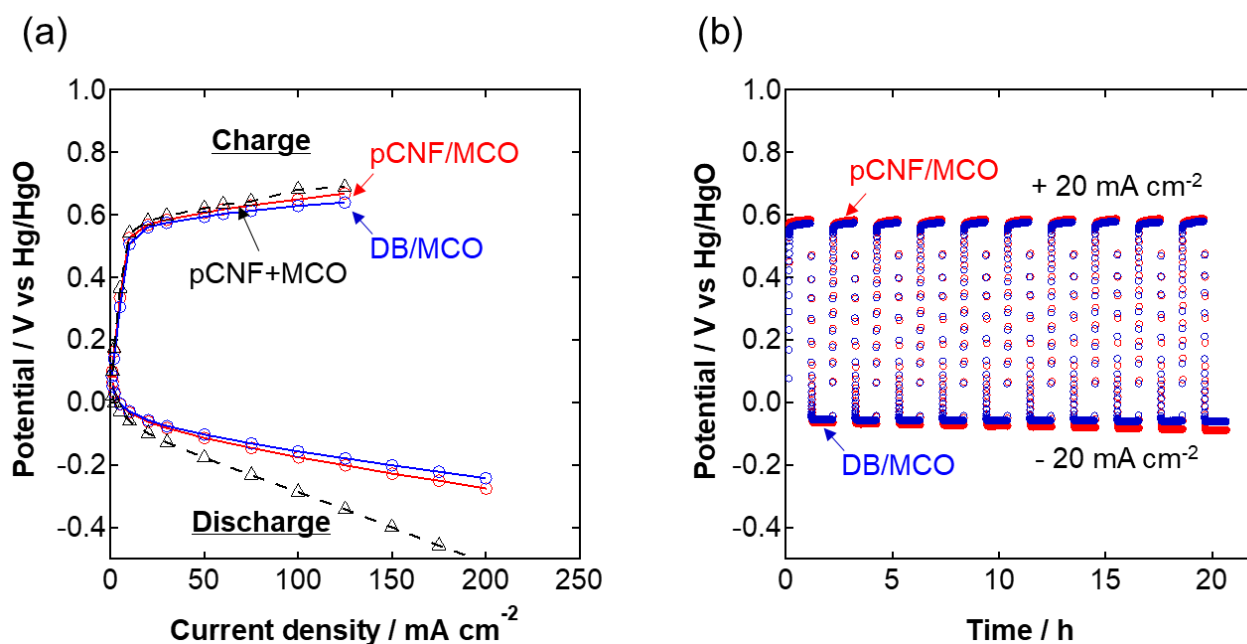


Fig. 5-11 Electrochemical performances of gas-diffusion electrodes with catalyst layers have the carbon/MCO hybrids synthesized in this thesis: (a) charge-discharge performance at 313K in 8.0 mol dm^{-3} KOH aqueous solution under the ambient atmosphere and (b) charge-discharge cycle performance at 20 mA cm^{-2} and 313K in 8.0 mol dm^{-3} KOH aqueous solution under the ambient atmosphere.

However, a decrease in activities was observed for both electrodes (Fig. 5-12). Fig. 5-12 shows the electrode potential changes during cycling for >200 h. The overpotential increase of DB/MCO is faster than the pCNF/MCO, *i.e.*, after 155 h operation, total overpotential, between the OER and ORR, of pCNF/MCO and DB/MCO is 0.84 V and 1.20 V, respectively. Therefore, the pCNF/MCO electrode shows better durability than the DB/MCO. This tendency agreed with the trend of TG analysis, *i.e.*, higher durability of pCNF/MCO than DB/MCO. However, after 170 h operation, pCNF/MCO electrode shows similar total overpotential increase and reached the durability test limits after 220 h operation. Namely, the durability enhancement due to the carbon material's replacement in the catalyst layer is limited compared with the excellent oxidation resistance under the present OER condition.

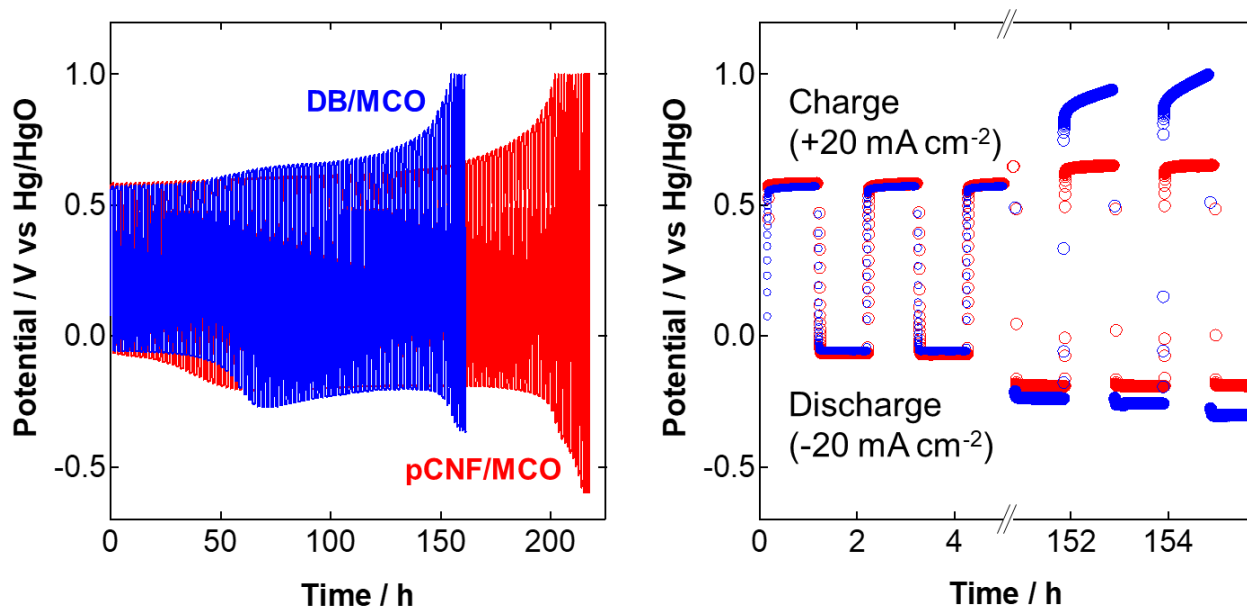


Fig. 5-12 Charge-discharge performances of gas-diffusion electrodes with catalyst layers containing pCNF/MCO and DB/MCO at 20 mA cm^{-2} and $40 \text{ }^\circ\text{C}$ in 8.0 mol dm^{-3} KOH aqueous solution under the ambient atmosphere.

5-3-4 Characterization of the gas-diffusion electrode after the durability tests

In order to understand the minimal improvement of the durability of pCNF/MCO, the catalyst layer was characterized. The GDE surface SEM images before and after the durability test are shown in Fig. 5-13. After the durability test, the electrode surface was covered with flake-like materials derived from MCO. Table 5-4 and Fig. 5-13e are the EDS chemical composition and Raman spectra of the carbon/MCO electrode, respectively. Before the durability test, the chemical compositions of both electrodes are almost similar; however, after the durability test, these compositions are dramatically changed. The Mn/Co ratios are almost 1:2 for both carbon/MCO before the durability test, and these values are changed 4:7 and 3:4 for pCNF/MCO and DB/MCO, respectively, indicating the Mn enrichment at the surface. The Raman spectroscopy discloses the phase change from spinel to a (CoMn)OOH phase. Before and after the durability test, the Raman spectra have two peaks around 490 and 600 cm^{-1} assigned with the MnCo_2O_3 phase [16, 17]. Additional strong peak around 555 cm^{-1} was confirmed after the durability test for DB/MCO electrode and pCNF/MCO electrode. This additional peak may be assigned to a (CoMn)OOH phase [35-38]. The flake-like morphology, observed by SEM, is a characteristic of oxyhydroxides, including CoOOH and MnOOH. Thus, it is suggested that after the durability test, the MCO changed to (CoMn)OOH on the surface. Such transition from metal-oxides to oxyhydroxide during electrochemical polarization in alkaline media was reported by many researchers [39-44]. They reported a positive effect, *i.e.*, electrocatalysis activation or surface area enhancement. However, manganese-based oxyhydroxides and hydroxides typically have poor electrocatalysis for OER and ORR in alkaline media [45, 46], compared with the original spinel-type metal oxides. Therefore, this phase transition may be one of the reasons for the degradation of the air electrode. The carbon contents of electrode surfaces were also analyzed using EDS (Table 5-4). The carbon content for the DB/MCO electrode was markedly reduced after the durability test, and the reduction was associated with carbon corrosion. In contrast, the carbon content reduction during the durability test was limited for the pCNF/MCO electrode because of the high

resistance of pCNF3000 for anodic corrosion. The loss of carbon by anodic corrosion in the catalyst layer loses the electron-conducting path from the current collector to the electrocatalyst, resulting in the faster degradation of DB//MCO than the pCNF/MCO.

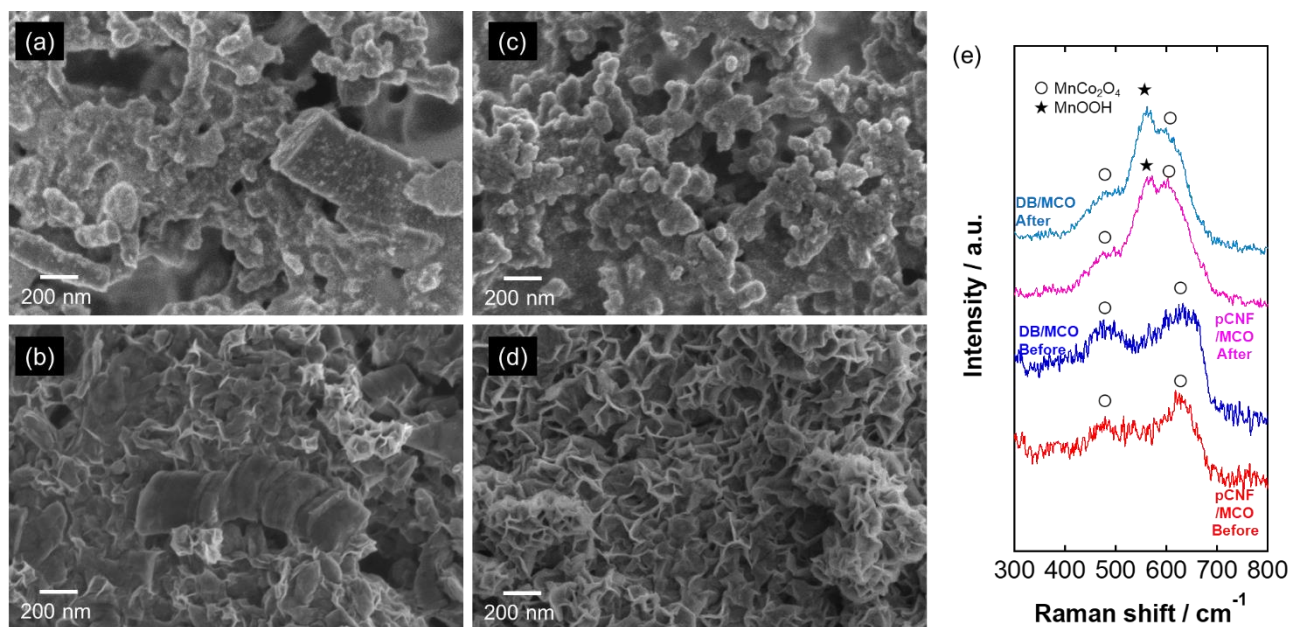


Fig. 5-13 (a-d) The GDE surface SEM images of (a, c) before and (b, d) after the durability tests. (a, b) and (c, d) correspond to pCNF/MCO and DB/MCO, respectively. (e) Raman spectra of gas-diffusion electrodes before and after the durability tests.

Table 5-4 The surface composition estimated by EDS analysis

	pCNF/MCO		DB/MCO	
	Before / at%	After / at%	Before / at%	After / at%
C	68.2±2.9	50.7±3.9	72.3±1.7	36.3±0.9
O	8.6±1.0	19.7±7.9	11.8±0.6	32.4±0.5
F	17.5±3.1	15.3±7.7	7.3±1.3	11.9±0.4
K	0.00	3.1±0.8	0.00	5.3±0.2
Mn	1.8±0.3	3.9±0.7	2.7±0.1	5.8±0.2
Co	4.0±0.4	7.1±0.7	5.8±0.3	8.3±0.4

The wettability of the electrode is another critical factor to provide triple phase boundaries. The water contact angle of the electrode surface was measured before and after the durability test (Fig. 5-14). The water contact angle was $>90^\circ$ before the durability test; the surface is hydrophobic. The surface changed to hydrophilic after the durability test. In particular, the water contact angle on the pCNF/MCO was as low as $\sim 25^\circ$, being smaller than that on the DB/MCO. The wetting of the gas-diffusion electrode reduces the number of triple-phase boundaries, causing reduced ORR activity. Thus, the transformation of the hydrophobic electrocatalyst layer to hydrophilic is detrimental, at least for the ORR activity.

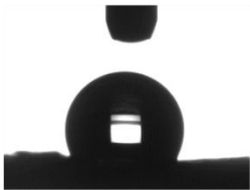
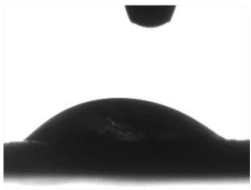
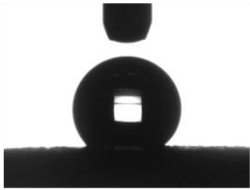
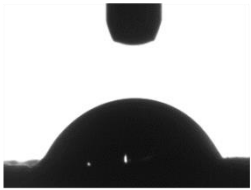
	Water contact angles of electrode surface before the durability test		Water contact angles of electrode surface after the durability test
pCNF/MCO Before	 110.9 ± 7.6 deg. ($n=5$)	pCNF/MCO 105 cycle	 25.5 ± 6.4 deg. ($n=5$)
DB/MCO Before	 127.9 ± 7.3 deg. ($n=5$)	DB/MCO 75 cycle	 58.3 ± 7.2 deg. ($n=5$)

Fig. 5-14 Water contact angles of each electrode before and after the durability test. The volume of water droplet was $2.0 \mu\text{L}$.

Fig. 5-15 shows the cross-sectional images before and after the durability test. The pCNF/MCO layer thicknesses before and after the durability test were 60 and 120 μm , respectively, and the 141- μm -thick DB/MCO layer reduced to 131 μm . The thickness variation may be associated with the non-uniformity of the catalyst layer. After the durability test, the cross-section of DB/MCO shows increased porosity. In contrast, the pCNF/MCO shows little change in the porosity during the durability test. The DB/MCO undergoes carbon dissolution, increasing the porosity. This carbon disappearance is a reason for the fast electrocatalysis degradation of DB/MCO electrodes. However, the pCNF/MCO electrode also shows similar degradation of electrocatalysis even with no carbon support dissolution. Therefore, electrode degradation is controlled by other factors. Table 5-5 summarizes the Mn/Co ratio at the three different depths. Before the durability test, both electrodes have a similar Mn: Co ratio of 1:2 regardless of depth. After the durability test, the ratio changed to 4:7 and 3:4 for pCNF/MCO and DB/MCO, respectively, at the surface region. Thus, an Mn enriched phase is formed. The Mn ratios are decreased for both electrodes after the durability test on the middle and bottom regions of the catalyst layer. Therefore, the Mn enrichment is probably caused by the Mn dissolution on the bottom and middle region and redeposition on the surface.

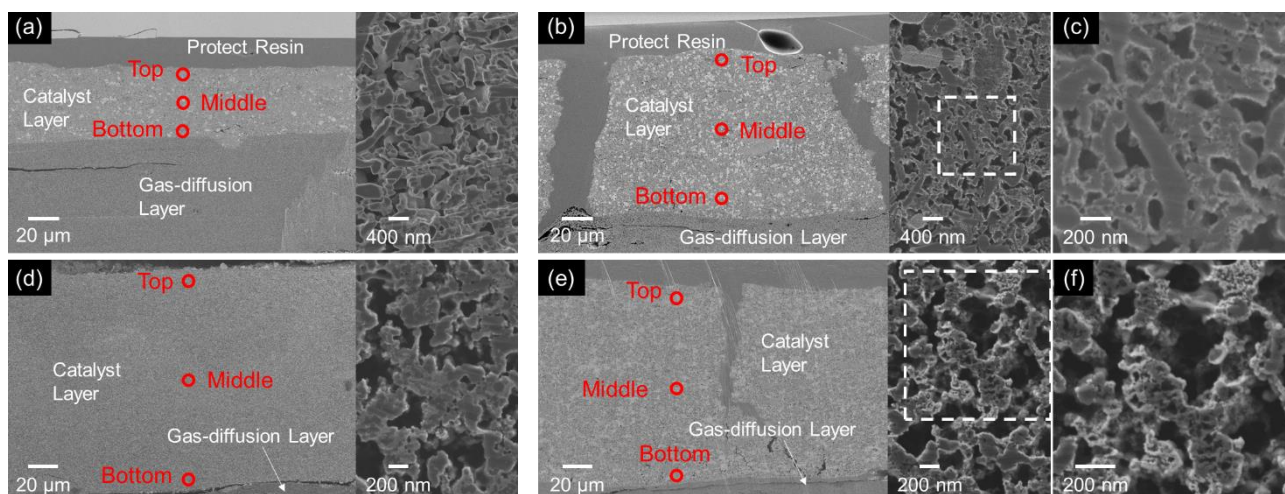


Fig. 5-15 Cross-sectional in-lens SE images of catalyst layer; (a) as-prepared pCNF/MCO, (b, c) pCNF/MCO after the durability test, (d) as-prepared DB/MCO, (e, f) DB/MCO after the durability test.

The red circle means the EDS analysis area which results are shown in Table 5-5.

Table 5-5 The Mn/Co ratio calculated from EDS analysis for the cross-sectional direction.

	pCNF/MCO		DB/MCO	
	Before / -	After / -	Before / -	After / -
Top	0.46±0.01	0.47±0.02	0.46±0.00	0.51±0.03
Middle	0.45±0.00	0.42±0.03	0.46±0.01	0.44±0.03
Bottom	0.46±0.00	0.42±0.03	0.48±0.01	0.42±0.01

In summary, the catalyst layer of carbon/MCO electrodes causes the following changes during the durability test: i) a phase transformation of ORR/OER active MnCo_2O_4 to poorly active $(\text{CoMn})\text{OOH}$, ii) the change from the hydrophobic surface to hydrophilic, reducing the number of triple phase boundaries, and iii) carbon corrosion in the DB/MCO electrode. These changes cause the reduction of OER/ORR activity during charge/discharge cycling, and slightly faster degradation of the DB/MCO may be associated with the faster carbon corrosion of DB. Thus, the actual electrode degradation is not controlled by carbon corrosion only.

The gas-diffusion layer (GDL) was also characterized by the cross-sectional SEM observation and contact angle measurements to evaluate their hydrophobicity. Fig. 5-16 shows the cross-sectional SEM images of GDL made of TB3855 carbon; (a) as-prepared sample, (b) after the durability test with DB/MCO layer, and (c) after the durability test with pCNF/MCO layer. All SEM images were obtained in the GDL near the catalyst layer, *i.e.*, depth in 10 μm from the surface. Before the durability test, the cross-section of GDL shows a relatively dense structure with carbon nanoparticles, with the diameter being around 100 nm. Undergoing the durability test, the GDL shows the increased porosity, and the diameter of carbon nanoparticles in the GDL decreased to around 50-20 nm. Moreover, the film-like material (Arrow in Fig. 5-14), probably the PTFE binder, is visible due to the carbon consumption. Thus, during the GDE operation, the GDL carbon layer undergoes carbon corrosion due to the anodic potentials. As a result, the GDL carbon particles dissolve together with the DB in the catalyst layer. It should be noted that no such corrosion was observed at depths deeper than 50 μm from the surface.

Since carbon corrosion influences wettability [47-49], the GDL wettability was examined before and after the durability tests (Fig. 5-17). The GDL wettability was evaluated on the surface of GDL, which was prepared by peeling off the catalyst layer using double-coated adhesive tape. Before the durability test, the GDL shows a contact angle of 130.7 ± 1.5 deg. These hydrophobic properties are lost after the durability test; for the pCNF/MCO electrode and DB/MCO electrode, the contact angles are changed to 94.5 ± 12.2 deg. and 98.1 ± 5.7 deg., respectively. For the gas-diffusion layer, it is essential to keep the suitable hydrophobicity to achieve rapid gas transportation and avoid water leaking. However, the hydrophobicity of GDL was lost during the durability test due to the carbon corrosion in GDL. These wettability degradations finally cause sluggish mass transportation and electrolyte leakage. Thus, the carbon corrosion in the GDL also has a high possibility to affect the degradation of GDE properties.

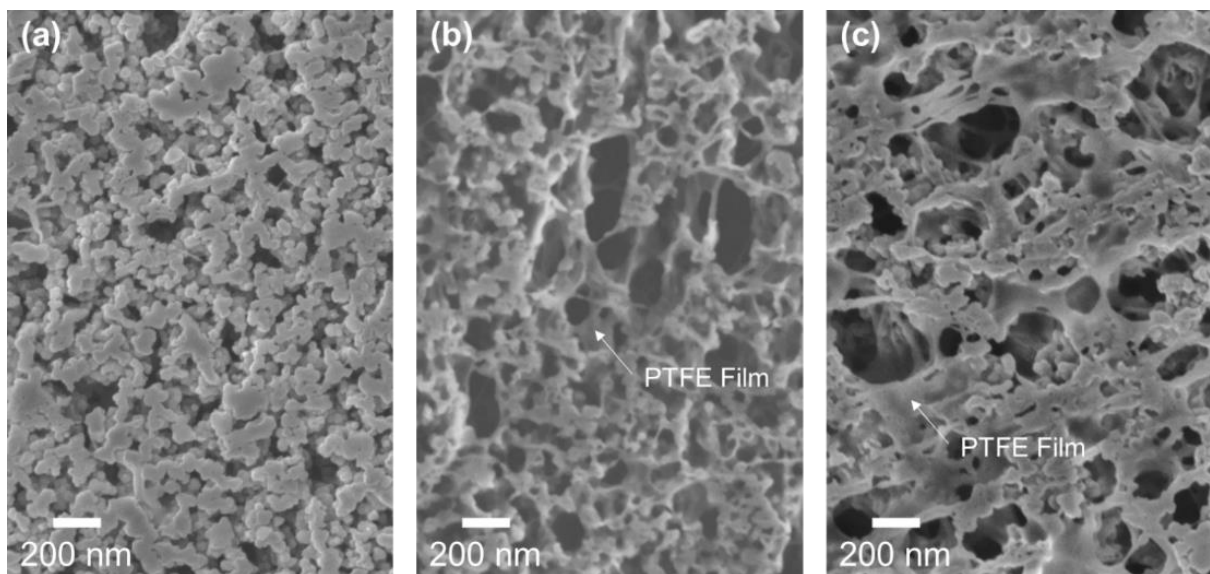


Fig. 5-16 Cross-sectional SEM images of the gas-diffusion layer; (a) as-prepared, (b) after the durability test with pCNF/MCO layer and (c) after the durability test with DB/MCO layer.

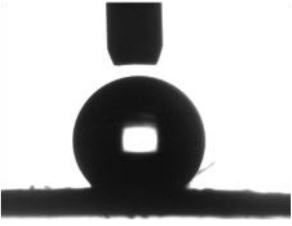
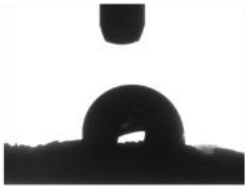

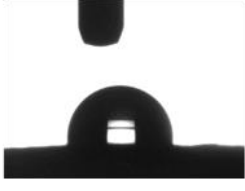
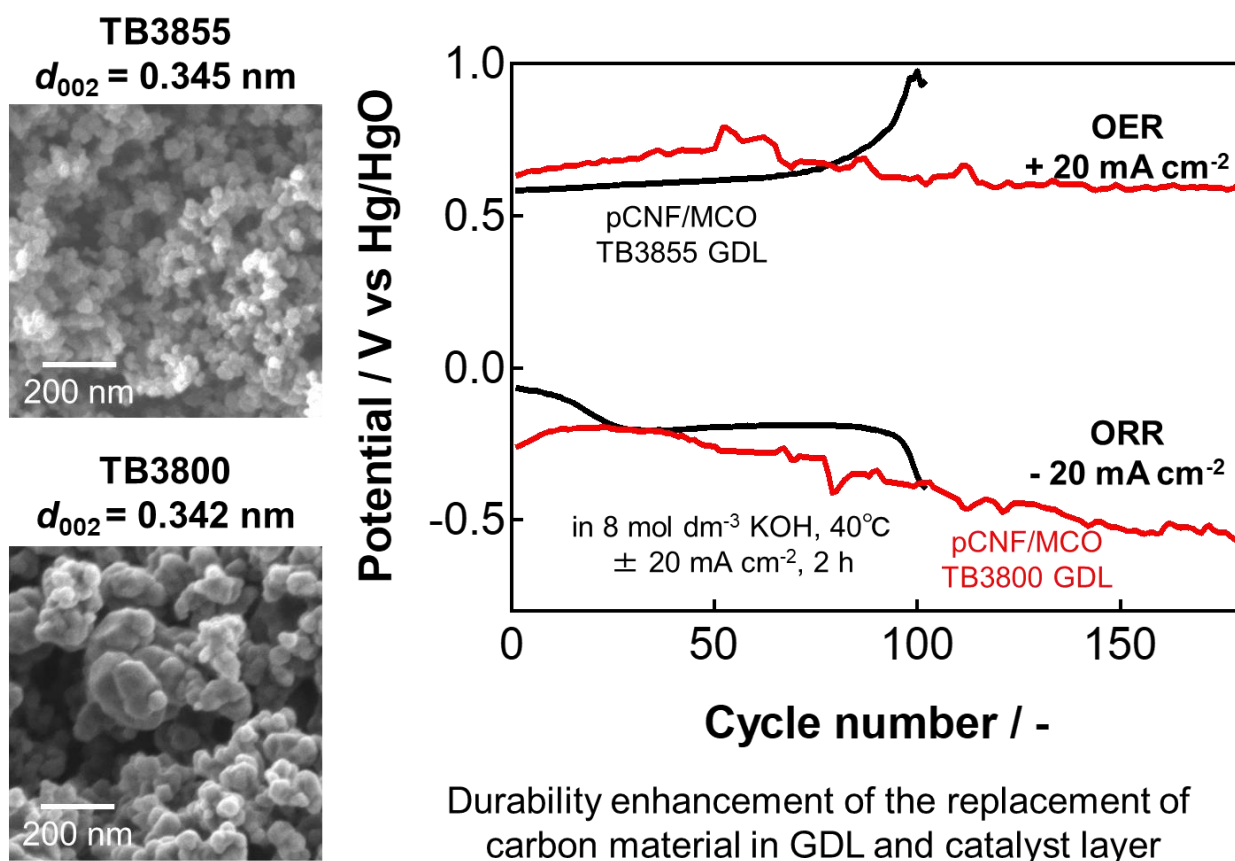
GDL initial water contact angle	GDL water contact angles after the durability test	
	pCNF/MCO 105 cycle	 94.5 ± 12.2 deg. (n=5)
	DB/MCO 75 cycle	 98.1 ± 5.7 deg. (n=5)
130.7 ± 1.5 deg. (n=5)		

Fig. 5-17 Water contact angles of the gas-diffusion layers before and after the durability test. The volume of water droplet was 2.0 μL .

In summary, the carbon corrosion in the GDL also affected the degradation of the GDE. The catalyst layer becomes hydrophilic during the charging/discharging cycles (Fig. 5-14), causing electrolyte penetration to the GDL and carbon corrosion in GDL. The carbon material in GDL is exposed at high potentials in an alkaline environment. It is requested that corrosion-resistant carbon materials be used for GDL. Thus, different carbon materials were examined in this chapter for GDL to investigate the influence of the type of carbon on durability. Two types of carbon blacks, *i.e.*, TB3800 and TB3855 were used here in addition to pCNF3000. Both TB3800 and TB3855 nanoparticles have a similar diameter of ~ 150 nm, but the former possesses a higher graphitization degree: the 002 lattice spacings of TB3855 and TB3800 are 0.345 nm and 0.342 nm, respectively. Fig. 5-17 compares the lifetime of carbon/MCO electrodes using TB3855 GDL and TB3800 GDL. Because of the large particle size of TB3800, the initial electrode overpotentials were larger than the TB3855 case. However, the TB3800 GDL electrode shows a looser increase of the overpotentials due to the suppression of the GDL corrosion.



Durability enhancement of the replacement of carbon material in GDL and catalyst layer

Fig. 5-16 The electrode potential change during the durability test for each carbon/MCO electrode.

5-3-5 Discussion

This chapter demonstrated the ORR activity enhancement of pCNF-based electrodes using solvothermal synthesis. The solvothermal synthesis successfully provided well-dispersed MCO nanoparticles on pCNF3000. The ORR activity of the pCNF3000/MCO electrode is close to the Pt/C one, and its OER activity is also sufficiently high. Thus, the pCNF3000/MCO is a promising bifunctional electrocatalyst.

The electrode durability of pCNF3000/MCO, which was evaluated by the GDE system, was higher than that of the DB-based electrode; however, the durability enhancement of the pCNF3000/MCO was limited, suggesting that other factors also influence the durability of GDE. The

characterizations of the degraded samples suggested that the corrosion inhibition of the carbon support and the stability of the oxide catalyst, hydrophilization of the electrode, and oxidative degradation of the gas diffusion layer carbon need to be improved possibly simultaneously in enhancing the durability of GDE in aqueous metal-air batteries.

The electrode potential change during the durability test shown in Fig. 5-12 suggests that the ORR overpotential of pCNF/MCO changes from 10 h to 50 h while no increment of overpotential in OER. In this stage, the overpotentials for OER and ORR of DB/MCO also show a slight increase. As described above, the interface between MCO and carbon support plays an essential role in the ORR electrocatalysis, while relatively weaker enhancement for OER is provided by such interface. Hence, this degradation, *i.e.*, no OER degradation while ORR activity degradation, should mean that the MCO/carbon interface for the pCNF/MCO electrode was destroyed during the durability test in the initial stage. This interface sites deterioration is probably related to the looped carbon disappearance of pCNF3000. As shown in the previous chapters, the looped carbon on the sidewall of pCNFs are disappeared during the anodic oxidation. This disappearance enabled the MCO nanoparticles detachment from the pCNF surface; as a result, the MCO/carbon interface for the pCNF/MCO electrode was destroyed. After the durability test, the SEM image of the pCNF/MCO electrode showed the bare pCNF surface and catalyst particle agglomeration (Fig. 5-13 b).

After the degradation of ORR for the pCNF/MCO electrode, the total overpotential increment of the DB/MCO electrode started around 50 h in the durability test. In contrast to the pCNF/MCO electrode degradation in the initial stage of the durability test, both overpotentials for OER and ORR were increased for DB/MCO electrodes after 50 h operation. Hence, both OER and ORR are degraded in this stage. It should be considered that this degradation of the DB/MCO electrode was possibly related to the carbon corrosion of DB. The SEM observation (Fig. 5-15) showed that visible carbon

corrosion was only observed in DB/MCO. This carbon corrosion should induce the disappearance of the catalytic interface site and the electrode resistance increment; thus, the carbon corrosion can affect both electrocatalysis for OER and ORR. In contrast, the pCNF/MCO electrode did not show degradation in this stage owing to the carbon corrosion; thus, it is evidence of the durability of pCNF support for OER and ORR in concentrated alkaline media under the gas-diffusion electrode environment.

However, this improvement of the corrosion resistance on the catalyst layer is insufficient to enhance the total lifetime of the gas-diffusion electrode because of the following degradation factors; the hydrophilization of the catalyst layer, the phase transformation of ORR/OER active MnCo_2O_4 to poorly active $(\text{CoMn})\text{OOH}$, and the carbon corrosion in the gas-diffusion electrode. As described above, carbon corrosion made the electrode surface hydrophilic owing to the transformation of MCO to oxyhydroxide and the introduction of the surface hydroxyl group on pCNF3000. Then, the oxygen provision from the gas phase to the porous electrode becomes difficult because of the thoroughly wetting of the porous electrocatalyst layer. Such hydrophilization has often been discussed as the ORR inhibitor phenomenon [50]. Therefore, for pCNF, the hydroxyl group formation on their sidewall caused the positive effect (passivation) and the negative effect (ORR activity degradation) as the GDE material. MCO's chemical/morphological change also possibly affects electrode degradation. The lower electrocatalytic activity of Mn-based oxyhydroxides than the spinel-type oxides was reported elsewhere [45, 46]. Thus, in all durability test periods, this catalyst degradation possibly affects the degradation of OER and ORR electrocatalysis. In addition to the catalyst layer degradation, carbon corrosion of GDL also be noted. Fig. 5-14 discloses the corrosion of carbon near the electrocatalyst layer of GDL. After the corrosion of GDL, electrolyte leakage was often found during the durability test. Hence, the enhancement of the durability of GDL is needed.

In summary, the carbon/MCO GDE causes the following changes during the durability test: i) a phase transformation of ORR/OER active MnCo_2O_4 to poorly active $(\text{CoMn})\text{OOH}$, ii) the change from the hydrophobic surface to hydrophilic, reducing the number of triple-phase boundaries, and iii) carbon corrosion in the DB/MCO catalyst layer and gas-diffusion electrode. These changes cause the reduction of OER/ORR activity during charge/discharge cycling, and slightly faster degradation of the DB/MCO may be associated with the faster carbon corrosion of DB. Thus, the actual electrode degradation is not controlled by carbon corrosion only. It is needed to enhance the lifetime of GDE to improve the durability of the oxide catalyst, the gas diffusion layer carbon, and the hydrophobization of the electrode in a complex manner.

5-4 Conclusions

In this chapter, bifunctional OER/ORR electrodes using a corrosion-resistant pCNF were fabricated using MnCo_2O_4 loading via the solvothermal method, and the OER/ORR activity and durability of the electrodes were evaluated. The following results were obtained.

(1) The solvothermal synthesis produces MCO crystalline nanoparticles uniformly dispersed on pCNF3000 and DB. The MCO/carbon hybrids showed comparable electrocatalytic activity to state-of-the-art bifunctional electrodes for ORR and OER. The pCNF/MCO hybrid activity for both ORR and OER is considerably higher than that of the physical mixture of pCNF and MCO because the strong interface connection between MCO and carbon provides the catalytic center for OER and ORR in highly concentrated alkaline media.

(2) The gas-diffusion electrode (GDE) study reveals the durability of pCNF3000/MCO electrode in the GDE system and the problems of the current GDE system for the metal-air rechargeable batteries. The pCNF/MCO electrode shows a relatively low overpotential for OER and ORR in GDE operation.

This pCNF-containing GDE improves durability compared to the DB/CMO electrode due to the corrosion tolerance of pCNFs. On the other hand, even suppressing the carbon corrosion of the catalyst layer, enough durability enhancement cannot be obtained due to the following reason: i) carbon corrosion in the diffusion layer (GDL), which is confirmed by the SEM observation and the contact angle measurements, ii) a phase transformation of ORR/OER active MnCo_2O_4 to poorly active $(\text{CoMn})\text{OOH}$, and iii) the change from the hydrophobic surface to hydrophilic, reducing the number of triple-phase boundaries.

5-5 References

1. Y. Zhu, W. Zhou, Z. Shao, "Perovskite/Carbon Composites: Applications in Oxygen Electrocatalysis", *Small*, **13**, 1603793 (2017).
2. L. Tao, Q. Wang, S. Dou, Z. Ma, J. Huo, S. Wang, L. Dai, Edge-rich and dopant-free graphene as a highly efficient metal-free electrocatalyst for the oxygen reduction reaction, *Chem. Commun.*, **52**, 2764–2767 (2016).
3. Y. Liang, H. Wang, J. Zhou, Y. Li, J. Wang, T. Regier, H. Dai, "Covalent Hybrid of Spinel Manganese–Cobalt Oxide and Graphene as Advanced Oxygen Reduction Electrocatalysts", *J. Am. Chem. Soc.*, **134**, 3517 (2012)
4. Y. Liang, H. Wang, P. Diao, W. Chang, G. Hong, Y. Li, M. Gong, L. Xie, J. Zhou, J. Wang, T. Regier, F. Wei, H. Dai, "Oxygen Reduction Electrocatalyst Based on Strongly Coupled Cobalt Oxide Nanocrystals and Carbon Nanotubes", *J. Am. Chem. Soc.*, **134**, 15849 (2012).
5. E.J. Yoo, T. Okata, T. Akita, M. Kohyama, J. Nakamura, I. Honma, "Enhanced Electrocatalytic Activity of Pt Subnanoclusters on Graphene Nanosheet Surface", *Nano Lett.*, **9**, 2255-2259 (2009).
6. T. Kondo, Y. Iwasaki, Y. Honma, Y. Takagi, S. Okada, J. Nakamura, "Formation of nonbonding π electronic states of graphite due to Pt-C hybridization", *Phys. Rev. B*, **80**, 233408.
7. Y. Liang, Y. Li, H. Wang, J. Zhou, J. Wang, T. Regier, H. Dai, " Co_3O_4 nanocrystals on graphene as a synergistic catalyst for oxygen reduction reaction", *Nature Mater.*, **10**, 780-786 (2011).
8. X. Zhao, F. Li, R. Wang, J.M. Seo, H.J. Choi, S.M. Jung, J. Mahmood, I.Y. Jeon, J.B. Baek, "Controlled Fabrication of Hierarchically Structured Nitrogen-Doped Carbon Nanotubes as a Highly Active Bifunctional Oxygen Electrocatalyst", *Adv. Funct. Mater.*, **27(9)**, 1605717 (2017).
9. S. Alinejad, J. Quinson, J. Schröder, J.J.K. Kirkensgaard, M. Arenz, "Carbon-Supported Platinum Electrocatalysts Probed in a Gas Diffusion Setup with Alkaline Environment: How Particle Size and Mesoscopic Environment Influence the Degradation Mechanism", *ACS Catal.*, **10(21)**, 13040-13049 (2020).
10. J. Suntivich, H.A. Gasteiger, N. Yabuuchi, Y.S. Horn, "Electrocatalytic Measurement Methodology of Oxide Catalysts Using a Thin-Film Rotating Disk Electrode", *J. Electrochem. Soc.*, **157**, B1263-B1268 (2010).

11. N. Yamada, D. Kowalski, C. Zhu, Y. Aoki, H. Habazaki, “High dispersion and oxygen reduction reaction activity of Co_3O_4 nanoparticles on platelet-type carbon nanofibers”, *RSC Adv.*, **9**, 3726-3733 (2019).
12. H.W. Liang, X. Zhuang, S. Brüller, X. Feng, K. Müllen, “Hierarchically porous carbons with optimized nitrogen doping as highly active electrocatalysts for oxygen reduction”, *Nat. Commun.*, **5**, 4973 (2014).
13. E. Tsuji, T. Motohashi, H. Noda, D. Kowalski, Y. Aoki, H. Tanida, J. Nikura, Y. Koyama, M. Mori, H. Arai, T. Ioroi, N. Fujiwara, Y. Uchimoto, Z. Ogumi, H. Habazaki, “Brownmillerite-type $\text{Ca}_2\text{FeCoO}_5$ as a Practicable Oxygen Evolution Reaction Catalyst”, *ChemSusChem.*, **10(14)**, 2864-2868 (2017).
14. N. Fujiwara, T. Nagai, T. Ioroi, H. Arai, and Z. Ogumi, “Bifunctional electrocatalysts of lanthanum-based perovskite oxide with Sb-doped SnO_2 for oxygen reduction and evolution reactions”, *J. Power Sources*, **451**, 227736 (2020).
15. H. Kumazawa, S. Annen, and E. Sada, “Hydrothermal synthesis of barium titanate fine particles from amorphous and crystalline titania”, *J. Mater. Sci.*, **30**, 4740-4744 (1995).
16. S. Yuvaraj, A. Vignesh, S. Shanmugam, R. Kalai Selvan, “Nitrogen-doped Multi-walled Carbon Nanotubes- MnCo_2O_4 microsphere as electrocatalyst for efficient oxygen reduction reaction”, *Int. J. Hydrog. Energy*, **41**, 15199-15207 (2016).
17. V. Venkatachalam, A. Alsalmeh, A. Alghamdi, and R. Jayavel, “High performance electrochemical capacitor based on MnCo_2O_4 nanostructured electrode”, *J. Electroanal. Chem.*, **756**, 94-100 (2015).
18. Douglas W. McKee, “Metal oxides as catalysts for the oxidation of graphite”, *Carbon*, **8**, 623-626 (1970).
19. S. Aksel, D. Eder, “Catalytic effect of metal oxides on the oxidation resistance in carbon nanotube–inorganic hybrids”, *J. Mater. Chem. A.*, **20**, 9149 (2010).
20. N. Alzate-Carvajal, L. M. Bolivar-Pineda, V. Meza-Laguna, V. A. Basiuk, E. V. Basiuk, E. A. Baranova, “Oxygen Evolution Reaction on Single-Walled Carbon Nanotubes Noncovalently Functionalized with Metal Phthalocyanines”, *ChemElectroChem*, **7**, 428-436 (2020).
21. D.T.D Weerathunga, T. Fujigaya, “The relationship between inherent properties of carbon nanotubes and electrochemical durability of supported-Pt catalysts”, *Diam. Relat. Mater.*, **97**, 107459 (2019).
22. K. Miyazaki, H. Shirakata, T. Abe, N. Yoshizawa, Z. Ogumi, “Novel Graphitised Carbonaceous Materials for Use as a Highly Corrosion-Tolerant Catalyst Support in Polymer Electrolyte Fuel Cells”, *Fuel Cells*, **10**, 960-965 (2010).
23. L. Tao, Q. Wang, S. Dou, Z. Ma, J. Huo, S. Wang, L. Dai, “Edge-rich and dopant-free graphene as a highly efficient metal-free electrocatalyst for the oxygen reduction reaction”, *Chem. Commun.*, **52**, 2764–2767 (2016).
24. X. Wu, C. Tang, Y. Cheng, X. Min, S. P. Jiang, S. Wang, “Bifunctional Catalysts for Reversible Oxygen Evolution Reaction and Oxygen Reduction Reaction”, *Chem. Eur. J.*, **26**, 3906-3929 (2020).
25. Y. Aoki, E. Tsuji, T. Motohashi, D. Kowalski, H. Habazaki, “ $\text{La}_{0.7}\text{Sr}_{0.3}\text{Mn}_{1-x}\text{Ni}_x\text{O}_{3-\delta}$ Electrocatalysts for the Four-Electron Oxygen Reduction Reaction in Concentrated Alkaline Media”, *J. Phys. Chem. C*, **122(39)**, 22301-22308 (2018).
26. M. Kuang, Q. Wang, H. Ge, P. Han, Z. Gu, A. M. Al-Enizi, G. Zheng, “ CuCoOx/FeOOH Core–Shell Nanowires as an Efficient Bifunctional Oxygen Evolution and Reduction Catalyst”, *ACS Energy Lett.*, **2**, 2498–2505 (2017).
27. L. An, B. Huang, Y. Zhang, R. Wang, N. Zhang, T. Dai, P. Xi, C. H. Yan, “Interfacial Defect Engineering for Improved Portable Zinc–Air Batteries with a Broad Working Temperature”, *Angew. Chem., Int. Ed.*, **58**, 9459-9463 (2019).
28. R. Akram, M. A. Ud Din, S. U. Dar, A. Arshad, W. Liu, Z. Wu, D. Wu, “From a ureidopyrimidinone containing organic

- precursor to excavated iron-nitrogen codoped hierarchical mesoporous carbon (Ex-FeN-MC) as an efficient bifunctional electrocatalyst”, *Nanoscale*, **10**, 5658-5666 (2018).
29. M. S. Ahmed, B. Choi, Y. B. Kim, “Development of Highly Active Bifunctional Electrocatalyst Using Co₃O₄ on Carbon Nanotubes for Oxygen Reduction and Oxygen Evolution”, *Sci. Rep.*, **8**, 2543 (2018).
 30. K. Nishio, S. Molla, T. Okugaki, S. Nakanishi, I. Nitta, Y. Kotani, “Effects of carbon on oxygen reduction and evolution reactions of gas-diffusion air electrodes based on perovskite-type oxides”, *J. Pow. Soc.*, **298**, 236-240 (2015).
 31. Y. Aoki, K. Takase, H. Kiuchi, Y. Sato, H. Toriumi, S. Kitano, D. Kowalski, H. Habazaki, “*in-situ* activation of a manganese perovskite oxygen reduction catalyst in concentrated alkaline media”, *J. Am. Chem. Soc.*, **143(17)**, 6505-6515 (2021).
 32. X. Ge, Y. Du, B. Li, T.S. Andy Hor, M. Sindoro, Y. Zong, H. Zhang, Z. Liu, “Intrinsically Conductive Perovskite Oxides with Enhanced Stability and Electrocatalytic Activity for Oxygen Reduction Reactions”, *ACS Catal.*, **6(11)**, 7865-7871 (2016).
 33. E. Fabbri, R. Mohamed, P. Levecque, O. Conrad, R. Kötz, T.J. Schmidt, “Composite Electrode Boosts the Activity of Ba_{0.5}Sr_{0.5}Co_{0.8}Fe_{0.2}O_{3-δ} Perovskite and Carbon toward Oxygen Reduction in Alkaline Media”, *ACS Catal.*, **4(4)**, 1061–1070 (2014).
 34. T. Poux, F.S. Napolskiy, T. Dintzer, G. Kéranguéven, S. Ya. Istomin, G.A. Tsirlina, E.V. Antipov, E.R. Savinova, “Dual role of carbon in the catalytic layers of perovskite/carbon composites for the electrocatalytic oxygen reduction reaction”, *Catalysis Today*, **189**, 83-92 (2012).
 35. C.C. Hu, Y.T. Wu, K.H. Chang, “Low-Temperature Hydrothermal Synthesis of Mn₃O₄ and MnOOH Single Crystals: Determinant Influence of Oxidants”, *Chem. Mater.*, **20**, 2890-2894 (2008).
 36. Z. Chen, C.X. Kronawitter, Y.W. Yeh, X. Yang, P. Zhao, N. Yaoe, B.E. Koel, “Activity of pure and transition metal-modified CoOOH for the oxygen evolution reaction in an alkaline medium”, *J. Mater. Chem. A*, **5**, 842-850 (2017).
 37. T. Zhou, C. Wang, Y. Shi, Y. Liang, Y. Yu, B. Zhang, “Temperature-regulated reversible transformation of spinel-to-oxyhydroxide active species for electrocatalytic water oxidation”, *J. Mater. Chem. A*, **8**, 1631-1635 (2020).
 38. J. E. Post, D. A. McKeown, P. J. Heaney, “Raman spectroscopy study of manganese oxides: Tunnel structures”, *American Mineralogist*, **105**, 1175–1190 (2020).
 39. M.W. Louie, A.T. Bell, “An Investigation of Thin-Film Ni-Fe Oxide Catalysts for the Electrochemical Evolution of Oxygen”, *J. Am. Chem. Soc.*, **135**, 12329–12337 (2013).
 40. M. Risch, A. Grimaud, K.J. May, K.A. Stoerzinger, T.J. Chen, A.N. Mansour, Y. Shao-Horn, “Structural Changes of Cobalt-Based Perovskites upon Water Oxidation Investigated by EXAFS”, *J. Phys. Chem. C*, **117**, 8628–8635 (2013).
 41. J.Q. Adolphsen, B.R. Sudireddy, V. Gil, C. Chatzichristodoulou, “Oxygen Evolution Activity and Chemical Stability of Ni and Fe Based Perovskites in Alkaline Media”, *J. Electrochem. Soc.*, **165**, F827-835 (2018).
 42. D. Kowalski, H. Kiuchi, T. Motohashi, Y. Aoki, H. Habazaki, “Activation of Catalytically Active Edge-Sharing Domains in Ca₂FeCoO₅ for Oxygen Evolution Reaction in Highly Alkaline Media”, *ACS Appl. Mater. Interfaces*, **11**, 28823-28829 (2019).
 43. Y. Sato, Y. Aoki, K. Takase, H. Kiuchi, D. Kowalski, H. Habazaki, “Highly Durable OER Catalyst: Amorphous Oxyhydroxide Derived from Brownmillerite-type Ca₂FeCoO₅”, *ACS Appl. Energy Mater.*, **3**, 5269-5276 (2020).
 44. J.W. Zhao, Z.X. Shi, C.F. Li, Q. Ren, G.R. Li, “Regulation of Perovskite Surface Stability on the Electrocatalysis of

- Oxygen Evolution Reaction”, *ACS Mater. Lett.*, **3**, 721-737 (2021).
45. P.C. Li, C.C. Hu, H. Noda, H. Habazaki, “Synthesis and characterization of carbon black/manganese oxide air cathodes for zinc–air batteries: Effects of the crystalline structure of manganese oxides”, *J. Power Sources*, **298**, 102-113 (2015).
 46. K.B. Ibrahim, M.C. Tsai, S.A. Chala, M.K. Berihun, A.W. Kahsay, T.A. Berhe, W.N. Su, B.J. Hwang, “A review of transition metal-based bifunctional oxygen electrocatalysts”, *J. Chin. Chem. Soc.*, **66**, 829-865 (2019).
 47. G. Chen, H. Zhang, H. Ma, H. Zhong, “Electrochemical durability of gas diffusion layer under simulated proton exchange membrane fuel cell conditions”, *Int. J. Hydrogen Energy*, **34**, 8185-8192 (2009).
 48. W. Wang, J. Luo, S. Chen, “Carbon oxidation reactions could misguide the evaluation of carbon black-based oxygen-evolution electrocatalysts”, *Chem. Commun.*, **53**, 11556-11559 (2017).
 49. H. Liu, M. G. George, M. Messerschmidt, R. Zeis, D. Kramer, J. Scholta, A. Bazylak, “Accelerated Degradation of Polymer Electrolyte Membrane Fuel Cell Gas Diffusion Layers”, *J. Electrochem. Soc.*, **164**(7), F695-F703 (2017).
 50. F. Bidault, D.J.L. Brett, P.H. Middleton, N.P. Brandon, “Review of gas diffusion cathodes for alkaline fuel cells”, *J. Power Sources*, **187**, 39-48 (2009).

Chapter 6
General Conclusions
and Future Prospects

Chapter 6 General Conclusions and Future Prospects

6-1 Conclusions

This thesis investigated the possibility of pCNFs as corrosion-resistant carbon materials for the positive electrodes of aqueous electrochemical energy conversion and storage devices, including alkaline water splitting and aqueous rechargeable air batteries. The pCNFs annealed at $\geq 2000^\circ\text{C}$ were polarized at OER potentials with and without electrocatalyst nanoparticles in a concentrated alkaline electrolyte to examine the corrosion behavior. For comparison, the corrosion behavior of carbon blacks, often used as conductive additives, with different graphitization degrees and multiwalled carbon nanotubes were also studied in this thesis. For the quantitative investigation of the corrosion rates of carbon materials used in this study, an ILSEM technique was introduced, and the corroded surfaces were examined using a STEM/EELS method. The results obtained in this thesis are summarized as follows.

- (1) Platelet-type carbon nanofibers (pCNFs) synthesized by the template-assisted liquid phase carbonization using the anodic alumina template have uniform fiber diameter, controlled by the template pore size. The graphitization degree of the pCNFs increases with increasing the heat treatment temperature and the carbon layers are aligned perpendicular to the fiber axis. In addition, looped carbon layers are developed on the sidewall of pCNFs at $\geq 2000^\circ\text{C}$. Thus, no carbon edge plane is exposed to the surface of the highly graphitized pCNFs. The graphitization degree of the carbon blacks is not enhanced by heat treatment above 2000°C and their surface is mainly composed of the carbon basal plane.
- (2) The identical-location SEM (ILSEM) study is useful for quantitatively determining the corrosion rate of carbon materials at high potentials in a KOH electrolyte. The corrosion rate of pCNFs under

oxygen evolution reaction in 4.0 mol dm⁻³ KOH electrolyte is highly anisotropic. The nanofibers end, consisting of the carbon basal plane, corrodes at a constant rate, and the corrosion rate reduces with an increase in the heat treatment temperature. This trend is also found for the carbon blacks. In contrast, the corrosion rate of the sidewall of pCNFs is extremely low, and there is no detectable corrosion loss by high-resolution SEM after 24 h. The corrosion rate of the sidewall is independent of the graphitization degree for the pCNFs heat-treated at $\geq 2000^\circ\text{C}$.

- (3) The looped carbon layers at the sidewall are eliminated, and the carbon edge plane is exposed to the electrolyte by anodic polarization within 2 h. The high corrosion resistance of the pCNFs is not due to the development of the looped carbon layers but due to the exposure of the graphitized carbon edge plane. A hydroxyl group is present on this carbon edge plane, whereas the content of oxygen is low on the surface of the carbon basal plane. Therefore, the high corrosion resistance of the pCNFs is associated with the passivation of the carbon edge plane by covering with the high density of hydroxyl species. It has been believed that the carbon edge sites are preferential sites of electrochemical oxidation of graphitic carbon. However, possibly high reactivity of the carbon edge plane produces the high density of hydroxyl species on the surface, inducing the passivation of pCNFs. The uniform coverage of the carbon edge plane with hydroxyl species should be a key for passivation.
- (4) The conductive support properties of pCNFs are comparable with the commercially available carbon black materials. pCNF2400/CFCO electrode shows similar onset potential for OER with carbon black/CFCO electrode and over 100 mA cm⁻² current at 1.7 V vs RHE using the rotating-disk-electrode system. The pCNF2400/CFCO shows no OER activity degradation even after a 1-month durability test while the carbon black/CFCO electrodes are degraded.

(5) The spinel-type MnCo_2O_4 nanoparticle loading on the pCNF surface effectively enhances the OER/ORR activity of the pCNF-based electrode. This enhanced electrocatalysis activity is comparable with the recent state-of-art bifunctional electrode materials. However, the durability enhancement due to the carbon material's replacement in the catalyst layer is minimal compared with the excellent oxidation resistance under OER conditions in the gas-diffusion electrode study. Namely, the durability enhancement of the GDE is insufficient even when the pCNFs are used as the catalyst support. Analysis of the degraded samples suggests that the corrosion inhibition of the carbon support and the stability of the oxide catalyst, hydrophilization of the electrode, and oxidative degradation of the gas-diffusion layer (GDL) carbon need to be improved simultaneously.

6-2 Future prospects

As described above, the author successfully prepared the corrosion-tolerance carbon material, *i.e.*, graphitized pCNFs, which can be applied for many applications. This section describes the future prospects obtained through this thesis study.

In Chapter 2, the author prepared pCNFs by the liquid-phase carbonization using an anodic alumina (AAO) template. This synthesis provides controlled diameter. However, using this method, the low yield can become a problem to apply the industrial scale. For example, using 20 g polyvinyl chloride precursor, the final amount of pCNF was only around 100 mg. For carbon nanotubes (CNT), some chemical-vapor-deposition (CVD) methods achieved high purity and inexpensive production costs [2, 3]. Such CVD techniques enable the annual production of 100 tons of CNTs [3]. For the pCNFs, Mochida *et al.* synthesized pCNFs by the CVD method [4]. Hence, further optimization studies of this CVD method for industrial scales, such as using inexpensive catalyst, diameter control techniques, and higher yield, are desired.

In Chapter 5, the durability of the gas-diffusion electrode (GDE) for the zinc-air secondary battery is discussed, and it was concluded that the actual degradation had not been controlled by the carbon corrosion in the catalyst layer only. Hence, in addition to the corrosion resistance of the catalyst layer carbon, optimization of other components in GDE is necessary to enhance the lifetime of GDE. As described in Chapter 5, the actual degradation factors are the following phenomenon in addition to the carbon corrosion in the catalyst layer; i) carbon corrosion in the diffusion layer (GDL), ii) a phase transformation of ORR/OER active MnCo_2O_4 to poorly active $(\text{CoMn})\text{OOH}$, and iii) the change from the hydrophobic surface to hydrophilic, reducing the number of triple-phase boundaries. Based on these factors, the author proposes future engineering studies (Fig. 6-1).

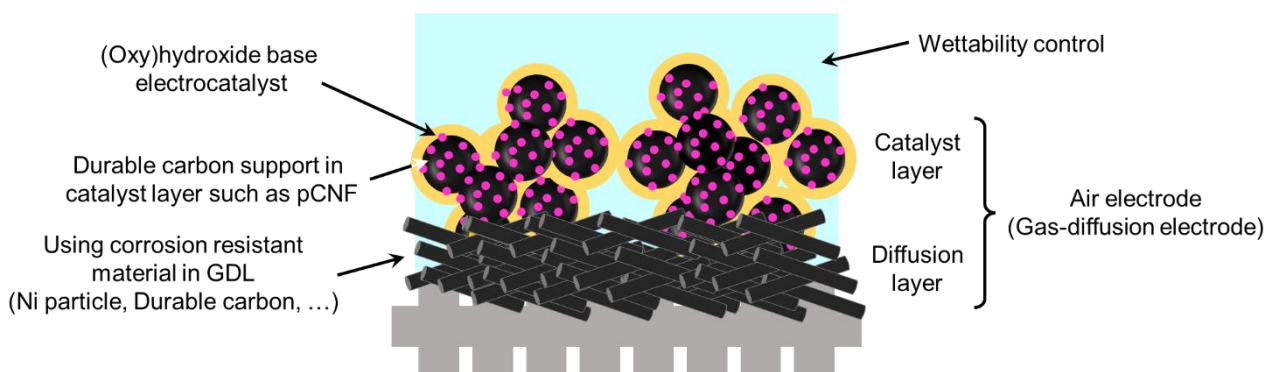


Fig. 6-1 Perspective of the durable gas-diffusion electrodes for metal-air rechargeable batteries.

- (1) GDL should be formed by the more-corrosion tolerance carbon or non-corrosive material such as Ni particles [5]. The GDL plays the role of achieving suitable mass transport, avoiding the electrolytes leaking, and introducing an electron-conducting path. Fig. 5-18 shows that highly graphitized carbon materials for the GDL enhance the electrode lifetime. However, carbon corrosion cannot be avoided even in the TB3800, as shown in Chapter 3. Hence, more durable carbon or alternative material utilization is needed. It should be noted that pCNFs showed the highest durability for the anodic corrosion; therefore, this type of material also can become a candidate as the corrosion tolerance carbon. However, the passivation for the pCNFs also negatively affects the GDL, *i.e.*, hydrophilization. Hence, the wettability control, which explained later, is needed.

- (2) Utilization of hydroxides/oxyhydroxides-based electrocatalysts is desirable. As mentioned above, it is suggested that the spinel-type MnCo_2O_4 oxide transforms to the oxyhydroxide under OER/OER cycling in the alkaline media. Similarly, the transition of some spinel and perovskite oxides to the corresponding hydroxides or oxyhydroxides has been reported [6-10]. Therefore, transition metal hydroxides or oxyhydroxides, which are thermodynamically stable in concentrated alkaline electrolytes, are suitable electrocatalysts for aqueous air batteries [11-13].

- (3) Durable carbon support, such as pCNF, utilization is needed in the catalyst layer. As mentioned in this study, durable carbon usage provides the lifetime enhancement of GDE. Additionally, carbon provides not only electro-conductivity but also the co-catalysis effect [14]. This co-catalysis is not reported in other materials and provides reasonable overpotentials. Due to this reason, some researchers, who are contributing to the carbon-free GDE, propose that carbon material used in the catalyst layer should be accepted [5]. Hence, in the catalyst layer, as the conductive support material, carbon materials should be used.
- (4) The control of the wettability of the electrocatalyst layer and GDL is also important, and the transition from hydrophobic to hydrophilic is detrimental to the electrode performance. In GDE high number of triple-phase boundaries are necessary. Graphitic carbon is usually hydrophobic, being suitable for the hydrophobic GDL and electrocatalyst layer. However, introducing the oxygen-containing functional groups changes the carbon to hydrophilic. In particular, the water contact angle of the pCNFs is very low after introducing the hydroxide group on the sidewall. Thus, for applying the pCNFs to GDL, it is necessary to modify the surface to keep hydrophobicity [15]. Establishing the surface treatment methods of pCNFs to control the surface wettability is crucial for future work.

In this thesis, the corrosion tolerance of pCNFs has been investigated in an alkaline electrolyte. Corrosion-tolerant carbon materials are also needed in polymer electrolyte fuel cells [16], polymer electrolyte electrolysis cells [17], alkaline membrane electrolysis cells, [18] and electrochemical capacitors [19]. These electrochemical devices are crucial for establishing a carbon-neutral society, in which various renewable energy sources must be converted to electricity and hydrogen. Thus, the corrosion tolerance of highly graphitized pCNFs needs to be examined in acid electrolytes and organic electrolytes. If the carbon materials are stably used at elevated temperatures, the corrosion-tolerant carbon is a promising electrode component of solid oxide fuel cells and solid oxide electrolysis cells. The studies on the oxidation behavior of pCNFs at elevated temperatures are also awaited.

The findings obtained through this thesis study provide a new design concept of corrosion-resistant carbon materials to develop durable electrochemical energy conversion devices, including rechargeable ZABs. The author hopes that this study will contribute to developing electrochemical energy conversion and storage technologies.

6-3 References

1. S. De Fonton, A. Oberlin, M. Inagaki, "Characterization by electron microscopy of carbon phases (intermediate turbostratic phase and graphite) in hard carbons when heat-treated under pressure", *J Mater Sci* **15**, 909–917 (1980).
2. 昭和電工ホームページ : 「カーボンナノチューブ「VGCF®-X」の量産を開始」 (in Japanese), https://www.sdk.co.jp/news/2010/aanw_10_1223.html retrieved 06/12/2021.
3. K. Hata, D.N. Futaba, K. Mizuno, T. Namai, M. Yumura, S. Ijima, "Water-Assisted Highly Efficient Synthesis of Impurity-Free Single-Walled Carbon Nanotubes", *Science*, **306**, 1362-1365 (2004).
4. S.H. Yoon, S. Lim, S.H. Hong, I. Mochida, B. An, K. Yokogawa, "Carbon nano-rod as a structural unit of carbon nanofibers", *Carbon*, **42**, 3087-3095 (2004).
5. Z.P. Cano, M.G. Park, D.U. Lee, J. Fu, H. Liu, M. Fowler, Z. Chen, "New Interpretation of the Performance of Nickel-Based Air Electrodes for Rechargeable Zinc–Air Batteries", *J. Phys. Chem. C*, **122**, 20153-20166 (2018).
6. M.W. Louie, A.T. Bell, "An Investigation of Thin-Film Ni–Fe Oxide Catalysts for the Electrochemical Evolution of Oxygen", *J. Am. Chem. Soc.*, **135**, 12329– 12337 (2013).

7. M. Risch, A. Grimaud, K.J. May, K.A. Stoerzinger, T.J. Chen, A.N. Mansour, Y. Shao-Horn, "Structural Changes of Cobalt-Based Perovskites upon Water Oxidation Investigated by EXAFS", *J. Phys. Chem. C*, **117**, 8628–8635 (2013).
8. Y. Sato, Y. Aoki, K. Takase, H. Kiuchi, D. Kowalski, H. Habazaki, "Highly Durable OER Catalyst: Amorphous Oxyhydroxide Derived from Brownmillerite-type $\text{Ca}_2\text{FeCoO}_5$ ", *ACS Appl. Energy Mater.*, **3**, 5269-5276 (2020).
9. J.W. Zhao, Z.X. Shi, C.F. Li, Q. Ren, G.R. Li, "Regulation of Perovskite Surface Stability on the Electrocatalysis of Oxygen Evolution Reaction", *ACS Mater. Lett.*, **3**, 721-737 (2021).
10. J.Q. Adolphsen, B.R. Sudireddy, V. Gil, C. Chatzichristodoulou, "Oxygen Evolution Activity and Chemical Stability of Ni and Fe Based Perovskites in Alkaline Media", *J. Electrochem. Soc.*, **165**, F827–F835 (2018).
11. J. Zhou, Y. Wang, X. Su, S. Gu, R. Liu, Y. Huang, S. Yan, J. Li, S. Zhang, "Electrochemically accessing ultrathin Co (oxy)-hydroxide nanosheets and operando identifying their active phase for the oxygen evolution reaction", *Eng. Env. Sci.*, **12**, 739-746 (2019).
12. S.H. Ye, Z.X. Shi, J.X. Feng, Y.X. Tong, G.R. Li, "Activating CoOOH Porous Nanosheet Arrays by Partial Iron Substitution for Efficient Oxygen Evolution Reaction", *Ang. Chem. Int. Ed.*, **57**, 2672-2676 (2018).
13. C. Dette, M.R. Hurst, J. Deng, M.R. Nellist, S.W. Boettcher, "Structural Evolution of Metal (Oxy)hydroxide Nanosheets during the Oxygen Evolution Reaction", *ACS Appl. Mater. Interfaces*, **11**, 5590–5594 (2019).
14. Y. Zhu, W. Zhou, Z. Shao, "Perovskite/Carbon Composites: Applications in Oxygen Electrocatalysis", *Small*, **13(12)**, 1603793 (2017).
15. F. Forouzandeh, X. Li, D.W. Banham, F. Feng, A.J. Kakanat, S. Ye, V. Birss, "Improving the corrosion resistance of proton exchange membrane fuel cell carbon supports by pentafluorophenyl surface functionalization", *Journal of Power Sources*, **378**, 732-741 (2018).
16. C.A. Reiser, L. Bregoli, T.W. Patterson, J.S. Yi, J.D. Yang, M.L. Perry, T.D. Jarvi, "A Reverse-Current Decay Mechanism for Fuel Cells", *Electrochem. Solid-State Lett.*, **8**, A273-276 (2005).
17. Byung-Seok Lee, Sang Hyun Ahn, Hee-Young Park, Insoo Choi, Sung Jong Yoo, Hyoung-Juhn Kim, Dirk Henkensmeier, Jin Young Kim, Sehkyu Park, Suk Woo Nam, Kwan-Young Lee, Jong Hyun Jang, "Development of electrodeposited IrO_2 electrodes as anodes in polymer electrolyte membrane water electrolysis", *Applied Catalysis B: Environmental*, **179**, 285-291 (2015).
18. I. Vincent, A. Kruger, D. Bessarabov, "Development of efficient membrane electrode assembly for low cost hydrogen production by anion exchange membrane electrolysis", *International Journal of Hydrogen Energy*, **42**, 10752-10761 (2017).
19. R. Tang, K. Taguchi, H. Nishihara, T. Ishii, E. Morallon, D. Cazorla-Amoros, T. Asada, N. Kobayashi, Y. Muramatsu, T. Kyotani, "Insight into the origin of carbon corrosion in positive electrodes of supercapacitors", *J. Mater. Chem. A*, **7**, 7480-7488 (2019).

Lists of academic contributions

Academic publications related to this thesis

1. **Y. Sato**, D. Kowalski, Y. Aoki, H. Habazaki, “Long-term durability of platelet-type carbon nanofibers for OER and ORR in highly alkaline media”, *Appl. Cat. A. General*, **597**, 117555 (2020).
2. **Y. Sato**, S. Kitano, D. Kowalski, Y. Aoki, N. Fujiwara, T. Ioroi, H. Habazaki, “Spinel-type metal oxide nanoparticles supported on platelet-type carbon nanofibers for OER/ORR”, *Electrochemistry (Tokyo)*., **88(6)**, 566-573 (2020).
3. **Y. Sato**, N. Yamada, S. Kitano, D. Kowalski, Y. Aoki, H. Habazaki, “High corrosion resistance and its mechanism of graphitized platelet-type carbon nanofibers under OER in concentrated alkaline electrolyte”, *J. Mater. Chem. A*, *Under Review*.

Other publications

1. 姉帯 一樹, 山田 千波, 奥山 遥, 杉浦 みのり, **佐藤 優樹**, S. Pletincx, H. Verbruggen, 千葉 誠, I. De Graeve, H. Terryn, 高橋 英明, “金属材料の防食のためのマイクロカプセル分散塗膜の自己修復能評価”, *材料と環境*, **65(4)**, 149-153 (2016)
2. M. Chiba, K. Anetai, C. Yamada, **Y. Sato**, H. Okuyama, M. Sugiura, S. Pletincx, H. Verbruggen, A. Hyono, I. De Graeve, H. Terryn, H. Takahashi, “Development of Self-Healing Coatings with Micro Capsules for Corrosion Protection of Metal”, *ECS Trans.*, **75(28)**, 89-99 (2017).
3. A. Zaffora, F. Di. Quarto, C. Kura, **Y. Sato**, Y. Aoki, H. Habazaki, M. Santamaria, “Electrochemical Oxidation of Hf-Nb alloys as a Valuable Route to Prepare Mixed Oxides of Tailored Dielectric Properties”, *Adv. Electron. Mater.*, **4(5)**, 1800006 (2018).

4. J. Cao, **Y. Sato**, D. Kowalski, C. Zhu, Y. Aoki, Y. Cheng, H. Habazaki, "Highly increased breakdown potential of anodic films on aluminum using a sealed porous layer", *J. Solid State Electrochem.*, **22(7)**, 2073–2081 (2018).
5. **Y. Sato**, H. Kobayashi, D. Kowalski, A. Koyama, C. Zhu, Y. Aoki, M. Suto, H. Habazaki, "Ultra-rapid formation of crystalline anatase TiO₂ films highly doped with substrate species by a cathodic deposition method", *Electrochem. Commun.*, **108**, 106561 (2019).
6. **Y. Sato**, Y. Aoki, K. Takase, H. Kiuchi, D. Kowalski, H. Habazaki, "Highly Durable OER Catalyst: Amorphous Oxyhydroxide Derived from Brownmillerite-type Ca₂FeCoO₅", *ACS Appl. Energy Mater.*, **3(6)**, 5269-5276 (2020).
7. R. Yamamoto, D. Kowalski, R. Zhu, K. Wada, **Y. Sato**, S. Kitano, C. Zhu, Y. Aoki, H. Habazaki, "Fabrication of superhydrophobic copper metal nanowire surfaces with high thermal conductivity", *Appl. Surf. Sci.*, **537**, 147854 (2021).
8. T. Komatsu, **Y. Sato**, M. Maeki, A. Ishida, H. Tani, M. Tokeshi, "Rapid, Sensitive Universal Paper-Based Device Enhances Competitive Immunoassays of Small Molecules", *Anal. Chim. Acta*, **1144**, 85-95 (2021).
9. N. Wang, H. Toriumi, **Y. Sato**, C. Tang, T. Nakamura, K. Amezawa, S. Kitano, H. Habazaki, Y. Aoki, "La_{0.8}Sr_{0.2}Co_{1-x}Ni_xO_{3-δ} as efficient triple conductor air electrodes for protonic ceramic cells", *ACS Appl. Energy Mater.*, **4(1)**, 554-563 (2021).
10. Y. Aoki, K. Takase, H. Kiuchi, **Y. Sato**, H. Toriumi, S. Kitano, D. Kowalski, H. Habazaki, "In-situ activation of a manganese perovskite oxygen reduction catalyst in concentrated alkaline media", *J. Am. Chem. Soc.*, **143**, 6505-6515 (2021).

Conference presentations related to this thesis

1. 佐藤 優樹, Damian Kowalski, 青木 芳尚, 幅崎 浩樹, “プレートレット構造カーボンナノファイバーを炭素担体とする酸素発生電極の耐久性”, 電気化学会 2017 秋季大会 (2017 年 9 月, 長崎)
2. Y. Sato, D. Kowalski, C. Zhu, Y. Aoki, H. Habazaki, “Temperature-dependent Structural Change of Platelet-type Carbon Nanofibers”, The 5th International Symposium on Ambitious Leader’s Program for Fostering Future Leaders to Open New Frontiers in Materials Science (November 2017, Sapporo, Japan) **Selected as the poster award**
3. 幅崎 浩樹, 佐藤 優樹, Damian Kowalski, 青木 芳尚, “多孔質アルミナを鋳型として合成した炭素ナノファイバーの金属-空気電池用空気極材料としての耐久性”, 表面技術協会 139 回講演大会 (2019 年 3 月, 横浜)
4. Y. Sato, D. Kowalski, C. Zhu, Y. Aoki, H. Habazaki, “Thermal Oxidation Behavior of Platelet-type Carbon Nanofibers”, The 10th Nagoya Univ.-Tsinghua Univ.-Toyota Motor Corp.-Hokkaido Univ. Joint Symposium (July 2019, Hakodate, Japan)
5. 佐藤 優樹, Damian Kowalski, 青木 芳尚, 幅崎 浩樹, “高アルカリ電解液中における酸素発生・酸素還元用炭素導電材料の酸化消耗に対するナノ構造依存性”, 電気化学会 2019 秋季大会 (2019 年 9 月, 甲府)
6. Y. Sato, H. Habazaki, “Carbon corrosion in the energy devices”, The Students Workshop of the 15th Nanjing University- Hokkaido University-NIMS Joint Symposium (November 2019, Nanjing, China)
7. Y. Sato, D. Kowalski, Y. Aoki, H. Habazaki, “Highly Durable Platelet-Type Carbon Nanofibers for Oer in Alkaline Electrolyte”, 237th ECS Meeting with the 18th International Meeting on Chemical Sensors (IMCS 2020), Accepted; <https://doi.org/10.1149/MA2020-01512805mtgabs>
8. Y. Sato, S. Kitano, D. Kowalski, Y. Aoki, T. Ioroi, N. Fujiwara, H. Habazaki, “Spinel-Type Metal Oxide Nanoparticles Supported on Platelet-Type Carbon Nanofibers for Oxygen Evolution

Reaction and Oxygen Reduction Reaction”, PRiME2020 (October 2020, On-line event)

9. 佐藤 優樹, Damian Kowalski, 北野 翔, 青木 芳尚, 幅崎 浩樹, “高黒鉛化プレートレット炭素ナノファイバーの塩基性溶液中酸素発生反応下における高耐久性機構”, 第 36 回ライラックセミナー・第 26 回若手研究者交流会 (2021 年 6 月, オンライン) (ポスター) ポスター賞受賞
10. 佐藤 優樹, Damian Kowalski, 北野 翔, 青木 芳尚, 幅崎 浩樹, “塩基性 OER 環境下で消耗しないナノ構造炭素材料の耐食機構”, 2021 年電気化学会秋季大会 (2021 年 9 月, オンライン)

Other conference presentations

1. Junhui Cao, 佐藤 優樹, Damian Kowalski, 朱 春宇, 青木 芳尚, 幅崎 浩樹, “封孔処理した多孔質アルミナ層の導入によるアルミニウムアノード酸化皮膜の絶縁破壊電圧の上昇”, 表面技術協会 137 回講演大会 (2018 年 3 月, 江東区)
2. 前田 陵我, 小松 雄士, 佐藤 優樹, 真栄城 正寿, 石田 晃彦, 谷 博文, 渡慶次 学, “ペーパーデバイスによる POCT のための高感度競合的 ELISA の実現”, 化学とマイクロ・ナノシステム学会 第 38 回研究会 (38th CHEMINAS) (2018 年 10 月, 札幌)
3. 青木 芳尚, 佐藤 優樹, Damian Kowalski, 幅崎 浩樹, “ブラウンミラー型 $\text{Ca}_2\text{FeCoO}_5$ の OER 電極触媒活性相の同定”, 第 60 回電池討論会 (2019 年 11 月, 京都)

その他, 自己修復機能高分子コーティングの研究に関連した講演 12 回,

電解析出二酸化チタン薄膜に関連した講演 6 回, 電極触媒材料に関連した講演 7 回。

Patents

1. “多層構造体及び多層構造体の製造方法”, 須藤 幹人, 鈴木 威, 中川 祐介, 小島 克己, 幅崎 浩樹, 佐藤 優樹, WO2018225861 (2017年6月出願, 2018年12月公開) .
2. “物質検出装置”, 渡慶次 学, 石田 晃彦, 小松 雄士, 佐藤 優樹, 特開 2020-20601 (2018年7月出願, 2020年2月公開)

Awards

1. 化学系学協会北海道支部 2015 年冬季研究発表会「優秀講演賞」(2015.1)
2. 旭川工業高等専門学校学生表彰「学術振興表彰」(2015.3)
3. 平成 26 年度日本化学会 「北海道支部賞」 (2015.3)
4. 北海道大学工学部 「大島義清先生記念賞」(2017.3)
5. The 5th International Symposium on AMBITIOUS LEADER’ S PROGRAM Fostering Future Leaders to Open New Frontiers in Materials Science “Poster award” (2017.11)
6. 電気化学会北海道支部 第 36 回ライラックセミナー・第 26 回若手研究者交流会「ライラックポスター賞」(2021.6)

Acknowledgements

This thesis study research has been carried out under the supervision of Professor Hiroki Habazaki and all staff in the Laboratory of Interfacial Electrochemistry (LIEc), Graduate school of Chemical Science and Engineering, Hokkaido University, from 2017 through 2022. I would like to show my gratitude to all people who always support and stimulate me.

I would like to express my significant and deepest gratitude to Professor Hiroki Habazaki for his supervision and leading through my six years at the LIEc. My acknowledged emotion for him is tough to explain and too huge. Anytime, anywhere, he supported me and guided me to become an advanced and doctoral researcher. I am not an intelligent and good-manner student; however, he did not give up supervising me. Now I could feel the inevitable growth of my ability through the lab work in LIEc. Every discussion, every memory, every occasion with him is the cornerstone of me as a researcher. As many of you know, he is one of the biggest electrochemists. I understand that learning from him is a precious and rare experience. I would like to learn more; however, now I should leave here. In Korean words, the term “going downhill” describes standing alone. Now, I will go downhill from “Habazaki-Mountain” and work for society. I think that the best way to repay him is that I work hard in the community and let Habazaki-sensei hear the good news. Now is the not goal and not final. I continue to improve myself. I believe in his eternal and fruitful success and health for the future.

I am also grateful to Professor Kazuhisa Azumi and Professor Kei Murakoshi, Hokkaido University, for their careful readings and suggestive advice and assessment to complete this thesis. They always supported me through continuous advice and supervision as my thesis examination committee member. In addition, for me, casual conversations with them were very stimulating, and I could learn many things from them. I would like to respect them and pray for their continued success and health.

I also would like to sincerely appreciate Associate Professor Yoshitaka Aoki (Hokkaido University), Assistant Professor Damian Kowalski (University of Warsaw), Specially Appointed Assistant Professor Sho Kitano (Hokkaido University), Ms. Yukako Yamashita (Hokkaido University), and Mr. Kentaro Takase (Murata Manufacturing Co., Ltd.) for their continuous and valuable suggestion and help through experimental and discussions with them. Their assistance constantly stimulated me, and I could learn many things from their attitude toward science. In addition, I am very proud to touch the RISING2 project with them. I sometimes felt this project troublesome; however, joining this project promoted my intelligence and capability considerably. Without their assistance, I could not continue to join this project. Every memory and experience with them are worth, suggestive, and precious for me. I would like to pray for their future success and health.

I would like to appreciate Dr. Naoko Fujiwara, Dr. Tsutomu Ioroi, and Ms. Akiko Nakamura at the National Institute of Advanced Industrial Science and Technology for their guidance and technical suggestions for the gas-diffusion electrode study described in Chapter 5. Without their assistance, I could not complete this thesis study. I could not help wishing for their continued success and health.

I also would like to declare my acknowledgments for Associate Professor Norihito Sakaguchi in Hokkaido University, Assistant Professor Hisao Kiuchi in the University of Tokyo, Mr. Ryo Ota, Mr. Ryuji Tanioka, Mr. Kenta Suzuki, Ms. Naomi Hirai, Ms. Yuko Mori, Ms. Ayako Yokohira, Mr. Kenji Okubo, Ms. Suzuka Yoshida, Ms. Emiko Obari, Ms. Yurika Yamanouchi, Ms. Rena Ishikawa, Mr. Shouhei Shimoda, Dr. Takashi Endo, and Assistant Professor Yongming Wang in Hokkaido University for their technical assistance and suggestions such as EXAFS measurements for $\text{Ca}_2\text{CoFeO}_5$, STEM/EELS analysis, SEM observation, Cross-sectional polishing, and nitrogen isotherm measurements.

I would like to sincerely thank Professor Chunyu Zhu in China University of Mining and Technology, Dr. Akira Koyama in Nippon Steel, Dr. Takeshi Komatsu in Asahikasei corporation, Professor Manabu Tokeshi in Hokkaido University, Associate Professor Koji Fushimi in Hokkaido University, Assistant Professor Akihiko Ishida in Hokkaido University, Professor Soo-Gil Park in Chungbuk National University, Professor Emeritus Masahiro Seo in Hokkaido University, and Associate Professor Etsushi Tsuji in Tottori University. They provided kind help, suggestive advice, and fruitful discussion for me. In addition, for me, casual conversations with them were very informative, and they enabled me to learn many things to be needed as a scientific researcher. I sincerely pray for their future success and health. Especially, Professor Manabu Tokeshi and Professor Akihiko Ishida supported me through the Lab-visiting program organized by the Ambitious Leader's Program -fostering Future Leaders to Open New Frontiers in Materials Sciences- (ALP) with Dr. Takeshi Komatsu. Through the Lab-visiting program, I could open my knowledge range and understand the common routine to solve the problem for every research area. Of course, this experience helped my thesis study. I hope for the eternal development and success of Tokeshi Laboratory.

My sincere appreciation also goes to Seongwoo Jeong, the best friend and rival for me in the electrochemical society and Korean people. We fought together and supported each other for these six years. For me, traveling everywhere with him through the academic conferences and educational program is one of the unforgettable memories in my life in LIec. He is a brilliant, engaging, and kind person. I strongly think he could become the researcher who can rule the world. I hope to meet again with him soon.

My sincere thanks also go to Professor Paweł J. Kulesza, Dr. Iwona Agnieszka Rutkowska, Ms. Kamila Brzozowska, and all members of Kulesza Laboratory at the University of Warsaw for their help through the Internship program held in 2019. I experienced many precious opportunities in

Warsaw and learned many things. On this occasion, Poland has become my most favorite nation! At first, starting science investigation in a completely new environment with no acquaintances and no Japanese-speaking people was too tricky for me. However, their assistance broke such difficulty. In addition, learning the Polish culture such as “Tłusty Czwartek” opened my mind for international understanding as a Doctoral student. I will never forget these precious memories in Warsaw. Bardzo Dziękuję!! Modlę się o ich przyszły sukces i zdrowie.

I could not skip declaring my appreciation for my former teachers and best friends in Asahikawa National College of Technology; especially, I would like to engrave the following names in this thesis; Associate Professor Makoto Chiba, Associate Professor Ryosuke Sakai, Professor Katsuyuki Tsuda, Associate Professor Takuya Konishi, Professor Emeritus Hideaki Takahashi, former Professor Tsuyoshi Dobashi, Assistant Professor Atsushi Hyono, Dr. Yoshinobu Mato, Hiroaki Kanayama, Masaya Kamishita, Ikumi Kobayashi, and Hirotaka Mihara. All of the experiences and memories of those days were essential to form my personality. They were sweet, joyful, and a necessary scene in my youthhood. I think that if I hadn't met them, I wouldn't be here now. I continue to pray for their future success and health.

My particular significant appreciation should go to my precious colleagues in Hokkaido University, and especially, I would like to engrave the following names: Seongwoo Jeong, Kentaro Takase, Keisuke Wada, Tomohiro Inoue, Yumehiro Manabe, Shuhei Yamasaki, Dr. Yoshinobu Mato, Ferreira da Rosa Pedro Paulo, Yu Ozawa, Rina Takahashi, Takuya Shimajiri, Kanami Sugiyama, Nobuaki Oyamada, and Ryogo Nakagawa. They, especially Seongwoo and Yumehiro, always stood by me and put up an umbrella when I faced the harrowing scene. They were good friends and good rivals for me. I would like to continue to work hard together. I could not help wishing for their fruitful life, success, and health in the future.

I also would like to thank Ms. Kanae Inoue, Ms. Yoko Iwata, Ms. Tomoko Ishikawa, Ms. Yoshie Sannami, Ms. Kumi Fukuda, Ms. Tamaki Watanabe, Ms. Seika Sato, and Ms. Maki Tanaka. They support me through the secretary work. Their quick and perfect works always helped my doctoral study on my budgets, office works, and trips. I could not help wishing for their continued success and health.

My thanks are also extended to all the students of the Laboratory of Interfacial Electrochemistry who have helped and made my research life so enjoyable; Dr. Khurram Rao Shazard, Dr. Cao Jinhui, Dr. Cheong Kim, Dr. Ning Wang, Dr. Laras Fadillah, Dr. Katsutoshi Nakayama, Dr. Chiharu Kura, Takuya Hiraga, Shiki Matsuura, Kazumasa Kikutani, Ryosuke Sakashita, Ryosuke Tomisawa, Taisei Kobayashi, Yuto Okazaki, Kosuke Kuroda, Atsushi Kasuga, Tomoyuki Yamaguchi, Yusuke Kunii, Xiangjun Shen, Naohito Yamada, Hikaru Kobayashi, Manami Takata-Agata, Miku Saito, Hajime Toriumi, Chunmei Tang, Tatsuyuki Takano, Jumpei Ikeura, Shin'ichi Nishimura, Ruijie Zhu, Naohiro Hasuo, Kensuke Sakuraba, Ryoya Masuda, Ryota Yamamoto, Katsuya Akimoto, Masahiro Nishimoto, Takahiro Mori, Yuya Yato, Shuya Fujita, Xiong Zetao, Reiko Takusari, Naoki Kamitani, Daisuke Endo, Jaewon Jeon, Mikio Nagae, Hisato Matsuya, Hiroya Motohashi, Takuya Takahashi, Kai Shuto and all international students/research fellows. The memories spent with them are treasures in my life. I pray for their future success and health.

The part of this thesis study results was obtained through the support by the following research program; Grant-in-Aid for Japan Society for the Promotion of Science (JSPS) Research Fellow (JP21J10674); Nanotechnology Platform Program (A-17-HK-0005, A-18-HK-0016, A-19-HK-0003, A-20-HK-0002, and A-21-HK-0035) and Hokkaido University Ambitious Leader's Program - fostering Future Leaders to Open New Frontiers in Materials Sciences- (ALP) of the Ministry of Education, Culture, Sports, Science and Technology, Japan. I would like to acknowledge such supports gratefully. In addition, the Laboratory of XPS analysis and Multi-Quantum Beam High Voltage

Electron Microscope Laboratory in Hokkaido University are well-acknowledged because a part of this thesis study was conducted there. I also would like to thank the financial support from the JSPS research fellow program and ALP. Some of the pictures/illustrations are reprinted and reused under permission from the American Chemical Society, Elsevier, Royal Society of Chemistry, and John Wiley and Sons Publishing.

Finally, I am particularly grateful to my family, Yuriko Sato and Naoki Sato, for their enduring understandings and support. Without their support, I could not complete this thesis study. I would like to show gratitude deeper than the sea.

March 2022

佐藤 優樹

Yuki Sato